



CIVIL ENGINEERING STUDIES
Illinois Center for Transportation Series No. 17-025
UIIU-ENG-2017-2025
ISSN: 0197-9191

EFFECT OF EARLY-AGE CONCRETE ELASTIC PROPERTIES ON FATIGUE DAMAGE IN PCC PAVEMENTS CONTAINING FIBERS

Prepared By
Mohsen A. Issa, PhD, PE, SE, F.ACI, F. ASCE
Professor of Structural and Materials Engineering

Department of Civil and Materials Engineering
University of Illinois at Chicago

Research Report No. FHWA-ICT-17-019

A report of the findings of
ICT PROJECT R27-154
Effect of Early-Age Concrete Elastic Properties on Fatigue
Damage in PCC Pavements Containing Fibers

TECHNICAL REPORT DOCUMENTATION PAGE

1. Report No. FHWA-ICT-17-019		2. Government Accession No. N/A		3. Recipient's Catalog No. N/A	
4. Title and Subtitle Effect of Early-Age Concrete Elastic Properties on Fatigue Damage in PCC Pavements Containing Fibers				5. Report Date December 2017	
				6. Performing Organization Code N/A	
7. Author Mohsen A. Issa, PhD, PE, SE, F.ACI, F. ASCE Professor of Structural and Materials Engineering Department of Civil and Materials Engineering University of Illinois at Chicago 2095 Engineering Research Facility, (M/C 246) 842 West Taylor St., Chicago, IL 60607				8. Performing Organization Report No. ICT-17-025 UILU-ENG-2017-2025	
9. Performing Organization Name and Address Illinois Center for Transportation Department of Civil and Environmental Engineering University of Illinois at Urbana-Champaign 205 North Mathews Avenue, MC-250 Urbana, IL 61801				10. Work Unit No. N/A	
				11. Contract or Grant No. R27-154	
12. Sponsoring Agency Name and Address Illinois Department of Transportation (SPR) Bureau of Research 126 East Ash Street Springfield, IL 62704				13. Type of Report and Period Covered Final Report: 1/1/2015 – 12/15/2017	
				14. Sponsoring Agency Code FHWA	
15. Supplementary Notes Conducted in cooperation with the U.S. Department of Transportation, Federal Highway Administration.					
16. Abstract The Illinois Department of Transportation (IDOT) is revising current specifications for opening new PCC (Portland cement concrete) pavements to traffic. These revisions will help keep closure times at a minimum by specifying the required concrete strength for resisting early-age fatigue damage. An extensive experimental program was conducted at the University of Illinois at Chicago to determine the elastic properties of IDOT pavement (PV) and patch (PP1, PP2) mixes at early concrete age. The experimental program included testing concrete specimens as early as 12 hr with two curing regimes (73°F and 50°F). The effect of fiber inclusion was investigated by considering two types of IDOT-certified synthetic macro-fibers (W.R. Grace Strux 90/40 and BASF MasterFiber MAC Matrix) with quantities of 0, 4, 6, and 8 lbs. /yd ³ . The experimental program initiated with determining mechanical properties of early-age pavement and patch concrete mixes for compressive strength, flexural strength, flexural toughness, static modulus of elasticity, and linear drying shrinkage. The fracture behavior, flexural fatigue performance, and durability against freezing and thawing were investigated at early concrete age. The study also evaluated the effectiveness of nondestructive measures such as maturity and dynamic modulus of elasticity tests for predicting the strength gain for IDOT pavements mixes. Experimental and numerical data was implemented into a practical solution for opening PCC pavements to traffic loads at an early age. The proposed step-by-step procedure evaluates the fatigue life of rigid pavements for a predefined thickness, soil condition, and concrete age. Designs aids were accordingly developed for accurately estimating concrete flexural strength, pavement tensile stress, and corresponding fatigue life through practical equations, charts, and nomographs. With fiber inclusion yielding an improved structural performance, the experimental testing program was further extended by evaluating the fatigue behavior of jointed, plain-concrete pavement (JPCP) specimens at early concrete age. For this experimental task, the loading sequence, fiber content, pavement thickness, and dowel presence were investigated for a critical loading case at contraction joints. Experimental results were satisfactory for plain and fiber-reinforced jointed-slab specimens subjected to early-age cyclic fatigue loading.					
17. Key Words concrete pavement, early opening to traffic, synthetic fibers, cyclic fatigue, dynamic modulus, toughness, fracture-mechanics, maturity, freeze-thaw, dowel bars, jointed-pavement			18. Distribution Statement No restrictions. This document is available through the National Technical Information Service, Springfield, VA 22161.		
19. Security Classif. (of this report) Unclassified		20. Security Classif. (of this page) Unclassified		21. No. of Pages 164 pp + appendices	22. Price N/A

ACKNOWLEDGMENT, DISCLAIMER, MANUFACTURERS' NAMES

This publication is based on the results of **ICT-R27-154, Effect of Early-Age Concrete Elastic Properties on Fatigue Damage in PCC Pavements Containing Fibers**. ICT-R27-154 was conducted in cooperation with the Illinois Center for Transportation; the Illinois Department of Transportation, Division of Highways; and the U.S. Department of Transportation, Federal Highway Administration.

Members of the Technical Review Panel were the following:

James Krstulovich – IDOT, BMPR, TRP Chair

Randell Riley – IL ACPA

Wanching Huang – Interra, inc.

Matt Mueller – Interra, inc.

Joshua Allen – ICT

Nathan Townsend – ICT

Patty Altstetter, ICT

Chuck Wienrank – IDOT

Derek Parish – IDOT

Kent DeMay – IDOT

Megan Swanson – IDOT

Michael Carnahan – IDOT

Ryan Sheley – IDOT

Tom Weck – IDOT

Charles Wienrank – IDOT

The research team would like to acknowledge the help provided by Ozinga, inc. for securing all aggregate materials, BASF Corporation for providing the required admixtures, and W.R. Grace and Company for providing fibers throughout the project. The research team would also like to acknowledge the department of civil and materials engineering at the University of Illinois at Chicago for providing the cost sharing.

The contents of this report reflect the view of the author(s), who is (are) responsible for the facts and the accuracy of the data presented herein. The contents do not necessarily reflect the official views or policies of the Illinois Center for Transportation, the Illinois Department of Transportation, or the Federal Highway Administration. This report does not constitute a standard, specification, or regulation.

Trademark or manufacturers' names appear in this report only because they are considered essential to the object of this document and do not constitute an endorsement of product by the Federal Highway Administration, the Illinois Department of Transportation, or the Illinois Center for Transportation.

EXECUTIVE SUMMARY

Increasing traffic volumes in the state of Illinois have raised the need for cost-effective and reliable methods to keep closure times at a minimum during road construction and rehabilitation work. Thus, the Illinois Department of Transportation (IDOT) is interested in reevaluating its current construction specifications to possibly allow criteria for opening newly poured rigid pavements or patches to traffic loads.

Per Articles 701.17(c)(5) and 701.17(e)(3) of IDOT's *Standard Specifications for Road and Bridge Construction*, current criteria pertaining to early opening to traffic require a certain concrete strength (compressive or flexural) to be attained (IDOT 2016). For example, prior to opening to traffic, Class PV pavement mixes should attain a minimum 3,500 psi in compressive strength or 650 psi in flexural strength, while Class PP-1 patching mixes should attain a minimum 3,200 psi in compressive strength or 600 psi in flexural strength. Although these figures are considered conservative, quantifying fatigue distresses in rigid concrete pavements at opening to traffic is key to any revision of the current standards.

For this purpose, a thorough experimental program was conducted at the University of Illinois at Chicago to evaluate the early-age elastic properties of standardized IDOT pavement and patch mixes. The laboratory testing program consisted of 84 batches of IDOT-specified mix designs. Curing was conducted at optimal (73°F) and cold (50°F) temperatures. Fiber inclusion in the concrete matrix was studied due to its promising benefits to provide enhanced concrete toughness and structural performance. Accordingly, fiber-reinforced concrete specimens with fiber dosage rates of 4, 6, and 8 lb/yd³ were cast, in addition to plain-concrete specimens. Two synthetic macro-fiber types were selected from IDOT's qualified product list (W.R. Grace Strux 90/40 and BASF MasterFiber MAC Matrix). Furthermore, with a growing interest in sustainable concrete solutions, the cement content of all pavement and patch-mix designs was partially substituted (30% by weight) with ground granulated blast-furnace slag (GGBFS).

The laboratory testing program began by defining the mechanical properties at early concrete ages. This phase consisted of 48 batches for compressive strength tests (ASTM C39/AASHTO T 22), flexural strength tests (ASTM C78/AASHTO T97), static modulus of elasticity tests (ASTM C469), flexural toughness tests (ASTM C1609), and linear drying shrinkage tests (ASTM C 157). These experiments were followed by fracture-mechanics tests based on the two-parameter fracture model proposed by Shah (1990) for sample ages as early as 9 hr. In addition, nondestructive measures such as maturity (ASTM C1074) and dynamic modulus of elasticity (ASTM C215) tests were performed throughout the experimental phase to evaluate the effectiveness of these techniques for in-situ and field monitoring of correlated opening criteria purposes. Testing was conducted at 12-hr; and 1-d, 2-d, 3-d, 7-d, 14-d, and 28-d concrete age.

The mechanical properties testing program showed that Class PV mixes reached the required strength criteria within 3 d of concrete age for a water-to-cement ratio of 0.42. For patch mixes, Class PP-1

mixes attained the minimum specified strength within 3 d of concrete strength with a water-to-cement ratio of 0.42, while Class PP-2 mixes reached the required strength at 2 d of concrete age with a water-to-cement ratio of 0.36. It was also shown that increasing fiber content can significantly improve the toughness and fracture energy of pavement and patch mixes. In addition, dynamic modulus tests showed excellent correlation with the strength state of the concrete specimens (compressive strength, flexural strength, and static modulus of elasticity), irrespective of curing regime, mix design, or concrete age.

With scarce literature on the subject of cumulative fatigue damage in rigid pavements, significant emphasis was given to the flexural cyclic fatigue performance of PV mixes for plain and fiber-reinforced concrete. For this testing program, 26 batches were mixed to be evaluated for four different stress levels (0.9, 0.8, 0.7, and 0.6). The testing schedule consisted of 12-hr, 1-d, 3-d, and 7-d ages. The experimental results showed significant improvement in fatigue life for fiber-reinforced specimens that contained higher quantities of fibers (8 lb/yd³).

Moreover, ten mixes were batched to study the effect of fatigue damage on concrete durability for plain and fiber-reinforced PV mixes. To that end, specimens were subjected to 175,000 flexural fatigue cycles at a stress level of 0.55 before being subjected to 300 cycles of rapid freezing and thawing cycles (ASTM C666 Procedure A). Results showed that fiber inclusion can improve pavement durability against surface scaling. All freeze–thaw mixes were batched with 7% fresh-air content, which was adequate for resisting internal crack growth.

Additionally, fatigue testing was expanded to include cyclic loading at the face of a contraction joint in 2- x 7-ft rigid pavement specimens with PV mix design at early concrete age (12-hr and 1-d). A total of five specimens were constructed according to IDOT specifications for jointed, plain-concrete pavements (JPCP). This experimental task investigated different pavement thicknesses (6 in. and 8 in.), fiber content (0, 4, and 8 lb/yd³), and dowel presence (doweled and undoweled joints). The fatigue performance was evaluated for a maximum static and dynamic load ranging from ½ ESAL (9 kip) to 36 kip by measuring the transfer efficiency of the joint. The first jointed-slab specimen (6 in., 8 lb/yd³, doweled) yielded satisfactory performance at 1-d loading with joint transfer remaining in a rigid state and no recorded pavement distress (dowel bearing failure, excessive faulting, or joint opening). Similar experimental results were observed for the second jointed-slab specimen (6 in., plain concrete, doweled). This experimental task was adjusted and improved with every testing iteration to obtain representative conditions of actual paved sections.

Finally, experimental data was incorporated with numerical results using finite-element analysis to simulate stress development in rigid pavements for different scenarios that included varying concrete ages, underlying soil conditions, and pavement thicknesses. Experimental and numerical results from the fatigue testing program were then implemented in a step-by-step procedure using formulae and/or a nomograph that helps in opening traffic to newly paved roads within the first week after pouring. This procedure utilized dynamic modulus–flexural strength relations, which are, as previously stated, independent of curing regime, mix design, or concrete age, and thus, provide a promising

option to employ nondestructive testing for opening. The implementation of this practical procedure was recommended for future roadway-construction practices in the state of Illinois.

CONTENTS

CHAPTER 1 INTRODUCTION	1
1.1 PROBLEM STATEMENT.....	1
1.2 RESEARCH OBJECTIVE	1
CHAPTER 2 LITERATURE REVIEW	3
2.1 FATIGUE IN CONCRETE PAVEMENTS.....	3
2.1.1 Fatigue Behavior of Concrete	4
2.1.2 Factors Influencing Flexural Fatigue in Concrete.....	4
2.2 MATURITY IN CONCRETE.....	6
2.2.1 Maturity Methods.....	6
2.2.2 Limitations.....	7
2.3 FRACTURE MECHANICS IN CONCRETE	8
2.3.1 The Linear Elastic Fracture Mechanics (LEFM) Analysis Method.....	9
2.3.2 Effect of Concrete Age on Fracture Parameters.....	11
2.4 EARLY OPENING TO TRAFFIC CRITERIA	13
2.4.1 Overview.....	13
2.4.2 The Effect of Early Opening to Traffic on Fatigue Life of Concrete Pavement (Suh 2005)	13
2.4.3 Use of Modulus of Rupture, Fatigue Resistance and Maturity in Determining Opening to Traffic Time for Concrete Pavements (Olek et al. 2002)	14
2.4.4 Investigation of Design and Construction Issues for Long Life Concrete Pavement Strategies (Roesler et al. 2000)	15
2.4.5 Early Opening of Portland Cement Concrete (PCC) Pavements to Traffic (Corvetti and Khazanovich 2005)	15
2.5 FATIGUE OF JOINTED CONCRETE SLABS.....	16
2.5.1 Overview.....	16
2.5.2 Study by Eddie et al. (2001): “Glass Fiber-Reinforced Polymer Dowels for Concrete Pavements”	16
2.5.3 Study by Vijay et al. 2009: “Design and Evaluation of Jointed Plain Concrete Pavement with Fiber Reinforced Polymer Dowels”	17
2.5.4 Study by Benmokrane et al. 2014: “Performance of Glass Fiber-Reinforced Polymer- Doweled Jointed Plain Concrete Pavement under Static and Cyclic Loadings”	18

CHAPTER 3 MATERIAL SELECTION.....	20
3.1 CEMENTITIOUS MATERIALS	20
3.2 AGGREGATES.....	21
3.3 SYNTHETIC FIBERS	22
CHAPTER 4 MIX DESIGN AND CURING METHODS.....	23
4.1 MIX DESIGN	23
4.2 CURING METHODS FOR LABORATORY TESTING	23
4.2.1 Room Temperature Curing.....	24
4.2.2 Cold Temperature Curing (40. 50 °F):	25
CHAPTER 5 LABORATORY TESTING PROGRAM.....	27
5.1 LABORATORY EQUIPMENT.....	27
5.2 MECHANICAL PROPERTIES OF CONCRETE MIXES	29
5.2.1 Fresh Concrete Properties.....	29
5.2.2 Strength Characteristics.....	30
5.2.3 Static Modulus of Elasticity.....	30
5.2.4 Dynamic Modulus of Elasticity	31
5.2.5 Flexure Toughness of Fibrous Concrete.....	34
5.2.6 Linear Drying Shrinkage	36
5.3 MATURITY MEASURES	37
5.4 FRACTURE MECHANICS TEST	39
5.5 FATIGUE TEST	43
5.5.1 Test Significance.....	43
5.5.2 Testing Program for Fatigue Test.....	43
5.5.3 Development of Strength Gain Curves for Fatigue Testing	49
5.6 EFFECT OF FATIGUE ON FREEZE/THAW PERFORMANCE	51
5.6.1 Test Significance.....	51
5.6.2 Testing Program for Fatigue-Freeze/Thaw test	51
5.6.3 Development of Strength Gain Curves for Fatigue-Freeze/Thaw Testing.....	55
5.7 ANALYTICAL STUDY AND FINITE ELEMENT MODELING.....	56
5.7.1 Task Significance	56

5.7.2 Software Description.....	57
5.7.3 Parametric Studies	58
5.8 FATIGUE PERFORMANCE OF JOINTED CONCRETE SLABS TEST DESCRIPTION.....	66
5.8.1 Test Significance.....	66
5.8.2 Testing Setup.....	66
5.8.3 Evaluation of Test Results	71
CHAPTER 6 LABORATORY TEST RESULTS.....	73
6.1 FRESH PROPERTIES	73
6.2. STRENGTH, ELASTIC PROPERTIES, AND MATURITY RESULTS	74
6.2.1 Compressive Strength Results.....	74
6.2.2 Flexural Strength Results.....	75
6.2.3 Flexure Toughness in Fibrous Concrete	76
6.2.4 Compressive Strength and Static MOE Relation	77
6.2.5 Maturity in Concrete Results	78
6.2.6 Relative Dynamic Modulus (E_D).....	79
6.2.7 Linear Drying Shrinkage	81
6.3. FRACTURE MECHANICS RESULTS	82
6.3.1 Load vs. CMOD Curves for PV mixes	82
6.3.2 Two Parameters Fracture Model Results (K_{IC} and $CTOD_c$ proposed by Shah 1990)	83
6.4. FATIGUE TEST RESULTS	84
6.4.1 Fatigue Life by Test Date.....	84
6.5 EFFECT OF FATIGUE ON FREEZE-THAW TEST RESULTS	88
6.5.1 Mass Loss Due to Freeze-Thaw	88
6.5.2 Relative Dynamic Modulus and Durability Factor.....	88
6.6 FINITE ELEMENT ANALYSIS RESULTS.....	89
6.6.1 Parametric Study #1 for Rigid Pavement	89
6.6.2 Parametric Study #2 for Jointed Pavement	92
6.6.3 Parametric Study #3 for Cross Traffic Case.....	93
6.7 FATIGUE PERFORMANCE OF JOINTED CONCRETE SLABS	94
6.7.1 Jointed Slab Specimen #1.....	94
6.7.2 Jointed Slab Specimen #2.....	102

6.7.3 Jointed Slab Specimen #3.....	107
6.7.4 Jointed Slab Specimen #4.....	112
6.7.5 Jointed Slab Specimen #5.....	116
6.7.6 Summary of Jointed Slab Performance.....	120
CHAPTER 7 IMPLEMENTATION OF RESEARCH RESULTS.....	122
7.1 INTRODUCTION	122
7.2 PROCEDURE STEPS.....	122
7.2.1 Step I: Estimating Flexural Strength Using Nondestructive Measures	122
7.2.2 Step II: Estimating Flexural Stresses in Concrete Pavement Using Analytical Model Results	123
7.2.3 Step III: Estimating Flexural Fatigue Life	124
7.2.4 Procedure Summary.....	124
7.3 NUMERICAL EXAMPLE	125
7.4 ANALYTICAL EVALUATION OF JOINTED PAVEMENT SLAB.....	141
7.4.1 Evaluation of Fatigue Life Using Implementation Procedure	141
7.4.2 Evaluation of Fatigue Life Using ISLAB2000 Jointed Pavement Slab Model.....	147
7.4.3 Estimation of Fatigue Life From Finite Element Analysis Using ABAQUS/CAE	150
CHAPTER 8 DESIGN AIDS FOR EARLY OPENING TO TRAFFIC	157
REFERENCES.....	159
APPENDIX A FRESH PROPERTIES OF CONCRETE MIXES	165
APPENDIX B COMPRESSIVE STRENGTH RESULTS.....	168
APPENDIX C FLEXURAL STRENGTH RESULTS.....	170
APPENDIX D FLEXURE TOUGHNESS CHARACTERISTICS	172
APPENDIX E COMPRESSIVE STRENGTH AND STATIC MOE RELATION.....	174
APPENDIX F MATURITY IN CONCRETE RESULTS	175
APPENDIX G DYNAMIC MODULUS RESULTS	178
APPENDIX H LINEAR DRYING SHRINKAGE RESULTS	184

APPENDIX I	FRACTURE MECHANICS RESULTS	189
APPENDIX J	FATIGUE TEST RESULTS.....	197
APPENDIX K	EFFECT OF FATIGUE ON FREEZE-THAW TEST RESULTS	205
APPENDIX L	FINITE ELEMENT ANALYSIS RESULTS	207
APPENDIX M	FATIGUE PERFORMANCE OF JOINTED CONCRETE SLABS.....	223
APPENDIX N	PROCEDURE CHARTS AND NOMOGRAPHS	258
APPENDIX O	DESIGN AIDS FOR EARLY OPENING TO TRAFFIC.....	269
APPENDIX P	CHEMICAL AND PHYSICAL PROPERTIES OF CEMENTIOUS MATERIALS	286

LIST OF FIGURES

Figure 2-1. Crossover effect due to curing temperatures (Alexander and Taplin 1962).....	8
Figure 2-2. Geometry and testing configuration (from Kazberuk 2012).	10
Figure 2-3. Variation of the normalized stress-intensity factor against time (Zollinger et al., 1993). ...	12
Figure 2-4. Comparison between the frozen concrete and reference concrete after 350 cycles (from Kazberuk 2012).	13
Figure 2-5. Failure modes showing proper crack initiation at the groove (a) and cracking at the zone beyond the dowel (b)(Vijay et al., 2009).	18
Figure 2-6. Static loading showing shear failure beyond the dowel-bar zone (Bricola et al. 2014).....	19
Figure 3-1. Gradation curves and limits for coarse and fine aggregates.....	22
Figure 4-1. Moisture room fully automated control panel (top) and controlled curing tank (bottom).25	
Figure 4-2. Controlled-temperature chamber with concrete specimens cured at 45°F.	25
Figure 4-3. Curing technique used in the temperature-controlled chamber.....	26
Figure 5-1. Instron 8500 system (left) and Tinius Olsen system (right).....	28
Figure 5-2. Petrographic analysis of concrete (left); and freeze–thaw cabinets (right).....	29
Figure 5-3. Test configuration for the compressive and flexural strength of concrete.	30
Figure 5-4. Static modulus of elasticity test setup.....	31
Figure 5-5. Supported specimens for E_D measurement.	32
Figure 5-6. DK-5000 dynamic resonance-frequency tester, ASTM C215.	33
Figure 5-7. Flexure–toughness test configuration.....	35
Figure 5-8. Example of flexure–toughness load–deflection curve (concrete with synthetic fibers). ...	35
Figure 5-9. Linear drying shrinkage-test configuration.	37
Figure 5-10. Temperature data loggers for maturity measure.	37
Figure 5-11. Temperature–time development in concrete at room temperature.	38
Figure 5-12. Maturity vs. age of concrete (left); compressive strength vs. maturity (right).....	39
Figure 5-13. Steel molds with Plexiglass notches for fracture-mechanics test.	39
Figure 5-14. Testing setup and configuration for the fracture-mechanics test.	40
Figure 5-15. Testing configuration and geometry of specimen (modified from Shah 1990).....	41
Figure 5-16. Typical load vs. crack-mouth-opening displacement curve.	41
Figure 5-17. Fatigue-testing setup.....	43

Figure 5-18. Cyclic loading development with respect to time.	44
Figure 5-19. Typical S-N curve for concrete.	45
Figure 5-20. Normalized flexural strength in PV mixes at early age.	50
Figure 5-21. Typical load-ramping case taken 1 hr after test initiation.	51
Figure 5-22. Fatigue/freeze–thaw testing setup.	52
Figure 5-23. Freeze–thaw cabinets (left) and petrographic analysis of concrete (right).	53
Figure 5-24. Flexural strength in PV mixes at early age.	56
Figure 5-25. Typical geometric and loading configurations using <i>ISLAB2000</i>	57
Figure 5-26. Typical output for bottom transverse stresses (a) and vertical deflections (b).	58
Figure 5-27. Rigidly connected-slabs model for parametric study 1.	60
Figure 5-28. Model for parametric study 2.	62
Figure 5-29. Study 3 model.	65
Figure 5-30. Test configuration of slab, dowels, and loading-plate geometry (plan view).	67
Figure 5-31. Test configuration of slab, dowels, and loading-plate geometry (elevation view).	67
Figure 5-32. 3D sketch of steel-enclosure fabrication.	69
Figure 5-33. Instrumentation setup showing LVDT placement.	70
Figure 5-34. Loading sequence for static and cyclic testing.	71
Figure 5-35. Example of typical LTE development for a jointed slab, as observed in the literature.	72
Figure 6-1. Section view along the length of the compacted backfill layer, showing wooden support.	94
Figure 6-2. Steel enclosure showing wooden support (a) and compaction of the first soil layer (b) using vibratory plate compactor.	95
Figure 6-3. Test setup of subgrade modulus reaction for the compacted CA6 layer.	96
Figure 6-4. Form enclosure (a) and dowel-bar placement (b).	97
Figure 6-5. Jointed-slab specimen after demolding, showing ½-in. offset from the steel form.	97
Figure 6-6. Groove position (a) and placement after casting (b).	98
Figure 6-7. Instrumentation setup during static testing for the jointed-slab specimen.	99
Figure 6-8. Compacted soil within removable steel enclosure added for Specimen 2.	103
Figure 6-9. Specimen 2 testing setup.	104
Figure 6-10. Embedded strain-gauge placement near the groove and at the dowel-end area (Specimen 2).	105

Figure 6-11. Specimen 3 testing setup.	108
Figure 6-12. Lateral and vertical deflection restraint.	109
Figure 6-13. Specimen 3 testing setup showing anchorage system (a) and embedded strain gauge placement (b).....	110
Figure 6-15. Specimen 4 testing setup showing anchorage system and strain gauge placement in the plan view (a) and the elevation view (b)	113
Figure 6-16. Prestressing system used for Specimen #4	114
Figure 6-17. Prestressing procedure (a) and specimen boundary condition after strand cutting (b) (Specimen 4)	114
Figure 6-18. Specimen #5 testing setup showing anchorage system in the plan view (a) and the elevation view (b).....	117
Figure 7-1. Flexural-strength estimation using trend line.	126
Figure 7-2. Stress estimation at 12-hr with $k = 50$ psi/in.....	127
Figure 7-3. Stress-determination nomograph at 12-hr concrete age.	128
Figure 7-4. Stress estimation at 1-d with $k = 50$ psi/in.	130
Figure 7-5. Stress-determination nomograph at 1-d concrete age.....	131
Figure 7-6. Stress estimation at 3-d with $k = 50$ psi/in.	133
Figure 7-7. Stress determination nomograph at 3-d concrete age	134
Figure 7-8. Flexural stress estimation at 7-d with $k = 50$ psi/in.....	136
Figure 7-9. Stress determination nomograph at 7-d concrete age.	137
Figure 7-10. Flexural-strength development for room and cold temperatures.....	139
Figure 7-11. Normalized flexural-strength development for room and cold temperatures.....	139
Figure 7-12. Compressive strength vs E_D for all RT and 50F mixes.....	140
Figure 7-13. Flexural-strength estimation, using trend line.	140
Figure 7-14. Modulus of rupture versus dynamic modulus showing flexural-strength estimation at 1-d concrete age.....	142
Figure 7-15. Plan view of the implementation pavement model.....	143
Figure 7-16. Tensile-stress evaluation at 1-d concrete age for a 6-in. pavement with $k = 324$ psi/in.	144
Figure 7-17. S-N results for PV, PVF1, PVF2, and PVF1-8lbs mixes at 1-d concrete age, showing estimated fatigue life of jointed-slab specimen.	146
Figure 7-18. Plan view of the jointed-pavement slab model.	147

Figure 7-19. Transverse-stress distribution in the bottom concrete layer at ½ ESAL.	148
Figure 7-20. Longitudinal-stress distribution in the bottom concrete layer at ½ ESAL.....	148
Figure 7-21. Deflection distribution in the bottom concrete layer at ½ ESAL.....	149
Figure 7-22. <i>S-N</i> results for PV, PVF1, PVF2, and PVF1-8lbs mixes at 1-d concrete age, showing estimated fatigue life of jointed-slab specimen (<i>ISLAB2000</i> model).	150
Figure 7-23. Isometric view of the solid modeling, showing supporting soil geometry.	150
Figure 7-24. Elevation view showing solid modeling of the jointed pavement.	151
Figure 7-25. Finite-element meshing of concrete slab and loading plate.....	151
Figure 7-26. Stress–strain curve for dowels.	152
Figure 7-27. Displacement contour in the elevation view for the pavement and the supporting soil at ½ ESAL.....	153
Figure 7-28. Longitudinal stress distribution.	153
Figure 7-29. Transverse stress distribution.	154
Figure 7-30. Tensile stress distribution in the dowels bars at ½ ESAL.....	154
Figure 7-31. Shear stress distribution in the dowels bars at ½ ESAL.....	155
Figure 7-32. <i>S-N</i> results for PV, PVF1, PVF2, and PVF1-8lbs mixes at 1-d concrete age, showing estimated fatigue life of jointed-slab specimen (ABAQUS/CAE model).....	156

LIST OF TABLES

Table 1-1. IDOT PV and PP-Mix Design and Strength Requirements for Traffic Opening.....	2
Table 2-1. Fatigue-Load Spectrum for Various Structures (Hsu 1981)	4
Table 3-1. Material Selection and Properties	20
Table 3-2. Chemical Composition of Cement and GGBF slag	21
Table 3-3. Physical Properties of Cement and GGBF slag.....	21
Table 3-4. Aggregate Properties	21
Table 3-5. Synthetic Fibers’ Properties	22
Table 4-1. Selected Concrete Mixes for Laboratory Testing.....	23
Table 5-1. Laboratory Test Methods and Number of Tests per Concrete Mix.....	29
Table 5-2. Summary of the Fatigue-Testing Dates and Duration for All PV Mixes.....	46
Table 5-3. Summary of the Fatigue-Testing Dates and Duration for All PVF1 Mixes	47
Table 5-4. Summary of the Fatigue-Testing Dates and Duration for All PVF1-8lbs Mixes	48
Table 5-5. Summary of the Fatigue-Testing Dates and Duration for All PVF2 Mixes	49
Table 5-6. Summary of the Fatigue/Freeze–Thaw Testing Dates and Duration for All PV Mixes	54
Table 5-7. Summary of the Fatigue/Freeze–Thaw Testing Dates and Duration for All PVF1 Mixes	54
Table 5-8. Summary of the Fatigue/Freeze–Thaw Testing Dates and Duration for All PVF1-8lbs Mixes.....	55
Table 5-9. List of Constant Input Parameters for Study 1	59
Table 5-10. Static MOE Values for Each Concrete Age	60
Table 5-11. List of Constant Input Parameters for Study 2	62
Table 5-12. List of Constant Input Parameters for Study 3	64
Table 5-13. Compressive Strength of PV Mixes with the Corresponding Shear Strength.....	66
Table 5-14. Dowel-Diameter Selection as per Standard Specification 420001-08.....	68
Table 7-1. <i>S-N</i> Relationships of the Fatigue-Testing Program Highlighting the Jointed-Slab Specimen Case (1-d loading, FRC)	146
Table 7-2. Input Parameters Obtained from the Experimental Setup	147
Table 7-3. Properties of Concrete	152
Table 7-4. Numerical Results Summary.....	155

CHAPTER 1: INTRODUCTION

1.1 PROBLEM STATEMENT

One of the challenges in highway construction and rehabilitation is providing cost-effective and durable Portland cement concrete (PCC) pavement with optimum performance for short- and long-term life cycles. This challenge is magnified in high-traffic zones, where the opening of PCC pavement to traffic is needed as early as possible.

Many techniques and methods were adopted in different states to expedite the construction of PCC pavements to keep the closure time at a minimum, thereby ensuring economic and environmental benefits. Numerous studies were done to specify the minimum strength required to carry the fatigue damage in PCC pavements when opened to early traffic. The current Illinois Department of Transportation (IDOT) specifications stipulate rigorous requirements for strength development in PCC pavement prior to opening to traffic. These requirements proved to be inefficient to limit delays in high-traffic zones.

The elastic properties development with age in concrete is proportional to its strength development; however, this development, in PCC pavements when subject to early opening to traffic (EOT), could lead to fatigue damage. This fatigue damage causes micro- and macro-crack growth due to repetitive movements of vehicles. Cracking in PCC pavements acts as a catalyst driving other forms of distress, as it leads to steady reduction in stiffness and durability performance, such as freeze–thaw resistance, spalling, and brittle failures.

Currently, IDOT is searching for a cost-effective and long-term solution to keep the closure time at a minimum for PCC pavements without negatively affecting their overall performance. A well-thought-out and thorough investigation is required for studying the fatigue damage and its related forms of distressing in PCC pavement at EOT, as it might impose detrimental effects and reduce the pavement life cycle drastically.

1.2 RESEARCH OBJECTIVE

Current IDOT specifications (e.g., Articles 701.17(c)(5) and 701.17(e)(3), *Standard Specifications for Road and Bridge Construction*, IDOT (2016)) for EOT of new concrete pavements and patches view the stress in the slab from the viewpoint of the stress relative to some later age strength (7, 28, or 90 days [d]); however, at early ages, the concrete is a more elastic material with a modulus that is very low compared to later ages, behaving more like “silly putty” than rigid concrete. The implication is that stresses may be considerably lower in “green” concrete than generally assumed; and thusly, it may be possible to open concrete pavements and patches earlier. The current minimum specifications for strength in PCC pavements and pavement patches at the time of opening to traffic are shown in Table 1-1 below, along with the minimum amount of cement or cementitious materials required.

This research may result in decreased construction time and time for opening to traffic, resulting in potential cost savings through use of shorter periods of traffic control, enhancing highway-user satisfaction and decreasing user complaints, and providing other cost savings. The objectives of this research are summarized as follows:

- Assess the effect of concrete pavements' elastic properties on their fatigue damage when opened to early traffic, by conducting an experimental lab- and field-testing program.
- Correlate lab results to field performance using maturity meters. Also, study the possibility of developing a relationship between maturity meters and strength or elastic properties of concrete pavements' post-fatigue damage. This relation could be utilized as a measure for the minimum closure time needed for newly poured PCC pavement.
- Perform analytical studies that mimic and enhance the experimental studies using finite-element models.
- Evaluate and revise the current specifications of IDOT on the minimum strength requirements in Articles 701.17(c)(5) and 701.17(e)(3) for pavements to be opened to traffic (*Standard Specifications for Road and Bridge Construction*, IDOT (2016)).
- Investigate the possible detrimental effects of residual strains/stress induced by loading early-age concrete on long-term fatigue life and durability, such as freeze-thaw performance.

The outcome of this project is expected to be new research-supported guidelines that will allow for the roadway to be opened to traffic at the appropriate time.

Table 1-1. IDOT PV and PP-Mix Design and Strength Requirements for Traffic Opening

Mix designation	Use	Cement factor cwt/yd ³		w/c ratio	Slump, in.	Air content, %	Min. compressive strength (flexural) ⁽⁵⁾ , psi		Min. strength required for opening to traffic, psi
		Min	Max				d		
PV	Pavement	5.65 ⁽¹⁾	7.05	0.32–0.42	2–4	5.0–8.0	14 d	28 ⁽⁶⁾ d Days	3,500 (650)
		6.05 ⁽²⁾					3,500 (650)	3,500 (650)	
PP: pavement patching	PP-1	6.5	7.5	0.32–0.44	2–4	4.0–7.0	3,200 (600)	at 48 hr	3,200 (600)
	PP-2	7.35	7.35	0.32–0.38	2–6	4.0–6.0		at 24 hr	1,600 (250)
	PP-3	7.35 ⁽³⁾	7.35 ⁽³⁾	0.32–0.35	2–4	4.0–6.0		at 16 hr	
	PP-4	6.00 ⁽⁴⁾	6.25 ⁽⁴⁾	0.32–0.50	2–6	4.0–6.0		at 8 hr	
	PP-5	6.75 ⁽⁴⁾	6.75 ⁽⁴⁾	0.32–0.40	2–8	4.0–6.0		at 4 hr	
(1) Central-mixed									
(2) Truck-mixed or shrink-mixed									
(3) Use Type III cement. In addition to the cement, use 100 lb/yd ³ of GGBF slag and 50 lb/yd ³ of silica fume.									
(4) The cement shall be a rapid-hardening cement from the department's "Approved List of Packaged, Dry, Rapid Hardening Cementitious Materials for Concrete Repairs" for PP-4 and calcium aluminate cement for PP-5.									
(5) Minimum strength requirements in pavements for traffic opening									
(6) If no strength tests are conducted, the pavement shall be opened to traffic after 28 d when fly ash or GGBF slag are used in the mix									

CHAPTER 2: LITERATURE REVIEW

2.1 FATIGUE IN CONCRETE PAVEMENTS

One of the leading causes of cracking in concrete pavements is fatigue damage. Fatigue cracking is considered the most significant form of distress in concrete pavement. This cause of damage can lead to expensive rehabilitation that might require replacing a large section of the concrete slab. The fatigue damage occurs due to the repeated vehicular loads, more likely heavy wheel load, eventually resulting in cracking the pavement slab. The fatigue failure of concrete pavements is caused by the development of flexural stresses or a combination of the flexural and compressive stresses. Fatigue damage can result in corner breaks and linear transverse cracking in concrete pavements, which tends to reduce the service.

Currently, the most common concrete pavement types include (1) plain-concrete pavements; (2) jointed, reinforced-concrete pavements (JRC); and (3) continuously reinforced-concrete pavements (CRCP). Pavements are designed to carry the truck loads expected during their design life. Truck-trailers and buses are considered among the heavy vehicles responsible for the flexural fatigue of concrete pavements. Localized distress due to fatigue in concrete pavement does not necessarily terminate its service life as long as the traffic load is transferred through the cracks and joints without causing excessive deflection (ACI Committee 215).

Research on the fatigue in concrete under flexure stresses dates back as early as the 1920s. Throughout the years, researchers conducted experimental and analytical investigations to study the failure mechanism in concrete pavements subject to fatigue and the factors influencing fatigue damage. Accordingly, analytical models and design procedures were developed to predict the service life of concrete pavements subject to fatigue. Most recent approaches to the design of concrete pavements follow the mechanistic-empirical approach. The mechanistic approach is first applied to determine the pavement responses, such as concrete stresses and strains. The empirical approach is then implemented through the transfer functions. The transfer functions are applied to estimate the design life of the concrete pavement: by predicting the damage in concrete pavement through the loading repetitions/cycles and exposure conditions (i.e., freeze-thaw, de-icing chemicals, alkali-silica reactivity, etc.). The resistance to fatigue damage is determined from an S-N curve (stress versus number of cycles) that relates the tensile/flexural stress in the pavement due to a load spectra or equivalent single-axle load (ESAL) to the number of applied ESAL required. Accordingly, it is essential that these transfer functions provide accurate predictions of the actual performance of concrete pavements under the expected load and exposure conditions. These findings will provide adequate thickness for concrete pavement that accommodates the traffic demand.

The S-N curve is used as an indicator to predict the number of load cycles that cause damage at a given stress level. Structures that experience high stress levels are expected to fail with a lower number of cycles. Table 2-1 shows the number of load cycles that are expected during the service life of various structures. Pavement structures can undergo between 100,000 and

10 million load cycles during their service life, depending on the pavement design life, truck traffic, subgrade and subbase properties, weather, quality of local materials, and maintainability.

Table 2-1. Fatigue Load Spectrum for Various Structures (Hsu 1981)

Category	Structure type	Number of load cycles
Low-cycle fatigue	Structures subjected to earthquake	0–1,000
High-cycle fatigue	Airport pavements	1,000–100,000
	Highway and railroad bridges; highway pavements, concrete railroad ties	100,000–10,000,000
Super-high-cycle fatigue	Mass rapid-transit structures	10,000,000– 5×10^7
	Sea structures	5×10^7 – 5×10^8

2.1.1 Fatigue Behavior of Concrete

Considerable research has been conducted to study the mechanism of fatigue failure in concrete. Murdock and Kesler (1960) explained the fatigue damage in concrete as a result of progressive deterioration between the coarse aggregate and the binding matrix, leading eventually to the fracture of the matrix.

One of the early experimental studies relating to the flexural fatigue in concrete was conducted by Clemmer (1922). Clemmer investigated the fatigue failure of concrete beams 6 x 6 x 36 in. supported as cantilevers and subjected to repeated loads at a rate of 40 cycles per min. His motive was derived after observing a series of failures at the corner of pavement slabs. As a result of his tests, Clemmer set a fatigue limit of 53% of the ultimate strength required not to cause failure under repetition. Crepps (1923) and Hatt (1924) conducted fatigue tests on concrete and mortar beams in bending but under reversal stresses. They concluded that the failure is governed by the tensile stresses. Their test results suggested a fatigue limit of 55% of the ultimate strength, which is in close agreement with Clemmer's (1922) suggestion.

Williams (1943) conducted flexural fatigue tests on lightweight aggregate concrete beams. His findings suggested that the fatigue limit varied, depending on the type of aggregate and whether the repeated load was pure tensile flexure or reversal. Williams suggested that during the fatigue test, several cracks were formed; but not all of them contributed to the propagation of the crack that leads to failure. He also suggested that the failure due to fatigue was enhanced by flaws in the aggregates.

2.1.2 Factors Influencing Flexural Fatigue in Concrete

Fatigue in concrete is influenced by many factors, such as the rate of loading, range of loading, concrete material characteristics and proportions, and environmental conditions. This section reports some of the common factors that influence the fatigue life in concrete. Other factors

that are not discussed might include but aren't limited to humidity, curing condition, water penetration, and wave forms of the fatigue test.

2.1.2.1 Aggregates

The type of coarse aggregate can have a significant effect on the fatigue damage in concrete. Klaiber and Lee (1982) investigated the effect of batching concrete with crushed limestone and river gravel. They observed that, at high stress levels, concrete made with gravel exhibited higher fatigue strength than that made with crushed limestone, while no notable difference was observed at lower stress levels. However, Suh (2005) observed better fatigue resistance for concrete made with crushed limestone than with river gravel, after conducting fatigue tests on concrete beams and full-scale concrete slabs.

2.1.2.2 Frequency

Kesler (1953) studied the effect of the speed of testing or frequency on the flexure fatigue in concrete. He used three different frequencies (70, 230, and 440 cycles per min). His results suggested that the speed of testing didn't show a notable difference in the fatigue response.

2.1.2.3 Stress Level and Gradient

Murdock and Kesler (1958) studied the effect of the range of stress on the flexure fatigue behavior of concrete. Their results showed that the stress range has a noticeable effect on the fatigue response. As the ratio of the minimum to the maximum applied load is increased, the overall fatigue strength was reduced.

2.1.2.4 Rest Periods

Murdock and Kesler (1958) observed that fatigue strength was increased when rest periods were introduced to concrete prisms subject to flexure fatigue. The fatigue loading was interrupted by intermittent rest periods such that 5 min of rest were introduced between 10 min of cyclic load. Hilsdorf and Kesler (1960) studied the effect of rest periods on flexure fatigue by varying the duration of the rest periods between 1 and 27 min. The duration of the rest periods ranged between 1 and 27 min. They concluded that the inclusion of rest periods was beneficial up to a certain duration, and it showed notable effect only for periods between 1 and 5 min.

2.1.2.5 Air Entrainment

Klaiber and Lee (1982) observed a decrease in the flexural fatigue strength of concrete beams with an increase in the air content. Inspection of their failed specimens revealed that the fatigue cracking was more likely to occur around the aggregate rather than through the aggregate for concrete mixes with higher air content.

2.1.2.6 Discontinuous Fibers

Fatigue performance of fiber-reinforced concrete has been addressed in several studies using steel fibers. The literature on the use of synthetic macro-fibers as FRC for concrete is scarce. Johnston and Zemp (1991) studied the effect of steel-fiber content (0, 0.5, 1, and 1.5% by

volume) and aspect ratio on flexure fatigue strength of concrete. The study revealed better fatigue resistance and higher a fatigue limit (set at 100,000 cycles) with higher content of steel fibers. Paskova and Meyer (1997) investigated the low-cycle fatigue damage of plain and fiber-reinforced concrete using steel and polypropylene as FRP. Their investigation showed improved performance to the fatigue resistance of fiber-reinforced concrete.

2.2 MATURITY IN CONCRETE

Maturity tests involve correlating concrete strength with age and temperature history. Temperature readings with respect to time can be linked with the compressive strength to identify a curve pattern for certain mix proportions (strength-maturity relationships). Results could be used to predict the strength of the concrete at an early age. Two methods are currently used to determine the maturity in concrete, as described in the following section.

2.2.1 Maturity Methods

2.2.1.1 Nurse–Saul Maturity Function

Strength-maturity curves are defined by plotting compressive strength results with respect to the maturity index. The Nurse–Saul maturity is described according to ASTM C1047 as the rate (slope) of strength gain in concrete that progresses linearly with time. The maturity index (or time–temperature factor, TTF) according to the Nurse–Saul function is calculated as follows:

$$M(t) = \sum (T_a - T_o)\Delta t \quad (2-1)$$

where

$M(t)$ = maturity index or temperature–time factor (TTF), °F x hr

T_a : average concrete temperature during each time interval

T_o : temperature below which cement hydration is assumed to cease (32°F)

Δt : time intervals, d or hr

2.2.1.2 Arrhenius Maturity Function

Another approach for calculating the maturity index is the Arrhenius maturity function, which is based on the rate of chemical reaction in concrete. The Arrhenius function is used in this case to calculate the maturity index as the time-equivalent age (t_e).

$$t_e = \sum e^{-Q\left(\frac{1}{273+T_a} - \frac{1}{273+T_s}\right)} \Delta t \quad (2-2)$$

where

t_e = equivalent age at a specified temperature, T_s

Q = apparent activation energy divided by universal gas constant (8.3144 J/mol·K)

T_a = average concrete temperature during time interval, ΔT (°C)

Δt = time intervals, d or hr

T_s = specified temperature (°C)

2.2.2 Limitations

Limitations to the strength-maturity results could be affected by the concrete-hydration factors such as curing temperature and humidity, concrete mixture properties, and fresh characteristics.

2.2.2.1 Effect of Water-to-Cementitious Ratio

According to the test results conducted by Nurse (1949), strength-maturity results could not be curve-fitted into a universal plot because each strength-maturity relationship is unique to the corresponding mix proportions used. An increase in the water-to-cement (w/cm) ratio results in a decrease in strength, thus rendering the comparison between maturity indices for different mix proportions unreliable.

2.2.2.2 Effect of Curing Temperature (Fresh-Concrete Property)

For a given mix proportion, strength-maturity tests conducted with varying curing temperatures have a significant effect on strength readings. While using the Nurse-Saul function, Alexander and Taplin (1962) confirmed this effect by testing specimens with a fixed w/cm ratio of 0.35 and cured at 41°F, 70°F, and 108°F. As predicted, the three mixes had their own unique maturity-strength relations as demonstrated in Figure 2-1.

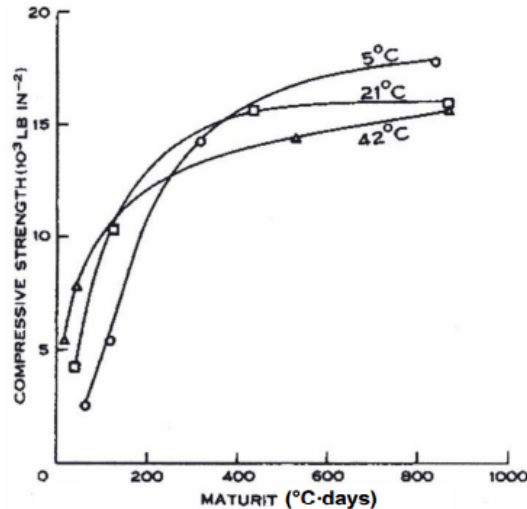


Figure 2-1. Crossover effect due to curing temperatures (Alexander and Taplin 1962).

This behavior was described as the crossover effect by Verbeck and Helmuth (1968), in which plots for concrete mixes cured at lower temperatures cross over the ones for warmer temperatures.

Strength-maturity curves were generated by Carino and Malhotra (1991), with similar curing temperatures used by Alexander and Taplin (1962), with the maturity index calculated from the Arrhenius function for estimating the time-equivalent age. Results show that for early age, a general trend could be attributed for different curing temperature curves. However, for a time-equivalent age of 1 d and more, results were significantly lower for concrete curing at higher temperatures. It was suggested that the cementitious material within mixes cured at high temperatures is subjected to a higher rate of hydration, thus reducing the bonding forces between the aggregates. Concrete strength is increased with higher curing temperature at early age; however, due to disruption of the hydration distribution in the concrete, significant strength losses occur over the long term.

2.3 FRACTURE-MECHANICS IN CONCRETE

Investigations at the micro-level of concrete have proved the existence of micro-cracks at the bond interface between the cement paste and the aggregate (Islam 2000). These micro-cracks play a vital role in the failure mechanism of concrete structures that could occur even under service-loading conditions. This mechanism is characterized by the bridging of micro-cracks and progression of the damage zone under the effect of loading. Despite this fact, the current design methods for concrete pavements do not take into consideration the fracture parameters of concrete. However, they are mainly focused on the hardened-material properties of concrete, such as the compressive and flexural strength. Given the fact that the nature of loading applied on concrete pavements is generally more aggressive than that on concrete buildings because it involves vehicular repetitive loading, causing fatigue damage and crack propagation in the concrete material, it is therefore important to characterize the fracture

parameters influencing the cracking behavior of the concrete pavement as an extension to the existing design parameters, to better understand the overall behavior of concrete pavements during their service life. Moreover, it is also important to identify the limits of the fracture parameters and their correlation with other concrete parameters such as the compressive strength, flexural strength, and age of concrete in order to identify the effect of early opening to traffic on the cracking behavior of concrete pavements.

2.3.1 The Linear Elastic Fracture-Mechanics (LEFM) Analysis Method

The theory of fracture-mechanics of brittle materials was initiated by Griffith in the early 1920s (Griffith 1921). It is divided into linear elastic fracture-mechanics (LEFM) and elastoplastic fracture-mechanics (EPFM). LEFM is well-developed and is characterized by calculating the stress-intensity factor (K) and energy-release rate (G). The applicability of LEFM is limited to materials that exhibit brittle failure and a negligible plastic response, which is the case of plain and fibrous concrete. However, the heterogeneity of concrete and the micro-cracks that may exist at the aggregate boundaries cause a nonlinear response associated with large-fracture process zones, rendering the stress-intensity factor and energy-release rate to be size-dependent (Zhang and Liu 2003, Kaplan 1961, and Strange and Bryant 1979). LEFM is applicable if the process zone is significantly small.

Jenq and Shah (1985a,b) realized that the calculation of the stress-intensity factor performed using LEFM is highly affected by the size effect. They proposed the two-parameter model, or effective Griffith crack model, to account for the nonlinear slow-crack growth caused by the size effect prior to peak load. The parameters are the critical stress-intensity factor (K_{IC}) and the critical crack-tip-opening displacement ($CTOD_c$). It was proven that these parameters vary independently from the size effect, which allows calculating the peak load of structures with arbitrary geometry. The proposed model was experimentally verified using single-edge notched beams (Type G Test) tested in a three-point bending configuration (see Figure 2-2). The test included three different beam sizes and five different mix proportions. The proposed geometric configurations included a span-to-depth ratio (S/d) of 4 and an initial notch depth set at 0.3 of the total beam depth ($a_0/d = 0.3$). The two-parameter model was utilized with unnotched concrete beams loaded in direct tension. The results indicate the tensile strength is size-independent, contrary to the modulus of rupture, which is not. The LEFM formulation for the three-point bending test of notched concrete specimens proposed in the two-parameter model are (taken from Jenq and Shah 1985a,b) as follows:

Stress-intensity factor (K_I):

$$K_I = \frac{6P}{bt} \sqrt{\pi a} F\left(\frac{a}{b}\right) \quad (2-3)$$

$$F\left(\frac{a}{b}\right) = \frac{1}{\sqrt{\pi}} \frac{1.99 - A(1-A)(2.15 - 3.93A + 2.7A^2)}{(1+2A)(1-A)^{3/2}} \quad (2-4)$$

For crack-mouth-opening displacement (*CMOD*):

$$CMOD = \frac{24Pa}{btE} V_1\left(\frac{a}{b}\right) \quad (2-5)$$

$$V_1\left(\frac{a}{b}\right) = 0.76 - 2.28A + 3.87A^2 - 2.04A^3 + \frac{0.66}{(1-A)^2} \quad (2-6)$$

where

a is the effective crack length, mm

b is the total depth of the specimen, mm

$A = a/b$

t is the total width of the specimen, mm

P is the peak load [N]

E is the modulus of elasticity, Mpa

$V_1\left(\frac{a}{b}\right)$ and $F\left(\frac{a}{b}\right)$ are dimensionless functions of the dimensions of the specimens.

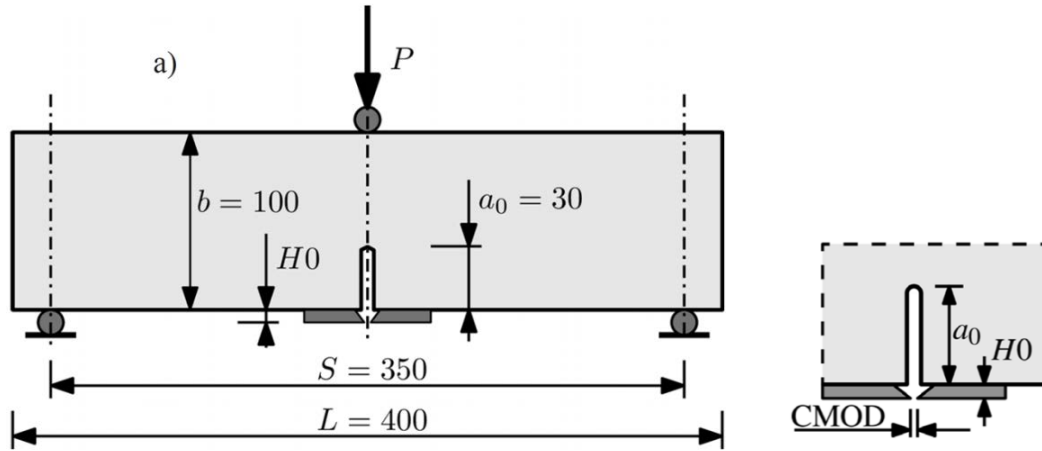


Figure 2-2. Geometry and testing configuration (from Kazberuk 2012).

Karihaloo and Nallathambi (1991) proposed the effective crack model for calculating the fracture parameters of notched concrete beams tested with three-point bending. The improved model takes into account the nonlinear behavior of concrete depicted in the ascending portion of the load-deflection plot. The effective crack method is based on replacing the various processes taking place at the fracture process zone and causing energy consumption by an

equivalent process. This process leads to the formation of a traction-free crack. This method is conceptually similar to the two-parameter model presented by Jenq and Shah (1985a,b). However, it is based on the load-deflection curve instead of the load-*CMOD* curve. The modulus of elasticity E is calculated, in this method, from the load-deflection curve or compression tests for cylinders, and substituted in a set of equations to calculate the toughness parameters. The effective crack model is found to be in good agreement with the two-parameter model and the size effect law proposed by Bazant and Planas (1998).

2.3.2 Effect of Concrete Age on Fracture Parameters

Wong and Miller (1990) studied the effect of concrete age on the fracture parameters (i.e., critical stress-intensity factor K_{IC} and critical crack-tip-opening displacement CTOD_c) using the two-parameter model developed by Shah (1985). The study involved concrete beam samples tested at 1, 3, and 5 d. It was noticed that the critical stress-intensity factor, K_{IC} , increased with concrete age. Similarly, Zollinger et al. (1993) studied the effect of concrete age on the fracture parameters, using the size effect model developed by Bazant and Planas (1998). The study involved fourteen batches of concrete mixtures with maximum aggregate size of 19 and 38 mm. The specimens were tested at 12 hr; and 1, 7, 21, and 28 d. The study confirmed similar findings, e.g., the stress-intensity factor and effective critical length (c_t) increased with the increase in age of the concrete. Moreover, Zollinger et al. (1993) proposed a relationship between the stress-intensity factor at any age normalized to the stress-intensity factor and the 28 d as a function of time. The relationship is written as follows:

$$\frac{K_{IC}}{K_{IC}^{28}} = \left(\frac{t}{28} \right)^{\frac{1}{4}} \quad (2-7)$$

The variation of the stress-intensity factor with time, both normalized to 28 d, is shown in Figure 2-3.

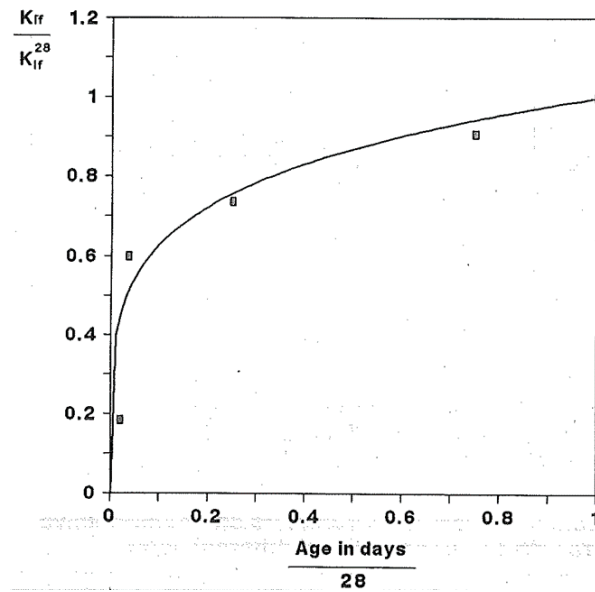


Figure 2-3. Variation of the normalized stress-intensity factor against time (Zollinger et al., 1993).

Kazberuk (2012) studied the effect of freezing and thawing combined with mechanical loading on the mechanical and fracture properties of concrete. The study involved concrete samples with an air-entraining admixture subjected to 360 cycles of freeze and thawing, and non-air-entrained samples subjected to 200 cycles. The study for the fracture properties was based on the two-parameter model by Jenq and Shah (1985a,b). The testing setup for the notched-beam samples used in this study is shown in the Figure 2-2.

It was found that the specimens subjected to freeze–thaw cycles exhibited significant decrease in the mechanical properties and the K_I values, accompanied by an increase in the $CMOD$ values, compared to the control specimens, indicating that damaged samples due to cyclic freezing and thawing exhibit more ductility, compared to undamaged samples. This behavior is apparent in the comparison plot between the reference concrete and the frozen concrete, as shown in Figure 2-4. It can be noticed that the frozen sample exhibits higher compliance than the reference sample.

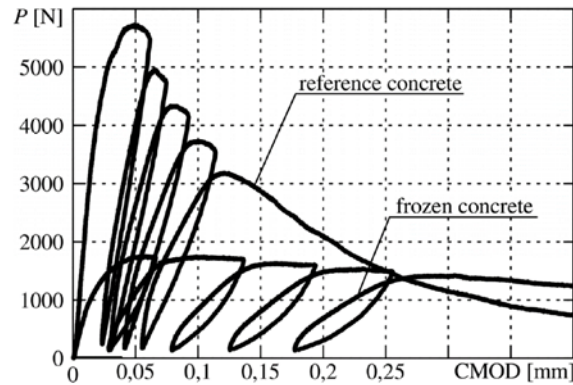


Figure 2-4. Comparison between the frozen concrete and reference concrete after 350 cycles (from Kazberuk 2012).

2.4 EARLY OPENING TO TRAFFIC CRITERIA

2.4.1 Overview

This section discusses the four studies that were mentioned in the proposal in order to better understand the experimental and analytical approaches of each study in determining the minimum strength requirements for traffic opening of PCC pavements.

2.4.2 The Effect of Early Opening to Traffic on Fatigue Life of Concrete Pavement (Suh 2005)

Suh (2005) studied the effect of EOT on the fatigue life of concrete pavements. He performed laboratory and full-scale, field slab-fatigue testing. The concrete-mix design adopted for the research was typical concrete paving mixes used in Texas. The cementitious materials content was 517 lb/yd³ with 30% class C fly ash, 0.40 w/cm ratio, and 5% target air content. Mixes were batched with two types of coarse aggregates: crushed limestone and siliceous river gravel.

The laboratory testing was first conducted to study the strength and elastic properties of the selected concrete mixes and to correlate them with maturity readings. Four different curing conditions were used (73°F moist curing; 50°, 75°, and 100° F dry curing). The test results showed a strong correlation between the strength properties and their corresponding maturity readings and reasonable R² values with the static elastic modulus.

Laboratory beam-fatigue testing was conducted at 3, 7, and 28 d. The size of the beams used for both static and fatigue tests was 6 x 6 x 36 in. The argument is that longer beams reduce the possibility of shear failure and generate greater displacement. The fatigue test was arranged at different stress levels, from 0.65 to 0.90 of the ultimate flexural strength, and was performed at 300 cycles per min (5 Hz) until failure or 2 million cycles, whichever occurred first.

Field fatigue testing was then conducted on six full-scale slabs (12 ft x 12 ft x 6 in.) to investigate the permanent deformation due to repetitive loadings and to compare the results with the laboratory fatigue test results. The test was conducted using a stationary dynamic

deflectometer (SDD) on a three-layer, rigid pavement system. Four LVDTs were attached to record the displacements. Prior to the fatigue test, slabs were loaded statically until a 9-kip force was reached, to obtain a load-displacement curve for subgrade reaction modulus back-calculations. The fatigue test was applied at a rate of 1,200 cycles per min (20 Hz) at 2, 7, and 28 d with a load variation of 9 to 30 kip.

The final step in this study was developing numerical models to evaluate the loss of life and determine the required flexural strength of concrete pavement at EOT, prior to approaching the design strength. The analysis was performed by varying the subgrade reaction modulus. The loss of life was calculated for an 8-in.-thick pavement opened to traffic at different ages and versus the corresponding modulus of rupture at the time of opening. The sensitivity analysis of the required flexural strength at the time of opening to traffic was quantified by varying the thickness in the concrete pavements, with a maximum number of equivalent single-axle load (ESAL) per d, subjected to interior and edge loadings.

The study had concluded that the thickness of the slab, the presence of edge loading, and the type of coarse aggregate used had a major contribution on the minimum required strength of concrete pavements prior to opening to traffic. The analytical model showed that change in the subbase stiffness had a minor effect on the required flexural strength. Also, it was found that the Texas Department of Transportation (TxDOT) minimum flexural strength of 450 psi, during that time, appeared to be reasonable only when the concrete was very thin.

2.4.3 Use of Modulus of Rupture, Fatigue Resistance, and Maturity in Determining Opening-to-Traffic-Time for Concrete Pavements (Olek et al. 2002)

Olek et al. (2002) conducted laboratory testing to study the possibility of determining the earliest opening time based on maturity, flexural strength, and fatigue test data. A typical mix design for concrete pavements used in Indiana was adopted for the study. The cementitious materials content was 512 lb/yd³ with ~14% class C fly ash, with a 0.42- to 0.45-w/cm ratio, and a 6.5% target air content. A special curing technique was adopted for this study.

The laboratory tests included measuring the compressive, flexural, and splitting tensile strength for concrete, as well as their corresponding maturity. Then fatigue testing was conducted at 3, 5, and 7 d's curing. The size of the beams used for both static and fatigue tests was 6 x 6 x 21 in., tested in third-point bending. The fatigue test was arranged at different stress levels of 60, 80, and 90% of the ultimate flexural strength and was performed at 300 cycles per min (5 Hz) until failure.

The findings of the study revealed that 6 x 6 x 21 in. beams cured for 3 d can withstand more than 100,000 cycles of load when the stress level is about 35% of the ultimate flexural strength. These results were based on Indiana Department of Transportation (INDOT) specifications that stipulate a pavement shall be opened to traffic when a concrete beam with a 6 x 9 in. cross section can withstand at least 7,000 cycles under a 9-kip load in third-point loading mode.

Accordingly, as long as stress in the pavement does not exceed 35% of the ultimate modulus of rupture (MOR) using equivalent 6 x 6 x 21 in., it will not experience fatigue damage during its service life. However, these results were deduced from the INDOT criteria for the maximum number of cycles required rather than conducting laboratory fatigue testing for a beam under 35 stress level of the ultimate MOR. The strength and maturity results showed a strong relation; but no solid correlation was found between the MOR, fatigue, and maturity.

2.4.4 Investigation of Design and Construction Issues for Long-Life Concrete Pavement Strategies (Roesler et al. 2000)

Roesler et al. (2000) studied the factors that affect the opening time to traffic for fast-setting hydraulic cement concrete (FSHCC) for pavement rehabilitations. They argued that opening new paved concrete to traffic at an early time might result in premature cracking in the slab. Also, if the flexural strength is not sufficient, then fatigue cracking occurs from repetitive truck loadings.

In this study, they conducted a brief fatigue analysis with an existing mechanistic–empirical rigid pavement design/analysis program called ILLICON. They used this software to estimate the cumulative damage in concrete pavement due to truck loading, using ESAL, and by varying the concrete thickness and strength, and the mean distance from the edge of the pavement slab. The analysis indicated that the required minimum flexural strength at the opening time to traffic varies, depending on the thickness of the slab and the traffic. A decrease in thickness can cause a drastic increase in the required minimum strength. Moreover, it was found that the mean distance from the edge of the pavement has a major effect on the required opening strength. Lower opening concrete strength is required when the mean distance of the truck axle from the edge of pavement increases.

2.4.5 Early Opening of Portland Cement Concrete (PCC) Pavements to Traffic (Corvetti and Khazanovich 2005)

Corvetti and Khazanovich (2005) studied the possibility of reducing the opening periods for PCC pavements by conducting field and laboratory testing of concrete specimens obtained from PCC pavement projects in Wisconsin. The focus was on the effect of EOT on the PCC pavement at the dowel bars' location. The hypothesis suggests development of excessive bearing stresses beneath dowels in the transverse joints that could result in micro- or macro-cracking in the PCC around the dowel.

Finite-element modeling was used to study the development of bearing stresses around dowels in PCC pavement at early age and under different loading conditions. The result of the finite-element analysis supports the Wisconsin Department of Transportation (WisDOT) requirements of a minimum 3,000 psi for a 10-in. PCC-slab thickness with 1.25-in. dowel bars, when subject to heavy loadings. Moreover, it was observed that 1.5-in. dowel bars reduced the minimum strength requirements to 2,200 psi under certain slab thickness, subgrade support, and axle loading.

Field and laboratory studies were also conducted to evaluate the effect of EOT on the strength gain on PCC pavement. Four different locations in Wisconsin with newly poured PCC mixes adopted by WisDOT were selected for the study. Specimens for laboratory testing were prepared on-site and included compressive cylinders, flexural beams, and 10 x 12 x 12 in. concrete blocks with exposed dowel bars, in order to determine the impact of early-age loading. Specimens were cured in the field to simulate the curing condition of the PCC pavements. The maturity test was also conducted at each site by attaching maturity probes in the pavements and specimens where correlations were made between the maturities measured in cylinders and pavement and between maturity and the strength properties of PCC specimens. The blocks with exposed dowels were subject to five cycles of 2,000 lb at different compressive strength levels in the range of 2,000 to 3,000 psi. Then specimens were field-cured and tested after 28 d.

Overall, the laboratory testing revealed a good correlation between the maturity readings and compressive strength and between the compressive and flexural strengths. However, poor correlation was found in the results of the tested blocks with exposed dowel bars.

2.5 FATIGUE OF JOINTED-CONCRETE SLABS

2.5.1 Overview

Previous work that involved cyclic fatigue loads on jointed, plain-concrete pavements (JPCP) was mainly concerned with evaluating the performance of fiber-reinforced polymer dowels (FRP) in comparison with steel dowels. This section highlights the testing considerations that are relevant to the jointed-pavement test described in section 5.8.

2.5.2 Study by Eddie et al. (2001): Glass-Fiber-Reinforced-Polymer Dowels for Concrete Pavements

The work done by Eddie et al. (2001), published by *ACI Structural Journal*, studied the structural performance of FRP and steel-doweled concrete slabs under static and cyclic loading. Specimen dimensions were 8 ft x 2 ft x 10 in., with one or two steel or FRP dowels. A 24 x 10 in. rectangular steel contact area was considered and was positioned at the edge of the joint. A total of twelve specimens were cast and tested over three phases. The first phase included testing with monotonic loading until failure. The underlying material in the first phase consisted of a series of springs with an equivalent modulus of subgrade reaction of 14 psi/in., representing a weak base layer. The static tests of phase one showed crack development in the loaded area of the slab. When the applied load exceeded 22.5 kip, it was noticed that the opening at the joint was reduced. In addition, concrete crushing at the interface between the slabs was noticed. The second phase featured a stiffer base layer consisting of compacted limestone aggregate with a subgrade reaction modulus of approximately 500 psi/in. The test resulted in higher peak loads (over 45 kip), compared with phase one. Failure was observed as the crushing of concrete at the joint due to bearing forces between the loaded and unloaded slab with dowels experiencing excessive deformation. The third phase consisted of cyclic loads ranging from 4.5 to 30 kip for a limestone aggregate base layer similar to the one in the second

phase. The test was conducted up to 1 million cycles at a frequency of 6 Hz. Intermediate monotonic loading tests were conducted to determine joint effectiveness during cyclic fatigue. At the end of each test, the base material was changed to account for the additional compaction caused by cyclic loading. All tested specimens of phase three showed no significant damage after 1 million cycles, with only minor hairline cracks being noticed.

2.5.3 Study by Vijay et al. 2009: Design and Evaluation of Jointed, Plain-Concrete Pavement with Fiber-Reinforced Polymer Dowels

Vijay et al. (2009) conducted a study for the U.S. Federal Highway Administration that investigated the fatigue performance of steel and FRP dowels in contraction joints for JPCPs. The specimen dimensions were 12 x 11 x 120 in., with either one or two dowels positioned at 5 in. below the top layer. Dowel bars were either FRP or steel, with either 1- or 1.5-in. diameter. Cyclic fatigue loading was conducted at the edge of the contraction joint where LVDTs were installed, to measure the relative deflection and the load-transfer efficiency. The testing was conducted using a frequency of 4 Hz. Static tests were conducted before cyclic loading and at an interval of every 1 million cycles. A maximum applied load of 12.5 kip was used for the static and fatigue tests for the first 1 million cycles. This load was later increased by 50% and was maintained at 18.75 kip until 5 million cycles.

The study indicated it was preferable to cast specimens directly on the base layer rather than to cast separately in forms because several samples showed failure near the dowel-edge zone away from the joint (Figure 2-5 (b)). In addition, it was mentioned that inadequate compaction, along with cyclic fatigue testing, can result in additional deflection from the testing machine. The added deflection resulted in reducing joint transfer performance in some specimens. It was also stated that casting concrete on the base ensures an even surface underneath the loaded area, causing the crack to be initiated underneath the saw-cut groove as intended (Figure 2-5 (a)). For determining the modulus of subgrade reaction, the authors suggested taking readings using standard steel plate tests at the end of every test to account for additional compaction from the cyclic and static loading. All specimens of this study showed high LTE values, over 90% after 1 million cycles of loading.

The analytical section in the report presents a procedure for calculating the relative deflection between loaded and unloaded slabs. The proposed example is based on the widely adopted works of Timoshenko and Lessels (1925) that treat dowels as beams on an elastic foundation. A comparison between analytical and experimental results shows a large variation due to the rough estimation of the modulus of dowel support. The modulus of dowel support was estimated based on values proposed by Yoder and Witczak (1975), due to the difficulty of obtaining accurate values theoretically.

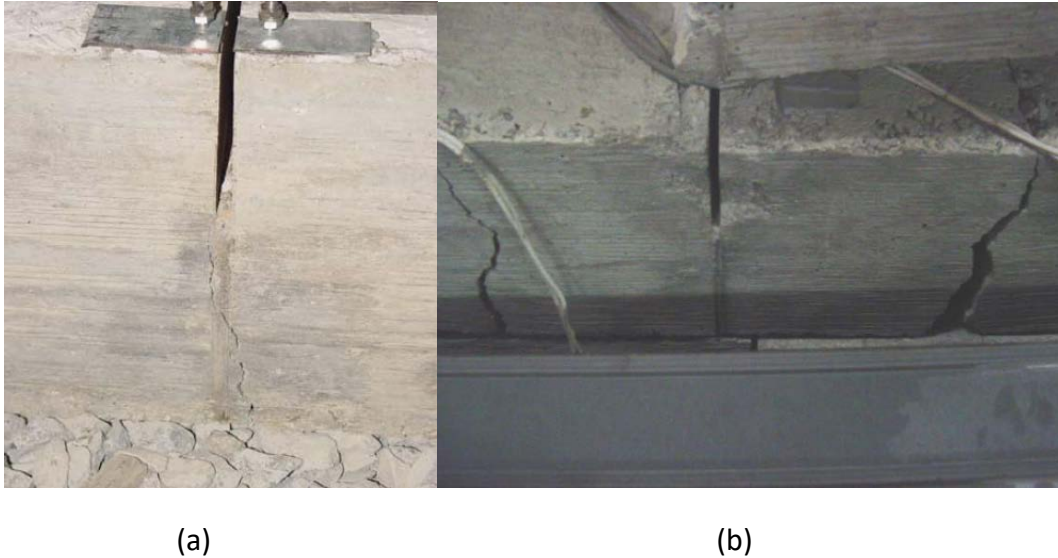


Figure 2-5. Failure modes showing proper crack initiation at the groove (a) and cracking at the zone beyond the dowel (b)(Vijay et al., 2009).

2.5.4 Study by Benmokrane et al. 2014: Performance of Glass-Fiber-Reinforced Polymer-Doweled, Jointed, Plain-Concrete Pavement under Static and Cyclic Loadings

Benmokrane et al. (2014) conducted a study published by *ACI Structural Journal* that investigated the structural performance of FRP and steel dowels in plain-concrete slabs under static and dynamic loading conditions. Sections of this study were also covered by the work of Bricola et al. (2014) for the Université de Sherbrooke, Canada. The work provided an excellent insight on the testing approach and was largely adopted for the “Fatigue Performance of Jointed-Concrete-Slabs Test Description” described in section 5.8. Specimen dimensions were 8 ft x 2 ft x 10 in. The specimens were cast with either two steel dowels (1.13-in. diameter) or two FRP dowels (either 1.38 in. or 1.5 in.), spaced at 12 in. at the mid-height of the slab. For the contact area, a circular steel plate (12-in. diameter) was positioned at the face of the joint (0.25 in. in width). The testing program consisted of two phases. In the first phase, three specimens were loaded monotonically up to 45 kip to induce cracks and then were loaded until failure. Cracks initiated at the level of the dowel bars at loads ranging from 28.1 to 31.6 kip. Shear failure was observed in the slabs where major vertical cracks appeared beyond the dowel-bar region of the loaded slab. The specimens of the first phase reached peak loads ranging from 107.5 to 113.9 kip. The second phase involved three specimens that were subjected to cyclic fatigue loads between 2.25 and 11.24 kip. Joint efficiency was measured with a static load test (9 kip) before fatigue and after a predefined number of cycles. The load-transfer efficiency (LTE) and joint effectiveness (E) were developed with respect to cycle progression. The three specimens obtained satisfactory results in accordance with ACPA recommendations for E (greater than 75%) or LTE (greater than 60%). After fatigue loading, the three slabs were tested with monotonic loading until failure. Peak loads ranged from 92.8 to 139.8 kip. As observed in Figure 2-6, the failure mode in the second phase was noticed to be a shear failure beyond the

dowel zone of the loaded slab. The authors noted that the unexpected increase in slab loading capacity in the second phase was mainly due to added compaction with every cyclic test. The authors also noted that casting the slabs on the base layer is preferred to avoid immediate deflection at the time of testing. Cyclic fatigue testing was conducted at a high frequency of 15 Hz, which corresponds to vehicular speeds of 50 mph, as per Canadian standards.

The analytical part of the study consisted of a proposed dowel-bar design by treating dowels as beams on an elastic foundation. The effectiveness of the proposed designs is presented as a ratio between the relative deflection of the selected dowel type and the relative deflection of the steel dowel-bar case. Calculations were done by assuming a modulus of dowel support of 1.5×10^6 psi/in., which is considered for more conservative results.



Figure 2-6. Static loading showing shear failure beyond the dowel-bar zone (Bricola et al. 2014).

CHAPTER 3: MATERIAL SELECTION

Selecting the materials to be adopted for the mix design is quite a challenge when dealing with green concrete. Due to the growing interest in sustainable development, IDOT is motivated more than ever to choose sustainable materials and produce what is known today as *green sustainable concrete*. The most recent ICT report submitted by the author (Issa, 2014) on the strength and durability properties of concrete for pavements had found similar performance between concrete with cement comprising more than 5% of limestone and inorganic processing and conventional cement available in the market. Concrete mixes were made with 375 lb/yd³ cement and 160 lb/yd³ (30% of the total cementitious content) of fly ash or slag and were batched with crushed limestone and natural sand or combined sand (50% natural and 50% manufactured). The study had shown favorable performance for slag over fly ash for early strength and freeze–thaw durability resistance of concrete. As a result of this work, IDOT raised the minimum cement level required for concrete pavements to 400 lb/yd³ but has adopted replacing the cement with 30% by weight of fly ash or slag. The materials selected for the mix design are presented in Table 3-1.

Table 3-1. Material Selection and Properties

Material	Type	Supplier
Cement	Type I	HOLCIM
GGBF slag	Grade 100	HOLCIM SKYWAY
Coarse aggregate	Crushed limestone	Material Service, Thornton, Illinois P/S No.: 50312-04 Material Code: 022CM1101 BD
Fine aggregate	Natural sand	TRI-CON, Hennepin, Illinois P/S No.: 51550-07 Material Code: 027FM01
Air-entraining admixture, AEA	ASTM C260 AASHTO M 154	BASF MasterAir AE 90
Water-reducing admixture, WRA	ASTM C494, Type A and Type F	BASF MasterGlenium 7511
Discontinuous fibers	Advanced synthetic	<ul style="list-style-type: none">• W.R. Grace Strux 90/40• BASF MasterFiber MAC Matrix

3.1 CEMENTITIOUS MATERIALS

Type I Portland cement conforming to ASTM C150 was used during the entire experimental study. Ground granulated blast-furnace slag (GGBFS) was selected as a supplementary cementitious material (SCM). The detailed chemical composition and physical properties of the cement and GGBF slag are shown in Table 3-2 and Table 3-3, respectively.

Table 3-2. Chemical Composition of Cement and GGBF Slag

Material	Source	Chemical Data, %														
		SiO ₂	Al ₂ O ₃	Fe ₂ O ₃	CaO	MgO	SO ₃	C ₃ S	C ₂ S	C ₃ A	C ₄ AF	Alkali	LOI ^a	IR ^b	Limestone	IPA ^c
Type I Portland	Holcim	19.4	4.5	3.2	64.2	2.5	3.5	64	5	6	9	0.55	2.7	0.37	3.1	0
GGBF slag	Skyway	37.7	7.71	0.48	38.3	10.57	2.4					0.26				

Table 3-3. Physical Properties of Cement and GGBF Slag

Material	Source	Blaine fineness, m ² /Kg	Compressive strength, psi		
			3 d	7 d	28 d
Type I Portland	Holcim	386	4,120	5,260	
GGBF slag	Skyway	558		3,770	6,140

3.2 AGGREGATES

The aggregate properties are presented in Table 3-4. The coarse aggregate is an IDOT quality “A” crushed limestone provided by Material Service Thornton quarry with a minimum of 45% passing the half-inch sieve. Suh (2005) showed that the type of coarse aggregate has a major contribution to the minimum strength required for pavement prior to opening to traffic. His study showed favorable performance for crushed limestone over siliceous river gravel. The fine aggregate is an IDOT quality “A” natural sand provided by TRI-CON, Hennepin, Illinois. Both the coarse and fine aggregate grading were ensured to meet the IDOT specification for aggregate gradations, as shown in Figure 3-1.

The coarse aggregates were prepared for saturated-surface dry condition, while the fine aggregates were prepared with a total moisture content ranging between 2 and 5%. Both materials were stored in sealed buckets to keep them under controlled-moisture conditions and prevent evaporation.

Table 3-4. Aggregate Properties

Aggregate type	Producer name	Location	P/S no.	Material code	SSD specific gravity	Oven-dried specific gravity	Water absorption, %
Coarse aggregate: ¾-in. crushed limestone	Material Service	Thornton, IL	50312-04	022CM1101	2.71	2.675	1.4
Fine aggregate: natural sand	TRI-CON	Hennepin, IL	51550-07	027FM01	2.63	2.584	1.8

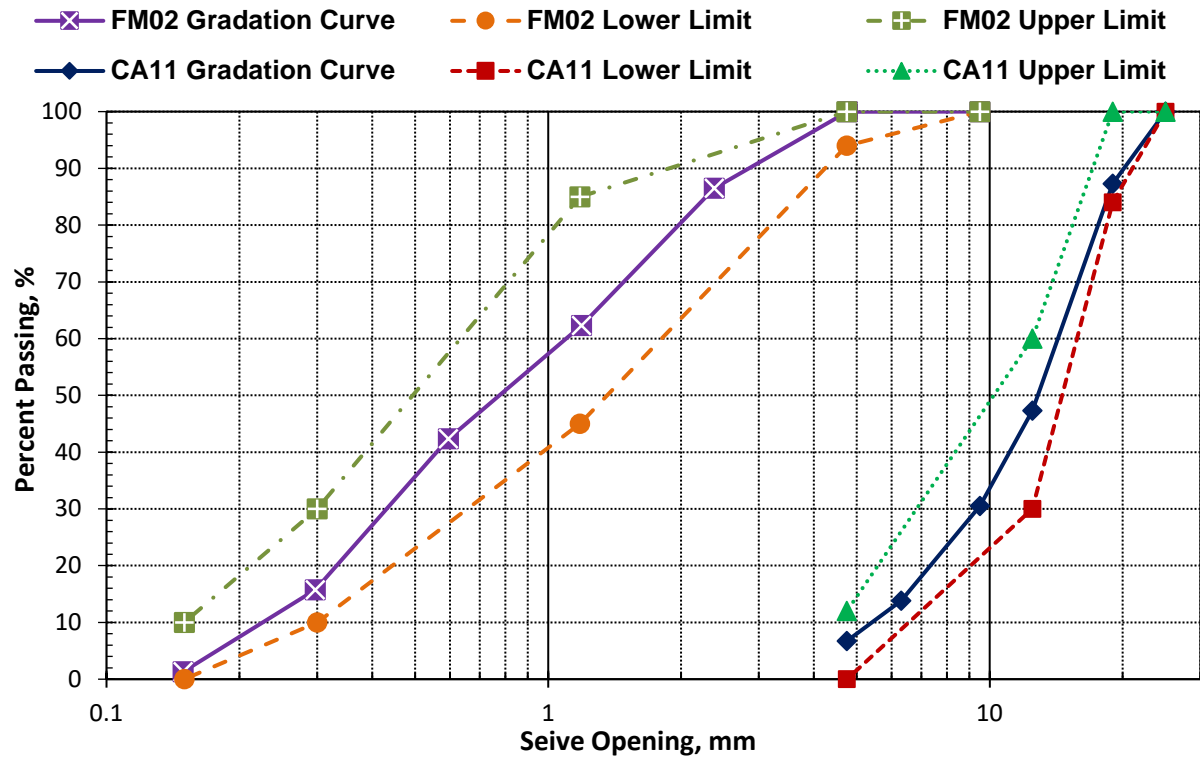


Figure 3-1. Gradation curves and limits for coarse and fine aggregates.

3.3 SYNTHETIC FIBERS

Two types of advanced synthetic macro-fiber are used as discontinuous fiber reinforcement in the concrete mixes, with their properties presented in Table 3-5: (1) W.R. Grace Strux 90/40, and (2) BASF MasterFiber MAC Matrix.

Table 3-5. Synthetic Fibers' Properties

Product designation	Source	Specific gravity	Alkali and chemical resistance	Tensile strength, ksi	Modulus of elasticity, ksi	Length, in.	Aspect ratio	Type	Material
Strux® 90/40	W.R. Grace	0.92	Excellent	90	1,378	1.55	90	flat	100% virgin polypropylene
MasterFiber MAC Matrix	BASF	0.91	Excellent	85		2.1	67	Embossed	

CHAPTER 4: MIX DESIGN AND CURING METHODS

4.1 MIX DESIGN

The concrete mixes were selected on the basis of the IDOT concrete pavement (PV) and patches (PP) presented in Table 1-1. For concrete patching, only PP-1 and PP-2 classes use Type I cement. The rest use Type III (PP-3) and rapid-hardening cements (PP-4 and PP-5) for high early strength. PP mixes required adding more cementitious materials than PV and had lower w/cm ratios in order to achieve the desired strength at an earlier period for EOT. Table 4-1 lists the concrete mixes under investigation. PV, PP-1, and PP-2 concrete mixes were to be conducted with and without fibers. The advantage of using fibers is their ability to modify ductility; resist impacts; and improve toughness by allowing uniform distribution of stresses without significantly affecting the placement, curing, or finishing characteristics of concrete. Dr. Issa's experience with synthetic fibers recommends using 4 lb/yd³ of advanced synthetic fibers, while premixing them with coarse aggregate for optimum performance of the fresh- and hardened-strength properties of concrete.

Table 4-1. Selected Concrete Mixes for Laboratory Testing

Mixture designation	Cementitious content, lb/yd ³	w/cm ratio	Slump, in.	Air content, %	Synthetic fiber*, lb/yd ³
PV-control	565	0.42	2–4	5.0–8.0	0.0
PV-fiber	565	0.42	2–4	5.0–8.0	4.0–8.0 [~]
PP-1-control	650	0.42–0.44	2–4	4.0–7.0	0.0
PP-1-fiber	650	0.42–0.44	2–4	4.0–7.0	4.0
PP-2-control	735	0.36	2–6	4.0–6.0	0.0
PP-2-fiber	735	0.36	2–6	4.0–6.0	4.0
*Two types of synthetic fibers were investigated (see Table 3-1).					
[~] PV-fiber mixes were made with 4.0, 6.0, and 8.0 lb of synthetic fibers.					

The mixes are designed based on a mortar factor of 0.88. The GGBF slag is used to replace 25% by weight of the total cementitious content.

4.2 CURING METHODS FOR LABORATORY TESTING

Curing at low temperature results in lower strength at early age for PCC pavements. The construction season in Illinois starts May 1 and ends November 30 where the average temperature in November is below 50°F. For this reason, two curing regimes were adopted for laboratory testing.

4.2.1 Room Temperature Curing

Concrete specimens that were cured at room temperature were covered with wet burlaps and stored indoors at 23 °C for 24 hr after casting, after which they were demolded and stored in a concrete-curing tank or moisture room under a controlled temperature of 23°C and 100% relative humidity. Details of the curing systems are explained below.

Controlled-moisture room for curing concrete: The moisture room has a controlled temperature of 73°F (23°C) and relative humidity of 100%, where the specimens are moist-cured. The size of the room is 158 ft². Recently, a fully automated, wall-mounted control panel was installed for the moisture room (see Figure 4-1, left). The system automatically blends hot and cold water supplies to keep the concrete-specimen-curing environment at precisely $73.4 \pm 3^\circ\text{F}$ ($23 \pm 1.7^\circ\text{C}$) and 100% humidity.





Figure 4-1. Moisture room fully automated control panel (top) and controlled curing tank (bottom).

Controlled concrete-curing tank: The tank is equipped with two water-circulation pumps and a heater capable of maintaining the temperature of the water at 73°F (23°C). The size of the tank is around 7 x 3 x 1.5 ft.

4.2.2 Cold Temperature Curing (40–50°F):

Concrete specimens that were cured at 40–50°F were first stored indoors under room temperature at 23°C until the initial setting time was reached, measured by the penetration resistance in accordance to ASTM C403, after which the specimens were transferred into a controlled temperature and humidity chamber at 40–50°F (see Figure 4-2, left). The size of the chamber is about 8 x 10 ft. The room has the capability to simulate any temperature and humidity around the nation.



Figure 4-2. Controlled temperature chamber with concrete specimens cured at 45°F.

The specimens, which included 6 x 6 x 21 in. concrete beams and 6 x 12 in. concrete cylinders, were placed in two 48 x 45 x 6.5 in. plastic tubs filled with water to a 5-in. level. The specimens were cured using a special curing technique (Olek et al. 2002), as shown in Figure 4-3. Once the specimens were placed in the water tub, they were completely covered with burlaps. The burlaps were then covered with plastic tarps and kept wet at all times by capillary rise of water and by sprinkling every 24 hr.

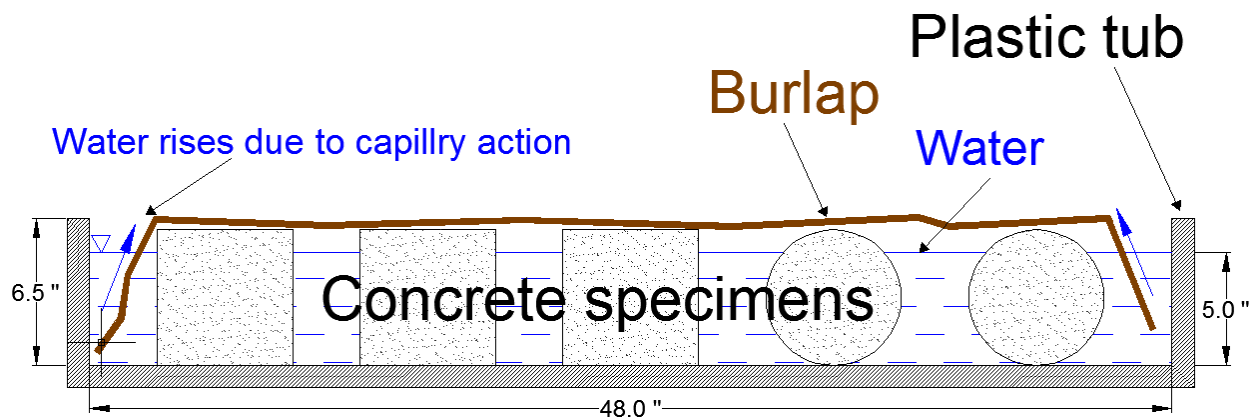


Figure 4-3. Curing technique used in the temperature-controlled chamber.

Although curing at higher temperatures can lower the ultimate strength, it is not a concern because it accelerates the concrete set time and increases its strength at early age.

CHAPTER 5: LABORATORY TESTING PROGRAM

The behavior of early-age PCC pavement is influenced by many factors, such as climatic conditions, concrete and subbase temperature, slab–subbase and interface restraint, curling and warping of concrete slab, and construction procedures. To minimize all these factors and accentuate on the fatigue damage due to EOT, a laboratory-mixing and -testing program was developed for this study. All the laboratory testing program required conducting laboratory concrete mixes in a controlled environment with controlled aggregate gradation and moisture content. This attention to control is advantageous to reduce production variability experienced from ready-mixed concrete provided from commercial suppliers. The laboratory test methods are carried out on the PCC mixes for pavements and patches, presented in Table 4-1.

This chapter includes conducting static, fracture-mechanics, and fatigue load tests on concrete, as well as maturity tests, and tests of the elastic properties and stiffness degradation before and after fatigue for concrete mixes with and without fibers. Once these tests are completed, freeze–thaw tests are conducted to test the durability performance post-fatigue.

5.1 LABORATORY EQUIPMENT

The 5,000 ft² material and structural laboratories at UIC are equipped with state-of-the-art equipment for testing and analysis required for this study. This section shows the equipment and facilities used during the course of the project. Presented below is a brief summary of the test equipment:

Instron 8500 Series Servo-hydraulic Testing System: This sophisticated system is used for the controlled testing of various materials. The actuator has a capacity of $\pm 50,000$ lb and can apply dynamic (fatigue) and static loading. The system has a steel bed 26-in. wide by 144 in. long. The system is highly controlled, using four distinct controlling schemes: load, deflection, strain, and crack opening, allowing for open- and closed-loop testing. Figure 5-1 (left) depicts the system.

Tinius Olson Compression Testing Machine: This universal testing machine is digitally controlled, with a variable cross-head speed and maximum capacity of 400,000 lb. It is used for testing concrete specimens for compression, modulus of elasticity, and flexural and shear strength (Figure 5-1, right).



Figure 5-1. Instron 8500 system (left) and Tinius Olsen system (right).

Freeze and Thaw Cabinet (ASTM C 666, Procedure A): The concrete laboratory is equipped with two freeze–thaw cabinets that accommodate 40 concrete specimens of 3 x 4 x 16 in. The testing machines are controlled by a fully automated operating system that frees the operator to perform other lab duties. This test method covers the determination of the resistance of concrete specimens to rapidly repeated cycles of freezing and thawing in the laboratory. This test method is used to determine the effect of variations in the properties and conditioning of concrete and its resistance to freeze–thaw cycles. Figure 5-2 (right) depicts the freeze–thaw cabinets with automated controller.

Resonant Frequency-Testing System (ASTM C 215): The concrete laboratory is also equipped with resonant frequency-testing equipment to measure the relative dynamic modulus of freeze-and-thaw-degraded specimens. It goes hand in hand with the freeze–thaw test method.

Petrographic Analysis of Hardened Concrete (CAS 2000): This system is used for petrographic analysis of hardened concrete. It is capable of performing both linear traverse and modified point-count measurement (ASTM C457). The system consists of motorized x and y axes under computer control, a 486-based PC with VGA color monitor, a Nikon SMZ-2T trinocular optical body, ½-in. Chromachip V high-resolution color camera (480 lines of horizontal resolution), Sony Trinitron PVM-1343 13-in. ultrahigh-resolution RGB color video monitor. Figure 5-2 (left) depicts the system.



Figure 5-2. Petrographic analysis of concrete (left); and freeze-thaw cabinets (right).

5.2 MECHANICAL PROPERTIES OF CONCRETE MIXES

The mechanical properties included measuring the compressive strength, flexural strength, and the static modulus of elasticity (MOE). Moreover, the relative dynamic modulus (RDM) was measured in accordance with ASTM C215. Linear drying shrinkage was also conducted to study the effect of adding synthetic fibers to concrete and the use of higher amounts of cementitious materials for class PP-1 and class PP-2 concrete mixes.

When dealing with unreinforced concrete, fracture-mechanics principles become extremely important. The strength, fracture toughness and roughness of concrete, the fractal dimensions, the size and shape of aggregates in concrete, and the incorporation of fibrous materials all contribute to crack initiation, the level of crack propagation in concrete, and the ability to resist it. For this purpose, the toughness of the fibrous concrete was measured with 6 x 6 x 21 in. beams in accordance with ASTM C1609 (*Flexural Performance of Fiber-Reinforced Concrete*). Table 5-1 lists the laboratory tests conducted.

Table 5-1. Laboratory Test Methods and Number of Tests per Concrete Mix

Test method	Description and testing times	Test standard	Sample size	Samples no. per test
Compressive strength	Test at ½, 1, 2, 3, 7, 14, and 28 d	ASTM C39	6 x 12 in. cylinder	3–4
Flexural strength	Test at ½, 1, 2, 3, 7, 14, and 28 d	ASTM C78	6 x 6 x 21 in. prism	2
Flexure toughness of fibrous concrete	Test at ½, 1, 2, 3, 7, 14, and 28 d	ASTM C1609	6 x 6 x 21 in. prism	2
Static modulus of elasticity	Test at ½, 1, 2, 3, 7, 14, and 28 d	ASTM C469	6 x 12 in. cylinder	2
Linear drying shrinkage	Start measuring after 1, 3, and 7 d	ASTM C157	3 x 3 x 11 in. prism	3
Relative dynamic modulus (RDM)	Test at ½, 1, 2, 3, 7, 14, and 28 d	ASTM C215	6 x 12 in. cylinder	3

5.2.1 Fresh-Concrete Properties

All concrete mixes are mixed according to ASTM C192/AASHTO T 126. The IDOT PCC Mix Design Version V2.4 was used. The slump, unit weight, fresh-air content (pressure meter per ASTM

C231), initial setting time, concrete-mix temperature, ambient temperature, and humidity were measured for each concrete mixture

5.2.2 Strength Characteristics

The compressive and flexural strength tests were carried out according to ASTM C39/AASHTO T22 and ASTM C78/AASHTO T97, respectively, at 12 hr; and 1, 2, 3, 7, 14, and 28 d of age.

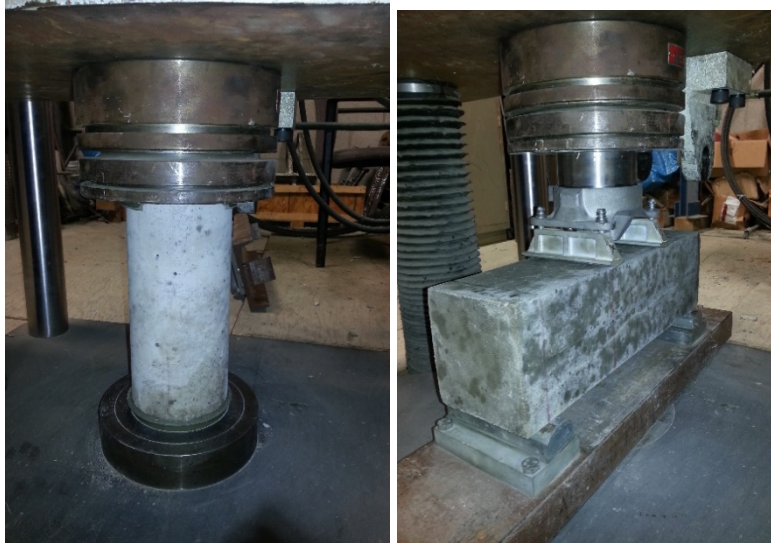


Figure 5-3. Test configuration for the compressive and flexural strength of concrete.

5.2.3 Static Modulus of Elasticity

The static modulus of elasticity (E_s) was conducted according to ASTM C469 at 12 hr; and 1, 2, 3, 7, 14, and 28 d of age. The test covers the determination of chord (Young's) modulus of concrete cylinders under compressive stress. The E_s is conducted by fixing a concrete cylinder inside a test fixture equipped with a compressometer connected to the testing machine. The compressometer is capable of measuring the strain in the concrete within a predefined length in the concrete cylinder, as shown in Figure 5-4.



Figure 5-4. Static modulus of elasticity test setup.

The calculation of E_s is calculated according to ASTM C469 as follows:

$$E_s = \frac{(S_2 - S_1)}{(\epsilon_2 - 0.000050)} \quad (5-1)$$

where

E_s = chord modulus of elasticity, ksi

S_2 = stress corresponding to 40% of ultimate load

S_1 = stress corresponding to longitudinal strain, ϵ_1 , of 50 microstrain ($\mu\epsilon$)

ϵ_2 = longitudinal strain produced by stress S_2

5.2.4 Dynamic Modulus of Elasticity

The dynamic modulus of elasticity (ED) test was conducted according to ASTM C215: *Fundamental Transverse, Longitudinal, and Torsional Resonant Frequencies of Concrete Specimens*. The test determines the resonant frequency of prismatic or cylindrical concrete specimens through the resonance-impact method described in ASTM C215. In this study, the test was carried out following the transverse and longitudinal resonant frequency on 6 x 12 in. concrete cylinders for compression tests at 9 and 12 hr; and 1, 2, 3, 7, 14, and 28 d of age. The purpose of the test is to determine the applicability of the ED as an effective nondestructive measure for predicting the compressive strength development of concrete cylinders. Relative

dynamic modulus tests were also conducted on 6 x 6 x 21 in. beams for flexural test at 12 hr; and 1, 3, and 7 d. Conducting these tests served as a means to ensure strength consistency between the beam samples, in addition to developing a correlation between the flexural strength and the dynamic modulus.

The test consists of a hammer and an accelerometer that is connected to a data-acquisition system for frequency measurement. The test conditioning depends on the shape and size of the specimens. Small specimens are usually placed on a two-point support bed, while large specimens such as 6 x 12 in. concrete cylinders or 6 x 6 x 21 in. concrete beams can be supported on a special flat sponge (see Figure 5-5). The accelerometer is then mounted on the surface of the specimen at a specific position depending on the mode of vibration (longitudinal, transverse, or torsional) of the resonant frequency that needs to be determined. The vibration is then excited by striking the hammer at the proper impact point (see Figure 5-6).

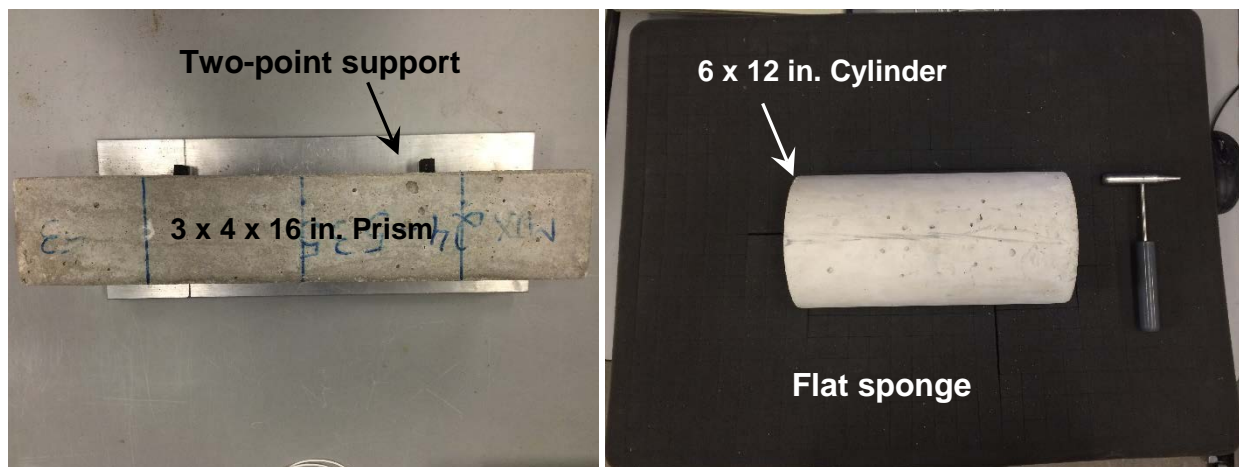


Figure 5-5. Supported specimens for E_D measurement.

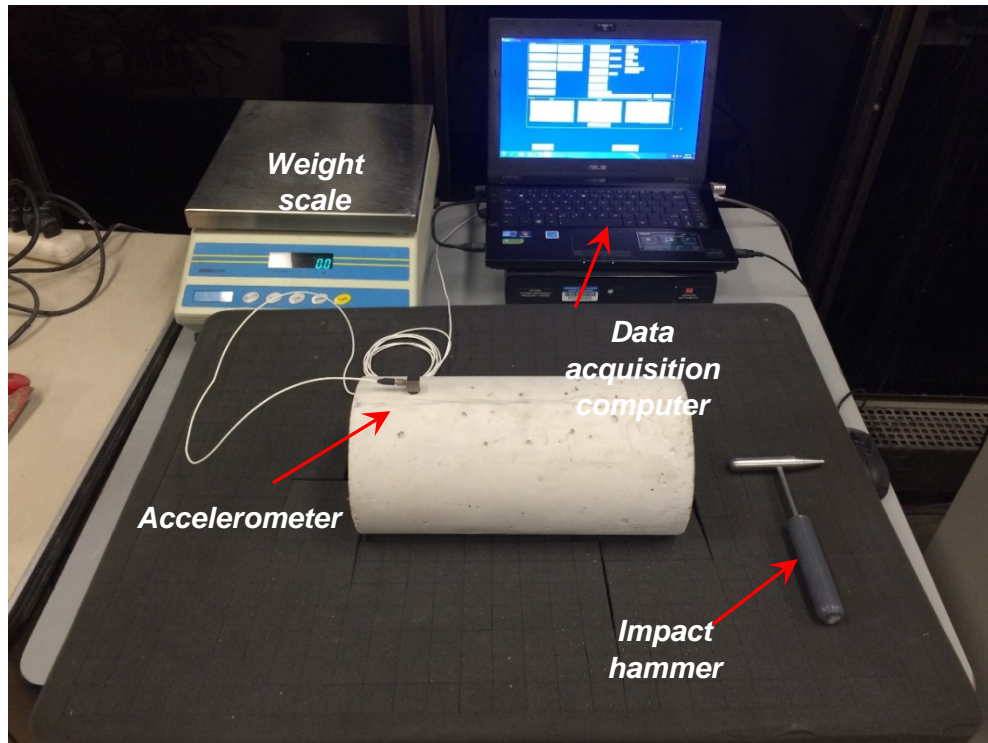


Figure 5-6. DK-5000 dynamic resonance-frequency tester, ASTM C215.

Once the transverse resonant frequency is measured, the E_D can be calculated as follows:

$$E_{D\,Trans.} = CMn^2 \quad (5-2)$$

where

E_D = dynamic modulus of elasticity, Pa

M = mass of specimen, kg

n = fundamental transverse frequency, Hz

$C = 1.6067 (L^3T/d^4)$ for a cylinder or $0.9464 (L^3T/bt^3)$ for a prism, m^{-1}

L = length of specimen, m

d = diameter of cylinder, m

t = thickness (depth) of prism, m

b = width of prism, m

T = correction-factor-based radius of gyration K ($d/4$ for a cylinder and $t/3.464$ for a prism) and Poisson's ratio μ found from Table 1 of ASTM C215.

The longitudinal frequency is measured similarly, with the following equation:

$$E_{D\ Long.} = DM(n')^2 \quad (5-3)$$

where

n' = fundamental transverse frequency, Hz

$D = 5.093 (L/d^2)$ for a cylinder, or $4 (L/bt)$ for a prism, m^{-1}

5.2.5 Flexure toughness of fibrous concrete

The flexure toughness of fibrous concrete was determined according to ASTM C1609: *Flexural performance of fiber-reinforced concrete*. The toughness of fibrous concrete is mainly influenced by the type and quantity of fiber, its physical properties, its strength, and its bond to concrete. The advantage of using these fibers in PCC pavement is their ability to modify ductility, resist impacts, and improve toughness by allowing uniform distribution of stresses without significantly affecting the placement, curing, or finishability of concrete.

The test is carried out on 6 x 6 x 21 in. concrete beams cured for 12 hr; and 1, 2, 3, 7, 14, and 28 d of age. The beams are tested in a third-point bending mode, as shown in Figure 5-7. A special jig is secured to the beam at its midsection directly above the supports where two transducers, to measure the net deflection, are mounted on the jig at mid-span of each face of the beam. The test is controlled by the transducer shown in the figure, using a closed-loop, servo-controlled testing system.

A typical flexure toughness load-deflection curve for a concrete beam with synthetic fibers is shown in Figure 5-8. The ultimate flexural strength is calculated from the peak load. The flexure toughness (T^D_{150}) is represented by the total area under the load-deflection curve, up to a net deflection of 1/150 of the span length of the beam.

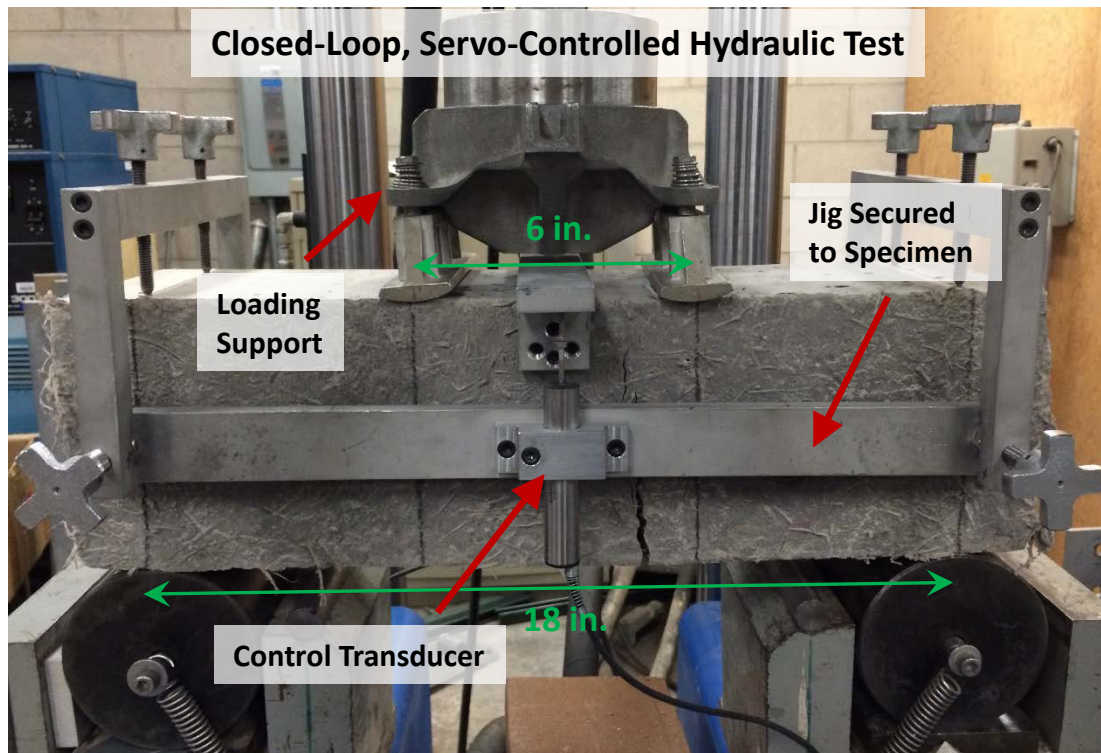


Figure 5-7. Flexure toughness test configuration.

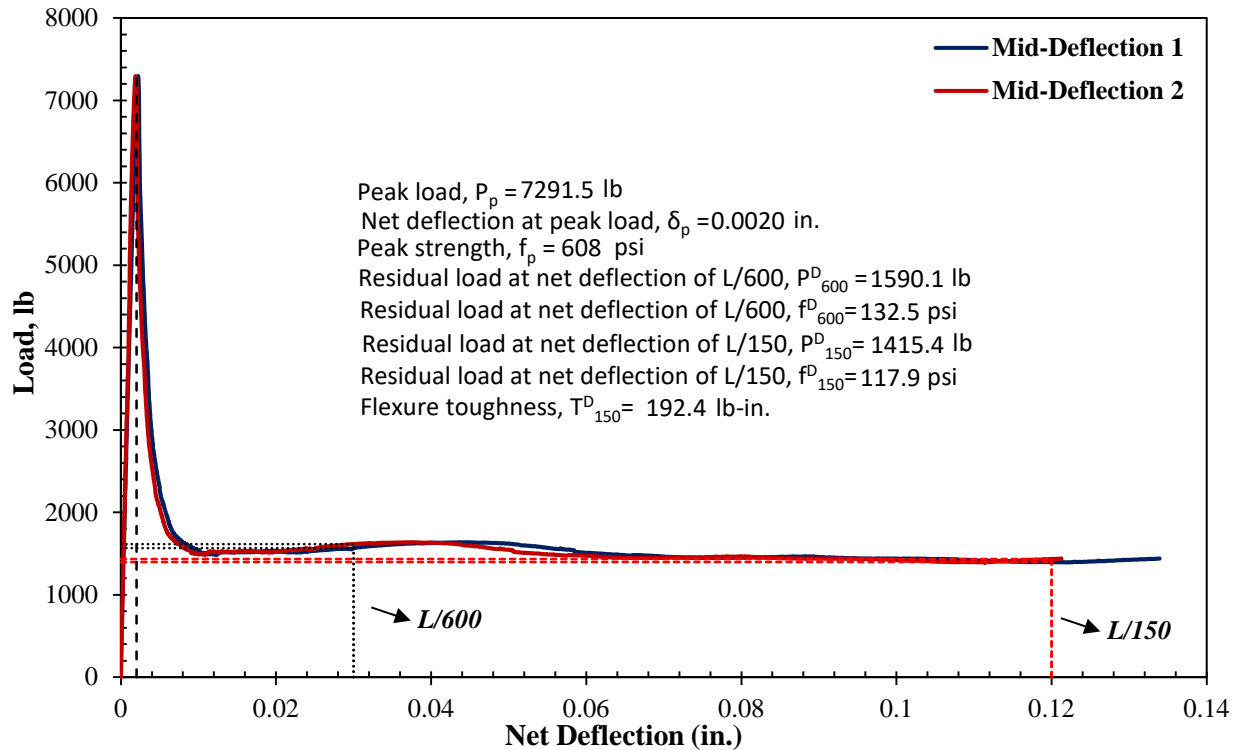


Figure 5-8. Example of flexure toughness load-deflection curve (concrete with synthetic fibers).

5.2.6 Linear Drying Shrinkage

From each concrete mixture, nine specimens for linear drying shrinkage were prepared. The specimens were cast in 76 x 76 x 286 mm (3 x 3 x 11¼ in.) steel prism molds meeting the requirements of ASTM C157. The specimens were unmolded after 24 hr. The shrinkage specimens from each mix were divided into three sets for curing, after which all specimens were stored in a control room at 73°F (23°C) temperature and 50% relative humidity.

Set I: 1-d curing (after unmolding)

Set II: 3-d curing

Set III: 7-d curing

After Sets II and III specimens were unmolded, they were stored in a water-curing tank at room temperature until the end of their specified curing period.

The linear drying shrinkage readings were measured in accordance with ASTM C490 (see Figure 5-9 for test setup). Measurements were recorded diurnally for the first 28 d of drying and then once a week to get a good representation of the shrinkage readings. The readings were collected over 120 d, while the samples were being dried under controlled room temperature and relative humidity as specified earlier. The calculation of shrinkage was made according to ASTM C426:

$$\Delta L_x = (L_I - R_{I(23)}) - (L_x - R_{x(23)}) \quad (5-4)$$

$$S_x = (\Delta L_x / G) \times 10^6 \quad (5-5)$$

where

ΔL_x = the change in the linear dimension of the specimen due to drying at any drying time, x, mm (in.)

L_I = the initial specimen-length reading immediately after removing from moisture-curing room, mm (in.)

$R_{I(23)}$ = the accompanying reference-bar length reading for L_I , mm (in.)

L_x = specimen-length reading at any time x, corrected for temperature, mm (in.)

S_x = linear drying shrinkage, at any time, x, %,

G = 254 mm (10 in.) test-specimen gauge length

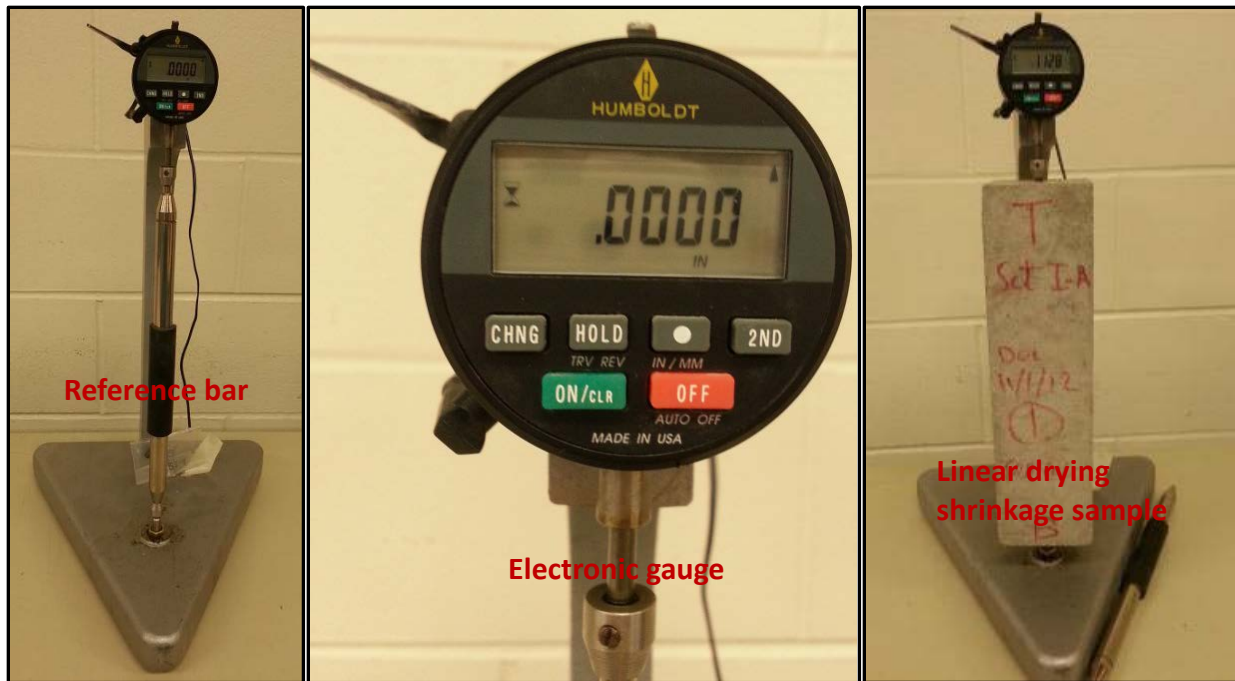


Figure 5-9. Linear drying shrinkage-test configuration.

5.3 MATURITY MEASURES

The maturity test was conducted according to ASTM C1074. To measure the maturity in concrete, Type K thermocouples were embedded in concrete control specimens and attached to a data logger that collects temperature readings from the specimens at regular time intervals (see Figure 5-10). Six Versalog TC data loggers were used to accommodate the large number of concrete mixtures conducted for all the aforementioned mechanical properties. The Versalog TC data logger has seven thermocouple channels and on-board thermistor reference temperature with programmable range and a sampling interval up to 20 milliseconds. The data loggers were configured to collect temperature readings at a regular 3-min interval. A typical time–temperature development in concrete is shown in Figure 5-11.

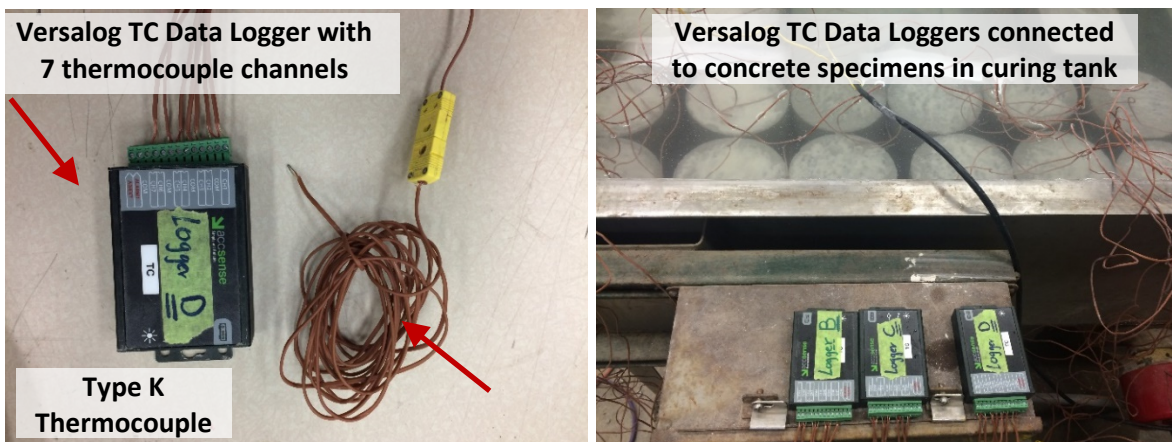


Figure 5-10. Temperature data loggers for maturity measure.

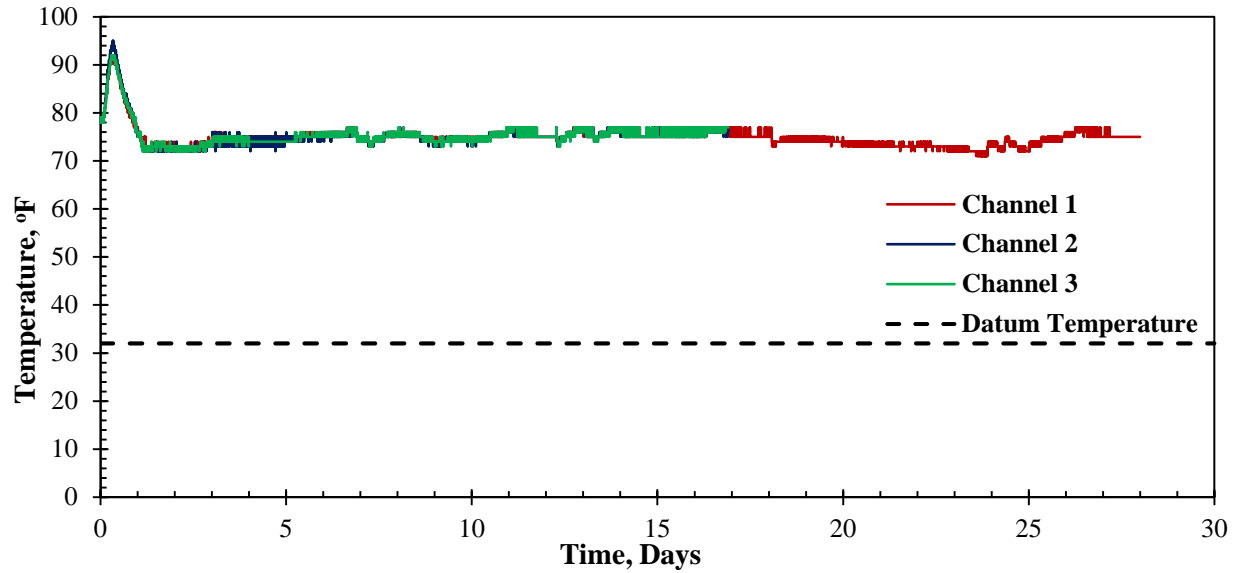


Figure 5-11. Temperature–time development in concrete at room temperature.

From the temperature–time development, the maturity–time factor $M(t)$ is calculated using the Nurse–Saul maturity function, as follows:

$$M(t) = \sum (T_a - T_o) \Delta t \quad (5-6)$$

where

T_a : average concrete temperature during each time interval

T_o : temperature below which cement hydration is assumed to cease (32°F)

Δt : time intervals, d or hr

Typical maturity- age and maturity–compressive strength relationships of concrete are shown in Figure 5-12. From the maturity measures, maturity-compressive and flexural strength and SMOE relations were developed for each concrete mix.

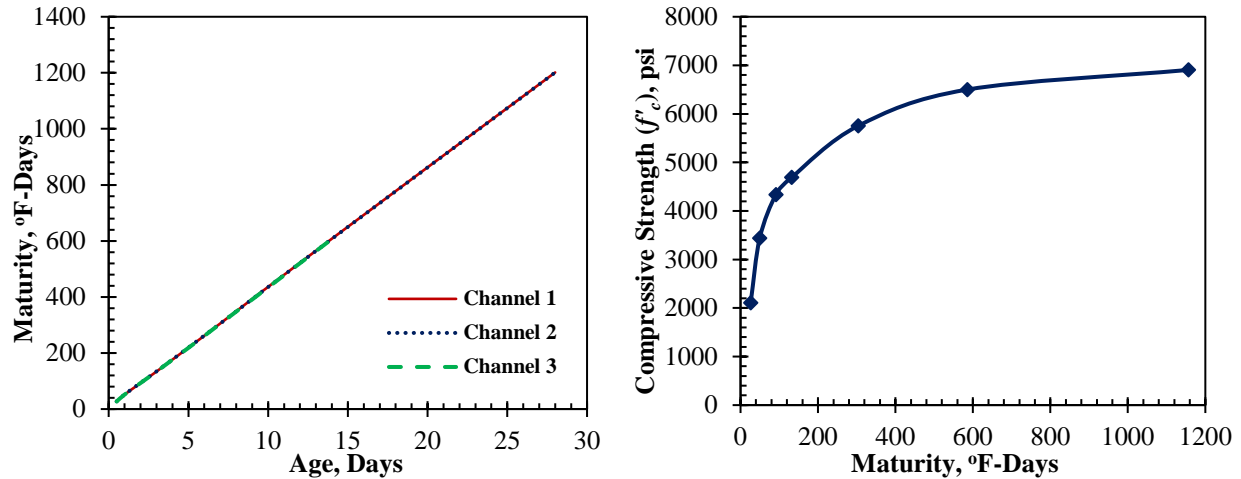


Figure 5-12. Maturity vs. age of concrete (left); compressive strength vs. maturity (right).

5.4 FRACTURE-MECHANICS TEST

The fracture-mechanics (FM) test in concrete was conducted on 3 x 4 x 16 in. notched prisms for PV, PP1, and PP2 concrete-mix combinations with and without synthetic fibers. For each mixture, sixteen notched prisms and sixteen concrete cylinders were cast. Special steel molds with a 5-mm-thick Plexiglass notch were used to cast the prisms, as shown in Figure 5-13. Testing of notched beams was conducted at 9, 12, and 13 hr and also at 1, 2, 3, 7, 14, and 28 d of age. For each FM test, two concrete cylinders were tested for RDM and compressive strength.

The RILEM recommendations for notched-beam testing, which are based on the work done by Jenq and Shah (1985a,b), are used to calculate the critical stress-intensity factor (K_{Ic}) and the critical crack-mouth-opening displacement, $CMOD_c$. The three-point bending test was conducted on notched beams having dimensions of 3 x 4 x 16 in. and a notch depth equal to 0.3 the depth of the beam (1.33 in.). The test is conducted through a closed-loop testing machine (Instron 8500), as shown in Figure 5-14. The $CMOD$ gauge clip is used to control the testing machine through a feedback signal (see Figure 5-15).

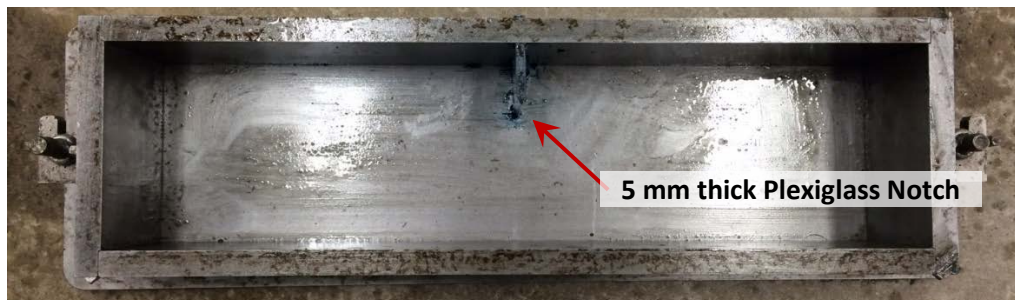


Figure 5-13. Steel molds with Plexiglass notches for fracture-mechanics test.

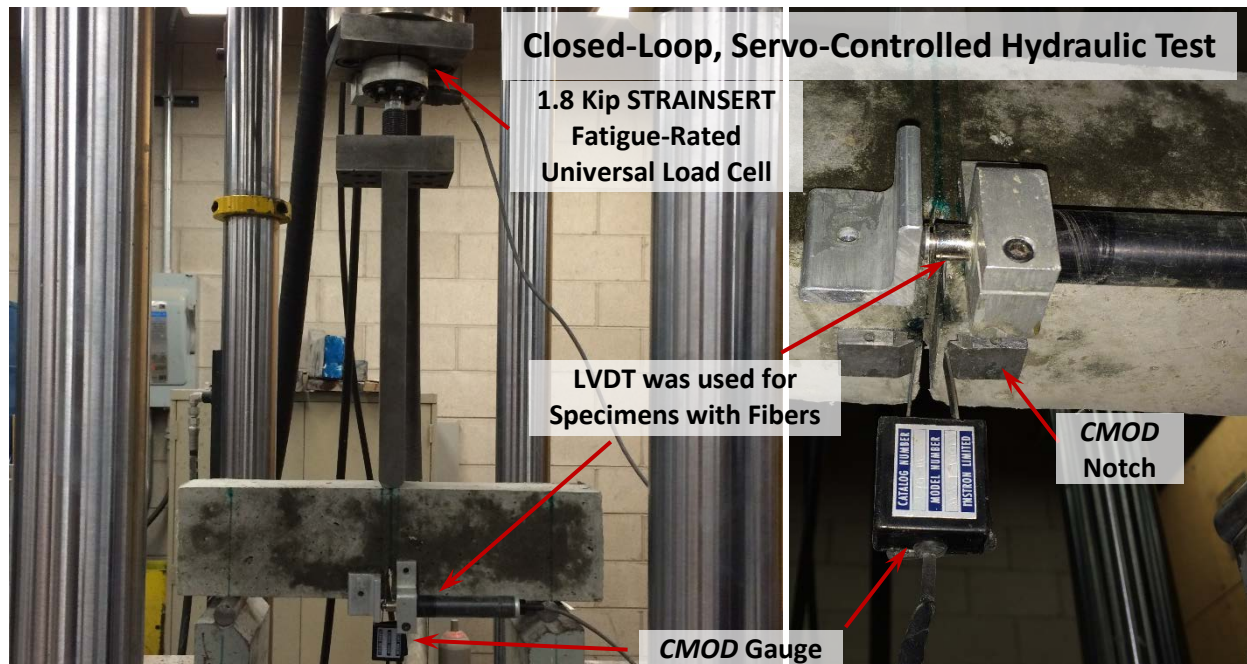


Figure 5-14. Testing setup and configuration for the fracture-mechanics test.

The capacity of the *CMOD* clip gauge is limited to an opening of 0.39 in. (10 mm). Concrete specimens reinforced with fibers can withstand a crack-mouth-opening displacement of around 1 in. (25.4 mm). Therefore, an LVDT is placed at the same level as the *CMOD* gauge to account for the opening beyond the capacity of the *CMOD* gauge, as shown in Figure 5-14 (right).

A load cell is used for the testing, with a maximum capacity of 1.8 kip and a sensitivity of ± 0.1 kip. The readings of the *CMOD* clip gauge and load cell are recorded through a data-logging system having a data-collection interval of 1 sec. Instron software is used to control the test and define the loading and unloading intervals. The specimens are loaded until the peak load is reached and dropped to 95%. The operator manually unloads the specimen through the software. The machine unloads the specimen until zero load is reached; then it automatically starts the second loading cycle. The software is set up such that the duration of the first cycle is around 5 min, with 1 min for the rest of the cycles. A total of ten cycles is performed for each specimen. The specimen is loaded to failure at the eleventh cycle. The test setup and a typical load versus *CMOD* (*P-CMOD*) curve are shown in Figures 5-15 and 5-16, respectively.

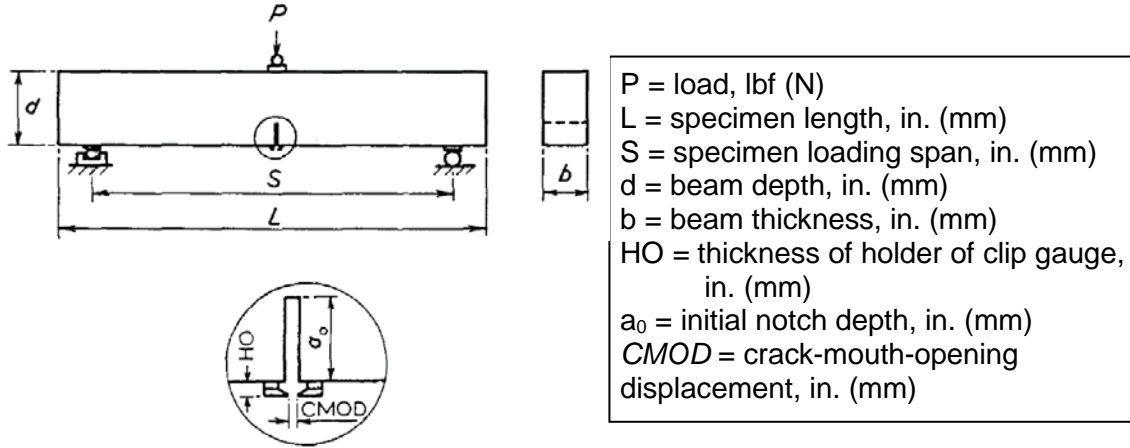


Figure 5-15. Testing configuration and geometry of specimen (modified from Shah 1990).

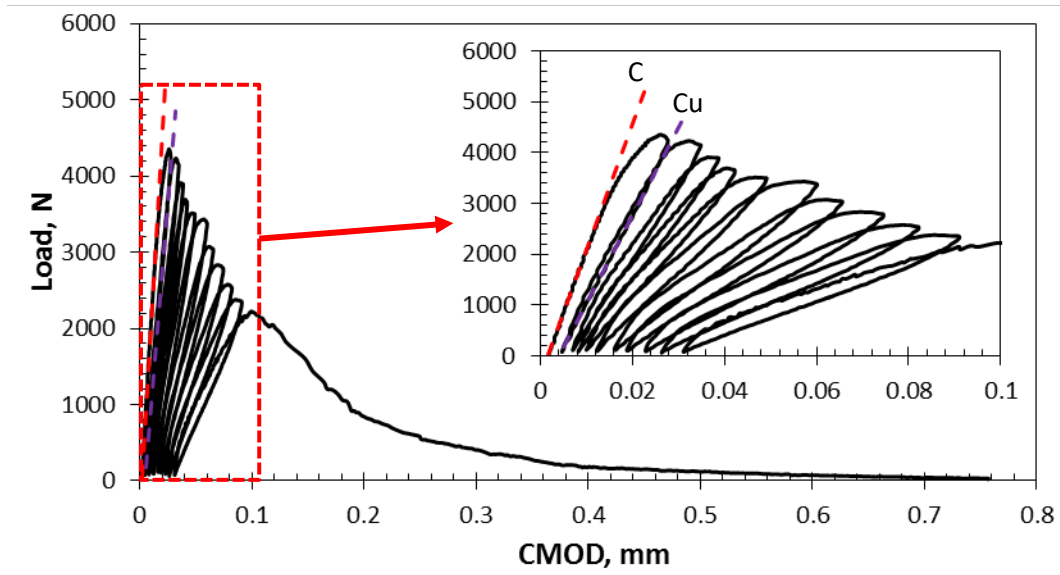


Figure 5-16. Typical load vs. crack-mouth-opening displacement curve.

After obtaining the P - $CMOD$ curve of each specimen, the modulus of elasticity is calculated from the initial loading compliance (C_i) using:

$$E = 6Sa_0V_1(\alpha) / C_i d^2b \quad [N.m^{-2}] \quad (5-7)$$

Where

$$V_1(\alpha) = 0.76 - 2.28\alpha + 3.87\alpha^2 - 2.04\alpha^3 + \frac{0.66}{(1-\alpha)^2} \quad (5-8)$$

And

$$\alpha = (a_o + HO)/(d + HO) \quad (5-9)$$

The critical effective crack length is defined as $a_c = a_o + \text{stable crack growth at peak load [m]}$. It is determined using an iterative procedure such that the modulus of elasticity from the loading compliance is equated with the modulus of elasticity from the unloading compliance such that:

$$E = 6 S a_c V_1(\alpha) / C_u d^2 b \quad [N.m^{-2}] \quad (5-10)$$

Then the critical stress-intensity factor, K_{IC}^S , can be evaluated from Equations 5.11 to 5.14. P_{max} is the maximum measured load in (N).

$$K_{IC}^S = 3(P_{max} + 0.5W) \frac{S (\pi a_c)^{0.5} F(\alpha)}{2 d^2 b} \quad [N.m^{-\frac{3}{2}}] \quad (5-11)$$

Where

$$F(\alpha) = \frac{1.99 - \alpha(1 - \alpha)(2.15 - 3.93\alpha + 2.7\alpha^2)}{\sqrt{\pi^{0.5}(1 + 2\alpha)(1 - \alpha)^{\frac{3}{2}}}} \quad (5-12)$$

And

$$\alpha = a_c/d \quad (5-13)$$

$$W = w_0 S/L \quad [N] \quad (5-14)$$

Where w_0 is the self-weight of the beam. Similarly, the value of the critical crack-mouth-opening displacement, $CTOD_c$, can be calculated from the critical effective crack length, a_c , using Equations 5.15 to 5.18.

$$CTOD_c = \frac{6P_{max} S a_c V_1(\alpha)}{E d^2 b} F(\beta) \quad (5-15)$$

$$F(\beta) = [(1 - \beta)^2 + (1.081 - 1.149\alpha)(\beta - \beta^2)]^{1/2} \quad (5-16)$$

Where

$$\alpha = a_c/d \quad (5-17)$$

$$\beta = a_0/a_c \quad (5-18)$$

5.5 FATIGUE TEST

5.5.1 Test Significance

The main objective of this study is to assess the effect of concrete pavements' elastic properties on their fatigue damage when opened to early traffic. The experimental lab-testing program for this task is characterized by performing cyclic loading on samples prepared using PV (without fibers), PVF1, and PVF2 (with a variable amount of fibers) at early age and at different stress levels. The purpose of this test is to study the resistance of these mixes to fatigue damage. The resistance to fatigue damage is determined through developing the S-N curves (stress versus number of cycles) for these mixes at different ages. The S-N curves are used as an indicator to predict the number of load cycles that causes damage at a given stress level. They relate the tensile/flexural stress in the pavement at certain age to the number of applied cycles until failure.

5.5.2 Testing Program for Fatigue Test

Flexural fatigue testing was conducted on 6 x 6 x 21 in. beams for all mixes with and without fibers. Plain-concrete mixes were batched according to the pavement-mix design (PV). The amount of fibers used was 4 and 8 lb/yd³ of Strux® 90/40 for PVF1 and PVF1-8lbs mixes respectively, and 4 lb/yd³ of MasterFiber MAC Matrix for PVF2 mixes. PVF1, PVF2, and PVF1-8lbs were batched to investigate the effect of the presence of fibers on concrete fatigue performance.



Figure 5-17. Fatigue testing setup.

Cyclic loading was applied using a four-point bending configuration for specimens, as shown in Figure 5-17. The specimens were tested at 12 hr; and 1 d, 3 d, and 7 d. For each mix, twelve beams were prepared from 6 ft³ batches of concrete. From the prepared beams, four beams were tested for fatigue; and the rest were used for static flexural testing. The following procedure was used to conduct the fatigue tests:

- Prior to each fatigue test, two beams were tested for static flexural strength to determine the *MOR* at the given age of concrete.

- The average of the *MOR* readings was used to determine the mean and amplitude of the cyclic loading for each stress level (S_i).
- The maximum stress applied is the average MOR obtained multiplied by the stress level (i.e., $\sigma_{i_max} = S_i \times MOR$). Whereas the minimum load applied is 10% of the maximum load (i.e., $\sigma_{i_min} = 0.1 \times \sigma_{i_max}$). A typical wave configuration for fatigue tests is shown in Figure 5-18.
- The stress levels (S_i) were set to 0.9, 0.8, 0.7, and 0.6 for all the mixes.
- Fatigue tests were performed at a frequency of 4 Hz, using an Instron 8500 closed-loop testing system.
- RDM readings were taken for each specimen to verify the accuracy of the identified stress level in the beam to be tested for fatigue. In other words, the MOR value of the fatigued beam obtained using the RDM–MOR developed earlier was compared to the average MOR obtained from static four-point testing for two beams to confirm its accuracy.
- The number of cycles (N_i) at failure was recorded.
- S-N curves were then plotted accordingly for different mix designs and different testing dates. A typical S-N curve for concrete is shown in Figure 5-19.

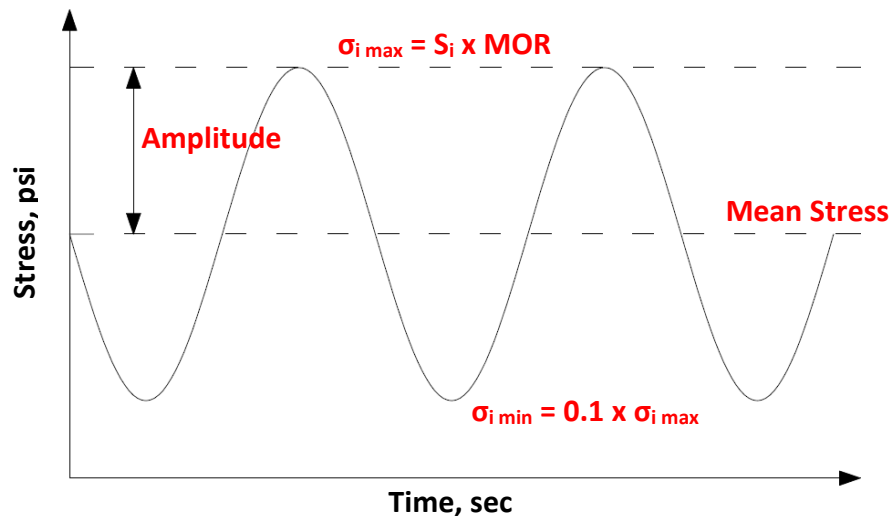


Figure 5-18. Cyclic loading development with respect to time.

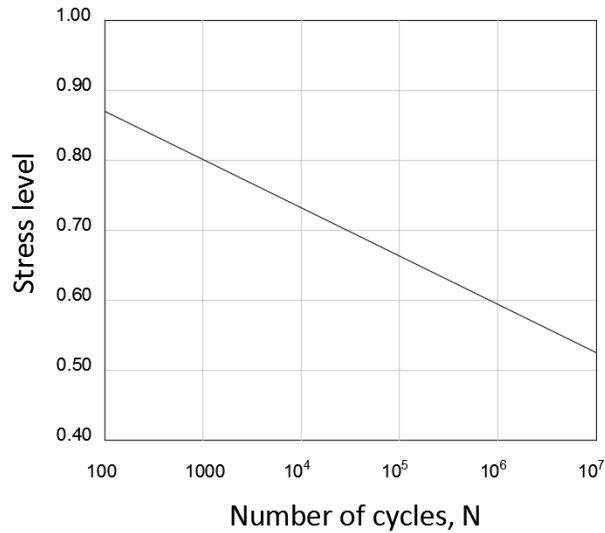


Figure 5-19. Typical S-N curve for concrete.

Beams tested at 0.6 stress level took a large number of cycles before failure (usually exceeding 24 hr), resulting in an overlap between testing times, especially between 12-hr and 1-d testing. To avoid this situation, each of the mixes batched for the 0.6 stress level were divided into two separate 3-ft³ mixes (instead of 6- or 7-ft³). Beams were tested at 12 hr and 3 d from the first mix and at 1 d and 7 d from the second mix. Tables 5-2 to 5-5 summarize all the mixing dates, testing dates, and duration until failure for each mix. The testing duration describes only the time during which the beams were subjected to fatigue loading. It does not include time related to prepare each mix, such as material preparation, material proportioning, mixing, unmolding, forms preparation, etc.

Table 5-2. Summary of the Fatigue Testing Dates and Duration for All PV Mixes

Mix name	Stress level	Mixing date	Testing date	Concrete age	Testing duration (hr)
PV-0.9-I	0.9	1/20/2016	1/20/2016	12-hr	0.01
PV-0.9-I	0.9		1/21/2016	1-d	0.03
PV-0.9-I	0.9		1/23/2016	3-d	0.02
PV-0.9-I	0.9		1/27/2016	7-d	0.03
PV-0.9-I	0.9		1/27/2016	7-d	0.06
PV-0.8-I	0.8	1/22/2016	1/22/2016	12-hr	5.51
PV-0.8-I	0.8		1/23/2016	1-d	2.29
PV-0.8-I	0.8		1/25/2016	3-d	0.03
PV-0.8-II*	0.8	1/25/2016	1/25/2016	12-hr	0.03
PV-0.8-II*	0.8		1/28/2016	3-d	0.09
PV-0.8-II	0.8		2/1/2016	7-d	0.07
PV-0.8-II*	0.8		2/1/2016	7-d	0.08
PV-0.8-III*	0.8	2/1/2016	1/25/2016	12-hr	0.12
PV-0.8-III*	0.8		1/26/2016	1-d	0.02
PV-0.8-III*	0.8		1/26/2016	1-d	0.03
PV-0.7-I	0.7	2/3/2016	2/3/2016	12-hr	7.85
PV-0.7-I	0.7		2/4/2016	1-d	10.77
PV-0.7-I	0.7		2/6/2016	3-d	0.58
PV-0.7-I	0.7		2/10/2016	7-d	0.06
PV-0.6-I**	0.6	2/26/2016	2/27/2016	1-d	38.11
PV-0.6-I**	0.6		3/4/2016	7-d	9.51
PV-0.6-II**	0.6	3/1/2016	3/1/2016	1-d	19.53
PV-0.6-II*	0.6		3/8/2016	7-d	15.2
PV-0.6-III**	0.6	3/14/2016	3/17/2016	3-d	7.07
* Repeated to confirm results.					
** Mixes with 0.6 stress levels were conducted in two groups: 12 hr and 3 d as one group and 1 and 7 d as another. This rescheduling was done to avoid testing time overlap because of the high number of cycles associated with testing at 0.6 stress level.					

Table 5-3. Summary of the Fatigue Testing Dates and Duration for All PVF1 Mixes

Mix name	Stress level	Mixing date	Testing date	Concrete age	Testing duration (hr)
PVF1-0.9-I	0.9	2/5/2016	2/5/2016	12-hr	0.01
PVF1-0.9-I	0.9		2/6/2016	1-d	0.06
PVF1-0.9-I	0.9		2/8/2016	3-d	0.01
PVF1-0.9-I	0.9		2/12/2016	7-d	0.02
PVF1-0.8-I	0.8	2/8/2016	2/8/2016	12-hr	0.02
PVF1-0.8-I	0.8		2/9/2016	1-d	0.04
PVF1-0.8-I	0.8		2/11/2016	3-d	0.08
PVF1-0.8-I	0.8		2/15/2016	7-d	0.3
PVF1-0.7-I	0.7	2/10/2016	2/10/2016	12-hr	11.48
PVF1-0.7-I	0.7		2/11/2016	1-d	0.27
PVF1-0.7-I	0.7		2/13/2016	3-d	0.92
PVF1-0.7-I	0.7		2/17/2016	7-d	0.09
PVF1-0.6-I*	0.6	4/26/2016	4/27/2016	1-d	18.93
PVF1-0.6-I*	0.6		4/29/2016	3-d	12.75
PVF1-0.6-II*	0.6	5/3/2016	5/4/2016	12-hr	10.35
PVF1-0.6-II*	0.6		5/11/2016	7-d	20.53

* Mixes with 0.6 stress levels were conducted in two groups: 12 hr and 3 d as one group and 1 and 7 d as another. This was done to avoid testing time overlap because of the high number of cycles associated with testing at 0.6-stress level.

Table 5-4. Summary of the Fatigue Testing Dates and Duration for All PVF1-8lbs Mixes

Mix name	Stress level	Mixing date	Testing date	Concrete age	Testing duration (hr)
PVF1-8lbs-0.9	0.9	3/10/2016	3/10/2016	12-hr	0.01
PVF1-8lbs-0.9	0.9		3/11/2016	1-d	0.01
PVF1-8lbs-0.9	0.9		3/13/2016	3-d	0.02
PVF1-8lbs-0.9	0.9		3/17/2016	7-d	0.03
PVF1-8lbs-0.8	0.8	3/19/2016	3/19/2016	12-hr	0.46
PVF1-8lbs-0.8	0.8		3/20/2016	1-d	0.26
PVF1-8lbs-0.8	0.8		3/22/2016	3-d	0.29
PVF1-8lbs-0.8	0.8		3/26/2016	7-d	0.73
PVF1-8lbs-0.7	0.7	3/22/2016	3/22/2016	12-hr	4.12
PVF1-8lbs-0.7	0.7		3/23/2016	1-d	18.31
PVF1-8lbs-0.7	0.7		3/25/2016	3-d	4.45
PVF1-8lbs-0.7	0.7		3/29/2016	7-d	6.06
PVF1-8lbs-0.6-I**	0.6	3/29/2016	3/29/2016	12-hr	12.27
PVF1-8lbs-0.6-I**	0.6		4/1/2016	3-d	17.87
PVF1-8lbs-0.6-II*	0.6	4/4/2016	4/4/2016	12-hr	81.41
PVF1-8lbs-0.6-II**	0.6		4/11/2016	7-d	5.9
PVF1-8lbs-0.6-III**	0.6	4/13/2016	4/14/2016	1-d	69.44
PVF1-8lbs-0.6-III*	0.6		4/20/2016	7-d	12.46
* Repeated to confirm results.					
** Mixes with 0.6 stress levels were conducted in two groups: 12 hr and 3 d as one group and 1 and 7 d as another. This was done to avoid testing time overlap because of the high number of cycles associated with testing at 0.6 stress level.					

Table 5-5. Summary of the Fatigue Testing Dates and Duration for All PVF2 Mixes

Mix name	Stress level	Mixing date	Testing date	Concrete age	Testing duration (hr)
PVF2-0.9-I	0.9	2/12/2016	2/12/2016	12-hr	0.02
PVF2-0.9-I	0.9		2/13/2016	1-d	0.01
PVF2-0.9-I	0.9		2/15/2016	3-d	0.02
PVF2-0.9-I	0.9		2/19/2016	7-d	0.01
PVF2-0.8-I	0.8	2/15/2016	2/15/2016	12-hr	0.04
PVF2-0.8-I	0.8		2/16/2016	1-d	0.04
PVF2-0.8-I	0.8		2/18/2016	3-d	0.02
PVF2-0.8-I	0.8		2/22/2016	7-d	0.03
PVF2-0.7-I	0.7	2/23/2016	2/23/2016	12-hr	7.09
PVF2-0.7-I	0.7		2/24/2016	1-d	3.09
PVF2-0.7-I	0.7		2/26/2016	3-d	2.3
PVF2-0.7-I	0.7		3/1/2016	7-d	0.9
PVF2-0.6-I*	0.6	5/6/2016	5/7/2016	1-d	19.31
PVF2-0.6-I*	0.6		5/13/2016	7-d	4.91
PVF2-0.6-II*	0.6	5/11/2016	5/11/2016	12-hr	12.6
PVF2-0.6-II*	0.6		5/14/2016	3-d	6.35
* Mixes with 0.6 stress levels were conducted in two groups: 12 hr and 3 d as one group and 1 and 7 d as another. This was done to avoid testing time overlap because of the high number of cycles associated with testing at 0.6 stress level.					

5.5.3 Development of Strength Gain Curves for Fatigue Testing

The time needed to open to traffic on a newly poured PCC pavement could be optimized by correlating data collected from the *S-N* curves with the equivalent applied stress level corresponding to the traffic volume. The development of *S-N* curves is directly related to the strength of concrete at a given age. For example, a load applied at 0.9 stress level is calculated by taking 90% of the concrete flexural strength at a certain age. The main challenge in performing fatigue tests on concrete at early age is to accommodate the continuous gain strength in concrete. When concrete gains strength, the applied fatigue load represents a lower stress level, compared to the original starting load. Therefore, a successful fatigue test should consistently account for strength gain in concrete at early age. To do that, an increasing amplitude and mean load were considered for the fatigue samples during cyclic load. The amplitude and mean load were increased with time to maintain a constant stress level during testing.

The increased applied load was based on a normalized function that was developed to predict the flexural strength gain at the early stages of concrete. The development of this function was made by conducting two 7-ft³ PV concrete mixes to prepare 24 beams. Flexural tests were performed on the beams at increasing time intervals, ranging from 1 to 3 hr for the first 12 to 48 hr after pouring. In other words, the beams were tested in the following fashion:

- For the period between 12 and 24 hr after pouring, two beams were tested at 12, 13, 14, 16, 18, 20, 22, and 24 hr.
- For the period between 24 and 48 hr after pouring, two beams were tested at 24, 26, 28, 33, 37, 45, and 48 hr.

The logarithmic trend line function was normalized with respect to the first MOR reading at 12 hr ($f'_r / f'_r 12 \text{ hr}$), as shown in Figure 5-20. Equations 5-19 and 5-20 were developed from the obtained logarithmic trend line. These equations were used to predict the strength gain over a 48-hr period, starting from the average MOR values obtained prior to each fatigue test. With this approach, constant stress levels were maintained during testing for the first 48 hr.

$$f'_r(t) / f'_r 12 \text{ hrs.} = \begin{cases} \frac{-733 + 374 \text{ Log}(t)}{196} & \text{for } 12 \text{ hrs.} \leq t \leq 24 \text{ hrs.} \\ 2.32 \frac{-302 + 225 \text{ Log}(t)}{413} & \text{for } 24 \text{ hrs.} < t \leq 48 \text{ hrs.} \end{cases} \quad \begin{matrix} (5.19) \\ (5.20) \end{matrix}$$

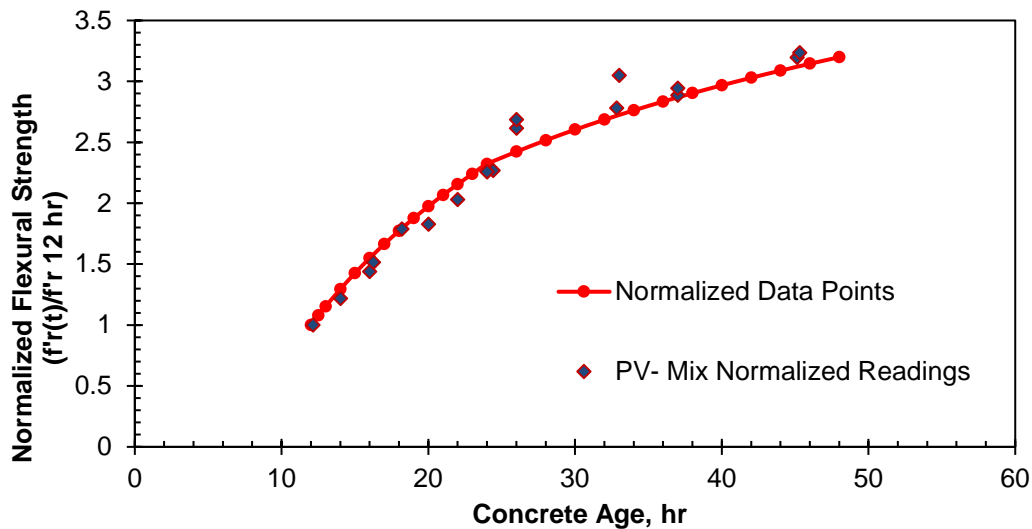


Figure 5-20. Normalized flexural strength in PV mixes at early age.

The increase in amplitude and mean load was done at intervals varying from 30 min to 2 hr. The testing machine was programed such that the load was ramped to the new mean and amplitude values at the end of each loading event. A typical load ramping taking 1 hr after test initiation is shown in Figure 5-21.

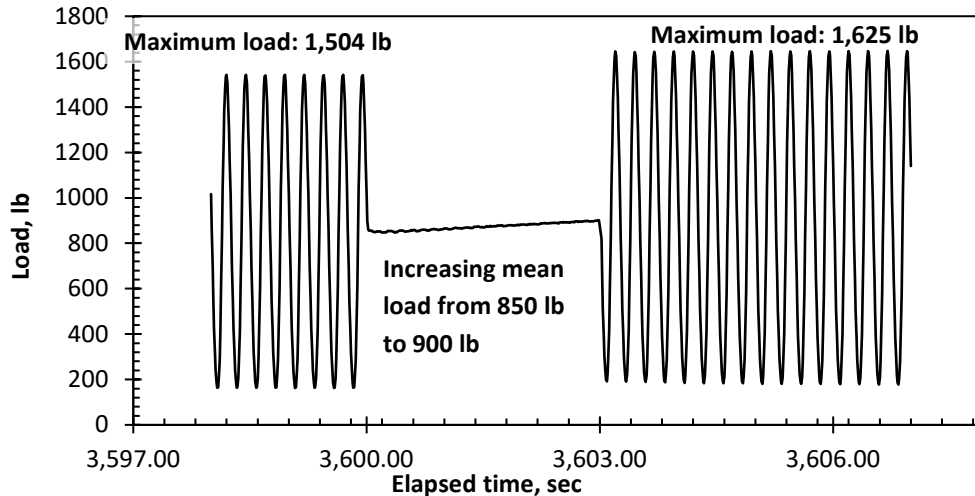


Figure 5-21. Typical load ramping case taken 1 hr after test initiation.

5.6 EFFECT OF FATIGUE ON FREEZE–THAW PERFORMANCE

5.6.1 Test significance

The second objective of this study was to investigate the possible detrimental effects of residual strains/stress induced by loading early-age concrete on long-term fatigue life and durability such as freeze–thaw performance. The experimental lab-testing program is characterized by performing cyclic loading on samples prepared using PV (without fibers) and PVF1 (with variable amount of fibers) at early age using a constant stress level (0.55) and then subjecting them to freeze–thaw cycles. The purpose of this test is to study the effect of fatigue loading at early age on the freeze–thaw performance. The effect of fatigue damage at early age on the freeze–thaw performance is determined through performing freeze–thaw testing as per ASTM C666 on concrete specimens after subjecting them to fatigue load.

5.6.2 Testing Program for Fatigue/Freeze–Thaw Test

Freeze–thaw testing was conducted on 3 x 4 x 16 in. beams for all mixes with and without fibers. Similar to the fatigue testing program, plain-concrete mixes were batched according to the pavement-mix design (PV). The amount of fibers used was 4 and 8 lb/yd³ of Strux® 90/40 for PVF1 and PVF1-8lbs mixes, respectively. PVF1 and PVF1-8lbs were batched to investigate the effect of the presence of fibers on the combined fatigue and durability performance.

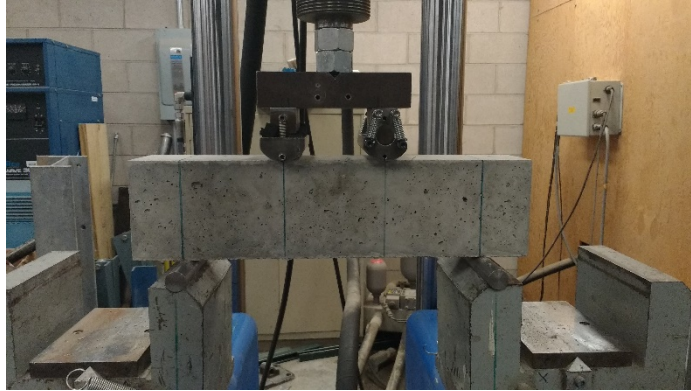


Figure 5-22. Fatigue/freeze–thaw testing setup.

Cyclic loading was applied using a four-point bending configuration for specimens, as shown in Figure 5-22. The specimens were tested at 12 hr; and 1, 3, and 7 d. For each mix, sixteen 3 x 4 x 16 in. beams and two 6 x 12 in. cylinders were prepared from 4 ft³ batches of concrete. From the prepared beams, four beams were tested for fatigue; and the rest were used for static flexural testing. All mixes were batched with air content as close as possible to 7% to maintain consistent test results. To obtain redundant results, each mix was repeated twice so that two samples of each testing date were obtained. Three control specimens and two specimens of each testing dates (12 hr; 1, 3, and 7 d) were placed in the freeze and thaw cabinets and subjected to freeze–thaw (ASTM C 666 procedure A), as shown in Figure 5-23 (left). The freeze–thaw cabinets can accommodate 40 concrete specimens of 3 x 4 x 16 in. They are controlled by a fully automated operating system.

Hardened air content analysis was also performed according to ASTM C457 on 1-in.-thick slices of the concrete cylinders. The test was performed using the petrographic machine (CAS 2000), as shown in Figure 5-23 (right). The parameters obtained from the hardened air content analysis for each mix were correlated with the freeze and thaw performance.

The following procedure was used to conduct the fatigue/freeze–thaw tests:

- Prior to each fatigue loading, two beams were tested for static flexural strength to determine the *MOR* at the given age of the concrete.
- The average of the *MOR* readings was used to determine the mean and amplitude of the cyclic loading, using a constant stress level (S_i) of 0.55.
- The maximum stress applied is the average *MOR* obtained multiplied by the stress level (i.e., $\sigma_{i_max} = 0.55 \times MOR$). Whereas the minimum load applied is 10% of the maximum load (i.e., $\sigma_{i_min} = 0.1 \times \sigma_{i_max}$).
- Fatigue tests were performed at a frequency of 4 Hz, using an Instron 8500 closed-loop testing system, until reaching 170,000 cycles.

- E_D readings were also collected for each specimen to verify the reliability of the average MOR used to determine the fatigue load characteristics (maximum load, minimum load, mean load, and amplitude).
- Fatigued beams were cured for 14 d in the moisture room under a controlled temperature of 23°C and 100% relative humidity.
- After curing, fatigued samples were transferred to the freeze–thaw cabinets, in which they were subjected to 300 cycles of freezing and thawing as per ASTM C666 procedure A.
- At every 35 cycles of freezing and thawing, the relative dynamic modulus (RDM) was calculated:

$$P_c = \left(\frac{E_c^2}{E_0^2} \right) \times 100 \quad (5-21)$$

where P_c = relative dynamic modulus of elasticity corresponding to c number of cycles, %

E_c = dynamic modulus of elasticity after c number of freeze–thaw cycles, ksi

E_0 = dynamic modulus of elasticity after 0 freeze–thaw cycles, ksi

- E_D readings are discontinued upon reaching 300 cycles or once the RDM reaches a value of 60%, whichever occurs first. The durability factor is then calculated:

$$DF = P.N/300 \quad (5-22)$$

where DF = durability factor, %

P = relative dynamic modulus at N number of cycles, %

N = number of cycles for whichever is reached first

$$\begin{cases} 300 \text{ cycles} \\ \text{number of cycles at which } P_c = 60\% \end{cases}$$



Figure 5-23. Freeze–thaw cabinets (left) and petrographic analysis of concrete (right).

Tables 5-6 to 5-8 summarize the mixing dates, testing dates, and duration of testing for each mix. The testing duration describes only the time during which the beams were subjected to fatigue loading. It does not include time related to preparing each mix, such as material preparation, material proportioning, mixing, unmolding, forms preparation, etc.

Table 5-6. Summary of the Fatigue/Freeze–Thaw Testing Dates and Duration for All PV Mixes

Mix name	Mixing date	Air content	Testing date	Age of concrete	Testing duration (hr)
PV-I	5/23/2016	7.2%	5/23/2016	12-hr	12
PV-I		7.2%	5/24/2016	1-d	12
PV-I		7.2%	5/26/2016	3-d	12
PV-I		7.2%	5/30/2016	7-d	12
PV-II	5/26/2016	6.9%	5/26/2016	12-hr	12
PV-II		6.9%	5/27/2016	1-d	12
PV-II		6.9%	5/29/2016	3-d	12
PV-II		6.9%	6/2/2016	7-d	12

Table 5-7. Summary of the Fatigue/Freeze–Thaw Testing Dates and Duration for All PVF1 Mixes

Mix name	Mixing date	Air content	Testing date	Age of concrete	Testing duration (hr)
PVF1-I	5/31/2016	7.6%	5/31/2016	12-hr	12
PVF1-I		7.6%	6/1/2016	1-d	12
PVF1-I		7.6%	6/3/2016	3-d	12
PVF1-I		7.6%	6/7/2016	7-d	12
PVF1-II	6/3/2016	6.6%	6/3/2016	12-hr	12
PVF1-II		6.6%	6/4/2016	1-d	12
PVF1-II		6.6%	6/6/2016	3-d	12
PVF1-II		6.6%	6/10/2016	7-d	12
PVF1-III*	6/8/2016	7.0%	6/8/2016	12-hr	12
PVF1-III*		7.0%	6/9/2016	1-d	12
PVF1-III*		7.0%	6/11/2016	3-d	12
PVF1-III*		7.0%	6/15/2016	7-d	12
PVF1-IV*	6/13/2016	6.9%	6/13/2016	12-hr	12
PVF1-IV*		6.9%	6/14/2016	1-d	12
PVF1-IV*		6.9%	6/16/2016	3-d	12
PVF1-IV*		6.9%	6/20/2016	7-d	12
* Repeated to control air content at 7.0%					

Table 5-8. Summary of the Fatigue/Freeze–Thaw Testing Dates and Duration for All PVF1-8lbs Mixes

Mix name	Mixing date	Air content	Testing date	Age of concrete	Testing duration (hr)
PVF1-8lbs-I	6/16/2016	7.0%	6/16/2016	12-hr	12
PVF1-8lbs-I		7.0%	6/17/2016	1-d	12
PVF1-8lbs-I		7.0%	6/19/2016	3-d	12
PVF1-8lbs-I		7.0%	6/23/2016	7-d	12
PVF1-8lbs-II	6/20/2016	7.0%	6/20/2016	12-hr	12
PVF1-8lbs-II		7.0%	6/21/2016	1-d	12
PVF1-8lbs-II		7.0%	6/23/2016	3-d	12
PVF1-8lbs-II		7.0%	6/27/2016	7-d	12

5.6.3 Development of Strength Gain Curves for Fatigue/Freeze–Thaw Testing

Similar to the fatigue testing program, the increased applied load for the fatigue/freeze–thaw was based on a normalized function developed to predict the flexural strength gain at the early stages of concrete. The development of this function was made by conducting two 3-ft³ PV concrete mixes to prepare 36 beams. Eighteen beams were tested during the 12- to 24-hr period, and eighteen beams were tested during the 24- to 48-hr period. Flexural tests were performed on the beams at increasing time intervals ranging from 1 to 3 hr for the first 12 to 48 hr after pouring. In other words, the beams were tested in the following fashion:

- For the period between 12 and 24 hr after pouring, two beams were tested at 12, 13, 14, 16, 18, 20, 22, and 24 hr.
- For the period between 24 and 48 hr after pouring, two beams were tested at 24, 26, 29, 32, 34, 37, 39, 45, and 48 hr.

The logarithmic trend line function was normalized with respect to the first MOR reading at 12 hr ($f'_r/f'_{r\ 12\ hrs.}$), based on the flexural strength values presented in Figure 5-24. Equation 5-23 was developed from the obtained logarithmic trend line. It was used to predict the strength gain over the 48-hr period, starting from when the average MOR values were obtained prior to each fatigue test. With this approach, a constant stress level of 0.55 was maintained during testing for the first 48 hr. The beams tested at 24 hr from both the 12-to-24 hr and the 24-to-48-hr testing matched perfectly. Therefore, only one equation was developed that combined both periods of testing.

$$f'_r(t)/f'_{r\ 12\ hrs.} = \frac{252.29 \ln(t) + 424.99}{203} \quad (5-23)$$

for 12 hrs. ≤ t ≤ 48 hrs.

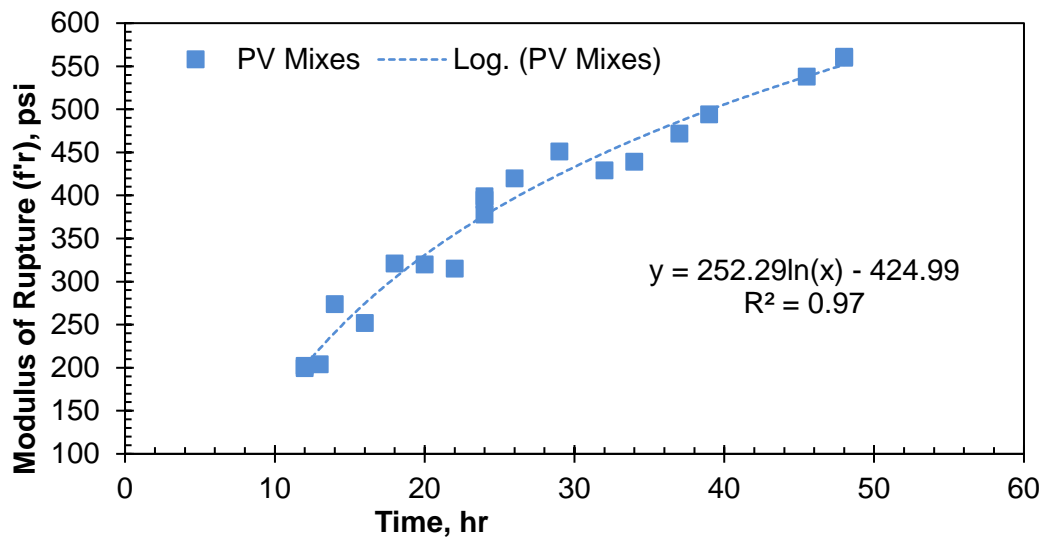


Figure 5-24. Flexural strength in PV mixes at early age.

The increase in amplitude and mean load was done at intervals varying from 30 min to 2 hr. The testing machine was programed such that the load was ramped to the new mean and amplitude values at the end of each loading event.

5.7 ANALYTICAL STUDY AND FINITE-ELEMENT MODELING

5.7.1 Task Significance

Finite-element analysis (FEA) was used to correlate the flexural strength and fatigue experimental results with PCC pavement-design parameters such as pavement thickness, concrete modulus of elasticity, modulus of subgrade reaction, and joint properties. FEA was performed using *ISLAB2000* software developed by ARA, incThe software simulates different design and loading cases using its 2-D modeling features and offers a fast and practical method to calculate stresses and deflections in rigid pavements due to traffic loads.

The parametric study was divided into three sections:

- *Study 1:* Evaluating the cost-effectiveness of fiber-reinforced concrete over plain concrete. FEA was used to analyze typical concrete pavements with varying design parameters. The finite-element-analysis results were related to the fatigue S-N curves to judge the fatigue performance of plain versus fiber-reinforced concrete.
- *Study 2:* Simulating different traffic load conditions for specific cases related to the purpose of the study, such as fatigue testing for slab joints with dowel-bar reinforcement. The stresses generated at critical positions due to ESAL can then be obtained and compared with the flexural capacity of the slab specimens to identify the applied stress level.

- *Study 3:* Evaluating the effect of heavy truck loads in the cross-traffic direction. A critical case of edge loading is considered to evaluate shear and flexural stresses at longitudinal joints in rigid pavements. This case corresponds to construction equipment loads that are applied on the pavement during the early stages of concrete.

5.7.2 Software Description

Finite-element modeling consisted of selecting slab dimensions over defined grid lines for the longitudinal and transversal directions. Basic input options were then selected for meshing, ground layers, reinforcement, and vehicle loads. Figure 5-25 shows a typical model for jointed pavements with dowel-bar reinforcement at the longitudinal joints and tie bars at the transversal joints. The main parameters of interest that are relevant to the subject of EOT are the following:

- Pavement thickness
- Modulus of elasticity (*MOE*)
- Modulus of subgrade reaction (*K*)
- Joint properties

A single-axle with single tires was considered for the applied load for all models. The ESAL load was set in accordance with AASHTO Guide for Design of Pavement Structures (1993):

- 18,000 pounds of applied load
- Two square contact areas equivalent to four circles of 4.51-in. radius each
- Tire pressure of 70 psi
- Axle width of 6 ft, as for typical truck loading

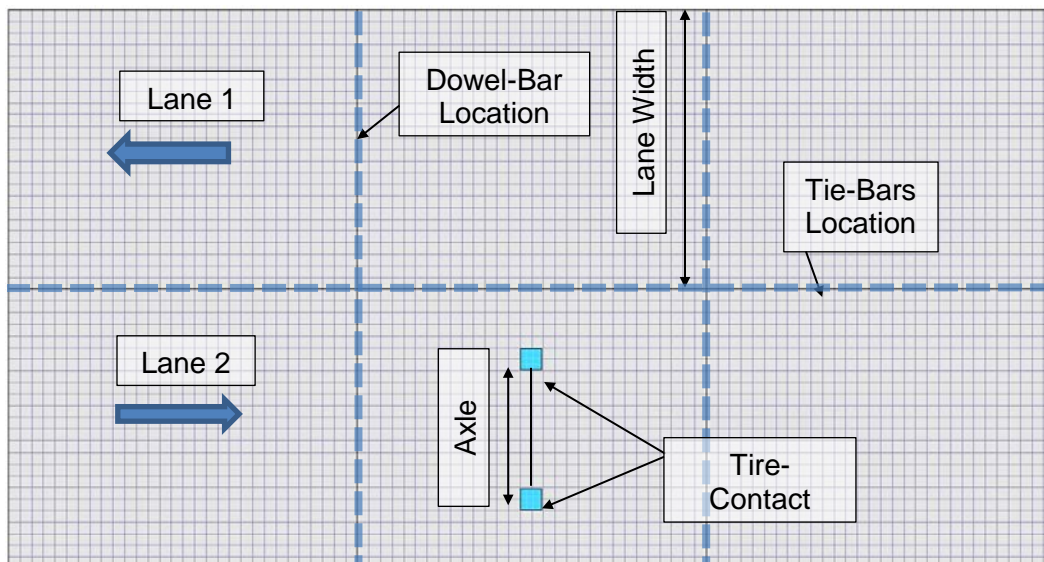
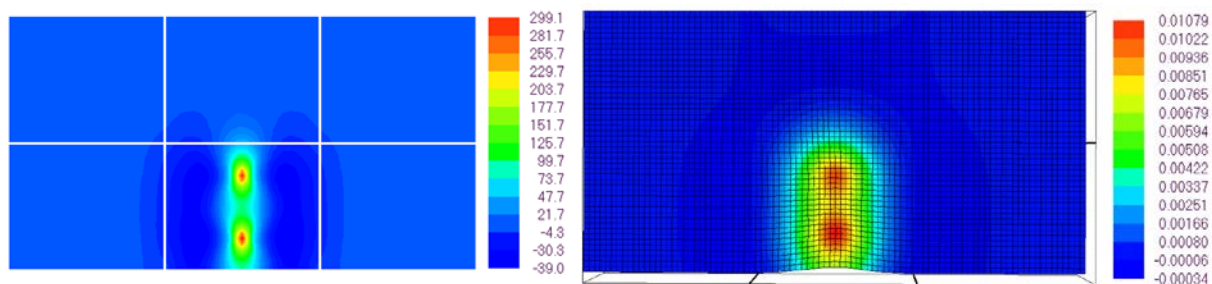


Figure 5-25. Typical geometric and loading configurations using *ISLAB2000*.

The output for stresses and deflections can be obtained at every node from the applied mesh along the x-y grid. The calculated output is the following:

- Flexural stresses in the transversal direction or x-axis (psi)
- Flexural stresses in the longitudinal direction or y-axis (psi)
- Shear stresses or x-y stresses (psi)
- Deflections (in.)

Figure 5-26 shows a typical output for the distribution of bottom flexural stresses in the transverse direction (Figure 5-26 (a)) and the deflections at the bottom level of a two-lane model consisted of six rigidly connected concrete slabs (Figure 5-26 (b)). The model is loaded with one ESAL at the middle of the second lane. In addition to calculating the maximum stress values, the software shows the distribution of the stresses and deflections through contour lines that identify the location of the critical areas of the pavement.



(a) Typical bottom stress distribution in the transverse direction; (b) typical deflections in the vertical direction.

Figure 5-26. Typical output for bottom transverse stresses (a) and vertical deflections (b).

5.7.3 Parametric Studies

Three parametric studies were conducted for the following purposes:

- *First parametric study:* To evaluate the flexural stresses and deflections for varying slab thicknesses, static modulus of elasticity, and modulus of subgrade reaction values. The output of the various run cases serves to evaluate plain concrete in rigid pavements for fatigue performance. The cost-effectiveness of using plain concrete for pavements is then evaluated from previous fatigue testing data.
- *Second parametric study:* To evaluate the flexural stresses and deflection for two jointed slabs. Joint parameters including load-transfer efficiency and aggregate interlock provide several cases of jointed, plain-concrete pavements (JPCP). The data provided serves in determining the structural behavior of slab-concrete specimens being considered for testing in the next phase of the study.

- *Third parametric study:* To evaluate the flexural and shear stresses due to heavy construction equipment loads for an edge loading case. This study represents a case of possible critical loads that can occur during the early stage of pavement construction. The data presented can be related to the flexural capacity and shear capacity of concrete PV mixes.

5.7.3.1 Parametric Study 1 for Rigid Pavement

The model was set with slab dimensions of 12 by 15 ft. Two lanes were considered by using two adjacent slabs in the transverse directions and multiple slabs in the longitudinal direction. Longitudinal joints were located at 15-ft intervals in accordance with IDOT definitions for jointed, plain-concrete pavements (JPCP). The slabs were rigidly connected at the joints in both directions, and the load location represented a typical interior loading case. The applied ESAL load was selected to be aligned with the centerline of one of the lanes, as seen in Figure 5-27.

The main parameters mentioned previously were studied with varying ranges to show their respective effect on stress and deflection calculations. The constant input values between each input case are shown in Table 5-9. Results of the parametric study are found in section 6.5.1.1 for all considered cases.

Table 5-9. List of Constant Input Parameters for Study 1

Model parameters	Slab dimensions	12 x 15 ft
	Number of lanes	2
	Number of slabs per lane	3
	Subgrade model type	Winkler model
	Mesh size	2 x 2 in. ²
Concrete parameters	Unit weight	144 lb/ft ³
	Poisson's ratio	0.15
Vehicle-load parameters	Axle type	Single-axle/Single-tire
	Aspect ratio of contact area	1
	Axle span (c-c of contact area)	6 ft
	Axle position (from bottom left)	264 in., 30 in.
	Axle load	18,000 lb
	Contact area of tires	257.1 in. ²
	Tire pressure	70 psi

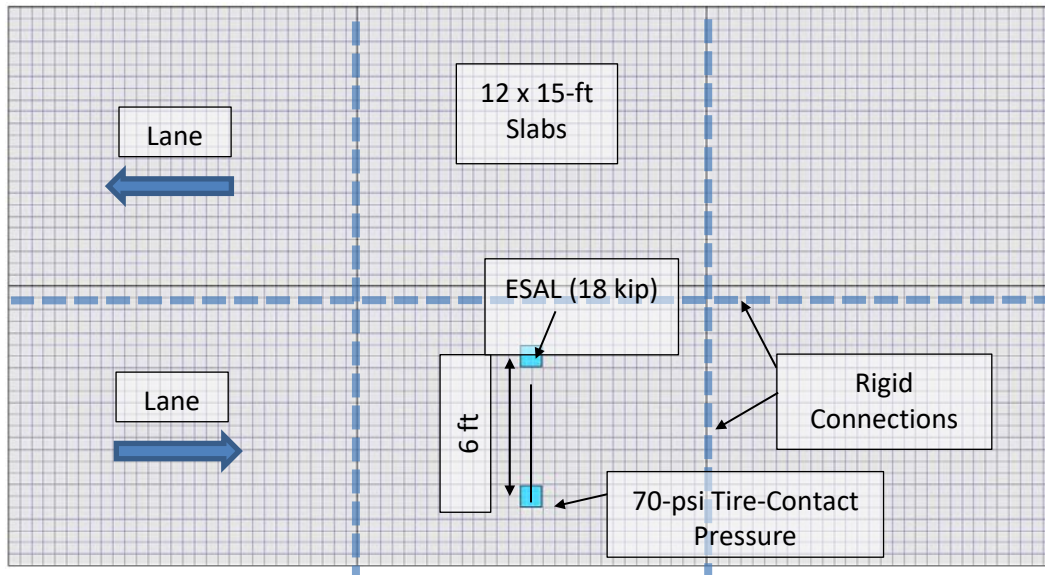


Figure 5-27. Rigidly connected-slabs model for parametric study 1.

5.7.3.1.1 Effect of static modulus of elasticity (*MOE*)

MOE values represent 12-hr; and 1, 3, and 7-d concrete age, in accordance with the fatigue testing program (section 5.5.2). Estimating the *MOE* for every case was achieved by using the following empirical equation obtained from testing results discussed in section 6.2.4. The equation correlates static modulus of elasticity values with average compressive strength readings. The *MOE* values considered are shown in Table 5-10:

$$E_s = \frac{1}{0.0027} (f'_c)^{-0.571} \quad (5-24)$$

where E_s : static modulus of elasticity, psi

f'_c : compressive strength, psi

Table 5-10. Static *MOE* Values for Each Concrete Age

Age	12 hr	1 d	3 d	7 d
f'_c (psi)	1,312.3	2,440	3,692.5	4,836
<i>MOE</i> (psi)	1.767E+06	2.518E+06	3.190E+06	3.722E+06

5.7.3.1.2 Effect of subgrade modulus reaction (*k*)

A Winkler-type subgrade option was selected for all the studied cases. The model considered translation and rotation springs at every node in the mesh. Subgrade modulus values were set to be representative of actual varying soil stiffness in the state of Illinois. As seen in previous

work from Chavan (2012), K values ranged from weak soil conditions (50 psi/in.) to stiff soil conditions (500 psi/in.) and were set at 50, 100, 200, 300, and 500 psi/in., accordingly.

5.7.3.1.3 Effect of varying pavement thickness (t)

The thickness of the PCC layer was set at 6, 8, 10, 12, 14, and 16 in. These cases are combined with every MOE and K value. The calculated stresses, along with flexural strength data for plain-concrete PV mixes, allowed us to determine the applied stress level corresponding to a typical ESAL load. The data provided by the parametric study was used to correlate fatigue performance of rigidly connected plain-concrete slabs with the performance of the fiber-reinforced concrete counterpart. $S-N$ curves for the fatigue testing program was used for that matter.

5.7.3.2 Parametric Study 2 for Jointed-Pavement

The second model consisted of two 12 x 15 ft jointed slabs with a single-axle, single-tire ESAL load at the edge of the joint location. The input parameters are shown in Table 5-11. The model included the presence of dowel bars at the joint (see Figure 5-28). This second parametric study took into account the load-transfer mechanisms through dowels and aggregate interlock. The data provided allowed us to study the structural behavior of real slab specimens subjected to fatigue loading.

Table 5-11. List of Constant Input Parameters for Study 2

Model parameters	Slab dimensions	12 x 15 ft
	Number of lanes	1
	Number of slabs per lane	2
	Subgrade model type	Winkler model
	Mesh size	2 x 2 in. ²
Concrete parameters	Unit weight	144 lb/ft ³
	Poisson's ratio	0.15
Vehicle-load parameters	Axle type	Single-axle/Single-tire
	Aspect ratio of contact area	1
	Axle span (c-c of contact area)	6 ft
	Axle position (from bottom left)	188 in., 30 in.
	Axle load	18,000 lb
	Contact area of tires	257.1 in. ²
	Tire pressure	70 psi
Joint parameters	Dowel-bar diameter	1 in.
	Dowel-bar length	18 in.
	Dowel-bar spacing	12 in.

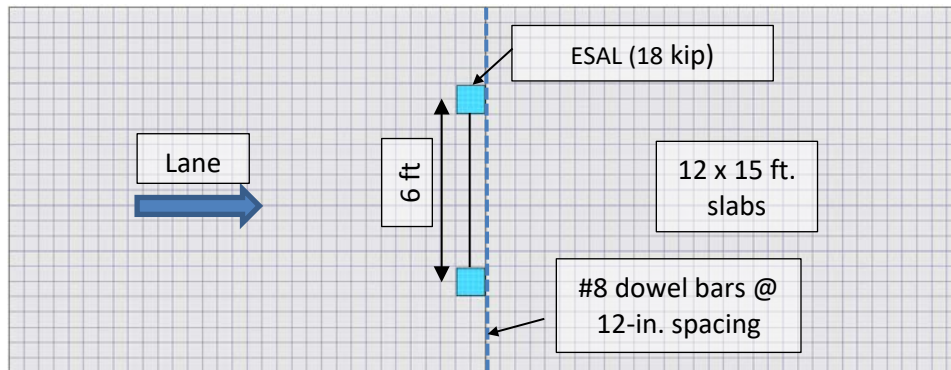


Figure 5-28. Model for parametric study 2.

5.7.3.2.1 Effect of load-transfer efficiency

Transverse joint performance is usually assessed by determining the load-transfer efficiency (*LTE*). *LTE* represents the ratio of the deflection of a loaded slab over the deflection of an unloaded slab, as shown in Equation 5.22. It has been shown in multiple studies that the *LTE* values do not exceed 95%. Therefore, *LTE* values were batched for 50, 60, 70, 80, 90, 91, 92, 93, 94, and 95%. Bottom slab stresses and deflections were then calculated accordingly.

$$LTE(\%) = \frac{\Delta_a}{\Delta_i} \times 100 \quad (5-25)$$

where Δ_a = approach slab deflection

Δ_i = approach slab deflection

5.7.3.2.2 Effect of load-transfer through dowel bars

Longitudinal reinforcement consisted of #8 bars (1-in. diameter), as recommended by IDOT for slabs with 6-in. in depth (National Conference Consortium questionnaire 2009). Dowel bars were 18 in. in length and spaced 12 in. (American Concrete Institute 1956).

5.7.3.2.3 Effect of load-transfer through aggregate interlock

Aggregate interlock (AGG) can contribute to the total stiffness of the joint by friction and bearing stresses acting on the aggregate particles (Popehn et al. 2003). Determining the aggregate interlock factor at a certain joint requires measuring the developed crack width. A more practical approximation of the AGG is offered by *ISLAB2000*. Equation 5.23 estimates the AGG values for a certain load-transfer efficiency. The proposed estimation is based on the work of Crovetto (1994) on the subject of joint stiffness and is set to be valid for LTE values ranging from 0% to 95%.

$$AGG = \left(\frac{\frac{1}{LTE} - 0.01}{0.012} \right)^{-\frac{1}{0.849}} \cdot K \cdot l \quad (5-26)$$

where AGG = aggregate interlock factor (psi)

LTE = load-transfer efficiency (%)

K = modulus of subgrade reaction (psi/in.)

L = radius of relative stiffness (in.)

It should be noted that the radius of relative stiffness is calculated using equation 5-28:

$$l = \sqrt[4]{\frac{E_{PCC} h_e^3}{12(1 - \mu^2)K}} \quad (5-28)$$

where E_{PCC} = modulus of elasticity of concrete (psi)

h_e = slab thickness (in.)

μ = Poisson's ratio of concrete

5.7.3.3 Parametric Study 3 for Cross-Traffic Case

The third parametric study addresses the possibility of flexural failure and shear failure in JPCP pavements due to heavy truck loads in the cross-traffic direction. The model consists of two lanes composed of three 12 x 15 ft slab panels. Figure 5-29 presents the model used for this study. A 22-kip single-axle load with 110-psi contact pressure is applied at the edge of the longitudinal joint in the second panel. The applied load corresponds to the maximum allowable front-axle load of a Class F truck (such as concrete truck mixer) as per IDOT's operation form 753. The value of the contact pressure corresponds to higher weights and tire inflation pressures for heavy trucks. Transverse and longitudinal joints are set with an LTE of 90%. The considered LTE value accounts for a 10% reduction due to possible void creation in the dowel-concrete interface, as mentioned by Yoder and Witczak (1975), and is generally used in design procedures. The transfer mechanism in the longitudinal joint relies solely on aggregate interlocking, therefore loading in the transverse direction can present a critical case during pavement construction. This parametric study serves to identify loading cases that can lead to possible distresses for longitudinal joints, such as faulting or corner breaking. The constant input parameters used for this model are listed in Table 5-11.

Table 5-12. List of Constant Input Parameters for Study 3

Model parameters	Slab dimensions	12 x 15 ft
	Number of lanes	2
	Number of slabs per lane	3
	Subgrade model type	Winkler model
	Mesh size	2 x 2 in. ²
Concrete parameters	Unit weight	144 lb/ft ³
	Poisson's ratio	0.15
Vehicle-load parameters	Axle type	Single-axle/Single-tire
	Aspect ratio of contact area	1
	Axle pan (c-c of contact area)	6 ft
	Axle position (from bottom left)	134 in., 229.2 in.
	Axle load	22,000 lb
	Contact area of tires	200 in ²
	Tire pressure	110 psi
Joint parameters	LTE	90%

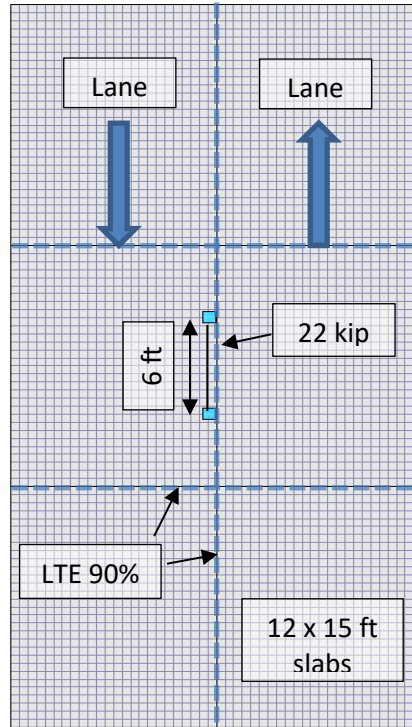


Figure 5-29. Study 3 model.

The varying input parameters were selected as follows:

- Pavement thickness, t , set at 6, 8, 10, 12, 14, and 16 in.
- Modulus of elasticity, MOE , corresponding to 12-hr; and 1-, 3-, and 7-d concrete age (Table 5-10)
- Modulus of subgrade reaction, k , set at 50, 100, 200, 300, and 500 psi/in.

The stresses developed for this section are compared with concrete flexural strength and shear strength for concrete PV mixes. Concrete flexural capacity is obtained from the mechanical testing program in section 6.2.2, and the shear-flexural capacity is empirically evaluated from the compressive strength results presented in section 6.2.1. Table 5-12 lists the compressive and shear strength of concrete PV mixes at 12-hr; and 1-, 3-, and 7-d concrete age. Equation 5-27 is used to evaluate the nominal shear strength for plain concrete, as per ACI Committee 318. The output of the *ISLAB2000* software is presented to identify the cases where flexural/shear failure is expected to occur for different underlying soil conditions, pavement thicknesses, and concrete age. High stresses due to moving construction equipment on the PCC pavement contributes to joint deterioration and loss of load-transfer. Therefore, evaluating the critical design cases can help avoiding excessive distresses and future rehabilitation expenses.

$$V_c = \frac{4}{3} \lambda \sqrt{f'_c} \quad (5-29)$$

where V_c = nominal shear stress of concrete (psi)

$\Lambda = 1$, normal weight concrete modification factor

f'_c = concrete compressive strength (psi)

Table 5-13. Compressive Strength of PV Mixes with the Corresponding Shear Strength

Concrete Age	12-h	1-d	3-d	7-d
f'_c (psi)	1,312	2,440	3,692	4,836
V_c (psi)	48	65	81	92

5.8 FATIGUE PERFORMANCE OF JOINTED-CONCRETE SLABS, TEST DESCRIPTION

5.8.1 Test Significance

The present literature focused on cyclic fatigue loads on jointed slabs, with the dowel material as a main variable. The performed studies mentioned before had specimens cured for 28 d. However, in this study, the fatigue performance of jointed-concrete slabs subjected to cyclic loading at EOT was the main purpose. The first specimen was constructed in accordance with current construction practices in the state of Illinois. Fiber-reinforced concrete PVF1 mixes with 8 lb/yd³ of Strux 90/40 were cast within an enclosure representing a contraction joint under an improved subgrade layer. For the loading setup, an edge loading case at the face of the contraction joint with ½ ESAL (9-kip load) was considered to study the combined effect of shear, bearing, and flexural stresses at 1-d concrete age. The testing program presents a complementary step to the flexural fatigue tests described and discussed in sections 5.5 and 6.4, respectively. The previous testing program considered simply supported concrete beams subjected to flexural fatigue loading at EOT. However, the testing setup of the jointed-slab specimen included a critical loading case that could be encountered in newly poured jointed pavements. For that purpose, joint deterioration due to cyclic fatigue loading at EOT was evaluated by means of relative deflection between the loaded and unloaded slab. To achieve this, the load-transfer efficiency (*LTE*) and the joint effectiveness (*E*) were measured throughout the loading phase by intermediate static tests at predefined cycle intervals.

5.8.2 Testing Setup

5.8.2.1 Concrete Jointed-Pavement Slabs

Dimensions for the concrete slabs are presented in Figures 5-30 and 5-31. The slabs were 2-ft wide, 7-ft long, and 6-in. thick. A plane of weakness was created through a 2-in.-deep notched joint as per standard specification 420001-08, *Standard Specifications for Road and Bridge Construction*, IDOT (2016), which divides the specimen into 2 x 3 ft and 2 x 4 ft slabs. This geometry was made to account for the contact loading area that should remain at the edge of the contraction joint. The centerline of the specimens and the 11.3 x 11.3 in. loading plate are aligned with the actuator of the servo-hydraulic Instron system. The specimen is cast on the

underlying compacted backfill layer as intended for JPCP construction practices in the state of Illinois.

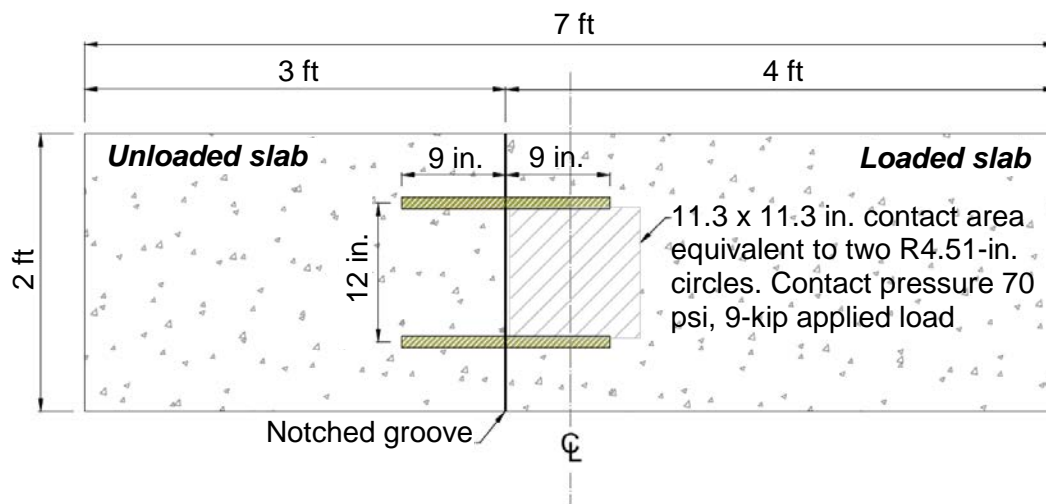


Figure 5-30. Test configuration of slab, dowels, and loading plate geometry (plan view).

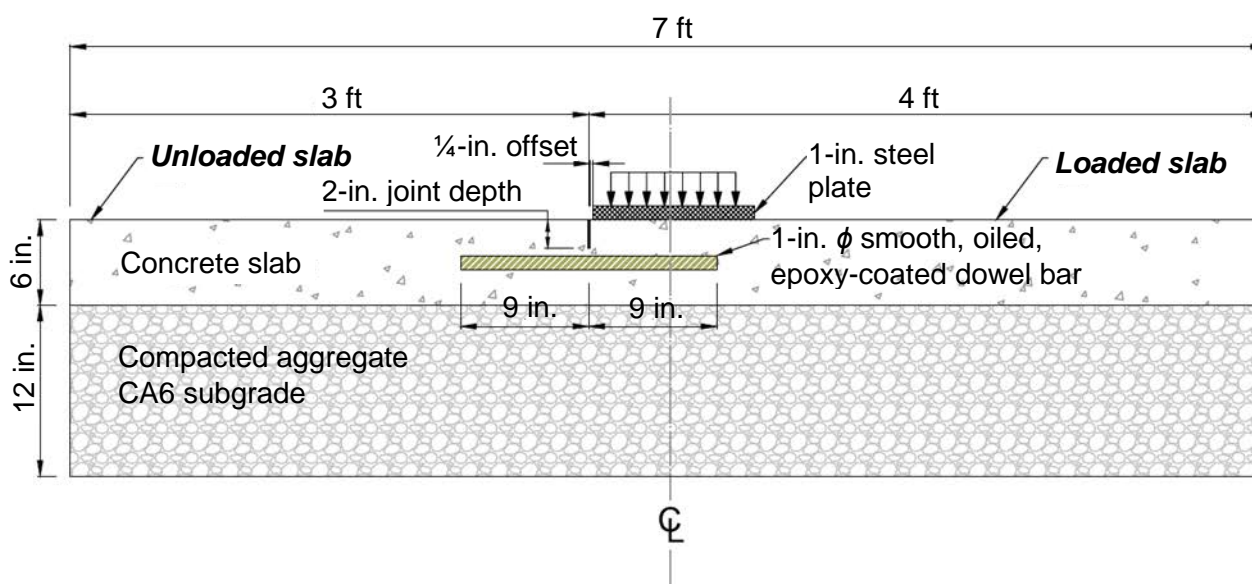


Figure 5-31. Test configuration of slab, dowels, and loading plate geometry (elevation view).

5.8.2.2 Dowel Bars

Two dowel bars were placed at the mid-depth of the pavement slab at the contraction joint with 12-in. spacing below the top surface of the slab. The dowels are round and epoxy-coated, grade 70 steel, as per Article 1006.11, *Standard Specifications for Road and Bridge Construction*, IDOT (2016). Prior to concrete casting, the dowel bars were lightly lubricated as per Article 420.05 c-2, *Standard Specifications for Road and Bridge Construction*, IDOT (2016). The bars are

1 in. in diameter, 18-in. long, and with 9-in. embedment in both slabs, as per standard 420001-08, *Standard Specifications for Road and Bridge Construction*, IDOT (2016).

Table 5-14. Dowel-Diameter Selection as per Standard Specification 420001-08

Pavement thickness	Dowel-bar diameter
8 in. or greater	1 ½ in.
7 in. to 7.99 in.	1 ¼ in.
Less than 7 in.	1 in.

5.8.2.3 Backfill Subgrade Material

The underlying subgrade consists of a 12-in. layer of compacted CA6 aggregate. The backfill material is IDOT approved, with material codes 022CM06/052CM06, and was provided by Ozinga Bros., Inc. The layer presented a case of an improved subgrade, as per IDOT *Bureau of Design and Environment Manual (BDE)*. An electric compactor plate was used for every 4 in. of added material. The backfill material was dampened with water for improved compaction. In addition, a tamper plate was used on the edges of the steel enclosure to ensure an even surface before casting.

To measure the subgrade modulus reaction, the loading plate (11.3 x 11.3 in.) was considered. The Instron testing machine was used to perform the plate test to determine any additional compaction that could occur due to fatigue loading prior to and after the completion the loading regime described in section 5.8.2.6. The subgrade modulus reaction was evaluated by measuring the slope of the pressure-deflection curve at 10 psi, as mentioned in ACI-360R.

5.8.2.4 Steel Form Enclosure

The steel enclosure used for containing the backfill material under the testing machine is shown in Figure 5-32. The enclosure is composed of two steel channels positioned in the longitudinal direction of the testing bed. The channels are 7 ft in length and 14 in. in height. The channels were bolted to the rigid bed of the testing machine and braced with steel rods to prevent lateral displacement due to subgrade modulus tests and during the testing procedure.

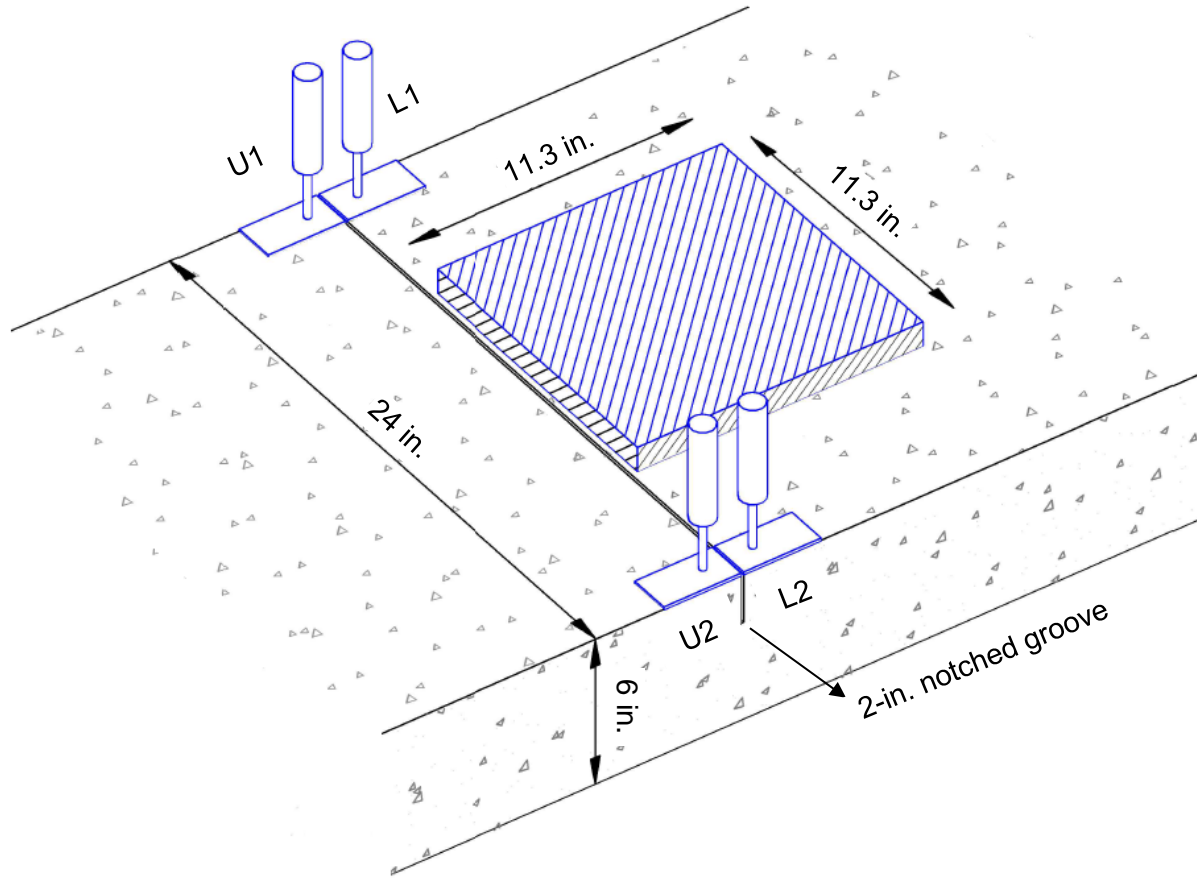


Figure 5-33. Instrumentation setup showing LVDT placement.

5.8.2.6 Loading Sequence

The loading program is presented in Figure 5-34 and can be summarized as follows:

1. Testing begins with static loading to determine the initial value of *LTE* and *E*.
2. Static tests are stroke-controlled, with a loading rate of 0.02 in./min.
3. During static tests, loading and deflection data provided by the LVDTs were collected using a data logger. The *LTE* and *E* values were calculated at the point that the load reached a maximum value of 9 kip ($\frac{1}{2}$ ESAL).
4. Cyclic fatigue loading started after each static test and was kept at a minimum of 0.9 kip, which is 10% of the maximum applied load of 9 kip.
5. At the end of 10,000; 100,000; 300,000; 700,000; and 1,000,000 cycles; the fatigue test was briefly stopped; and a monotonic static load test was conducted to measure the change in *LTE* and *E* values due to cyclic fatigue loading.

6. Fatigue cycles were applied with a frequency of 4 Hz, similar to the previous flexural fatigue programs, sections 5.5 and 5.6.
7. The testing ended after 1 million cycles, at which point the specimen was subjected to one last static test.

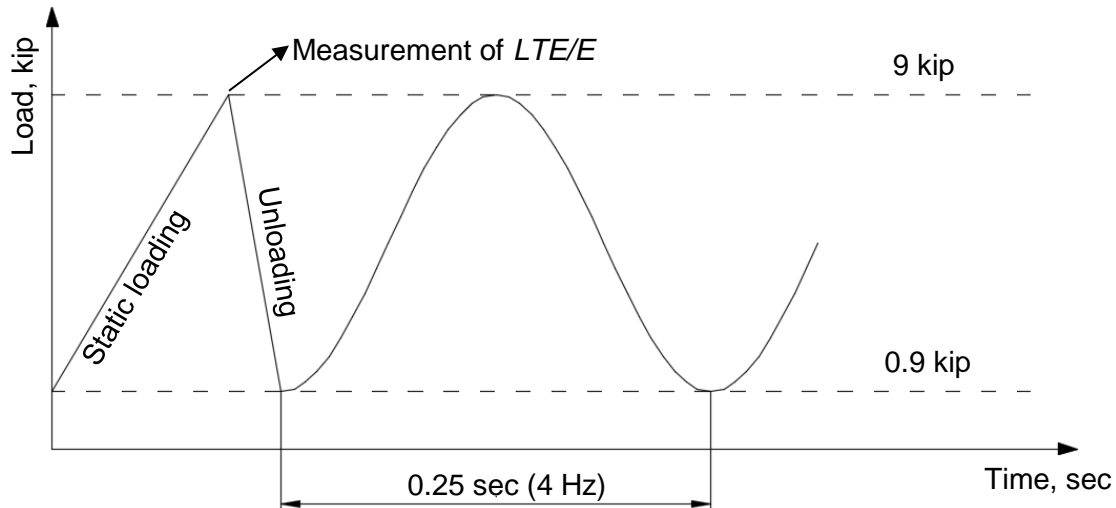


Figure 5-34. Loading sequence for static and cyclic testing.

5.8.3 Evaluation of Test Results

A typical jointed-slab performance under cyclic fatigue loading is presented in Figure 5-35, where LTE is plotted versus the corresponding number of cycles. This relationship is seen in the literature for jointed slabs subjected to fatigue loading, as discussed in section 2.4. Assuming no excessive distress occurs in the induced plane of weakness, specimens are expected to reach 1 million cycles for all testing dates. As presented in the previous literature, cumulative fatigue damage in JPCPs is considered acceptable when LTE and E values are greater than 60 and 75%, respectively. In addition, joint deterioration limits are checked as per Article 53-2.03, *BDE Manual, IDOT (2016)* where faulting and joint-widening limits are set at a low, medium, and high degree of severity.

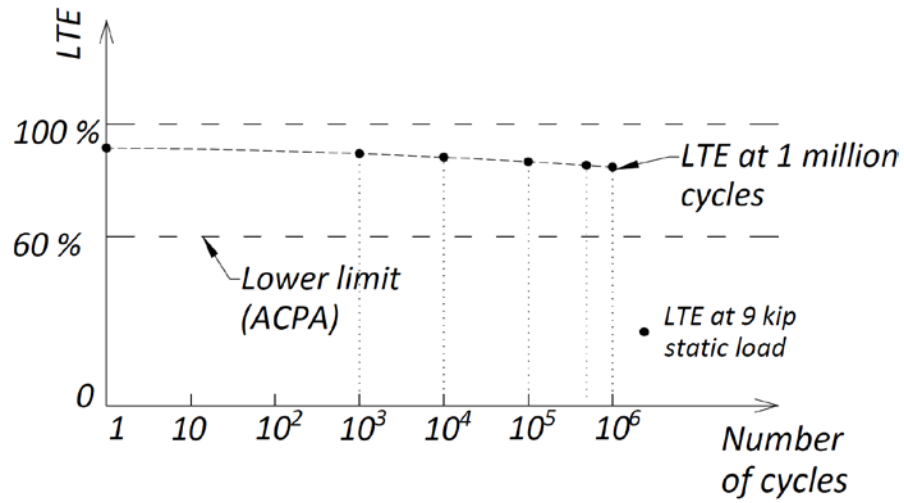


Figure 5-35. Example of typical LTE development for a jointed-slab, as observed in the literature.

CHAPTER 6: LABORATORY TEST RESULTS

For each mix design and for each curing regime described in section 4.2, two batches of concrete were prepared. The first batch (Batch 1), which was 6 ft³ in size, was prepared to cast 25 6 x 12 in. concrete cylinders for the compressive strength, static ES, and relative dynamic modulus ED. The second batch (Batch 2), which was 7 ft³ in size, was prepared to cast fourteen 6 x 6 x 21 in. concrete beams to measure flexure strength and toughness. The maturity was measured for both batches of each concrete mix, where five Type K temperature probes were embedded in concrete cylinders for Batch 1 and four in concrete beams for Batch 2. A third batch, 7 ft³ in size, was prepared to cast fracture-mechanics prisms, linear drying shrinkage samples, and cylinders for compressive strength.

6.1 FRESH PROPERTIES

The fresh properties included measuring the slump, unit weight, and fresh-air content. The mix designations are described as follows:

PV: pavement

PP1: pavement patch 1

PP2: pavement patch 2

RT: mixture cured at room temperature

45F: mixture cured at 40°–50°F

F1: Strux 90/40 fiber

F2: MasterFiber MAC Matrix fiber

FM: fracture-mechanics

FT: freeze–thaw

For example, mix designation PP1F1-45F stands for a PP1 mix made with 4 lb of MasterFiber MAC Matrix and cured in the temperature-controlled chamber at a temperature of 45°F.

The mechanical properties were investigated under two different curing regimes (room temperature and 45°F) and were tested at 12 hr; and 1, 2, 3, 7, 14, and 28 d of age. PV mixes were investigated using two different types of synthetic fibers (Strux 90/40 and MACMatrix). The addition rate for the Strux 90/40 ranged from 4 to 8 lb, while the MACMatrix was added in 4-lb quantities. The PP1 and PP2 mixes were investigated using one type of synthetic fiber (Strux 90/40) and with a 4-lb addition rate.

The fresh properties and the chemical admixtures addition rates for the PV mixes are presented in Table A-1. The slump level ranged from 3 to 5.5 in. The fresh-air content ranged between 5 and 7.4%, and the unit weight between 143.04 and 146.88 lb/ft³.

The fresh properties for PP1 and PP2 mixes with their chemical admixtures addition rates are presented in Table A-2. The slump level for PP1 mixes ranged from 3.5 to 5.75 in.; the air content from 6 to 7%; and the unit weight from 143.1 to 144.1 lbs/ft³. The slump level for PP2 mixes ranged from 3.25 and 4.75 in.; the air content from 5.6 to 5.9%; and the unit weight from 145.2 to 146.3 lb/ft³.

6.2. STRENGTH, ELASTIC PROPERTIES, AND MATURITY RESULTS

This section includes the results for the compressive strength, flexural strength and toughness, static elastic modulus (E_s), relative dynamic modulus (E_D), linear drying shrinkage, and maturity, for the PV, PP1, and PP2 concrete-mix designs with and without fibers.

6.2.1 Compressive Strength Results

6.2.1.1 Compressive Strength for PV Mixes

The development of the compressive strength (f'_c) versus age in PV mixes is shown in Figure B-1. The average f'_c for RT mixes ranged from 1,050 to 1,810 psi at 12 hr of age, and 2,380 to 2,860 psi at 1 d. The minimum required compressive strength for the PV to be opened to traffic, which is 3,500 psi, was reached at 3 d of age for the RT mixes, ranging from 3,665 to 4,090 psi, with the highest for PVF1-RT. At 28 d, the average f'_c ranged from 5,930 to 6,150 psi, with the lowest for mix PV-RT, while PVF1-RT and PVF2-RT had similar f'_c . The f'_c results at 45 °F were much lower and ranged from 430 to 570 psi at 12 hr, and from 1,140 to 1,400 psi after 1 d. The minimum required strength was reached after 7 d of curing at 45°F, and the f'_c results ranged from 3,770 to 4,030 psi. The 28-d strength was slightly lower at 45°F and ranged from 5,400 to 5,790 psi. The type and amount of synthetic fibers did not seem to have a significant effect on the strength results, as is apparent in Figure B-1, between the PV mix and PVF1, PVF2, PVF1-6, and PVF1-8.

6.2.1.2 Compressive Strength for PP1 Mixes

The development of the f'_c versus age in PP1 mixes is shown in Figure B-2. PP1 mixes were first made with w/cm of 0.44, but it was reduced to 0.42 to reach the minimum required strength after 2 d for PP1 to be opened to traffic (3,200 psi). The average f'_c for RT mixes ranged from 1,220 to 1,320 psi at 12 hr of age, and 2,440 to 2,860 psi at 1 d. The minimum required compressive strength was reached at 2 d of age for the RT mixes with 0.42 w/cm ratio, ranging from 3,200 to 3,500 psi, with the highest for PVF1-RT. At 28 d, the average f'_c ranged from 5,440 psi for mix PP1-RT-0.44 to 6,220 psi for mix PP1F1-RT-0.42. The f'_c results at 45°F ranged from 420 to 490 psi at 12 hr, and from 1,170 to 1,380 psi after 1 d. The minimum required strength of 3,200 psi was reached after 7 d of curing at 45°F, and the f'_c ranged from 3,400 to 3,870 psi. The 28-d strength was lower at 45°F, compared to the RT, and ranged from 4,930 psi for PP1-45F-0.42 to 5,520 psi for PP1F1-45F-0.42. Similar to the findings in PV mixes, the synthetic fibers did not show a significant increase in the strength results, as is apparent in Figure B-2, between the strength gain of PP1 mixes and PP1F1 mixes.

6.2.1.3 Compressive Strength for PP2 Mixes

The development of the f'_c versus age in PP2 mixes is shown in Figure B-3. PP2 mixes were made with w/cm of 0.36. The average f'_c for RT mixes at 12 hr of age ranged from 2,110 to 2,470 psi, almost double the strength of PV and PP1 mixes. The minimum required compressive strength of 3,200 psi was reached at 1 d and ranged from 3,440 to 3,760 psi for mix PP2F1-RT. At 7 d, the average f'_c ranged from 5,750 to 6,090 psi, which is equivalent to the 28 d f'_c for PV mixes. The 28 d f'_c ranged from 6,900 to 7,130 psi. The higher strength in PP2 mixes is attributed to the lower w/cm ratio and higher cementitious content, in comparison to PV and PP1. The f'_c results at 45°F ranged from 660 to 750 psi at 12 hr, and from 2,120 to 2,180 psi after 1 d. The minimum required strength of 3,200 psi was reached after 2 d of curing at 45°F, and the f'_c ranged from 3,280 to 3,350 psi. The 28-d strength was slightly lower at 45°F and ranged from 6,700 psi for PP2F1-45F to 6,750 psi for PP2-45F. Similar to the findings in PV and PP1 mixes, the synthetic fibers did not show a notable effect on the compressive strength results, as is apparent between the strength gain of PP2 mixes and PP2F1 mixes.

6.2.2 Flexural Strength Results

6.2.2.1 Flexural Strength for PV Mixes

The development of the flexural strength (f'_r) versus age in PV mixes is shown in Figure C-1. The average f'_r for RT mixes ranged from 195 to 247 psi at 12 hr of age, and 436 to 477 psi at 1 d. The minimum required flexural strength for the PV to be opened to traffic, which is 600 psi, was reached at 3 d of age for the RT mixes, where it ranged from 602 to 640 psi, with the highest for PVF2-RT. At 28 d, the average f'_r ranged from 886 psi for mix PVF1-6-RT to 936 psi for PVF2-RT. The f'_r results at 45°F were much lower and ranged from 126 to 161 psi at 12 hr, and from 269 to 306 psi after 1 d, with the highest strength gain for mix PV-RT. The f'_r at 7 d were 635 psi for PV-45F, 582 psi for PVF1-45F, and 544 psi for PVF2-45F. The f'_r in PVF1 and PVF2 exceeded 600 psi only after 14 d. The 28-d strength was much lower at 45°F than at RT and was inconsistent with the strength gain for PV-45F. The synthetic fibers did not show any notable influence on the flexural strength at all ages, as is apparent in Figure C-1, between the strength in PV mixes and PVF1 and PVF2 mixes.

6.2.2.2 Flexural Strength for PP1 Mixes

The development of the f'_r versus age in PP1 mixes is shown in Figure C-2. The average f'_r for RT mixes ranged from 270 to 290 psi at 12 hr of age, and 408 to 455 psi at 1 d. The f'_r at 2 d did not reach the minimum required flexural strength of 600 psi and ranged from 530 to 570 psi, but it was exceeded at 3 d of age for all the mixes with 0.42 or 0.44 w/cm ratio. Therefore, it is recommended to further reduce the w/cm ratio to 0.40 to maintain the minimum flexural strength requirement of 0.40 at 2 d. The maximum f'_r at 28 d ranged from 811 psi for mix PP1-RT-0.44 to 879 psi for mix PP1F1-RT-0.44, slightly lower than the 28-d strength for PV mixes. The f'_r results at 45°F ranged from 139 to 167 psi at 12 hr, and from 240 to 290 psi after 1 d. The minimum required f'_r was reached after 7 d of curing at 45°F for mixes with w/cm of 0.42 with f'_r ranging from 658 to 669 psi, but reached only 508 psi for mix PP1F1-45-0.44. The 28-d flexural strength was lower at 45°F and ranged from 634 psi for PP1F1-45F-0.44 to 804 psi for

PP1-45F-0.42. Similar to the findings in PV mixes, the synthetic fibers did not show a significant increase in the flexural strength results, as is apparent in Figure C-2, between the strength gain of PP1 mixes and PP1F1 mixes.

6.2.2.3 Flexural Strength for PP2 Mixes

The development of the f'_r versus age in PP2 mixes is shown in Figure C-3. The average f'_r for the RT mixes at 12 hr of age was around 370 psi for both PP2-RT and PP2F1-RT, which is almost double the strength of PV and PP1 mixes. At 1 d, the f'_r ranged from 504 to 549 psi. The minimum required flexural strength of 600 psi was reached at 2 d and ranged from 652 to 674 psi for mix PP2F1-RT. At 7 d, the average f'_r ranged from 864 to 882 psi, which is equivalent to the 28-d f'_r for PV mixes and is even higher than the PP1 28-d flexural strength. The 28-d f'_r ranged from 1,000 to 1,015 psi. The f'_r results at 45°F ranged from 169 to 227 psi at 12 hr, and from 349 to 361 psi after 1 d. The minimum required strength of 600 psi was reached after 3 d of curing at 45°F, and the f'_r ranged from 589 to 639 psi. The 14-d f'_r ranged from 784 psi to 821 psi. However, the 28-d strength was not consistent with strength gain and was much lower than the 14-d f'_r . There isn't a valid explanation for this strength drop, but it could be attributed to improper conditioning while curing and testing of the specimens. Similar to the findings in PV and PP1 mixes, the synthetic fibers did not show a notable effect on the flexural strength results, as is apparent between the strength gain of PP2 mixes and PP2F1 mixes.

6.2.3 Flexure Toughness in Fibrous Concrete

The description of the flexure toughness test is presented in section 5.2.5. The ultimate flexural strength is calculated from the peak load, and the flexure toughness (T^D_{150}) is represented by the total area under the load-deflection curve up to a net deflection of 1/150 of the span length of the beam (see Figure 5-8).

6.2.3.1 Flexure Toughness Characteristics in PV, PP1, and PP2 Mixes

The flexure toughness, T^D_{150} , of PV, PP1, and PP2 mixes made with 4 lb of Strux 90/40, versus flexural strength development is presented in Figure D-1. The flexure toughness with 4 lb of Strux 90/40 was tested for concrete mixes cured at RT and at 45°F. Inspection of Figure D-1 reveals no notable difference in the flexure toughness between PV, PP1, and PP2 mixes and between the curing regimes at RT and 45°F. There was quite some scattering between the toughness and flexural strength results, especially for f'_r greater than 600 psi. However, it can be observed there is an increasing trend in the toughness with the increase f'_r . The increase in toughness can be attributed to the better bond between the cement paste and fibers at higher flexural strength. This behavior can be confirmed in the increasing trend in toughness versus f'_r less than 600 psi, where the T^D_{150} ranged from 65 lb in. at 140 psi flexural strength to 190 lb in. at 565 psi f'_r . Although there was quite an inconsistent trend between the toughness and f'_r greater than 600 psi, this finding indicates that the flexure toughness, which ranged from 160 to 250 lb in., for all concrete mixes, irrespective of their mixture proportion and curing regime, is quite similar when the flexural strength exceeds 600 psi.

6.2.3.2 Effect of Fiber Type on Flexure Toughness (Strux 90/40 and MACMatrix)

Flexure toughness versus flexural strength for PV mixes made with Strux 90/40 and MACMatrix is presented in Figure D-2. The figure reveals better toughness results for MACMatrix versus Strux 90/40 except when the flexural strength is less than 200 psi. It is observed that the toughness increases at a higher rate in the MACMatrix fibers, with a maximum T_{150}^D reaching 345 lb in., in comparison to 250 lb in. with Strux 90/40 fibers. Because both the Strux 90/40 and MACMatrix have similar elastic properties (see Table 3-5), the improved flexure toughness in concrete with MACMatrix fibers is attributed to its physical properties, in comparison to the Strux 90/40. The MACMatrix fiber length (2.1 in.) and their embossed and deformed texture give them the advantage to form better bonds and have less slippage with the cement paste, in comparison to the Strux 90/40, which is shorter in length (1.55 in.) and has a very smooth texture.

6.2.3.3 Effect of Amount of Fibers on Flexure Toughness

Increasing the amount of fibers can improve the toughness characteristics at the expense of reducing the workability and finishability of concrete. Shown in Figure D-3 is the effect of the amount of Strux 90/40 fibers on the load versus the net deflection in PV concrete beams, after 14 d of curing, tested according to ASTM C1609. The difference in toughness among the three concrete beams is apparent in the residual load carried by the fibers after reaching peak load. The residual load in the 4-lb fibers reached 1,450 lb at its peak and dropped slightly to 1,260 lb after 0.12-in. net deflection. The residual load reached 2,270 and 3,400 lb at its peak in the concrete mixes with 6 and 8 lb of fibers, while dropping to 1,260 and 1,670 lb, respectively, after 0.12-in. net deflection.

Figure D-4 reveals the relation between flexure toughness and flexural strength with varying content of Strux 90/40 fibers (4.0, 6.0, and 8.0 lb). It is apparent from the figure that increasing the fiber content increases the flexure toughness in concrete. Moreover, the difference in the T_{150}^D was almost the same at different flexural strength levels. Based on the toughness results, it is noteworthy to mention that the effect of increasing the fibers from 6 to 8 lb was more pronounced on the T_{150}^D than increasing the fibers from 4 to 6 lb. The maximum T_{150}^D for concrete with 6 lb of fibers was 270 lb in. in comparison to 230 lb in. for mixes with 4 lb of fibers; whereas concrete mixes with 8.0 lb of fibers reached T_{150}^D of 330 lb in. This observation indicates that the T_{150}^D increased by 17% when increasing the fiber content to 6 lb, while it increased by 43% when increasing the fiber content to 8 lb.

6.2.4 Compressive Strength and Static MOE Relation

The static modulus of elasticity (E_s) was tested for PV, PP1, and PP2 mixes with and without fibers, at RT and 45°F curing temperatures. Presented in Figure E-1 is the relation between the compressive strength results and the E_s for all the concrete mixes. The results reveal a consistent trend, with an excellent correlation coefficient ($R^2 = 0.97$) between f'_c and the corresponding E_s . In addition, the results show that the E_s was not influenced by the mixture combination (PV, PP1, or PP2), the curing regime (RT or 45 °F), or the addition of fibers. The design E_s according to ACI-318, was applied ($33w_c^{1.5}\sqrt{f'_c}$) to compare it with the experimental E_s ,

where w_c is the unit weight of concrete. As shown in Figure E-1, the trend of the experimental E_s is revealed to be in good agreement with the ACI E_s , where the latter slightly over-predicted the E_s by 150 to 200 ksi.

6.2.5 Maturity in Concrete Results

Temperature development was monitored for all the concrete mixes under investigation (PV, PP1, and PP2) to correlate the maturity with the strength characteristics of concrete. The maturity was calculated using the Nurse–Saul equation described in section 5.3.

6.2.5.1 Development of Maturity with Time

Temperature development in concrete is shown in Figure F-1, representing the temperature trends in 6 x 12 in. concrete cylinders or 6 x 6 x 21 in. concrete beams cured at RT and 45°F. Concrete specimens cured at 45°F were left to be cured at 73°F until the initial set was reached, after which they were transferred to the temperature-control chamber to be cured at 45°F until the day of testing. The maturity development with age for all the concrete mixes (PV, PP1, and PP2) is shown in Figure F-2. The figure reveals that the maturity in all the mixes, irrespective of their mixture proportion, was influenced by the curing regime; and the maturity for concrete cured at 45°F was much lower, owing to the lower temperature development with time.

Maturity readings were also conducted in most fatigue mixes as a means to ensure consistent curing at room temperature (73°F). Figure F-3 shows the maturity development in 6 x 6 x 21 in. concrete beams within the first 7 d after pouring.

6.2.5.2 Correlation of Maturity with Compressive and Flexural Strength

The f'_c maturity and f'_r maturity relations are shown in Figures F-4 and F-5, respectively. Both figures show the strength relation with maturity for mixes PV, PP1, and PP2, with and without fibers, cured at RT and 45°F. Inspection of Figure F-4 reveals the f'_c maturity relation is influenced by the f'_c development with time. The f'_c development was affected by the mixture proportion, w/cm ratio, total air content, and curing regime. First, for PV mixes, it is observed that the f'_c maturity trend is consistent between mixes cured at RT and 45°F when the f'_c was less than 4,000 psi, or when the age of the concrete was less than 7 d. As the f'_c increased, the maturity trend became less consistent between RT and 45°F, because the f'_c for concrete cured at 45°F was approaching the f'_c for concrete cured at RT, with the latter possessing higher maturity. This observation is also apparent in PP1 and PP2 mixes; i.e., the 28-d f'_c for PP2 cured at RT and 45°F ranged from 6,900 to 7,130 psi and 6,700 to 6,750 psi, respectively, while the maturity at RT was $1,155^\circ\text{F} \times \text{d}$ and at 45°F was $415^\circ\text{F} \times \text{d}$. This observation is also apparent in the f'_r maturity relation, where for PP1 mixes, the f'_r cured at RT and 45°F, ranged from 810 to 880 psi and 770 to 805 psi, respectively, while the maturity at RT was $1,160^\circ\text{F} \times \text{d}$ and at 45°F was $380^\circ\text{F} \times \text{d}$.

Although, PV and PP1 have different mixture proportions, with the latter comprising higher content of cementitious materials (635 lb/ft³ in comparison with 565 lb/ft³), the strength–maturity relation between them was quite consistent because strength development with time at RT and 45 °F for PV and PP1 was comparable. To the contrary, the strength-maturity relation

between PP2, on the one hand, and PV and PP1, on the other, were inconsistent, which is attributed to higher strength development with time for PP2. For example, at a maturity of 40°F x d, the reported f'_c and f'_r in PV and PP1 mixes were roughly 2,300 and 400 psi, respectively, while in PP2 mixes, the f'_c and f'_r were roughly 3,300 and 540 psi. This implies that for the same maturity, the compressive strength in PP2 was higher by 1,000 psi, while the flexural strength was higher by 140 psi. The higher strength in PP2 mixes is attributed to the higher cementitious content (735 lb/ft³), lower w/cm ratio (0.36), and lower air content (~5.5%). These findings stipulate many restrictions on the use of maturity as a means for predicting strength characteristics of concrete. However, it is useful to predict the strength of PV, PP1, and PP2, based on the strength-maturity relations developed in Figures F-4 and F-5.

6.2.6 Relative Dynamic Modulus (E_D)

The relative dynamic modulus (E_D) was investigated as a means for predicting the strength in concrete specimens cured indoors and outdoors without the need for conducting the strength tests per ASTM C39, ASTM C78, and ASTM C496. The E_D was measured for the PV, PP1, and PP2 concrete mixes with 6 x 12 in. cylinders with and without fibers, and cured at RT and 45°F. The description of the test and measurement of E_D , which was conducted according to ASTM C215 using the transverse frequency method, is explained in section 5.2.4.

6.2.6.1 Development of E_D with Time

The E_D development with time for PV, PP1, and PP2 mixes is shown in Figure G-1. The test results show an increasing trend in the E_D with time, similar to the compressive- and flexural strength development, while being more progressive at early age. The E_D development in PP2 was more pronounced than in PV and PP1, which is consistent with the strength development. Moreover, the results reveal the effect of the curing regime, where it's apparent that PV, PP1, and PP2 mixes cured at 45°F exhibited lower E_D with time than their counterparts cured at RT.

6.2.6.2 Correlation of E_D with Compressive Strength and Static E_s

The relation between compressive strength and E_D is shown in Figure G-2. The figure presents the results of all the concrete mixes with and without fibers and cured at RT and 45°F. The results reveal a consistent and perfect trend, with an excellent correlation coefficient ($R^2 = 0.98$) between f'_c and the corresponding E_D . The compressive strength results ranged from 430 to 7,130 psi; and the corresponding E_D ranged from 1,740 to 6,110 ksi, respectively. In addition, the results show that the E_D was not influenced by the mixture combination (PV, PP1, or PP2), the curing regime (RT or 45 °F), or the addition of fibers. The E_s according to ACI-318 was compared to the experimental E_D , as shown in Figure G-2. It can be revealed that the trend of the experimental E_D is much higher than E_s , as expected because the relative dynamic modulus in concrete, which represents the elastic modulus of concrete subject to impact load, is equivalent to the initial tangent of the compressive stress versus strain curve in concrete. Based on these findings, a best-fitting equation can be implemented between f'_c and E_D in the following form:

$$E_D = 70,000\sqrt{f'_c} + 500,000 \text{ psi} \quad (6-1)$$

where both f'_c and E_D are in psi. The relationship is also demonstrated between the experimental E_S and corresponding E_D , as shown in Figure G-3. There exists a linear relationship between the E_S and its corresponding E_D , where a best-fitting equation can be implemented between them in the following form:

$$E_S = 0.79E_D - 500,000 \text{ psi} \quad (6-2)$$

where E_S and E_D are expressed in psi. Given the fact that the E_D was not influenced by any external factors, as it was revealed in the relationship between f'_c and E_D , on the one hand, and E_S and E_D , on the other, it can be concluded that the E_D test can be used as an excellent reliable measure to predict the strength and elastic characteristics of concrete specimens cured indoors or outdoors, irrespective of their mixture proportion and curing conditions.

6.2.6.3 Correlation of E_D with Compressive Strength and Static E_S for Fracture-Mechanics Mixes

The validity of the E_D test was further investigated as part of the fracture-mechanics testing program. Figure G-4 shows the development of the $f'_c - E_D$ relations for all PV and PP fracture-mechanics mixes corresponding to 6 x 12 in. concrete cylinders aged from 9 hr to 28 d. The readings yielded similar results to the discussion in section 6.2.6.2, while maintaining a high coefficient of correlation ($R^2 = 0.98$). The compressive strength readings varied from 336 to 7,630 psi, corresponding to E_D readings ranging from 2,077 to 6,131 ksi, respectively. Figure G-5 shows the strength–dynamic modulus development is consistent for all mixes irrespective of the mix design proportions and fiber presence/content. In addition, the E_D test method was also verified by developing E_D values from both transversal and longitudinal resonant frequencies for all patch mixes (PP1, PP1F1, PP2, and PP2F1). Figure G-6 shows that strength development with respect to the dynamic modulus is consistent for both frequencies, with the transverse frequency-based E_D yielding slightly higher values than the longitudinal frequency-based E_D .

6.2.6.4 Correlation of E_D with Flexural Strength

Relative dynamic modulus (E_D) and flexural bending tests were conducted on 6 x 6 x 21 in. beams as part of the fatigue testing program. The modulus of rupture (f_r) development with respect to E_D is shown in Figure G-7 for all pavement mixes. Inspection of the figure reveals a consistent relationship with a high coefficient of correlation ($R^2 = 0.98$). These readings represent concrete beam samples aged from 12 hr to 7 d; f_r values ranged from 143 to 801 psi, while E_D values ranged from 2,234 ksi to 5,117 ksi. Figures G-8 to G-11 show the $f_r - E_D$ relations for PV, PVF1, PVF2, and PVF1-8lbs, respectively. The results show a similar increase in flexural strength with respect to the dynamic modulus regardless of the fiber presence/content, similar to the testing results in sections 6.2.6.3 and 6.2.6.4. The data presented offer a reliable method for empirically estimating concrete flexural strength by measuring E_D :

$$f_r = 49.86 e^{5.29 \cdot 10^{-4} E_D} \quad (6-3)$$

where

f_r = modulus of rupture of concrete, psi

E_D = dynamic modulus of concrete, based on the longitudinal resonant frequency, ksi

6.2.7 Linear Drying Shrinkage

The following section presents linear drying shrinkage results for pavement design mixes designated PV, PVF1, PVF1-6lbs, PVF1-8lbs, and PVF2 and patch-design mixes designated PP1 and PP2. For each mix design, nine prisms (3 x 3 x 11 ¼ in.) were cast and unmolded at 24 hr of concrete age. Of the nine cast prisms, three specimens (Set I) were stored in a control room with 50% relative humidity at 73°F after unmolding; three other specimens (Set II) were cured in lime-saturated water for 3 d of concrete age; and the last three specimens (Set III) were cured in lime-saturated water for 7 d of concrete age. Water-curing was followed by transferring Sets II and III to the control room, where drying shrinkage measurements were conducted for 120 d for Sets I, II, and III. Shrinkage measurements were based on the average value of three concrete prisms for every mix design, as per ASTM C157. The mixes considered are listed in Table H-1 with the corresponding water-to-cement ratio, total cementitious content, fiber content, air content, slump, and unit weight.

Shrinkage development after curing is presented in Figures H-1 to H-7 for PV, PVF1, PVF1-6lbs, PVF1-8lbs, PVF2, PP1, and PP2 mixes, respectively. The data was curve-fitted with a high coefficient of correlation ($R^2 \approx 1$) to predict shrinkage for a desired elapsed number of d. The fitted curves followed a logarithmic or a rational trend, as presented in the equations shown below. Accordingly, terms A, B, and C were determined for every mix design:

$$Shrinkage = A \times \text{Log}[Time] + B \quad (6-4)$$

$$Shrinkage = \frac{A}{B + Time^C} \quad (6-5)$$

An inspection of Figures H-1, H-4, and H-7 reveals the typical effect of water-curing time, with Set I samples having the highest amount of shrinkage, followed by Set II and Set III samples for PV, PVF1-8lbs, and PP2 mixes. An observation of Figures H-2, H-3, and H-5 reveals that the effect of water-curing is less evident between Set I and Set II samples for PVF1, PVF1-6lbs, and PVF2 mixes. Moreover, PVF2 shrinkage measurements are shown to converge to a similar trend after an approximate elapsed time of 70 d. In addition, patch-mix PP1 results (Figure H-6) show Sets II and III shrinkage measurements to be similar. Shrinkage values ranged from 353 to 602 $\mu\epsilon$ at 120 d for all pavement PV mixes. Patch-mix PP1 readings ranged from 431 to 529 $\mu\epsilon$, while PP2 readings ranged from 498 to 679 $\mu\epsilon$.

Figure H-8 summarizes shrinkage readings for all mixes at 30, 60, 90, and 120 d. For pavement mixes ($w/c = 0.42$, 565 lb/yd³ cementitious content), shrinkage in Set I samples was reduced by 3 and 13% when compared with Sets II and III samples, respectively. Similarly, patch-mix PP1 ($w/c = 0.42$, 650 lb/yd³ cementitious content) shrinkage readings were reduced by 13 and 18%, while patch-mix PP2 ($w/c = 0.36$, 735 lb/yd³ cementitious content) readings were reduced by 9 and 26%. An observation of these trends indicates that the effect of synthetic macro-fiber in reducing drying shrinkage is more evident when considering 8 lb/yd³. This effect is shown in Figure H-8 (d), where the lowest Sets II and III shrinkage strains for all specimens, respectively, reached 432 and 353 $\mu\epsilon$ after 120 d. It can be also observed that lowering the water-to-cement ratio for PP2 samples ($w/c = 0.36$) did not yield lower shrinkage values when compared with pavement and PP1 samples ($w/c = 0.42$).

6.3. FRACTURE-MECHANICS RESULTS

This section presents the results for the fracture-mechanics (FM) test, which includes the tension-softening curves, critical stress-intensity factor (K_{IC}), critical crack-mouth-opening displacement ($CMOD$), and critical effective crack length, for the PV concrete-mix designs with and without fibers. The mixtures were cured at RT. The FM tests were conducted at 9 to 10 hr; 12 to 13 hr; and 1, 2, 3, 7, 14, and 28 d of age. The 9-hr testing was necessary to represent the 12-hr compressive strength of concrete cured at 45°F.

6.3.1 Load vs. $CMOD$ Curves for PV Mixes

The variations of load (P) versus $CMOD$ for the PV concrete mixes, without fibers, with 4, 6, and 8 lb of Strux 90/40 and 4 and 6 lb of MasterFiber MAC Matrix are shown in Figures I-1 to I-6, respectively. The peak load (P_{max}), which is the maximum load reached by the specimen, is used to calculate the critical fracture parameters, i.e., the critical stress-intensity factor (K_{IC}) and the critical crack-tip-opening displacement ($CMOD$). It is generally obtained in the first loading cycle for the specimens without fibers. For the specimens with fibers, the peak load could be obtained at the second cycle of loading, as more fibers are engaged in the load-resistance process after the initial cracking of the beam that occurred in the first cycle. In other words, each specimen was loaded until initial cracking in the first cycle and then unloaded. Then, more fibers engaged in the load-resistance as the $CMOD$ increases in the second cycle. The plots are generally characterized by an increasing load at a very low $CMOD$ value until reaching the peak load. It was then followed by a gradual drop in the load with the increase of $CMOD$ value until reaching a zero load, indicating the total failure of the specimen. Investigation of Figure I-1 indicates that the PV mix without fibers shows an increasing peak load with concrete age. The minimum and maximum values of the peak loads were 509 N (115 lb) and 5010 N (1130 lb) obtained at 9 and 28 d, respectively. It can be noticed that the specimens at early age show a slower drop in load after reaching the peak load, compared to the specimens at older age, where the drop in load is steeper. This pattern was also the case of the mixtures with fibers. It also appears that the specimens gain most of the peak load strength within the first 3 d. After 3 d, the increase in the peak load is less significant. In fact, around 82% of the peak load value obtained at 28 d was gained within the first 3 d. This fact holds for PV mixes with fibers. The

load vs. *CMOD* shown in Figures I-2 and I-6 are only presented up to a *CMOD* value of 1 mm—to clearly present the initial behavior at a very low *CMOD* value.

The load in the PV mix without fibers drops to zero at a *CMOD* value of about 1 mm. However, the PV mix with 4 lb (PVF1) and 6 lb Strux 90/40 fibers (PVF1-6) drops to zero at around 25 mm (1 in.). This behavior is due to the effect of fibers, which helps sustain the load at higher *CMOD* values. This difference is clearly depicted in Figure I-7, in which a comparison is shown between the PV, PVF1, PVF1-6 lbs, FVF1-8 lbs, PVF2, and PVF2-6 lbs at 28 d. The vast increase in the ultimate failure point indicates that the addition of fibers leads to increase in the total fracture energy G_F of the concrete specimen. The total fracture energy G_F as represented by Bazant and Planas (1998) is the area under the cohesive-softening curve of concrete (load vs. *CMOD*); and it varies during crack propagation depending on the size and boundary effect of the aggregates, as well as the amount of fibers. In other words, the energy needed to break the specimen in half is much higher if the amount of fibers is increased. Moreover, further investigation of Figures I-2 and I-6 shows that the amount of fibers plays an important role in increasing the post-peak behavior of the specimens at early age. This result is consistent with the flexure toughness results in which the flexure toughness values of the specimens reinforced with 6 lb of fibers (Strux 90/40) were slightly higher at early age than those reinforced with and 4 lb; however, they were close at older ages. Moreover, it is noticed that the addition of 8 lb of fibers helps further enhance the peak load and post-peak load behavior.

The variations of load (P) versus the *CMOD* for the PP1 and PP2 concrete mixes without fibers and with 6 lb of Strux 90/40 are shown in Figures I-8 to I-11. The behavior of the PP1 and PP2 mixes shows a similar behavior to that of the PV mixes. It was characterized by an increasing load at a very low *CMOD* value until reaching the peak load. It was followed by a gradual drop in the load with the increase of *CMOD* value until reaching a zero load, which indicated the total failure of the specimen. Similar to the behavior of the PV mixes, PP1 and PP2 mixes without fibers show an increasing peak load with concrete age, as shown in Figures I-8 and I-11 for PP1, PP1F1, PP2, and PP2F1, respectively. The value of the peak load ranged from 573 N (128 lb) to 5894 N (1,325 lb), obtained at 9 hr and 28 d, respectively. The post-cracking behavior of the PP1 and PP2 specimens was similar to that of the PV mixes. The specimens at early age show a slower drop in load after reaching the peak load, compared to the specimens at older age, where the drop in load is steeper. This pattern was the case of PP1 and PP2 mixes with and without fibers. Within the first 3 d, specimens developed 50 to 65% of the maximum peak load strength obtained at 28 d.

6.3.2 Two-Parameters Fracture Model Results (K_{IC} and $CTOD_c$, Proposed by Shah 1990)

The development of the K_{IC} versus concrete compressive strength (f'_c) for PV mixes is presented in Figure I-12. Investigation of Figure I-12 shows that the K_{IC} increases with the gain of compressive strength. The maximum values of the stress-intensity factor ranged from 1,400 $N \cdot m^{-3/2}$ (1.27 lb in.^{-3/2}) and 1,800 $N \cdot m^{-3/2}$ (1.64 lb in.^{-3/2}). The development of the K_{IC} shows rapid increase at low strength. Moreover, similar to the peak load behavior, it is noticed that the increase is slower at later age. In fact, 70 to 81% of the K_{IC} results at 28 d is gained within the

first 3 d. This observation is depicted in Figure I-13, where it is noticed that the values of the K_{IC} at 3 d ranged from 1072 N.m^{-3/2} (0.97 lb in.^{-3/2}) to 1332 N.m^{-3/2} (1.21 lb in.^{-3/2}) for all concrete mixes and from 1510 N.m^{-3/2} (1.37 lb in.^{-3/2}) to 1645 N.m^{-3/2} (1.49 lb in.^{-3/2}) at 28 d. It is also noticed that there is very close correlation between K_{IC} values for all mixes, due to the fact that the critical stress-intensity factor is calculated at the first loading cycle. The specimens are loaded until the onset of cracking is detected. At this stage, the fibers are not really engaged at the initiation of the cracking. However, the effect of fibers greatly appears in the post-cracking behavior of the concrete specimen, as mentioned earlier. This fact also holds for the critical crack-mouth-opening displacement $CMOD_c$ that is also calculated from the first loading cycle. The reason for calculating these parameters from the first loading cycle is to study the rate of increase in compliance (or in other words, in the rate of increase in stiffness degradation) from uncracked concrete and during crack propagation.

Similarly, the development of the $CMOD$ versus f'_c is presented in Figure I-14. Investigation of Figure I-14 shows that the $CMOD$ increases with gain in compressive strength. The maximum values of the $CMOD$ ranged from 0.026 to 0.038 mm. The development of the $CMOD$ shows rapid increase at low strength. Moreover, analogues to the K_{IC} , it is noticed that the increase is slower at a later age. In fact, around 93 % of the $CMOD$ results at 28 d is gained within the first 3 d.

The development of the K_{IC} versus concrete compressive strength (f'_c) for PP1 and PP2 mixes is presented in Figures I-15 and I-16. Investigation of these figures shows that the K_{IC} increases with the gain of compressive strength. Similar to PV mixes, the development of the K_{IC} for PP1 and PP1F1 mixes shows a rapid rate of increase at low strength and a slow rate of increase at later age. In fact, 55 to 68% of the K_{IC} results for PP1 and PP1F1 mixes at 28 d, respectively, was gained within the first 3 d. It was noticed that the values of the K_{IC} ranged from 887 N.m^{-3/2} (0.8 lb in.^{-3/2}) at 3 d to 1,586 N.m^{-3/2} (1.44 lb in.^{-3/2}) at 28 d for PP1 and from 1,050 N.m^{-3/2} (0.95 lb in.^{-3/2}) at 3 d to 1,534 N.m^{-3/2} (1.39 lb in.^{-3/2}) for PP1F1 mixes. The development of the K_{IC} for PP2 and PP2F1 mixes shows a consistent rate of increase at all ages. The variation of K_{IC} versus concrete compressive strength (f'_c) for PP2 and PP2F1 follows an almost linear trend, as shown in Figure I-16. For PP2 mixes, the values of the K_{IC} ranged from 906 N.m^{-3/2} (0.82 lb in.^{-3/2}) at 3 d to 1691 N.m^{-3/2} (1.53 lb in.^{-3/2}) at 28 d and from 889 N.m^{-3/2} (0.81 lb in.^{-3/2}) at 3 d to 1744 N.m^{-3/2} (1.58 lb in.^{-3/2}) for PP2F1 mixes.

6.4 FATIGUE TEST RESULTS

6.4.1 Fatigue Life by Test Date

This section discusses the fatigue data for a testing regime of 12 hr; and 1, 3, and 7 d after casting and for 0.9, 0.8, 0.7, and 0.6 stress levels. The number of cycles at failure (N) is shown for every stress level case. Fatigue readings for PV, PVF1, PVF2 and PVF1-8lbs mixes are plotted for the purpose of studying the effect of the inclusion of fibers in concrete on flexural fatigue performance.

6.4.1.1 Twelve-Hour Testing Results

The fatigue testing results at 12-hr for PV, PVF1, PVF2, and PVF1-8lbs are shown in Table J-1. Analysis of Table J-1 shows the total testing time for all mixes is 97.9 hr, from which 55% were taken by the 0.6 stress level testing. It was noticed that the PVF1-8lbs mixes at 0.6 stress level testing did not fail, and it was stopped after exceeding 1 million cycles. Table J-1 also shows an increasing number of cycles with reducing stress level. The result is further described in Figure J-1.

Figure J-1 shows stress level versus number of cycles to failure (S-N curve) for PV, PVF1, PVF2, and PVF1-8lbs at 12 hr after concrete casting. Investigation of J-1 reveals that the number of cycles to failure (N) ranged from 45 to 189 cycles for a stress level of 0.9. The 0.9 stress level represents a clear case of low-cycle loading (ranging from 1 to ≈ 100 life cycles, as presented by Hsu (1981)). This small range shows that the effect of fibers on the fatigue performance at 0.9 stress level cannot be accurately determined. A larger range is observed for the 0.8 stress level, with N ranging from 182 to 6,470 cycles. The upper bound of this range (6,470 cycles) is affected by the performance of the PVF1-8lbs mix. In fact, the upper bound of the range is significantly reduced to a maximum value of 1,628 cycles (for PV mix) when not considering the reading for the PVF1-8lbs beam. Because high-cycle fatigue for concrete pavements is set from 10^3 to 10^6 life cycles (Hsu, 1981), it can be assumed that the 0.8 stress level readings were on the lower boundary of the high-cycle fatigue range. This finding indicates that concrete behavior is relatively similar to the low-cycle fatigue testing seen at the 0.9 stress level. The range between the numbers of cycles until failure for the 0.9 and 0.8 stress levels is insufficient to draw a clear conclusion of the effect of fibers.

Past literature suggested that fatigue performance at 28 d can be improved at low cycles when using fiber-reinforced concrete (Yin and Hsu, 1995). The failure occurs as cracks in the mortar paste rather than in the bond interface between the paste and the aggregate. However, this behavior is different at early age. It was found that an insignificant improvement was achieved at 12 hr for the PV, PVF1, and PVF2 mixes. In this case, the failure mode occurred in the bond interface between the mortar paste and aggregates for both 0.9 and 0.8 stress levels. PV, PVF1, and PVF2 mixes yielded close readings, which suggests that 4lbs/yd³ of fibers did not affect the overall fatigue behavior in concrete.

Fatigue readings for the 0.7 stress level ranged from 59,255 to 165,182 cycles, with the minimum and maximum values corresponding to the PVF1-8lbs and PVF1 beam readings, respectively. All 0.7 stress level readings are well within the high-cycle fatigue range. The readings are consistent with what was previously observed by Grzybowski et al. (1993). The latter suggested that the fibers can have a dual effect on the fatigue performance:

- 1) Fibers can bridge micro-cracks and arrest their propagation in case of failure in mortar. This case is usually seen in concrete with strong paste (at 28 d) with low-cycle fatigue.
- 2) For high-cycle fatigue loading at early age, bond cracks occur slowly until failure. The effect of fibers in concrete can actually increase the density of the initial micro-cracks, causing a decrease in strength.

However, a significant improvement in fatigue performance is observed for a 0.6-stress level, where the PVF1-8lbs beam reading exceeded 1 million cycles; and the failed beam readings ranged from 148,975 to 281,167 cycles with no major advantage for the PVF1 and PVF2 mixes over the PV mix. This behavior is due to the fact the bond interface gained strength throughout the testing period, resulting in failure in the mortar paste or in both bond and mortar (mixed mode of failure). The linear-regression for the PVF1-8lbs data mix showed a higher coefficient of correlation (0.96) when compared with plain-concrete readings (0.86).

From the results of the 12-hr fatigue testing for all mixes, the following conclusions can be drawn:

- Early-age concrete exhibits bond failure in flexural fatigue due to low mortar strength.
- 4 lb/yd³ of fibers did not have a major role on fatigue performance for all stress levels for both Strux® 90/40 and MasterFiber MAC Matrix fibers.
- The introduction of higher amounts of fibers (8 lb/yd³) can improve fatigue life for a stress level of 0.6.

The PVF1-8lbs S-N curve appears to predict more cycles when compared with the PV mix results, even with excluding that of the 0.6-stress level for the PVF1-8lbs S-N curve.

6.4.1.2 One-Day Testing Results

The fatigue testing results at 1 d for PV, PVF1, PVF2, and PVF1-8lbs are shown in Table J-2. Analysis of Table J-2 shows that total testing time for all mixes is 178.7 hr (including all repeated samples), from which 81.6% were registered by the 0.6-stress level testing. It was noticed that the PVF1-8lbs mixes at 0.6-stress level testing did not fail, and it was stopped after exceeding 1 million cycles. Table J-2 shows an increasing number of cycles with reducing stress level.

Figure J-2 shows stress level versus number of cycles to failure (S-N curve) for PV, PVF1, PVF2, and PVF1-8lbs at 1 d after concrete casting. Investigation of Figure J-2 reveals that the number of cycles to failure (N) ranged from 49 to 881 for a stress level of 0.9. These readings appear to be similar for the 0.9 stress level at 12-hr testing, with no significant contribution to the fatigue performance for the added fibers. N values ranged from 151 to 3,685 cycles at the 0.8 stress level and from 35,802 to 263,597 cycles at the 0.7 stress level. For both 0.8 and 0.7 stress levels, the PVF1-8lbs reading was the highest, with no noticeable trend for the PVF1 and PVF2 mixes when compared with plain-concrete readings for PV mixes. Similarly, for the 0.6 stress level, the PVF1-8lbs sample did not fail; the test was stopped at 1 million cycles. Testing after 1 d from casting proved to be sufficient time for the mortar paste to gain strength and for the fibers to take part in arresting the development of micro-cracks in the cement paste. Results are shown in Figure J-2, where the trend line for the PVF1-8 readings is estimating higher values of cycles when compared with plain concrete. The PVF1 trend line showed an excellent coefficient of correlation ($R^2 = 0.99$). Plain-concrete readings were less consistent ($R^2 = 0.74$), with PVF1 and PVF2 mixes yielding no definitive trend between the two cases of PV and PVF1-8lb.

From the results of the 1-d fatigue testing for all mixes, the following conclusions can be drawn:

- Fatigue testing after 24 hr can be sufficient time for the cement paste to gain bond strength with the added fibers for the PVF1-8lbs mix, which improved fatigue performance.
- 4 lb/yd³ of fibers did not greatly affect fatigue performance for all stress levels for both Strux® 90/40 and MasterFiber Mac Matrix fibers.

6.4.1.2 Three-Day Testing Results

The fatigue testing results at 3 d for PV, PVF1, PVF2, and PVF1-8lbs are shown in Table J-3. Analysis of Table J-3 shows that the total testing time for all mixes is **52.7** hr, from which 83.5% were registered by the 0.6-stress level testing. Table J-3 shows an increasing number of cycles with reducing stress level.

Fatigue readings at 3 d of testing showed similar behavior to the previous 1-d testing. Figure J-3 shows stress level versus number of cycles to failure (S-N curve) for PV, PVF1, PVF2, and PVF1-8lbs at 3 d after concrete casting. Investigation of Figure J-3 reveals that the number of cycles to failure (*N*) ranged from 9 to 126 cycles at 0.9 stress levels, with no apparent difference between mixes without fibers and with 4 lb/yd³ of Strux 90/40 and Mac Matrix. For the 0.8 stress level, the maximum number of cycles was achieved by the PVF1-8lbs reading (4,092 cycles). The PVF2 reading showed a very low number of cycles (108 cycles) when compared with the rest of the readings at 0.8 stress level. The number of cycles (*N*) ranged from 8,184 to 63,972 cycles for the 0.7 stress level and from 91,480 to 257,393 cycles for the 0.6 stress level. The highest number of cycles for 0.8, 0.7 and 0.6 stress levels were all provided by the PVF1-8lbs reading. S-N curves for both PV and PVF1-8lbs mixes show high coefficient of correlations (0.98 and 0.96, respectively).

From the results of the 3-d fatigue testing for all mixes, the following conclusions can be drawn:

- S-N curves show that PVF1-8lbs mixes gave higher *N* values for any given stress level, when compared with the plain-concrete PV mixes.
- PVF1 and PVF2 did not present any significant difference in fatigue performance when compared with plain-concrete PV mixes.

6.4.1.3 Seven-Day Testing Results

The fatigue testing results at 7 d for PV, PVF1, PVF2, and PVF1-8lbs are shown in Table J-4. Analysis of Table J-4 shows that the total testing time for all mixes is **76.9** hr, from which 89% were registered by the 0.6-stress level testing. Table J-4 shows an increasing number of cycles with reducing stress level.

Figure J-4 shows stress level versus number of cycles to failure (S-N curve) for PV, PVF1, PVF2, and PVF1-8lbs at 7 d after concrete casting. Inspection of Figure J-4 reveals that the number of cycles to failure (*N*) ranged from 77 to 707 cycles at the 0.9 stress level, with no apparent difference between mixes without fibers and with 4 lb/yd³ of Strux 90/40 and Mac Matrix. Results at 7-d testing showed wider spread of data readings for all stress levels, when compared to previous testing date results.

N ranged from 330 to 10,359 cycles at the 0.8 stress level; from 1,137 to 87,120 cycles for the 0.7 stress level; and from 70,773 to 295,672 cycles at the 0.6 stress level. Trend lines for the PVF1-8lbs and PV mixes yielded R^2 values of 0.91 and 0.84 respectively.

The 7-d testing produced similar observations as the 3-d testing. These observations can be summarized as follows:

- PVF1-8lbs readings showed higher values when compared with plain-concrete PV mixes.
- 4 lb/yd³ of fiber for mixes PVF1 and PVF2 showed an inconsistent trend when compared with PV and PVF1-8lbs-mix readings.

6.5 EFFECT OF FATIGUE ON FREEZE–THAW TEST RESULTS

This section presents concrete durability performance against rapid freeze–thaw cycles for samples subjected to cyclic fatigue loading at 12-hr; and 1-d, 3-d and 7-d concrete age. Testing also included control samples with no fatigue loading. Mixes were composed of plain-concrete PV mixes and mixes containing 4 lb/yd³ and 8 lb/yd³ of fibers designated F1. Mass loss and the decrease in transverse resonant frequency are monitored throughout testing, and the durability factor is calculated for every mix by the end of the test. Concrete durability performance against freeze–thaw is evaluated through the degree of surface scaling (mass loss) and interior crack growth (drop in the dynamic modulus readings).

6.5.1 Mass Loss Due to Freeze–Thaw

Table K-1 summarizes the average mass loss for PV, PVF1, and PVF1-8lbs mixes. The readings correspond to 300 cycles of freezing and thawing. Mass loss values ranged from 0.74% to 1.65% for all mixes. Plain-concrete PV mixes averaged a 1.56% mass drop for eleven samples, PVF1 mixes averaged 0.93% mass drop for twelve samples, while PVF1-8lbs averaged a 0.75% mass drop for eleven samples. An investigation of the testing results indicates an improved resistance to surface scaling is achieved with the inclusion of synthetic fibers. In addition, including larger amounts of synthetic fibers increased resistance to scaling by a greater degree. It can be observed that synthetic fibers can prevent surface separation in concrete by arresting cracks due to expanding, freezing water. Mass loss was consistent between samples of the same mix design, with no apparent distinction between samples subjected to fatigue loading prior to freeze–thaw and control samples not subjected to fatigue loading.

6.5.2 Relative Dynamic Modulus and Durability Factor

The minimum criterion for concrete freeze–thaw durability was met, with all samples passing the 300th cycles while maintaining a relative dynamic modulus significantly greater than 60%, as per ASTM C666. The durability factor values for the PV, PVF1, and PVF1-8lbs mixes are presented in Table K-2. An observation of the DF values shows similarity between all mixes regardless of fiber presence or fiber content, with values ranging from 89.3 to 91.9%. Figure K-1 shows the development of RDM with respect to the number of freeze–thaw cycles, where the last relative dynamic modulus reading represents the durability factor. The plots show a similar trend for all mixes. A sharp drop in RDM is observed for the first reading at the 35th cycle,

followed by a descending curve that reaches an approximate value of 90% when reaching the 300th cycle. Moreover, no distinct advantage was noticed between loaded and non-loaded samples in this test. Results of the freeze–thaw test indicate that the controlling parameter in concrete durability against freeze–thaw is air content, which is kept close to 7%. The test proved that, with a 7% fresh-air content, an adequate amount of air pores is created in the concrete matrix. The induced air pores allowed water expansion at freezing temperatures, which contributes to releasing internal pressure and prevents further development of internal crack propagation. This mechanism is demonstrated by the low loss of dynamic modulus after 300 cycles for all mixes.

6.6 FINITE-ELEMENT ANALYSIS RESULTS

6.6.1 Parametric Study 1 for Rigid Pavement

This section describes the output results of flexural stresses and deflections in rigidly connected pavement slabs. The collected data provides several cases in which the fatigue performance of plain concrete for PV mixes can be compared to that of the fiber-reinforced concrete for PVF1-8lbs mixes. The model was run with varying modulus of elasticity (*MOE*) values to simulate the increase in concrete stiffness with respect to time. Varying values of the modulus of subgrade reaction (*K*) were also considered to simulate different soil conditions. Several slab thicknesses were considered for all *MOE* and *K* values.

6.6.1.1 Output Results and Discussion

The stresses developed in the longitudinal direction (*y*-axis) and in the transversal direction (*x*-axis) are shown in Tables L-1 and L-2, respectively, for all cases. The values represent the maximum tensile stresses at the bottom level of the pavement. Table L-3 shows the maximum deflections developed for all cases considered. The results in these tables are discussed in the following sections.

6.6.1.1.1 Effect of *MOE*

Results reported in Tables L-1 to L-3 show an increase in the maximum tensile stresses in both longitudinal and transverse directions and a decrease in maximum slab deflection for an increasing concrete age. For example, a typical case of a modulus of subgrade reaction equal to 100 psi/in. and for a slab thickness of 8 in. is considered to study these changes. For this case, results for stresses and deflections are summarized in Table L-4. Variations of stresses/deflections are shown as a percentage of the difference between every two consecutive concrete ages, ranging from 12 hr to 7 d.

Transverse tensile stresses slightly increased by 2.8% from 12 hr to 1 d, 1.7% from 1 to 3 d, and 1.1% from 3 to 7 d. Similarly, longitudinal tensile stresses increased by a relatively larger margin of 6.4% from 12 hr to 1 d; 4.4 % from 1 to 3 d; and 2.9% from 3 to 7 d. The maximum recorded deflection was reduced by 10.7% from 12 hrs to 1 d; 7.3% from 1 to 3-d; and 5 % from 3 to 7-d. It can be inferred that an increase in age (i.e., increase in *MOE*) causes reduction in the strain developed at the bottom, which also corresponds to the decrease in deflections. Because all

cases were in the elastic range, increased *MOE* readings and their corresponding strain readings yielded higher stresses. Results for *MOE* variations for all pavement thicknesses and for a constant *k* of 100 psi/in are shown in Figure L-1 for the transverse stresses and longitudinal stresses and in Figure L-2 for deflections. Inspection of Figure L-2 shows that the effect of increasing *MOE* was more evident in the longitudinal direction compared with the effect on the stresses in the transverse direction. Longitudinal stresses were shown to be higher than the transverse stress for all considered cases at *K* = 100 psi/in. This observation is a result of having a greater span length and a higher load concentration in the longitudinal direction for the interior loading case. Typical variation of the transverse and longitudinal stresses in the form of contour lines for 12 hr are shown in Figures L-3 and L-4, respectively.

6.6.1.1.2 Effect of modulus of subgrade reaction

A reduction in the tensile stresses and deflection was observed for increasing *K* values. An example for one of the typical cases of 3-d concrete age with a slab thickness of 8 in. is shown in Table L-5. By comparing two extreme cases of soft soil (50 psi/in.) and stiff soil (500 psi/in.), results show a decrease in transverse stresses by 12%. Stresses in the longitudinal direction decreased by a larger margin of 23.5%, compared to transverse stresses. Deflections showed a significant decrease of 65.6%. Results conform to the Winkler model, in which the soil is idealized as a series of translation and rotation elastic springs: stiffer springs yield lower strains and, consequently, lower stresses for the same applied *ESAL*. Transverse/longitudinal stresses and deflection results for all *K* variations for 3-d concrete age are shown in Figures L-5 and L-6, respectively. Inspection of Figure L-5 shows that longitudinal stresses (solid lines) are likely to be affected more by the increase in the modulus of subgrade reaction, when compared with transverse stress values (dashed lines). Tensile stresses at the bottom of the slab appeared to be higher in the longitudinal direction for all cases considered for the 3-d-age concrete. An increase in the thickness yields the same subgrade modulus effect with smaller stress values.

6.6.1.1.3 Effect of slab thickness

A decrease in tensile stresses and deflection is observed for an increase in slab thickness for all cases. The effect of increasing slab thickness for a typical case of 3-d concrete age with a subgrade modulus of 100 psi/in. is shown in Table L-6. The results show a significant decrease in stresses and deflections: An increase of concrete pavement thickness by 2 in. caused a decrease in the transverse and longitudinal stresses by 40 and 35%, respectively, and deflections by 24%. Further increase in slab thickness resulted in a considerable effect on stress reduction, as seen in the case of 12-in. slab thickness. Tensile stresses in the transversal and longitudinal direction were reduced by 71 and 63%, respectively. Deflections were reduced by 51%. The percentage difference is shown with respect to the 6-in.-depth case.

6.6.1.2 Fatigue Performance for Selected Cases

To determine the stress level due to *ESAL* in the model, flexural strength results for plain-concrete PV mixes are taken into consideration. The flexural strength values corresponding to the fatigue testing program were extracted from section 6.2.2.2 and summarized in Table L-7.

To evaluate the effectiveness of fiber reinforcement on concrete fatigue life, the following steps are taken:

- *MOE* values were set for 12 hr; and 1 and 3 d of concrete age.
- *K* values were set for 100 and 300 psi/in., with the first value corresponding to a typical subgrade reaction. The greater value of 300 psi/in. is considered to show the effect of a stiffer soil on concrete fatigue performance.
- Slab thickness was set to 6 and 8 in.
- The maximum longitudinal flexural tensile stresses σ_y was evaluated by the software, given the *MOE*, *K*, and slab thickness.
- The stress level, *S*, was set by dividing σ_y by *MOR* (obtained from Table L-4), i.e., $S = \frac{\sigma_y}{MOR}$
- *S-N* linear-regression formulas corresponding to the concrete age and type were used; and the number of cycles until failure for both plain-concrete (PV mixes) and fiber-reinforced concrete, FRC, (PVF1-8lbs mixes) was calculated (Table L-8).

The results of slabs having a thickness of 6 in. are shown in Table L-6 and can be summarized as follows:

- Opening to traffic at 12 hr resulted in excessive stresses due to *ESAL*. The flexural capacity of the concrete was exceeded in this case.
- Similarly, opening to traffic at 1 d resulted in failure in the concrete. For *K* = 100 psi/in., the applied stresses exceeded the flexural capacity. Life cycles for a soil with *k* = 300 psi/in. can sustain only a very limited number of traffic loads before failure.
- Opening to traffic on the third day is plausible with a 0.64 stress level. For plain-concrete slabs, failure due to fatigue is expected after 1 hr and 5 hr for *K* = 100 psi/in. and *K* = 300 psi/in., respectively. Fiber-reinforced concrete (FRC) slabs failed after 17 and 278 hr after opening to traffic for *K* = 100 psi/in. and *K* = 300 psi/in., respectively.

It should be noted for that the described method could be advantageously conservative in its estimation of fatigue life, due to the following:

- The applied dynamic load is set at a frequency of 4 Hz, which may overestimate real traffic load frequencies.
- The selected slab thickness (6 in.) represents the minimum depth that can be adopted for PCC pavements. Stress levels could be considerably reduced for slabs with greater depth, as is clearly evident in the 8-in. case discussed below.

The results are shown in Table L-10 for slabs with 8-in. thickness. Results vary significantly when compared with the previous case of 6-in. slabs:

- EOT at 12 hr remains not applicable. The applied stresses are higher than the flexural capacity of concrete despite the considerable drop in stress values.
- EOT at 1 d is plausible for a typical subgrade value of 100 psi/in. with fiber reinforcement. Plain concrete fails after 15 hr, while FRC fails after 56 hr.

- For a stiffer soil with 300 psi/in., opening to traffic is seen to be acceptable at 1 d for a stress level of 0.56. Fatigue life has exceeded 1 million cycles for plain and fiber-reinforced concrete.
- An addition of 2 in. in concrete thickness has significant improvement on fatigue life at early age.

6.6.2 Parametric Study 2 for Jointed-Pavement

The results of the second parametric study are shown and discussed in this section. The maximum transverse tensile stresses, longitudinal tensile stresses, and deflections are presented with respect to varying values of the load-transfer efficiency (*LTE*). *LTE* values were then used to estimate the aggregate interlock contribution to the joint stiffness, in addition to dowel-bar presence. The structural behavior of the model considered can be estimated before testing actual specimens of a given scale.

6.6.2.1 Effect of load-transfer efficiency

Table L-11 shows the effect of increasing *LTE* on transverse stresses, longitudinal stresses, and deflections. For an increasing *LTE*, results showed a significant decrease in transverse stresses, from 419 to 302 psi. Deflections decreased from 0.0382 to 0.03079 in. Longitudinal stresses slightly increased from 112.6 to 134.2 psi. Figures L-7 and L-8 show the stress development versus *LTE*, and deflections versus *LTE*, respectively. The model considered represents a case of edge loading, in which the developed stresses are greater in the transverse direction when compared with the longitudinal stresses, as seen in the typical output stress contours in Figures L-9 and L-10 (corresponding to an *LTE* of 50 %).

6.6.2.2 Effect of dowel bars and aggregate interlock

Table L-12 shows the stress/deflection development with respect to *LTE*, while accounting for dowel-bar placement as described in section 5.7.3.2. When aggregate interlock was neglected, stresses in the transverse and longitudinal directions were 410 and 130.8 psi, respectively, with a maximum deflection of 0.03151 in. After calculation of *AGG* factors for *LTE* values ranging from 50 to 95%, the stresses and deflections were reevaluated and compared with the doweled case with no *AGG* contribution. Transverse stresses significantly decreased by 23.7 %, while an increase is observed for the longitudinal stresses by 8.6 %. Deflections were slightly decreased by 4.5%. Figures L-11 and L-12 show the development of stresses and deflections versus *LTE* for both *LTE*-based cases and dowel-transfer cases. *LTE*-based values and dowel-transfer cases are seen to have a similar development of stresses with an increasing *LTE*. Deflections for the *LTE*-based cases showed greater values than for the dowel-based cases. Deflections for the dowel-transfer cases converge to the *LTE*-based values for a load-transfer efficiency higher than 90%. It should be noted that *LTE* values ranging from 90 to 95% represent the expected *LTE* in real jointed slabs.

The outcome for parametric study 2 can be summarized as follows:

- Estimating the effect of the aggregate interlock contribution on stresses is consistent with the assumed load-transfer efficiency case for all *LTE* values.

- Estimating the effect of the aggregate interlock contribution on deflections is valid only for higher values of LTE (90–95% range).
- Aggregate interlock can considerably reduce tensile stresses for high *LTE* values, but its effect on deflections is not as evident.
- The output provided can benefit identifying the structural aspects of real jointed pavements subjected to cyclic *ESALs*. The model serves to estimate the overall structural behavior of such pavements.

6.6.3 Parametric Study 3 for Cross-Traffic Case

This section presents the results of the third parametric study. Flexural and shear stresses are evaluated and compared with the nominal concrete strength of PV mixes. The cases in which the developed stresses exceed the nominal capacity are highlighted and discussed for varying soil stiffness, pavement thickness, and concrete age.

6.6.3.1 Flexural stresses

Flexural stress that developed at the bottom of the PCC layer are presented in Table L-13. The values presented correspond to the stresses in the transverse direction (x-axis), which controls when compared with flexural stresses in the longitudinal direction (y-axis) for all considered cases. An investigation of the results shows that failure is plausible for pavement thicknesses lower than 12 in. with a subgrade modulus of 50 psi/in. at 12-hr concrete age. At 1-d concrete age, the controlling case is found at $t = 8$ in. and $k = 100$ psi/in. At 3-d concrete age, the controlling case is reduced to the extreme design condition of $t = 6$ in. and $k = 50$ psi/in. The 7-d stresses are shown to be lower than concrete flexural capacity, and therefore no flexural failure is expected at this phase. The distribution of the transverse flexural stresses is shown in Figure L-13 for one of the cases where $t = 8$ in. and $k = 50$ psi/in. for 12-hr concrete age. It can be noticed from Figure L-13 that flexural stresses are found to be more significant beneath the contact area of the tires at the bottom layer of the PCC pavement.

6.6.3.2 Shear stresses

Shear stresses can contribute greatly to joint distresses due to heavy loads which can be more evident in longitudinal joints that are constructed according to 420001-08, *Standard Specifications for Road and Bridge Construction*, IDOT (2016), in which shear transfer is done solely by concrete with no dowels for shear transfer. In addition, saw-cutting along the longitudinal joint creates a plane of weakness where shear becomes more significant, especially for lower slab thicknesses. The results of the shear stresses are presented in Table L-14. An investigation of the results shows that the controlling case is found at $t = 10$ in. and $k = 50$ psi/in. at 12-hr concrete age. At 1-d concrete age, the controlling case is found at $t = 8$ in. and $k = 100$ psi/in. At the 3-d and 7-d concrete age, most cases with $t = 6$ in. show stresses that exceed the concrete capacity. The shear stresses distribution is shown in Figure L-14 for a case of $t = 8$ in., $k = 50$ psi/in., at 12-hr concrete age. It is noticed that a maximum shear stress is expected at the longitudinal joint and near the corner area of the loaded slab panel.

6.7 FATIGUE PERFORMANCE OF JOINTED-CONCRETE SLABS

Jointed-slab specimens were constructed in the sequence of Table M-1. Joint deterioration was investigated for different slab thicknesses (6 and 8 in.), different fiber content (0, 4, and 8 lb yd³), and for doweled and non-doweled joints.

6.7.1 Jointed-Slab Specimen 1

The following section covers the experimental approach and outcome of the first tested jointed-slab specimen, as per section 5.8. The first specimen consisted of a 6-in., fiber-reinforced (8 lb yd³), doweled jointed-slab (1-in. diameter), as per Table M-1.

6.7.1.1 Subgrade Layer Preparation and Subgrade Modulus Reaction Measurement

Prior to concrete placement, the supporting soil layer beneath the jointed-slab specimen was prepared within a steel enclosure to simulate an improved soil condition. This layer was 12-in. deep and consisted of CA6 granular material, which is commonly used for backfilling. Wooden supports were placed beneath the soil to avoid direct contact with the rigid steel bed of the Instron testing machine. This adjustment was done to limit the effect of overestimating the subgrade modulus reaction when the soil is placed on a rigid support. The supporting formwork is presented in Figure 6-1. The soil was compacted in 4-in. lifts by using an electrical vibratory-plate compactor, as shown in Figure 6-2. The soil was also dampened with water for improved compaction. In addition, the edges of the soil confined within the enclosure were compacted using a steel tamper plate to ensure an even surface before concrete placement. Moreover, steel bracing was installed during compaction in the transverse direction of the steel enclosure to prevent any lateral displacement while measuring the subgrade modulus reaction and while applying static/cyclic loading.

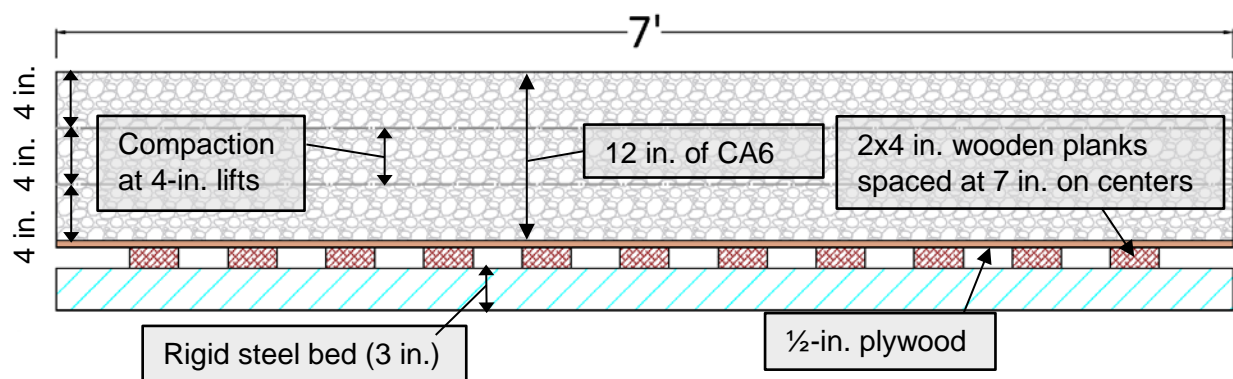


Figure 6-1. Section view along the length of the compacted backfill layer, showing wooden support.

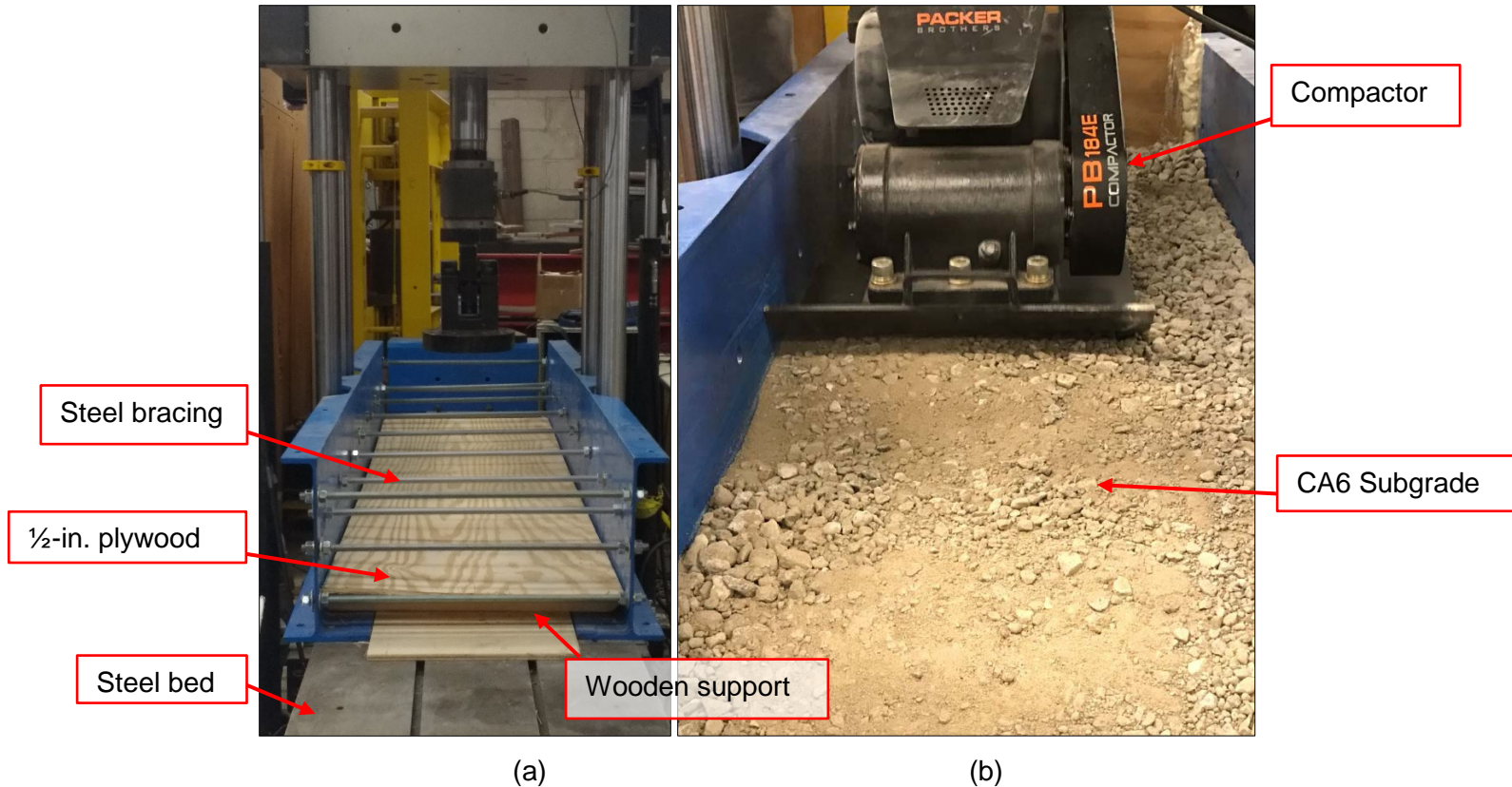


Figure 6-2. Steel enclosure showing wooden support (a) and compaction of the first soil layer (b) using vibratory-plate compactor.

Measuring the modulus of subgrade reaction requires conducting plate-loading tests with circular plates that are 30 in. in diameter, as per ASTM D1196. Due to geometric constraints of the testing setup, the circular plate was replaced by an 11.3 x 11.3-in. rectangular plate, as shown in Figure 6-3. The plate was bolted to a self-adjusting fixture that prevented any bending while testing. The load and deflection increments of the Instron machine were collected through a data-acquisition system from which the pressure vs. deflection curve of the compacted backfill layer was constructed. The pressure vs. deflection plot is shown in Figure M-1. Inspection of Figure M-1 reveals that the subgrade modulus reaction of the compacted CA6 layer was around 324 psi/in. This value was derived from the slope of the tangent at a plate-contact pressure of 10 psi, as specified by ACI Committee 360 (1992). Due to the nonlinear behavior of the soil, more data points were required to obtain a linear trend for calculating the subgrade modulus (Tarr and Farny, 2008). Therefore, the load was increased until 15-psi plate pressure was achieved. The compacted backfill material showed an almost linear behavior for pressure values greater than 10 psi, which is consistent with the description of Barker and Alexander (2012) for granular materials.



Figure 6-3. Test setup of subgrade modulus reaction for the compacted CA6 layer.

6.7.1.2 Concrete-Mix Design and Concrete Placement

Two 6 ft³ concrete mixes were batched to cast the jointed-slab within the forms, as shown in Figure 6-4. IDOT pavement mixes designated “PVF1-8lbs” were considered with 8 lbs./cu-yd of Strux 90/40. The amount of fibers provided for this specimen was determined in accordance with the fatigue testing program described and discussed in sections 5.5 and 6.4, respectively. From each mix, four beams and five cylinders were cast and tested for flexural and compressive strength at 1-, 2-, and 7-d concrete age. A ½-in. gap between the pavement specimen and the steel form was maintained to avoid direct contact, as shown in Figure 6-5. Dynamic modulus tests were also conducted, as per ASTM C215 for beam and cylinder specimens, to estimate the concrete strength at the time of every static load testing. Cylinder and beam specimens used for dynamic modulus tests were kept at ambient lab temperatures to achieve a similar exposure condition.

As shown in Figure 6-4, the jointed-slab specimen represents a 24-in. strip of a 6-in. rigid pavement. To achieve the required placement, spacers were used to position the dowels at the mid-height (3 in.) with 12-in. spacing.

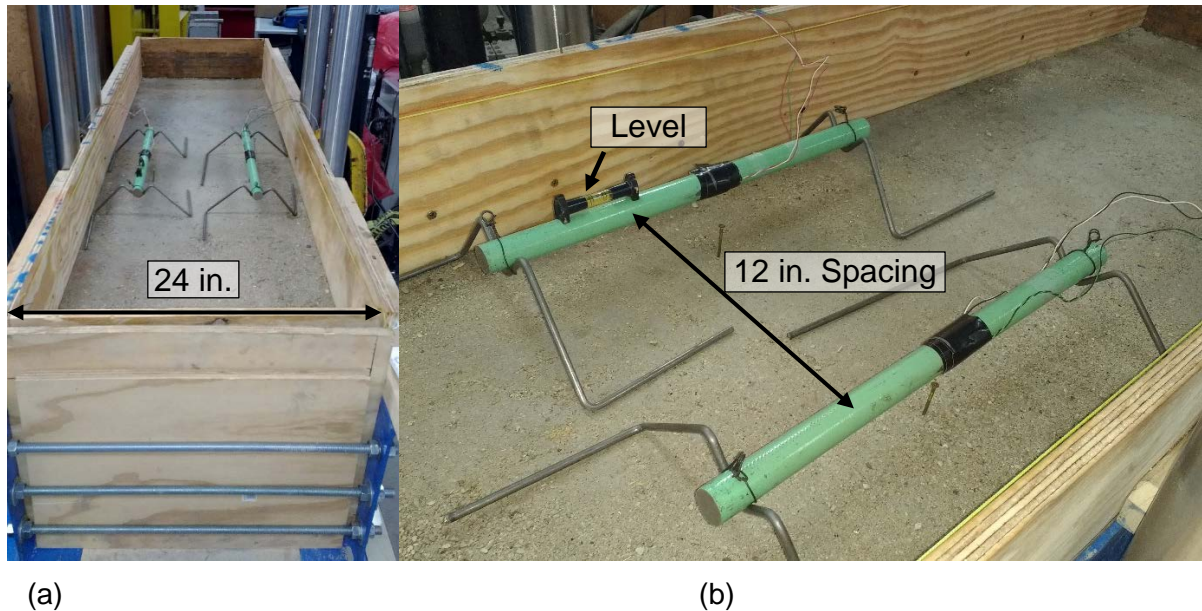


Figure 6-4. Form enclosure (a) and dowel-bar placement (b).



Figure 6-5. Jointed-slab specimen after demolding, showing ½-in. offset from the steel form.

A 2-in. groove was created with a ¼-in. offset from the loading plate, as shown in Figure 6-6. The groove was made by using a 0.07-in. steel plate, in accordance with Standard 420001-08, *Standard specifications for road and bridge construction, IDOT (2016)*. The steel plate was greased and then removed after 12 hr from casting the specimen. The fresh properties of the mixes are presented in Table A-1.

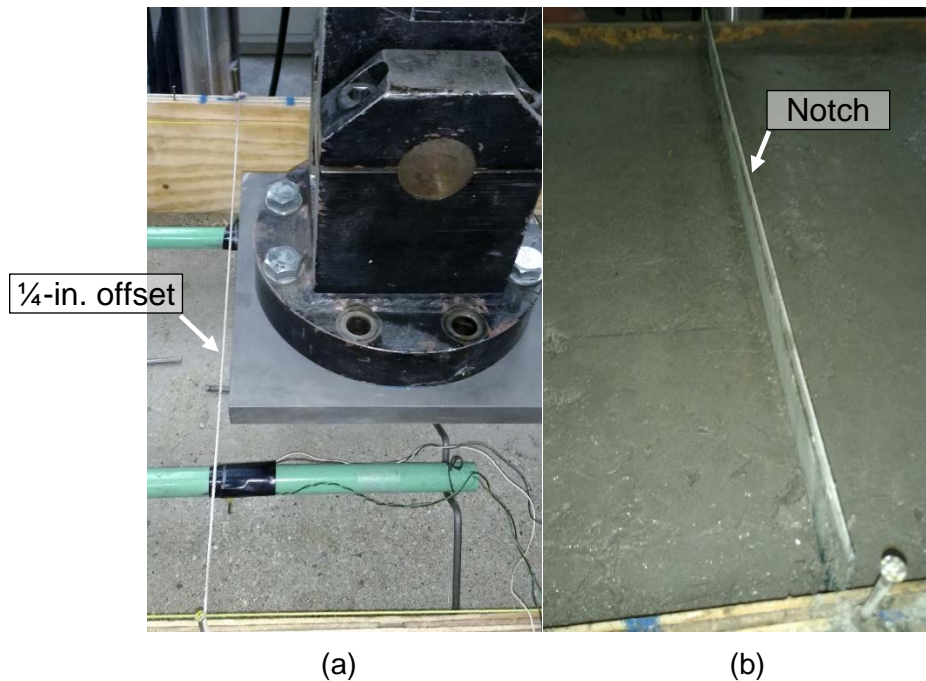


Figure 6-6. Groove position (a) and placement after casting (b).

6.7.1.3 Testing Setup for Static Loading

The joint effectiveness (E) and the load-transfer efficiency (LTE) for static tests were evaluated as per Equations 5.28 and 5.29. Four LVDTs with a 25-mm (1-in.) capacity were installed at the corners of the groove to record any differential displacement between the loaded and unloaded portions of the slab. In addition to joint parameters calculations (E and LTE), the average value of the four LVDT readings was used to evaluate the maximum deflection of the specimen at peak loads and the residual deflection after unloading. The LVDTs were installed with magnetic bases fixed at the steel enclosure to ensure consistent readings at every static test. The instrumentation setup for jointed-slab specimens is shown in Figure 6-7.

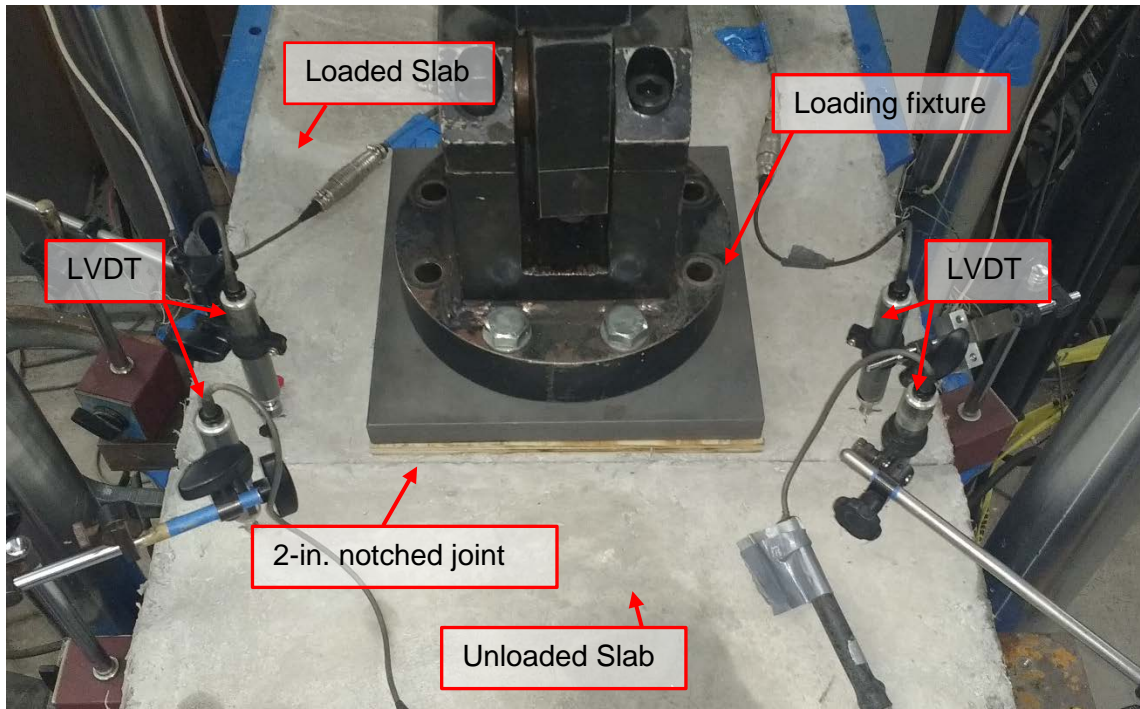


Figure 6-7. Instrumentation setup during static testing for the jointed-slab specimen.

6.7.1.4 Loading Schedule

Static and cyclic fatigue loading were applied on the casted specimen at 1-d concrete age from 2/11/2017 to 2/28/2017. Cyclic loading was applied with a rate of 4 Hz, in accordance with the fatigue testing program of sections 5.5 and 5.6, to induce consistent fatigue damage. Static loading was applied with a stroke rate of 0.02 in./min to measure the relative displacement between the loaded and unloaded slabs after a predetermined number of applied cyclic loads. The structural performance of the joint was then evaluated in terms of transfer efficiency parameters LTE and E , as described in section 5.8.2. Joint performance was considered adequate when LTE and E parameters maintained a value greater than 60 and 75%, respectively, after 1 million cyclic loads with $\frac{1}{2}$ ESAL.

The loading schedule consisted of five segments: The first segment consisted of 2.3 million cyclic loads, with a maximum load of $\frac{1}{2}$ ESAL (9 kip, 70-psi plate-contact pressure), as described in section 5.8.2. In Segment 2, the test was extended with a 50% increase in the maximum applied load (13.5 kip, 106-psi plate-contact pressure) for 1 million cycles of fatigue loading. To induce deterioration in the jointed specimen, six monotonic loads with increasing peaks were applied in Segment 3. These loads represented a low-cycle fatigue regime with peak values ranging from 24 kip (188-psi plate-contact pressure) to 40 kip (313-psi plate-contact pressure). These monotonic loads were followed by Segment 4, which included applying 1 million cycles of fatigue loading with a maximum load of 30 kip (235-psi plate-contact pressure). The test included one final loading segment that considered a maximum load of 36 kip (282-psi plate-contact pressure). Segment 5 consisted of 1 million cycles. In total, the loading regime

combined 5.3 million cycles of fatigue loads and 42 static load tests. The loading regime schedule and characteristics for the jointed-slab specimen are presented in the Table M-2.

6.7.1.5 Experimental Test Results for Segment 1 (0–2.3 Million Cycles)

Segment 1 of the loading regime was applied over a 6.6-d period with 2.3 million cycles of fatigue loads and thirteen static load tests. Loading started with static testing to evaluate the initial joint transfer-efficiency parameters LTE and E . Load-deflection relationships are presented in Figure M-2 for the first applied static load. Inspection of Figure M-2 shows that the deflection for the loaded and unloaded slab is similar, with a maximum deflection of 0.024 in. at a load of 9 kip. This observation corresponds to an initial LTE and E of 100%. The results also reveal that the specimen did not experience any crack initiation during load ramping because the slopes of the load-deflection curves were monotonic with no sudden change. The remaining 12 static tests were conducted in the same manner and yielded similar load-deflection relationships to Figure M-2. The experimental results of Segment 1 satisfied the aforementioned requirements of section 5.8.3 with no significant loss in transfer efficiency, as the joint remained rigid ($LTE/E > 90\%$ at 1 million cycles). The jointed-slab specimen did, however, experience settlement due to added compaction of the backfill layer. In addition, deflection development with respect to the number of fatigue cycles is presented in Figure M-3 for the maximum applied load (9 kip) and at rest (0 kip), with the latter corresponding to residual settlement. An inspection of Figure M-3 reveals that the maximum deflection at 9 kip ranged from 0.024 to 0.057 in., with residual deflection at 0 kip ranging from 0.009 to 0.046 in. Static load testing results for Segment 1 are listed in Table M-3. The test results reveal that settlement values increased at a high rate in the early stages of testing. It can also be noticed that cyclic loading produced similar deflection values after 500,000 cycles, with a small increase in settlement. Moreover, the development of concrete compressive and flexural strength corresponding to the time at which every static test was conducted is presented in columns 6 and 7 of Table M-3. Strength readings were estimated empirically by conducting dynamic modulus tests in addition to conducting actual strength measurements at 1-, 2-, and 7-d concrete age.

6.7.1.6 Experimental Test Results for Segment 2 (2.3–3.3 Million Cycles)

The second loading segment was applied over a 3-d period. For Segment 2, a 50% increase in the maximum applied load was considered for static and cyclic tests, to accelerate joint-fatigue damage. This segment consisted of 1 million cyclic fatigue loads and eight static tests. The static tests were performed at the end of a predefined number of fatigue cycles, as shown in Table M-4. Similar to Segment 1, the specimen did not show significant deterioration or loss of transfer efficiency. The static testing schedule of Segment 2 and the corresponding maximum and minimum deflections are presented in Table M-4. Deflection development with respect to the number of cycles is also presented in Figure M-4. The maximum deflection at 13.5 kip ranged from 0.058 to 0.062 in., while the residual deflection after unloading ranged between 0.046 and 0.050 in. The data presented show that an additional 0.004 in. of settlement occurred in the backfill layer due to the 50% increase in peak load.

6.7.1.7 Experimental Test Results for Segment 3

The main objective of Segment 3 was to study the behavior of a cracked specimen, as seen in the literature review in section 2.4.4. Loading was composed of six consecutive static tests applied over 50 min, with a stroke rate of 0.02 in./min, for loading and unloading. The load development with respect to the average deflection readings of the four LVDTs is shown in Figure M-5. During this testing sequence, visual inspection was carried out to track any crack development. The first loading attempt reached a peak load of 24 kip (188-psi plate-contact pressure) with no cracking being observed. Then, a higher peak load was considered for the second cycle (28 kip, 219-psi plate-contact pressure), where cracking eventually did occur beneath the joint area at the bottom layer of the slab. Loading was increased until reaching the fifth cycle (40 kip, 313-psi plate-contact pressure) with no additional cracking being observed. Moreover, no significant deterioration in the jointed specimen was recorded as *LTE* (96%) and *E* (98%) remained unchanged throughout loading Segment 3. The results of test Segment 3 are summarized in Table M-5. The table includes deflection values at peak loads and at unloading. The results show that a 0.012-in. settlement occurred in the backfill layer due to additional compaction for higher loads.

6.7.1.8 Experimental Test Results for Segment 4 (3.3–4.3 Million Cycles)

Segment 4 of the loading regime was applied over a 3-d period. This phase consisted of 1 million cyclic fatigue loads and seven static load tests. The maximum applied load for the cyclic fatigue and the static loads was 30 kip. Deflection and settlement measurements for Segment 4 are listed in Table M-6. The development of deflection with respect to the number of cycles is shown in Figure M-6. Inspection of the experimental results shows that a settlement of 0.035 in. was added to the overall deflection of the specimen due to the compaction of the backfill layer. Initiation of new cracks had occurred in the specimen after 100,000 cycles in Segment 4. Cracking occurred beyond the dowel-bar region of the loaded slab as a result of the added compaction beneath the loaded area of the specimen. However, the joint remained in a rigid state with no significant decrease in *LTE* and *E* measurements.

6.7.1.9 Experimental Test Results for Segment 5 (4.3–5.3 Million Cycles)

The last segment of the loading regime was applied over a period of 3-d. Segment 5 included 1 million cyclic fatigue loads and eight static load tests. The maximum applied load was increased to 36 kip for static and cyclic fatigue testing. Deflection at the peak loads and residual deflection measurements of Segment 5 are listed in Table M-7. In addition, deflection development with respect to the number of cycles is presented in Figure M-7. An observation of the experimental results reveals an additional settlement of 0.020 in. for the backfill layer. By the end of Segment 5, no additional loss in transfer efficiency was recorded as *LTE* and *E* remained unchanged.

6.7.1.10 Crack Initiation and Propagation

Visual inspection near the loaded area of the jointed-slab specimen was carried out to record any crack initiation and development throughout the loading schedule. The cracking pattern is presented in Figure M-8 in the elevation views on the tested specimen. In Segment 1 of the loading regime, the first cracks initiated beneath the groove of the joint after 250,000 cycles

with a maximum applied load of ½ ESAL (9 kip). Crack propagation near the groove area was recorded during the second cycle of Segment 3 at 28 kip. These hairline cracks had no significant effect on the efficiency of the joint. Additional cracking occurred in Segment 4 during cyclic fatigue testing with a maximum load of 30 kip. These cracks initiated near the dowel ends of the loaded slab after 100,000 cycles. The development of such cracks can be attributed to the excessive compaction of the loaded area, which allowed more deflection and eventually created a plane of weakness near the dowel-bar end region. This added deflection had no apparent effect on the efficiency of the joint. In addition, the failure mode of the concrete layer specimen 1 was shown to be in flexure, where cracks developed from the bottom layer and did not propagate to the top of the concrete layer due the presence of 8 lb/yd³ of synthetic fibers.

6.7.1.11 Summary and Conclusions (Specimen 1)

A jointed-concrete-pavement slab with two dowel bars was constructed and tested. The pavement slab was 2 ft x 7 ft x 6 in. and was subjected to early-age loading at 1-d concrete age. The experimental findings of the first conducted testing can be summarized as follows:

- Early-age loading at 1-d concrete age yielded no loss of transfer after applying 1 million cycles with a maximum load of ½ ESAL (9 kip). The load-transfer efficiency (LTE= 96%) and the joint effectiveness (E= 98%) values corresponded to a rigid joint behavior.
- Joint deterioration was observed only after gradually increasing the maximum applied cyclic load from 9 to 36 kip over a span of 5.3 million cycles. By the end of the test, *LTE* and *E*, respectively, reached 92 and 96%, which is well above the ACPA design standards (60 and 75%, respectively). It can be concluded that the system remained rigid, with no significant relative displacement being recorded between the loaded and unloaded slab.
- Settlement of 0.117 in. was recorded by the end of the test underneath the contraction joint. This added deflection was due to the added compaction of the subgrade layer from the applied static and cyclic loads, which lead to the creation of a plane of weakness near the dowel-end region of the loaded slab.

6.7.2 Jointed-Slab Specimen 2

The following section covers the experimental results of the second jointed-slab specimen. Specimen 2 consisted of a 6-in., plain-concrete, doweled (1-in. diameter), jointed-slab, as per Table M-1.

6.7.2.1 Subgrade Layer Preparation and Subgrade Modulus Reaction Measurement

The CA6 material was refilled, dampened, and compacted again for the second jointed-slab specimen. This adjustment was done to account for the excessive compaction from the previous test. Accordingly, the subgrade modulus reaction was measured by recording the contact pressure from the loading plate (11.3 x 11.3 in.) with respect to the Instron machine deflection. Plate pressure development with respect to deflection is presented in Figure M-10. Similarly to section 6.7.1.1, the subgrade modulus reaction was measured as the slope of the

near-linear portion of the curve for plate pressures ranging from 10 to 15 psi. An investigation of the pressure-deflection curve reveals a subgrade modulus reaction of 395 psi/in.

6.7.2.2 Concrete-Mix Design and Concrete Placement

Two 7-ft³ concrete mixes were batched according to the plain-concrete PV mix. Pouring was done in a 2 ft x 7 ft x 6 in. form enclosure, and in seven 6 x 6 x 21 in. prisms. The fresh properties of the concrete mixture for Specimen 2 are listed in Table A-1. Concrete strength was tracked with regular compressive and flexural strength tests at 1-, 2-, 3-, and 7-d concrete age. In addition, dynamic modulus tests were carried out at each static loading test to predict the modulus of rupture. Concrete pouring was conducted in a removable steel enclosure, as seen in Figure 6-8. These steel channels ensured an even slab surface and allowed for improved finishing. Dowel-bar placement and groove positioning were conducted as described in section 6.7.1.2.



Figure 6-8. Compacted soil within removable steel enclosure added for Specimen 2.

6.7.2.3 Testing Setup for Static Loading

Joint deterioration was measured with intermediate static loading tests after an elapsed number of cyclic loads, as per section 5.8.2.5. The four LVDTs used for this task were elevated on a rigid steel frame, as shown in Figure 6-9, to eliminate any interference that might occur while conducting monotonic loading tests. Moreover, the jointed-slab specimen was constrained at both ends of the loaded and unloaded slab to prevent any vertical translation during static/cyclic loading. Prior to specimen casting, four PMFL-60-2LJRTA embedded strain gauges were positioned at the joint location and at the dowel-end region of the loaded slab, as shown in Figure 6-10 to record any crack initiation/propagation throughout static loading tests. Strain-gauge placement was based on the findings of section 6.7.1.10 for the first jointed specimen. Accordingly, two strain gauges positioned at 1 and 3 in. from the bottom pavement

layer were installed at the groove region. Another two strain gauges were installed at 1 and 5 in. from the bottom pavement layer at the dowel-end region.

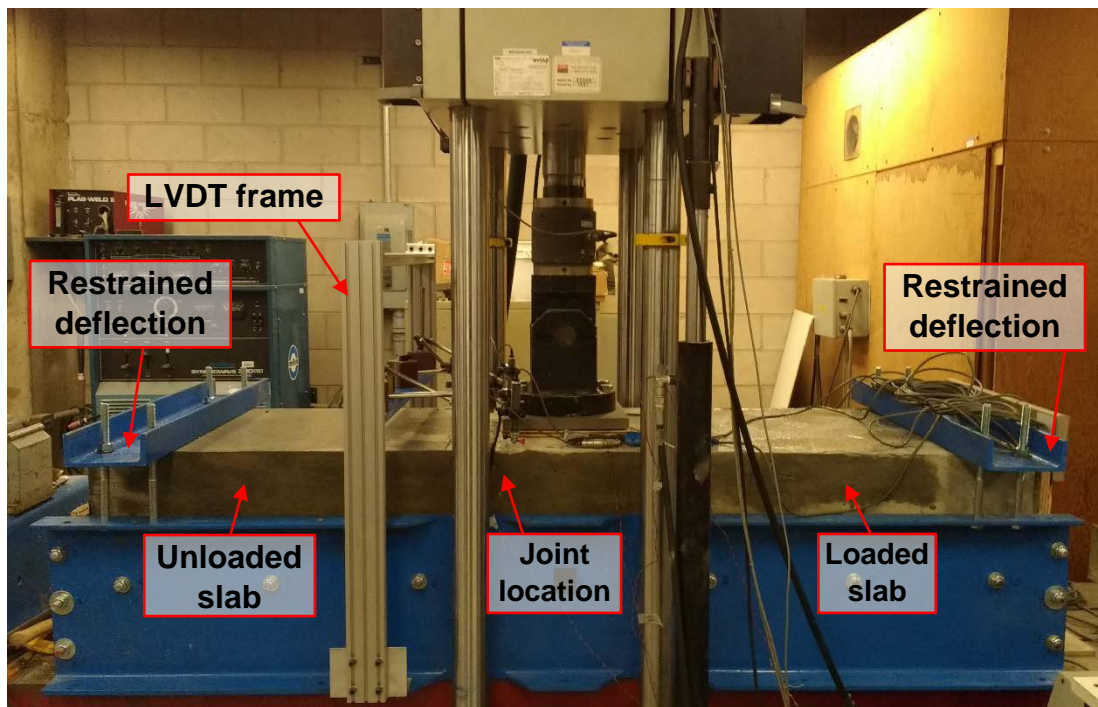
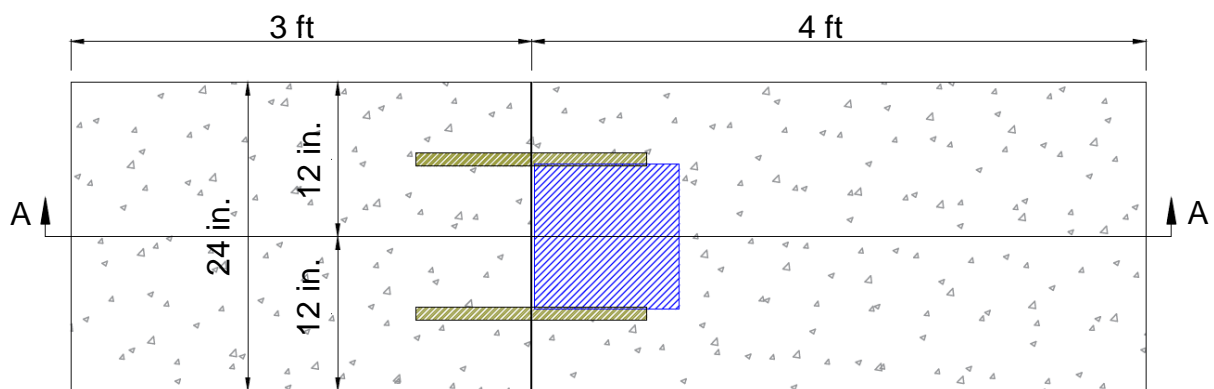
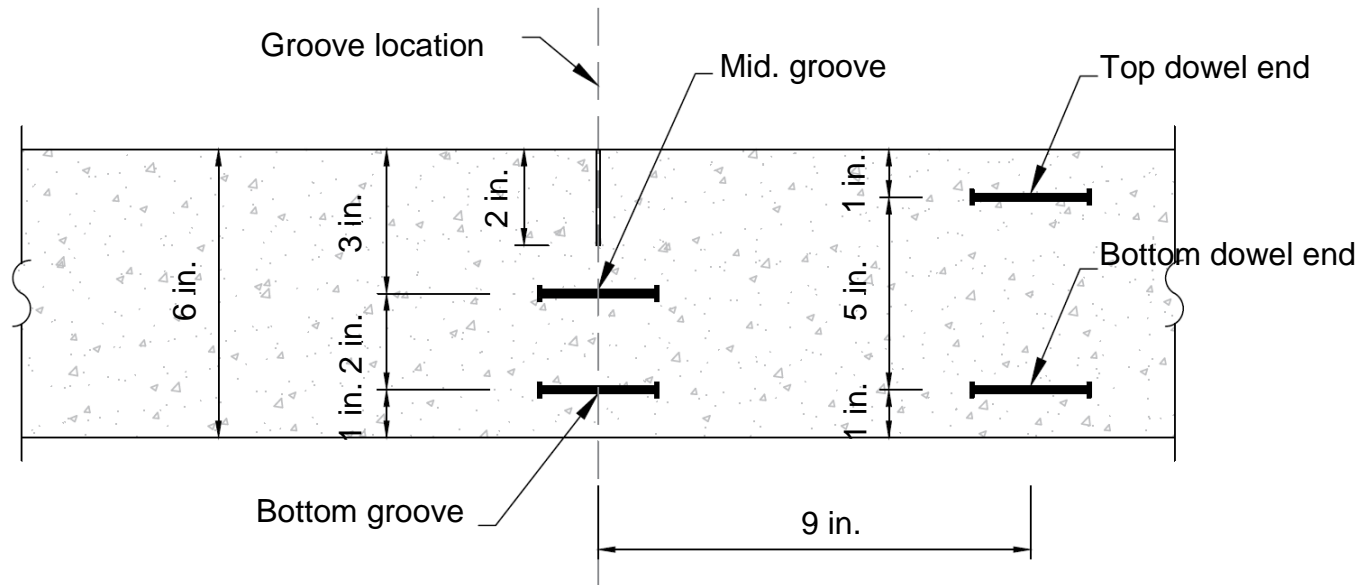


Figure 6-9. Specimen 2 testing setup.



(a) Plan view



(b) Section A-A elevation view

Figure 6-10. Embedded strain-gauge placement near the groove and at the dowel-end area (Specimen 2).

6.7.2.4 Loading Schedule

Static and cyclic fatigue loading was applied from 6/1/2017 to 6/7/2017 on the casted specimen once it attained 1-d concrete strength. Cyclic loading was applied with a frequency of 4 Hz, while static loading was applied at a rate of 0.02 in./min. The loading schedule included three segments: The first segment consisted of 1 million loading cycles at $\frac{1}{2}$ ESAL (9 kip, 70 psi plate-contact pressure). After attaining 1 million cycles in Segment 1, the maximum applied static/cyclic load was increased by 50% in Segment 2. This second segment was applied for another 1 million cycles (13.5 kip, 106-psi plate-contact pressure). A monotonic load (44 kip, 344-psi plate-contact pressure) was finally applied to obtain the failure mode of Specimen 2. A summary of the loading schedule is presented in Table M-9.

6.7.2.5 Experimental Test Results for Testing Segment 1 (0–1 Million Cycles)

Segment 1 of the loading regime was applied over a 2.9-d period with 1 million cycles of fatigue loads and nine static load tests. Typical flexural strength values for concrete PV mixes ranged from 436 to 477 psi at 1-d concrete age (section 6.2.2.1). Accordingly, loading was postponed to 1 d and 12 hr of concrete age with a closely estimated flexural strength of 427 psi. This delay was made to account for the low flexural strength estimated at 375 psi at 1-d concrete age. Load versus deflection of the first applied static load is shown in Figure M-11 (a). A maximum applied load of $\frac{1}{2}$ ESAL (9 kip) resulted in a 0.004-in. average deflection and a residual deflection of 0.002 in. The specimen was subjected to a second monotonic load to account for the large residual deflection of the first loading. Loading development with respect to deflection for the second cycle is shown in Figure M11 (b), where the loaded and unloaded slab reveal 100% transfer (*LTE*, *E*). In addition, strain development at the groove and at the dowel-end regions for

the first and second static loading tests is presented in Figure M-12. An investigation of these figures reveals a maximum tensile strain of $50\ \mu\epsilon$ at the bottom dowel-end region and a maximum compressive strain of $30\ \mu\epsilon$ at the top dowel-end region. The strain development curves reveal that no cracking occurred throughout the first two monotonic loads. Hairline cracking was visually noticed near the groove region only after 500,000 cyclic loads (2-d, 23-hr concrete age). Deflection development with respect to the number of applied cyclic loads is presented in Figure M-12. An investigation of Figure M-12 reveals that the deflection at the maximum applied load ($\frac{1}{2}$ ESAL) ranged from 0.004 to 0.012 in., while residual deflection at unloading ranged from 0.002 to 0.007 in. Moreover, deflection values and the corresponding flexural strength for every static test instance are presented in Table M-10. Segment 1 of the loading schedule resulted in satisfactory structural performance, as crack initiation at the groove area did not affect joint transfer. The maximum tensile strain reading was located at the bottom dowel-end region, where strain development with respect to the number of applied cyclic loads is presented in Figure M-13. Inspection of Figure M-13 reveals that tensile strain ranged from 54 to 74 $\mu\epsilon$ at the maximum applied load ($\frac{1}{2}$ ESAL), while residual tensile strain at unloading ranged from 10 to 39 $\mu\epsilon$.

6.7.2.6 Experimental Test Results for Testing Segment 2 (1–2 Million Cycles)

The second segment of the loading schedule was applied over a 3-d period with a maximum applied load of 13.5 kip (50% load increase) for static/cyclic loading. This segment consisted of eight static loading tests and 1 million cyclic loads. A summary of the second loading segment is presented in Table M-11, which includes deflection and concrete flexural strength measurements for every static test. Segment 2 deflection measurements revealed an increased specimen deflection with no loss in transfer at the joint region. Deflection development with respect to the number of applied cyclic loads is presented in Figure M-15. An investigation of Figure M-15 reveals that the deflection at the maximum applied load (13.5 kip) ranged from 0.014 to 0.023 in., while residual deflection at unloading ranged from 0.007 to 0.016 in. In addition, tensile strain development is presented in Figure M-16 for the dowel-end region. Tensile strains are shown to range from 92 to 113 $\mu\epsilon$ at a maximum applied load of 13.5 kip, while residual strains ranged from 39 to 63 $\mu\epsilon$ at unloading.

6.7.2.7 Experimental Test Results for Testing Segment 3

With no joint deterioration being measured after 2 million applied cyclic loads (Segments 1 and 2), Segment 3 included a single monotonic loading test to induce cracking. The monotonic load was applied at a rate of 0.02 in./min for a maximum value of 44 kip (344-psi plate pressure). Visual inspection revealed that cracking initiated near the dowel-end region on both ends of the jointed-slab at around 34 kip. The load-deflection relationship of Segment 3 is presented in Figure M-17. The trend reveals that cracking load (34 kip) corresponded to a deflection of 0.028 in. A residual deflection of 0.022 in. was recorded after unloading the 44-kip load. The jointed region of Specimen 3 remained rigid, with no loss in LTE of E values at the peak load of 44 kip. Concrete-strain development with respect to loading at the dowel-end region is presented in Figure M-18. An observation of the strain development reveals that cracking had occurred upon reaching a load of 34 kip. This state corresponds to a tensile strain of 236 $\mu\epsilon$, after which a sudden drop in strain measurement was observed with the increased load.

6.7.2.8 Crack Initiation and Propagation

The cracking pattern for Specimen 2 is presented in Figure M-19 in the elevation view for both sides of the jointed-slab. Hairline cracking initiated at the groove location in the first loading segment (9 kip) after 500,000 cyclic loads. Cracking in loading Segment 1 did not affect joint performance, as LTE and E values remained above 90%. Major cracking in Segment 3 (34-kip load) occurred only at the dowel-end region. The mode of failure in these cracks is shown to be in flexure, as crack initiation occurred at the bottom concrete layer (Figure M-20). Table M-12 presents cracking instances for Specimen 2.

6.7.2.9 Summary and Conclusions (Specimen 2)

Experimental results for the second jointed-slab specimen can be summarized as follows:

- Similarly to Specimen 1, early-age loading (1-d concrete *strength*) yielded no loss of transfer after applying 1 million cycles with a maximum load of $\frac{1}{2}$ ESAL (9 kip). The joint effectiveness ($E = 91\%$) and the load-transfer efficiency ($LTE = 95\%$) remained well above the allowable limits.
- An increase in the maximum applied static/cyclic load (50%) did not result in loss of transfer after an additional 1 million applied loading cycles. Failure was achieved by monotonic loading at 34 kip, with flexural failure being observed at the dowel-end region of the loaded slab.

6.7.3 Jointed-Slab Specimen 3

The following section describes the structural performance of the third jointed-slab specimen at early-age loading. The third specimen consisted of a 6-in., fiber-reinforced (8 lb yd³), undoweled jointed-slab, as per Table M-1.

6.7.3.1 Subgrade Layer Preparation and Subgrade Modulus Reaction Measurement

The CA6 material was refilled, dampened, and compacted again for the third tested jointed-slab specimen. This adjustment was done to account for the excessive compaction from the previous test. Accordingly, the subgrade modulus reaction was measured by recording the contact pressure from the loading plate (11.3 x 11.3 in.) with respect to the Instron machine deflection. Plate pressure development with respect to deflection is presented in Figure M-21. Similarly to section 6.7.1.1, the subgrade modulus reaction was measured as the slope of the near-linear portion of the curve for plate pressures ranging from 10 to 15 psi. An investigation of the pressure-deflection curve reveals a subgrade modulus reaction value of 405 psi/in.

6.7.3.2 Concrete-Mix Design and Concrete Placement

Two 7 ft³ concrete mixes were batched according to IDOT pavement mixes designated “PVF1-8lbs.” Pouring was done in a 2 ft x 7 ft x 6 in. form enclosure, and in eight 6 x 6 x 21 in. prisms. The fresh properties of the concrete mixture for Specimen 3 are listed in Table A-1. Concrete strength was tracked with regular compressive- and flexural strength tests at 1-, 2-, 3-, and 7-d concrete age. In addition, dynamic modulus tests were carried out at each static loading test to

predict the modulus of rupture at the time of loading. The groove was constructed as described in section 6.7.1.2.

6.7.3.3 Testing Setup for Static/Cyclic Loading

The structural performance of Specimen 3 was conducted as per section 5.8.2.5. In addition to vertical restraint at the ends of the jointed-slab, the experimental testing setup for Specimen 3 included lateral anchorage to simulate the continuity of actual paved sections. The anchorage was achieved by using two threaded rods at the mid-height of the concrete layer from both ends of the specimen, as shown in Figures 6-11 and 6-12. The threaded rods (5/8-in. diameter) were embedded at 2 ft from the loaded and unloaded ends of the specimen, as shown in Figure 6-13 (a). The rods were anchored to 8 x 20 x 1 ½ in steel plates that were rigidly connected to the steel bed of the Instron testing machine. Specimen 3 also included six embedded strain gauges (PMFL-60-2LJRTA) to track stress development and crack initiation/propagation throughout the loading phase. Strain-gauge placement is presented in Figure 6-13 (b) in the elevation view.

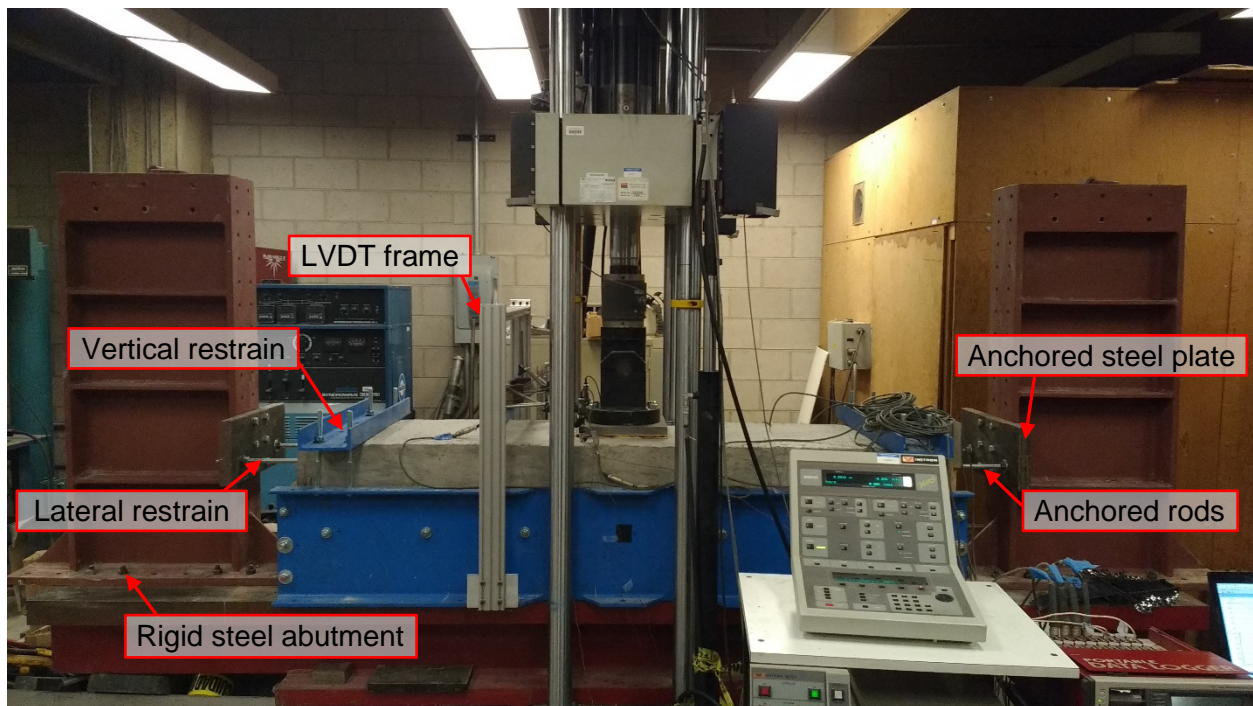


Figure 6-11. Specimen 3 testing setup.

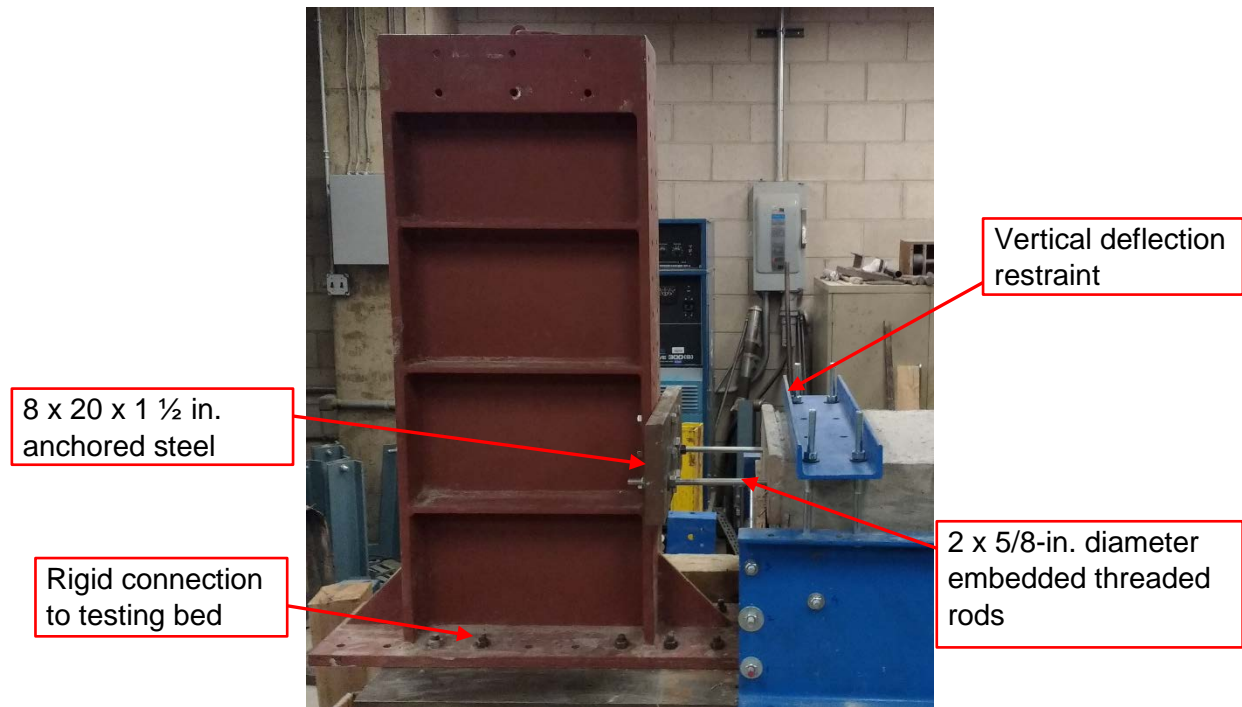
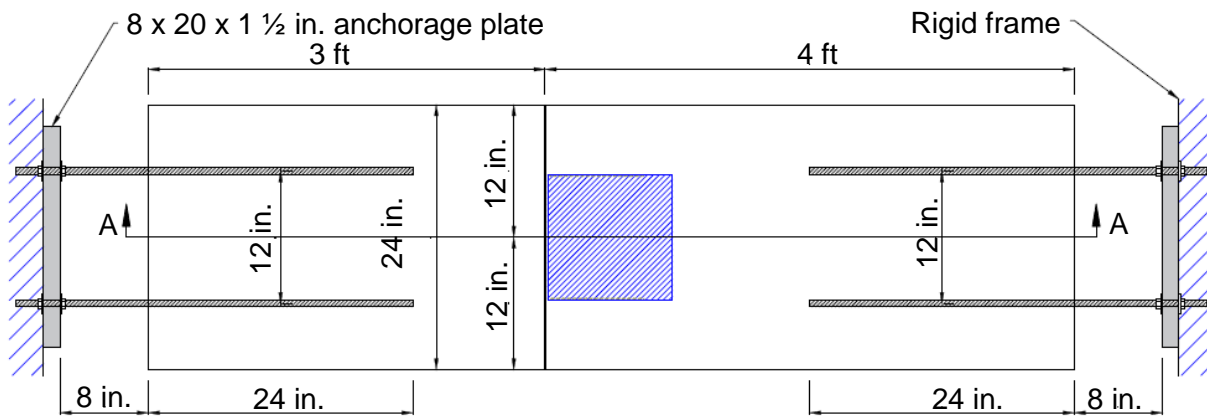


Figure 6-12. Lateral and vertical deflection restraint.



(a) Plan view

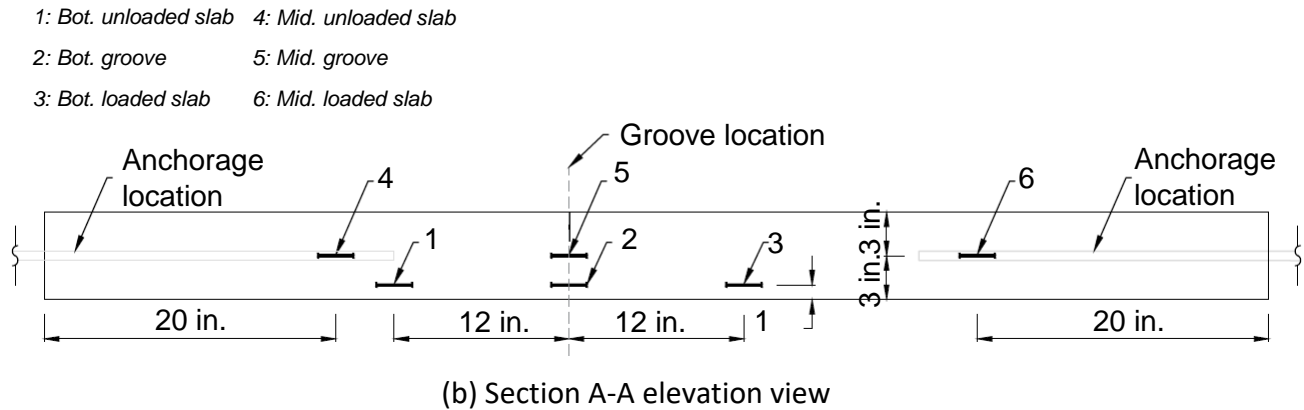


Figure 6-13. Specimen 3 testing setup showing anchorage system (a) and embedded strain-gauge placement (b).

6.7.3.4 Loading Schedule

Static and cyclic fatigue loading was applied on the casted specimen once it attained 1-d concrete strength, from 6/29/2017 to 7/5/2017. Cyclic loading was applied with a frequency of 4 Hz, while static loading was applied at a rate of 0.02 in./min. The loading schedule included three segments: The first segment consisted of 1 million loading cycles at $\frac{1}{2}$ ESAL (9 kip, 70 psi plate-contact pressure). After attaining 1 million cycles in Segment 1, the maximum applied static/cyclic load was increased by 50% in Segment 2. This second segment was applied for another 1 million cycles (13.5 kip, 106 psi plate-contact pressure). A monotonic load (44 kip, 344 psi plate-contact pressure) was finally applied to obtain the failure mode of Specimen 3. A summary of the loading schedule is presented in Table M-13.

6.7.3.5 Experimental Test Results for Testing Segment 1 (0–1 Million Cycles)

Segment 1 of the loading regime was applied over a 3-d period with 1 million cycles of fatigue loads and eleven static load tests. The loading sequence for Specimen 3 was postponed to 1-d, 18-hr of concrete age to achieve the required flexural strength (493 psi). This delay was done to account for the 1-d flexural strength (331 psi), which did not attain the typical strength at 1-d concrete age for PV mixes (436–477 psi, as per section 6.2.2.1). Load versus deflection of the first applied static load is shown in Figure M-22. A maximum applied load of $\frac{1}{2}$ ESAL (9 kip) resulted in a 0.008 in. average deflection and a residual deflection of 0.004 in. Inspection of Figure M-22 reveals a differential displacement between the loaded and unloaded slab (0.0087 in., 0.0075 in.), due to the large initial settlement of the first loading cycle. The differential settlement decreased for the following cycles until reaching a similar loading curve as presented in M-22 (b) for cycle 100. In addition, concrete-strain development with respect to loading is presented in Figure M-23 for the first loading cycle and the 100th loading cycle at the groove region of Specimen 3. Inspection of Figure M-23 (a) reveals that tensile strain reached $36 \mu\epsilon$, while compressive strain reached $50 \mu\epsilon$ at 9 kip. Figure M-23 (b) reveals that tensile strains ranged from 13 to $42 \mu\epsilon$, while compressive strains ranged from 15 to $55 \mu\epsilon$, after 100

applied cycles. Deflection development with respect to the number of applied cyclic loads is presented in Figure M-24. An investigation of Figure M-24 reveals that the deflection at the maximum applied load ($\frac{1}{2}$ ESAL) ranged from 0.008 to 0.018 in., while residual deflection at unloading ranged from 0.004 to 0.015 in. Moreover, deflection values and the corresponding flexural strength for every static test instance is presented in Table M-14. Specimen 3 showed a satisfactory performance by the end of loading Segment 1 with no significant loss of *LTE* (94%) and *E* (97%), and no cracking at the concrete layer.

6.7.3.6 Experimental Test Results for Testing Segment 2 (1–2 Million Cycles)

The second segment of the loading schedule was applied over a 3-d period with a maximum applied load of 13.5 kip (50% load increase) for static/cyclic loading. This segment consisted of seven static loading tests and 1 million cyclic loads. A summary of the second loading segment is presented in Table M-15, which includes deflection and concrete flexural strength measurements for every static test. Segment 2 deflection measurements revealed an increased specimen deflection with no loss in transfer at the joint region. Deflection development with respect to the number of applied cyclic loads is presented in Figure M-25. An investigation of Figure M-25 reveals that the deflection at the maximum applied load (13.5 kip) ranged from 0.020 to 0.027 in. while residual deflection at unloading ranged from 0.015 to 0.021 in.

6.7.3.7 Experimental Test Results for Testing Segment 3

With no joint deterioration being measured after 2 million applied cyclic loads (Segments 1 and 2), Segment 3 included a single monotonic loading test to induce cracking. The monotonic load was applied at a rate of 0.02 in./min for a maximum value of 44 kip (344 psi plate pressure). Visual inspection revealed that cracking initiated underneath the loading plate region on both ends of the jointed-slab at around 21.5 kip. The load-deflection relationship of Segment 3 is presented in Figure M-26. The trend reveals that the cracking load (21.5 kip) corresponds to a deflection of 0.029 in. A residual deflection of 0.061 in. was recorded after unloading the 44 kip load. The jointed region of Specimen 3 remained rigid with no loss in *LTE* of *E* values at the peak load of 44 kip.

6.7.3.8 Crack Initiation and Propagation (Specimen 3)

The cracking pattern for Specimen 3 is presented in Figure M-27 in the elevation view for both sides of the jointed-slab. Cracking initiated underneath the loaded region in Segment 3 (21.5 kip). These cracks initiated at 8 $\frac{1}{2}$ and 11 in. from the groove in the loaded segment of Specimen 3. Cracking did not affect joint performance, as *LTE* and *E* values remained above 90%. The mode of failure in these cracks is shown to be in flexure, as crack initiation occurred at the bottom concrete layer (Figure M-28).

6.7.3.9 Summary and Conclusions (Specimen 3)

Experimental results for the third jointed-slab specimen can be summarized in the following:

- Similarly to specimens 1 and 2, for Specimen 3, early-age loading (1-d concrete *strength*) yielded no loss of transfer after applying 1 million cycles with a maximum load of $\frac{1}{2}$ ESAL

(9 kip). This was evident in the joint effectiveness ($E = 97\%$) and load-transfer efficiency ($LTE = 94\%$) measurements after 1 million cyclic loads.

- An increase in the maximum applied static/cyclic load (50%) did not result in loss of transfer after an additional 1 million applied loading cycles. Failure was achieved by monotonic loading at 21.5 kip, with flexural failure being observed underneath the loading plate.

6.7.4 Jointed-Slab Specimen 4

The following section describes the experimental results of the fourth jointed-slab specimen. The specimen consisted of a 6-in., fiber-reinforced (4 lb/yd³) pavement with two dowels (1-in. diameter) at the location of the saw-cut joint, as per Table M-1.

6.7.4.1 Subgrade Layer Preparation and Subgrade Modulus Reaction Measurement

The CA6 material was refilled, dampened, and compacted again for the fourth tested jointed-slab specimen. This adjustment was done to account for the excessive compaction from the previous test. Accordingly, the subgrade modulus reaction was measured by recording the contact pressure from the loading plate (11.3 x 11.3 in.) with respect to the Instron machine deflection. Plate pressure development with respect to deflection is presented in Figure M-29. Similarly to section 6.7.1.1, the subgrade modulus reaction was measured as the near-linear portion of the curve for plate pressures, ranging from 5 to 10 psi. An investigation of the pressure-deflection curve reveals a subgrade modulus reaction value of 316 psi/in.

6.7.4.2 Concrete-Mix Design and Concrete Placement

Two 7-ft³ concrete mixes were batched according to IDOT pavement mixes designated “PVF1.” Pouring was done in a 2 ft x 7 ft x 6 in. form enclosure, and in seven 6 x 6 x 21 in. prisms. The fresh properties of the concrete mixture for Specimen 4 are listed in Table A-1. Concrete strength was tracked with regular compressive and flexural strength tests at 1-, 2-, 3-, and 7-d concrete age. In addition, dynamic modulus tests were carried out at each static loading test to predict the modulus of rupture at the time of loading. Dowel-bar placement and groove positioning were conducted as described in section 6.7.1.2.

6.7.4.3 Testing Setup for Static Loading

The structural performance of Specimen 4 was conducted as per section 5.8.2.5. Prior to static/cyclic loading, cracking at the groove location was initiated by using 7-wire strands (0.6 in. dia.) that were embedded at the mid-height of the concrete layer (3 in.). Strand placement and instrumentation is presented in Figure 6-15 for Specimen 4. The prestressing wires were positioned 6 in. away from the saw-cut region such that the crack would initiate at the plane of weakness without interfering with the relative displacement of the joint. Embedded strain gauges (PMFL-60-2LJRTA) were positioned at the corners the jointed region to monitor crack initiation and to ensure consistent prestressing on both ends of the specimen. This process was achieved at 20 hours of concrete age using a prestressing system shown in Figure 6-16. After crack initiation at the groove location, the four strands were cut to prevent additional crack opening during static/cyclic loading tests (Figure 6-17).

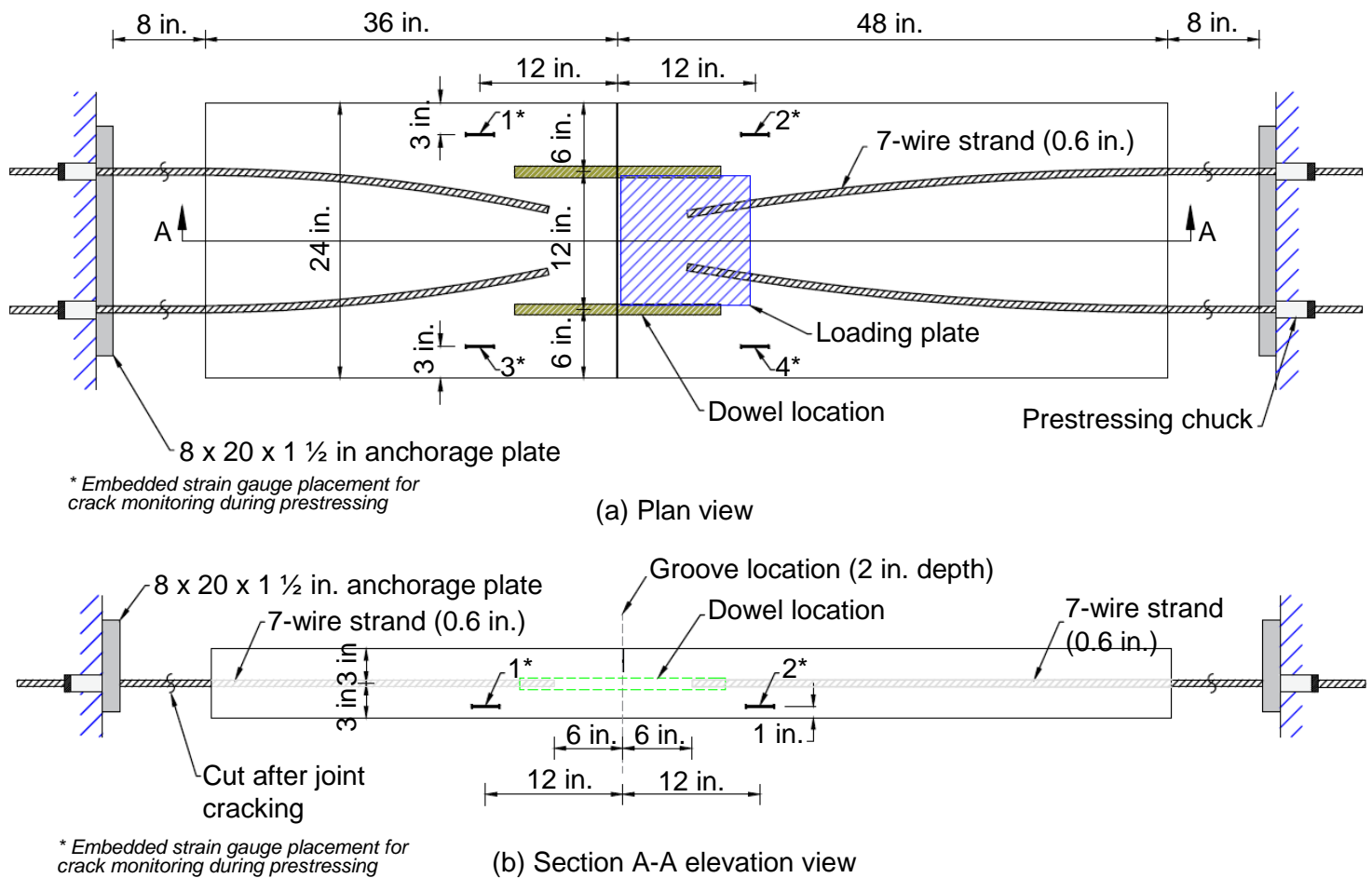


Figure 6-15. Specimen 4 testing setup showing anchorage system and strain-gauge placement in the plan view (a) and the elevation view (b).

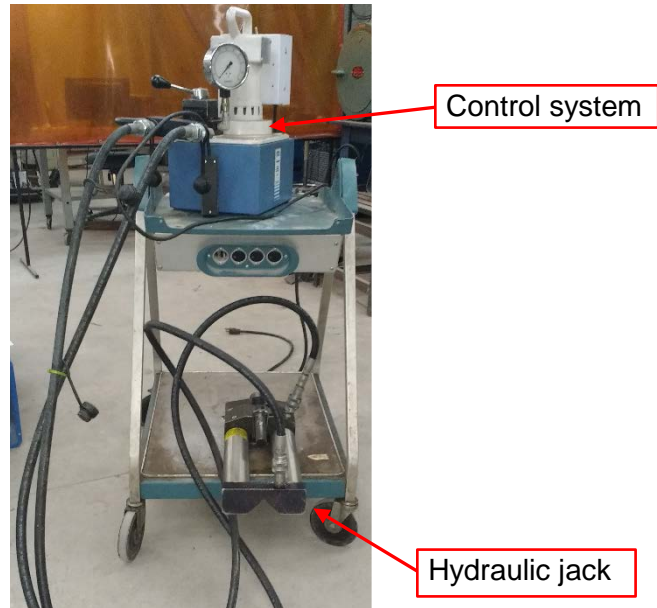


Figure 6-16. Prestressing system used for Specimen #4.

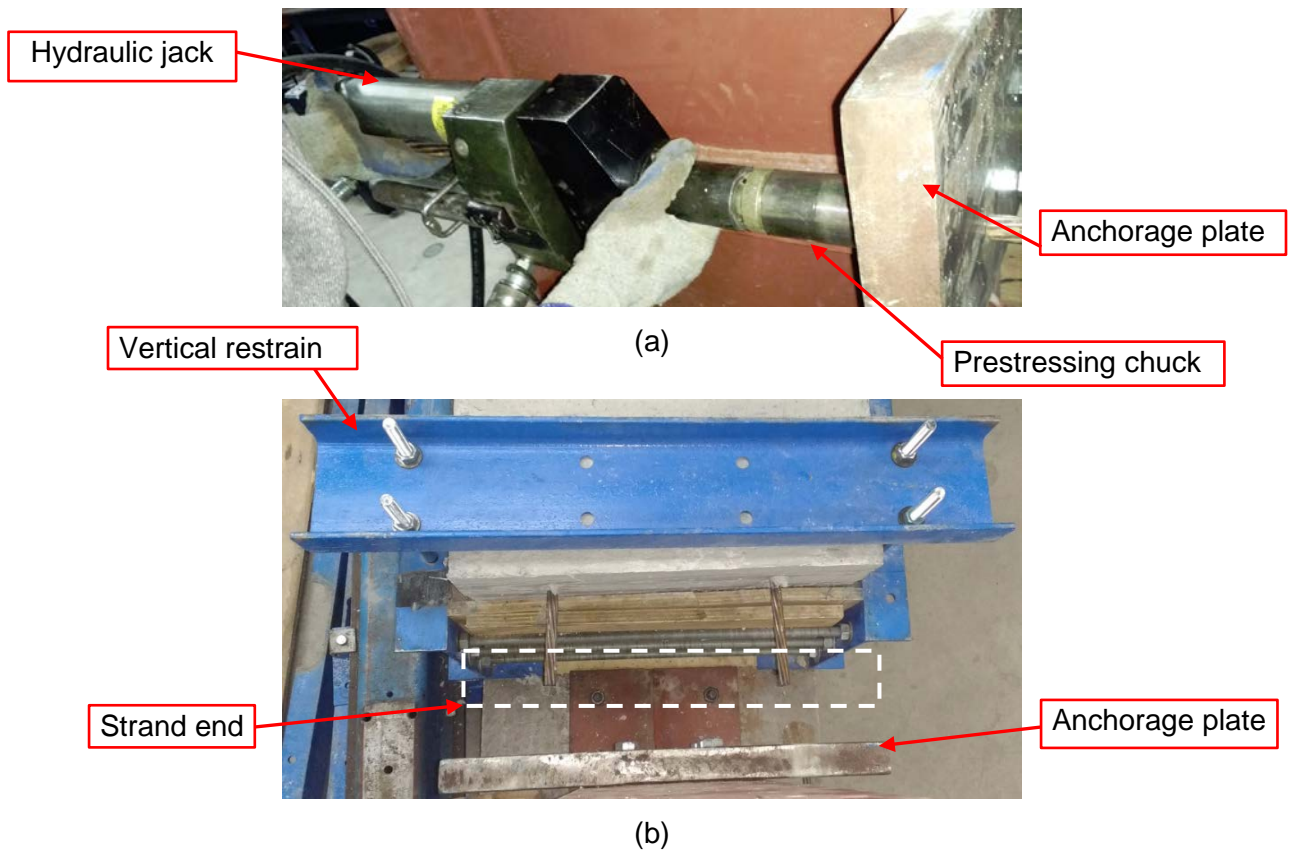


Figure 6-17. Prestressing procedure (a) and specimen boundary condition after strand cutting (b) (Specimen 4).

6.7.4.4 Loading Schedule

Static and cyclic fatigue loading was applied on the casted specimen once attaining 1-d PV concrete strength from 7/18/2017 to 7/27/2017. Cyclic loading was applied with a frequency of 4 Hz while static loading was applied at a rate of 0.02 in./min. The loading schedule included two segments: The first segment consisted of 1 million loading cycles at ½ ESAL (9 kip, 70 psi plate-contact pressure). After attaining 1 million cycles in Segment 1, the maximum applied static/cyclic load was increased by 50% in Segment 2. This second segment was applied for another 2 million cycles (13.5 kip, 106 psi plate-contact pressure). A summary of the loading schedule is presented in Table M-16.

6.7.4.5 Experimental Test Results for Testing Segment 1 (0-1 Million Cycles)

Segment 1 of the loading regime was applied over a 3-d period with 1 million cycles of fatigue loads and nine static load tests. Load-deflection relationships are presented in Figure M-30 for the first applied static load. The load-deflection curves reveal that the loaded and unloaded slabs had similar response with maximum deflection of 0.022 in. at a load of 9 kip. This corresponds to an initial LTE and E of 100%. The remaining eight static tests were conducted in the same manner and yielded similar load-deflection patterns of Figure M-30. The load versus deflection curve deflection development with respect to the number of applied cyclic loads is presented in Figure M-31. An investigation of Figure M-31 reveals that the deflection at the maximum applied load (1/2 ESAL) ranged from 0.022 to 0.049 in. while residual deflection at unloading ranged from 0.006 to 0.021 in. Moreover, deflection values and the corresponding flexural strength for every static test instance is presented in Table M-17. No significant loss of transfer was measured at the end of loading Segment 1 with *LTE* and *E* remaining close to 100%.

6.7.4.6 Experimental Test Results for Testing Segment 2 (1-2 Million Cycles)

Segment 2 of the loading regime was applied over a 6-d period with 2 million cycles of fatigue loads and eleven static load tests. Deflection development with respect to the number of applied cyclic loads is presented in Figure M-32. An investigation of Figure M-32 reveals that the deflection at the maximum applied load (13.5 kip) ranged from 0.052 to 0.063 in. while residual deflection at unloading ranged from 0.021 to 0.033 in. Moreover, deflection values and the corresponding flexural strength for every static test instance is presented in Table M-18. Similarly to Segment 1, no deterioration was measured after the application of 2 million cyclic loads by the end Segment 2 (*LTE*, *E* ≈ 100%).

6.7.4.7 Crack Initiation and Propagation

The cracking pattern for Specimen #4 is presented in Figure M-33 in the elevation views of the jointed-slab. Cracking initiated at the joint area prior to static/cyclic loading to simulate the effect of curling stresses in newly paved concrete sections. These cracks did not affect joint performance, as *LTE* and *E* values remained close to 100% by the end of 3 million applied cyclic loads.

6.7.4.8 Summary and Conclusions (Specimen 4)

Experimental results for the fourth jointed-slab specimen can be summarized in the following:

- Similarly to Specimen #1, #2, and #3, for Specimen 4, early age loading (1-d concrete age) yielded no loss of transfer after applying 1 million cycles with a maximum load of ½ ESAL (9 kip). The joint effectiveness ($E=99\%$) and load-transfer efficiency ($LTE=98\%$) measurements indicated limited fatigue damage at the jointed region.
- A 50% increase in the maximum applied static/cyclic load (13.5 kip) did not result in loss of transfer after an additional 2 million applied loading cycles.

6.7.5 Jointed-Slab Specimen 5

The following section describes the experimental results of the fifth jointed-slab specimen. The specimen consisted of an 8-in., fiber-reinforced (8 lb yd³) pavement with two dowels (1.25-in. diameter) at the location of the saw-cut joint, as per Table M-1.

6.7.5.1 Subgrade Layer Preparation and Subgrade Modulus Reaction Measurement

The CA6 material was refilled, dampened, and compacted again for the fifth tested jointed-slab specimen. The backfill layer was reduced to 10 in. to account for the increased thickness of the PCC layer (8 in.) This adjustment was made such that no forming modifications were needed prior to concrete placement. Accordingly, the subgrade modulus reaction was measured by recording the contact pressure from the loading plate (11.3 x 11.3 in.) with respect to the Instron machine deflection. Plate pressure development with respect to deflection is presented in Figure M-35. Similarly to section 6.7.1.1, the subgrade modulus reaction was measured as the near-linear portion of the curve for plate pressures, ranging from 5 to 10 psi. An investigation of the pressure-deflection curve reveals a subgrade modulus reaction value of 219 psi/in. This value corresponded to a decreased level of compaction, as recommended by the technical review panel.

6.7.5.2 Concrete-Mix Design and Concrete Placement

Three 7 ft³ concrete mixes were batched according to IDOT pavement mixes designated “PVF1-8lbs.” Pouring was done in a 2 ft x 7 ft x 8 in. form enclosure, twelve 6 x 6 x 21 in. prisms, and sixteen 6 x 12 cylinders. The fresh properties of the concrete mixture for Specimen 5 are listed in Table A-1. Concrete strength was tracked with regular compressive and flexural strength tests at 1-, 2-, 3-, and 7-d concrete age. In addition, dynamic modulus tests were carried out at each static loading test to predict the modulus of rupture at the time of loading. Dowel-bar placement and groove positioning were conducted as described in section 6.7.1.2.

6.7.5.3 Testing Setup for Static Loading

The structural performance of Specimen 5 was conducted as per section 5.8.2.5. Prior to static/cyclic loading, cracking at the groove location was initiated by using 7-wire strands (0.6 in. dia.) that were embedded at the mid-height of the concrete layer (4 in.). Strand placement and instrumentation is presented in Figure 6-18 for Specimen 5. The 8 x 20 x ½ in. anchorage

plates were lowered from the previous testing setup (Section 6.7.4.3) to account for the added thickness of the PCC layer (8 in.).

This process was achieved at 24 hours of concrete age as intended for PCC cracking due to curling stresses. After crack initiation at the groove location, the four strands were cut to prevent additional crack opening during static/cyclic loading tests (Figure 6-17).

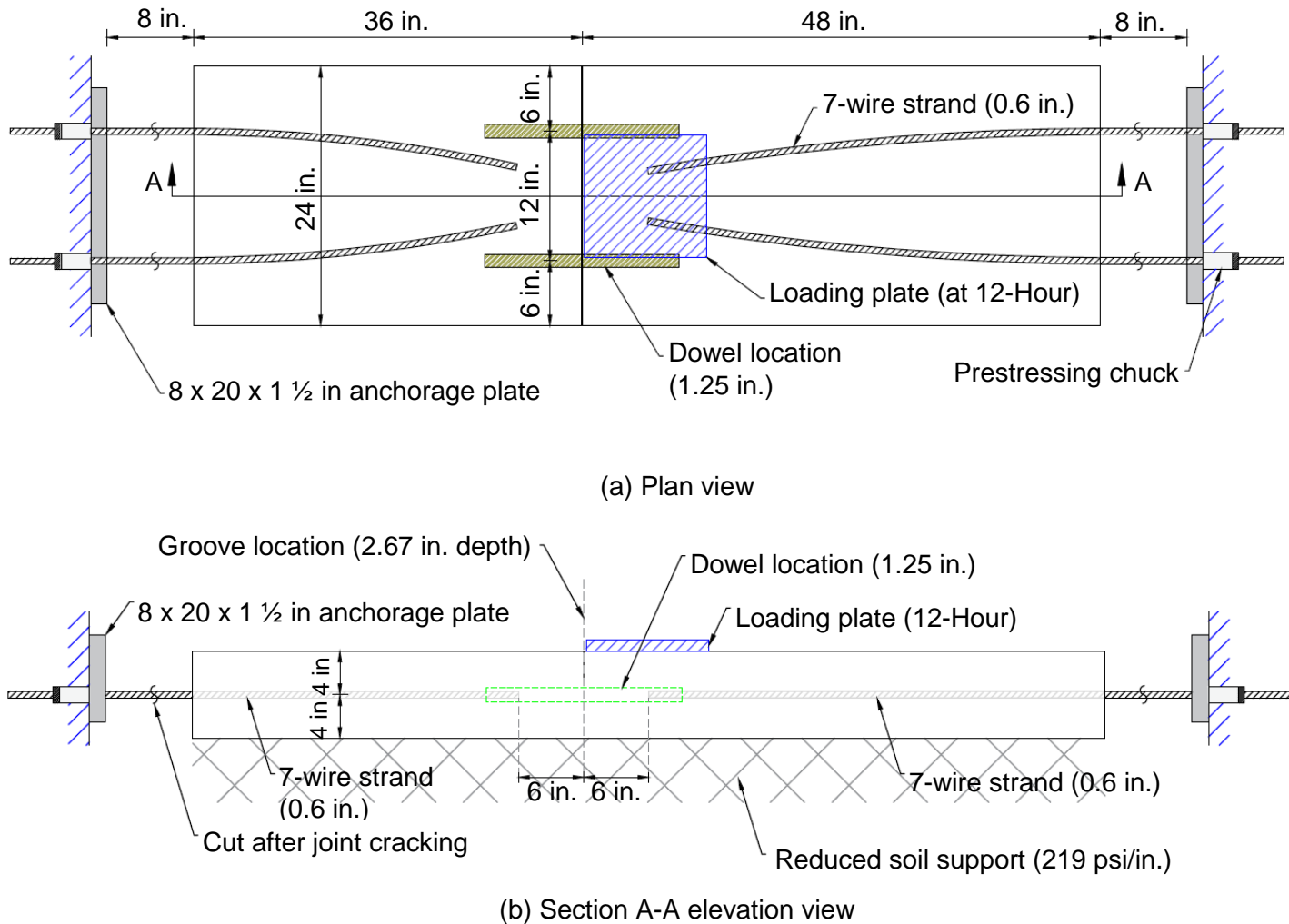


Figure 6-18. Specimen #5 testing setup showing anchorage system in the plan view (a) and the elevation view (b).

6.7.5.4 Loading Schedule

Static and cyclic fatigue loading was applied on the casted specimen once attaining 12-Hr PV concrete strength from 9/24/2017 to 10/10/2017. Cyclic loading was applied with a frequency of 4 Hz, while static loading was applied at a rate of 0.02 in./min. The loading schedule included five segments: The first segment consisted of 1.2 million loading cycles at $\frac{1}{2}$ ESAL (9 kip, 70 psi plate-contact pressure). After attaining 1 million cycles in Segment 1, the maximum applied static/cyclic load was increased by 50% in Segment 2 (13.5 kip, 105 psi plate-contact pressure).

The load amplitude was later increased with the application of every one million loading cycles. In total, Specimen 5 was subjected to 5.2 million loading cycles. The maximum applied load ranged from ½ ESAL (9 kip, 70 psi plate-contact pressure) to 4 ESALs (36 kip, 280 psi plate-contact pressure). A summary of the loading schedule is presented in Table M-19.

6.7.5.5 Experimental Test Results for Testing Segment 1 (0-1.2 Million Cycles)

Segment 1 of the loading regime was applied over a 3.5-d period with 1.2 million cycles of fatigue loads and nine static load tests. Load-deflection relationships are presented in Figure M-36 for the first applied static load. The load-deflection curves of the first static load reveal that the loaded and unloaded slabs had similar response with maximum deflection of 0.016 in. at a load of 9 kip. This relative deflection corresponded to an initial *LTE* and *E* of 93 % and 96 %, respectively. The load versus deflection curve deflection development with respect to the number of applied cyclic loads is presented in Figure M-37. An investigation of Figure M-37 reveals that the deflection at the maximum applied load (1/2 ESAL) ranged from 0.016 to 0.067 in. while residual deflection at unloading ranged from 0.011 to 0.053 in. A significant increase in deflection is noticed after prestressing operations (150,000 cycles, 1-d concrete age). This response is attributed to crack initiation at the groove location, which allowed for additional relative displacement between the loaded and unloaded slabs and increased overall specimen deflection. Moreover, deflection values and the corresponding flexural strength for every static test instance is presented in Table M-20. No significant loss of transfer was measured at the end of loading Segment 1 with *LTE* (89%) and *E* (94%) remaining well above the acceptable ACPA limits (60% and 75% respectively).

In an attempt to accelerate the damage process of the jointed specimen, a number of loading segments were added with increasing peak loads. Segment 2 to 5 are described in the following sections:

6.7.5.6 Experimental Test Results for Testing Segment 2 (1.2-2.2 Million Cycles)

Segment 2 of the loading regime was applied over a 3-d period with 1 million cycles of fatigue loads and eight static load tests at 13.5 kip (¾ ESAL, 105 psi plate-contact pressure). Deflection development with respect to the number of applied cyclic loads is presented in Figure M-38. An investigation of Figure M-38 reveals that the deflection at the maximum applied load (13.5 kip) ranged from 0.067 to 0.080 in. while residual deflection at unloading ranged from 0.053 to 0.064 in. Moreover, deflection values and the corresponding flexural strength for every static test instance is presented in Table M-21.

6.7.5.7 Experimental Test Results for Testing Segment 3 (2.2-3.2 Million Cycles)

Segment 3 of the loading regime was applied over a 3.1-d period with 1 million cycles of fatigue loads and eight static load tests at 18 kip (1 ESAL, 140 psi plate-contact pressure). Deflection development with respect to the number of applied cyclic loads is presented in Figure M-39. An investigation of Figure M-39 reveals that the deflection at the maximum applied load (18 kip) ranged from 0.083 to 0.094 in. while residual deflection at unloading ranged from 0.064 to 0.072 in. Moreover, deflection values and the corresponding flexural strength for every static test instance is presented in Table M-22.

6.7.5.8 Experimental Test Results for Testing Segment 4 (3.2-4.2 Million Cycles)

Segment 4 of the loading regime was applied over a 3-d period with 1 million cycles of fatigue loads and eight static load tests at 27 kip (1½ ESALs, 210 psi plate-contact pressure). Deflection development with respect to the number of applied cyclic loads is presented in Figure M-40. An investigation of Figure M-40 reveals that the deflection at the maximum applied load (27 kip) ranged from 0.097 to 0.129 in. while residual deflection at unloading ranged from 0.071 to 0.097 in. Moreover, deflection values and the corresponding flexural strength for every static test instance is presented in Table M-23.

6.7.5.8 Experimental Test Results for Testing Segment 5 (4.2-5.2 Million Cycles)

Segment 5 of the loading regime was applied over a 3-d period with 1 million cycles of fatigue loads and eight static load tests at 36 kip (2 ESALs, 280 psi plate-contact pressure). Deflection development with respect to the number of applied cyclic loads is presented in Figure M-41. An investigation of Figure M-41 reveals that the deflection at the maximum applied load (36 kip) ranged from 0.131 to 0.194 in. while residual deflection at unloading ranged from 0.074 to 0.139 in. Moreover, deflection values and the corresponding flexural strength for every static test instance is presented in Table M-24.

6.7.5.9 Crack Initiation and Propagation

The cracking pattern for Specimen #5 is presented in Figure M-42 in the elevation views of the jointed-slab. Cracking was initiated at 1-d concrete age to simulate the effect of curling stresses in newly paved concrete sections. No further cracking occurred within the loading sequences of specimen #5 despite excessive loading and increased slab deflection of the specimen. In addition, crack widths remained small as shown in Figure M-43 during slab removal.

6.7.5.10 Summary and Conclusions (Specimen 5)

Experimental results for the fifth jointed-slab specimen (8 in. - 219 psi/in. - 8 lbs./cu-yd - Doweled) can be summarized in the following:

- A decreased support condition ($K = 219 \text{ psi./in.}$) resulted in added overall slab deflection without affecting joint performance.
- Early age loading at 12-Hr yielded minimal loss of transfer after applying 1 million cycles with a maximum load of ½ ESAL (9 kip). The joint effectiveness ($E = 94\%$) and load-transfer efficiency ($LTE = 89\%$) measurements indicated limited fatigue damage at the jointed region.
- An increase in the maximum applied static/cyclic load (up to 36 kip) did not contribute to specimen deterioration. However, the overall slab deflection measurements have increased.

6.7.6 Summary of Jointed-Slab Performance – All Specimens

The structural performance of all constructed jointed-slab specimens is summarized and discussed in the following section. As of October, 2017, all 6 in. slabs were constructed and tested at 1-d PV concrete strength in accordance with section 5.8.2. An additional specimen with increased PCC thickness (8 in.) was also included for the experimental task. The main experimental differences between the specimens are presented in Table M-19. Slabs were constructed with doweled or non-doweled joints, and with different amounts of synthetic fibers (0, 4, 8 lb/yd³). Table M-19 also presents the subgrade modulus reaction values for every testing iteration. It is observed that k values reasonably ranged from 316 to 405 psi/in for the for the 6 in. specimens while Specimen 5 was constructed with decreased support (219 psi/in).

In an effort to improve the experimental approach for JPCP cyclic fatigue behavior, the boundary conditions of the constructed specimens were adjusted and alternated with each testing iteration. An additional alternative included restraining the specimens at the edges in the lateral direction (Specimen 3) and vertical direction (Specimen 2, 3, 4, and 5) during testing setup. Table M-20 lists these experimental considerations with respect to cracking instances at the groove location; the table includes crack development, cracking age, boundary restrains, and joint conditions for each constructed specimen. An observation of Table M-20 reveals that cracking at the groove location occurred at 1.73-d (Specimen 1) and 3-d (Specimen 2) of concrete age for specimens that were not pre-cracked. The cracking ages of Specimen 1 and Specimen 2 are shown to be acceptable as crack instances range from 0.2-d to 2.2-d when sawing at 1/3 the PCC depth (Wang et al., 2009). While proper crack development did occur for Specimens 1 and 2, no cracking was observed within the loading segments of Specimen 3. However, it should be noted that no shrinkage cracks occurred within the loaded region of Specimen 3 despite vertical and lateral boundary constraints. Based on this observation, curling stresses were simulated in the construction of Specimens 4 and 5. Specimens 4 and 5 were subjected to prestressing to induce tensile cracking at the groove location as illustrated in section 6.7.4.3 and 6.7.5.3. Moreover, Specimen 4 was not restrained in the lateral direction in order to avoid additional crack widening during loading segments.

The structural performance of all specimens is summarized in Table M-21 at 1 million cyclic loads as per section 5.8.3. The table includes the load-transfer efficiency (LTE) and joint efficiency (E) parameters evaluated at $\frac{1}{2}$ ESAL (9 kip). The table also includes the differential displacement between the loaded and unloaded slab. An observation of the results shows that LTE values ranged from 89 to 98% while E values ranged from 94 to 99%. These high figures are shown to be well above the limit for LTE (60%) and E (75%) as per ACPA (1991), indicating that no considerable fatigue damage has occurred in the jointed region. The LTE and E development with respect to the applied load is presented in Figures M-45 through M-48 for all specimens after 1 million cyclic load. An inspection of these curves reveals that LVDT measurements yield more consistent deflection after a certain amount of applied load. The LTE/E values are then obtained at the peak applied load (9 kip) as recommended in section 3.3, ASTM D4694. Moreover, joint faulting at $\frac{1}{2}$ ESAL (9 kip) is shown to vary from 0.002 to 0.016 inches in Table M-21. Despite the increased overall pavement deflection, the relative deflection between the approach slabs (loaded) and leave slabs (unloaded) remained within the acceptable value (0.2 in) in accordance with section 53-2.03, *Bureau of Design and Environment Manual (BDE)*, IDOT (2016).

With the fabrication, construction, and testing of all five jointed slabs, the outcome of this ongoing experimental task can be summarized as follows:

- Opening newly paved PCC sections to high-traffic volumes at early concrete age is shown to be plausible: Five, full-scale, jointed segments constructed according to IDOT specifications yielded promising structural performance after the application of 1 million $\frac{1}{2}$ ESALs (9 kip). The jointed-slab specimens remained rigidly connected with adequate joint transfer performance: LTE ranged from 89 to 98% while E ranged from 94 to 99% which met the ACPA (1991) requirements ($LTE = 60\%$, $E = 75\%$).
- IDOT standards for joint faulting were met for all tested specimens: Relative deflection values ranged from 1.97×10^{-4} to 1.61×10^{-3} in, well within the allowed limit (0.2 in).
- No crack initiation occurred within the region of the loaded slabs at $\frac{1}{2}$ ESAL (9kip): As cracking develops at the groove location, the loaded region (approach slab) becomes more susceptible to higher stress concentration. Cracking beyond the dowel-bar region only occurred through high monotonic/cyclic loads, surpassing any conventional tire contact pressure.

The test represents a highly critical loading case thus making the findings of this experimental task conservative:

- Most specimens were constructed at the minimum design thickness of PCC pavements in the state of Illinois (6 in.).
- The specimens were unrestrained at the transverse boundaries. The continuity of the specimens is only representative of the actual slabs in the longitudinal direction, this case allows for additional deflection and therefore accelerated flexural fatigue damage at the bottom of the PCC layer.
- The traffic loads were simulated with a cyclic load at frequency of 4 Hz and a sinusoidal wave form ranging from 0.9 to 9 kips; the first one million cycles of applied $\frac{1}{2}$ ESALs were reached within 3 days, which greatly overestimates actual traffic volumes.
- While fiber inclusion does not directly affect strength characteristics, macro synthetic fibers showed promising structural benefits in jointed-slab performance as demonstrated in Specimen 3. Despite no crack initiation near the groove region, the non-doweled joint sustained 1 million cyclic fatigue loads at 1-d concrete PV strength with no flexural crack development in the region of the loaded slab.

CHAPTER 7: IMPLEMENTATION OF RESEARCH RESULTS

This section proposes an implementing action for research data in a practical procedure for construction practices that involve EOT. Dynamic modulus tests, flexural strength tests, numerical FEA data, and flexural fatigue life (N) results are utilized in this procedure.

7.1 INTRODUCTION

As recommended by the TRP in the June 28, 2016, progress meeting in Springfield, IL, the data collected from the experimental testing and numerical modeling programs are represented in a simple and practical procedure for possible implementation in field-construction practices. First, nondestructive measures such as E_D tests will be used because these tests proved to be reliable in accurately estimating concrete flexural strength. The estimated strength results, along with the expected developed stresses obtained from numerical modeling, will be used to estimate flexural fatigue performance. A decision can later be determined regarding opening newly constructed pavements to traffic.

7.2 PROCEDURE STEPS

The following procedure assumes that pavement design is predetermined by the engineer with the following known parameters:

- *PCC mix design:* Concrete mix-design proportions follow IDOT's pavement mixes designated "PV."
- *Subgrade modulus reaction:* A required parameter for classifying underlying soil conditions that is usually provided by the geotechnical report. The subgrade modulus reaction (K) is an essential parameter used in the mechanistic design method and in the modified AASHTO design method currently adopted by IDOT.
- *Pavement thickness:* The PPC thickness is determined as per chapter 54 of the IDOT *BDE Manual*.

7.2.1 Step I: Estimate flexural strength using nondestructive measures.

Current specifications of the *BDE* Article 53-3.01(b) mention that even though nondestructive testing (NDT) has significant advantages over destructive testing (DT), destructive measures are needed to ensure adequate strength assessment. For rigid PCC pavements, current practices involve conducting splitting tensile tests on 4- to 6-in. cored samples. The flexural strength is then estimated through empirical correlations. However, this method is not practical and does not address the case of early opening to traffic. Current IDOT monitoring practices can be significantly improved through considering dynamic modulus tests (E_D) as a substitute for coring samples from pavements, while still ensuring accurate strength assessment. Flexural strength versus dynamic modulus relations are presented in Figure N-1 for PV, PVF1, PVF2, and PVF1-8lbs mixes. Every reading in the plot represents a 6 x 6 x 21-in. beam that was subjected to the E_D test (ASTM C215) prior to the flexural bending test (ASTM C78). Concrete beams were tested

at 12-hr; 1-, 3-, and 7-d schedules. Investigation of Figure N-1 shows an excellent fitting curve with a high coefficient of correlation ($R^2 = 0.98$). Therefore, based on this promising outcome, Equation 7.1 was developed as a relationship between f_r and E_D readings and is recommended as a reliable reference for flexural strength prediction.

$$f_r = 49.86 e^{5.29 \cdot 10^{-4} E_D} \quad (7-1)$$

where f_r = modulus of rupture of concrete at any age, psi

E_D = dynamic modulus of concrete at any age, ksi

Consequently, estimating concrete flexural strength can be greatly simplified by implementing E_D tests: When paving new PCC sections, a desired number of concrete beams can be cast in 6 x 6 x 21 in. molds. The beams are cured in the same conditions as the newly constructed pavements to ensure resonant frequency readings that are representative of the actual pavement condition. The frequency readings are valid for concrete ages as early as 12 hr and can be performed using portable, heavy-duty data-acquisition systems such as the DK-5000 system currently used at the University of Illinois at Chicago.

7.2.2 Step II: Estimate flexural stresses in concrete pavement using analytical model results.

Numerical modeling was conducted by considering several design parameters to correlate development of tensile stresses with different PCC thicknesses and varying soil conditions, and for an increasing concrete age. Flexural stress results shown in Figures N-2 to N-11 represent the variation of tensile stresses with respect to the following parameters:

- *PCC thickness:* ranging from 6 to 16 in.
- *Underlying soil condition:* with modulus of subgrade reaction values ranging from soft soil ($k = 50$ psi/in.) to stiff soil ($k = 500$ psi/in.)
- Concrete age: at 12-hr; and 1-, 3-, and 7-d

Depending on the designed PCC layer thickness, underlying subgrade stiffness, and concrete age, the maximum tensile stresses due to ESAL (18 kip) can be predicted through the use of the charts shown in Figures N-2 through N-11. For every concrete age, the corresponding static modulus of elasticity (MOE) was assigned as a material property in the pavement model. Static MOE results were determined through empirical relations with compressive strength, as discussed in section 6.2.4 of the experimental program. These values are presented in Table N-1.

An alternative representation of the numerical analysis is given through the nomographs presented in Figures N-12 to N-15 for 12-hr; and 1-, 3-, and 7-d concrete age. Each nomograph consists of three logarithmic axes: The left axis is set for the subgrade modulus reaction (psi/in.), the right axis is set for pavement thickness (in.), and the intermediate axis represents the maximum tensile stress that can develop at the bottom layer of the PCC pavement due to ESAL load (18 kip). Evaluating tensile stresses can be done by connecting the subgrade reaction

value (left axis) and the pavement thickness (right axis) with a straight line. The stress value is then obtained by intersecting this line with the intermediate axis.

7.2.3 Step III: Estimate flexural fatigue life.

Estimating concrete fatigue life can be achieved by obtaining the stress level corresponding to the applied ESAL. The stress level (S) is calculated by dividing the generated tensile stresses obtained from the finite-element analysis (Step II) over the modulus of rupture of the concrete obtained through E_D tests (Step I) for a certain age; in other words:

$$S = \frac{\sigma_y}{f_r} \quad (7-2)$$

Where S = stress level ratio

σ_y = maximum tensile stress developed at the bottom of the PCC pavement due to ESAL load obtained from *Step II*, psi

f_r = modulus of rupture of concrete at a given age obtained from *Step I*, psi

Flexural fatigue performance can be evaluated through a number of cyclic loadings before failure (N). Section 6.4 discussed developing S - N relationships for that matter and concluded that concrete flexural fatigue performance can be significantly improved with the addition of synthetic fibers. Thus two linear-regression formulas were developed for both plain and fiber-reinforced concrete (FRC) mixes for every concrete age. Table N-2 summarizes the fatigue testing results presented in section 6.4.

The estimated lifetime from the moment of opening to traffic until failure can be obtained by converting the number of cycle results to a time-equivalent value as per Equation 7-3:

$$\text{Fatigue life (sec)} = N / 4 \quad (7-3)$$

where

N = number of cycles until failure

The outcome of *Step III* describes the pavement's readiness to be opened to traffic in a practical manner and will ultimately help decision making in field-construction practices. This step can be conducted on each testing-day schedule (12-hr; and 1-, 3-, and 7 d) until achieving a stress level low enough to ensure no significant fatigue damage is done after opening to traffic.

7.2.4 Procedure Summary

Implementation of results in field-construction practices can be summarized as follows:

- On the day of paving, cast at least eight concrete beams (6 x 6 x 21-in.).

- Maintain curing conditions for the cast beams similar to those of the newly constructed pavements.
- Unmold two beams at 12 hr and test for E_D .
- Estimate flexural f_r strength from E_D using Equation 7-1 or the plot shown in Figure N-1.
- Estimate the developed stresses using Figures N-2 to N-11 for the corresponding soil condition, pavement thickness, and concrete age. The same value for stress estimation can be obtained through the nomographs presented in Figures N-12 to N-15.
- Calculate the stress levels using Equation 7-2.
- Estimate fatigue performance using Table N-2 for either plain or fiber-reinforced concrete and convert the number of cycles to a time-equivalent value by using Equation 7.4.
- Repeat the same procedure for 1-, 3-, and 7-d concrete age until achieving a satisfactory fatigue life

7.3 NUMERICAL EXAMPLE

The following example represents a realistic case for early opening to traffic by considering:

- PPC thickness set to 7 in.
- Modulus of subgrade reaction set to 50 psi/in. to represent a case of poor subgrade, as mentioned in the mechanistic design method adopted by IDOT *BDE Manual (2016)*
- Concrete flexural strength development set to a low value to replicate realistic curing regimes that may not be ideal, such as construction during cold weather conditions

The example is presented with the aforementioned considerations to help designers in construction practices that are related to the subject of EOT in a simple manner:

1. Test two 6 x 6 x 21 in. concrete beams at 12 hr for E_D .

Unmold two beams at 12 hr

Test Beam 1:

mass = 28 kg

resonant transverse frequency = 1,050 Hz

The dynamic modulus is calculated using Equation 5-2, mentioned in section 5.2.4:

$$\begin{aligned}
 E_{D1} &= C M n^2 \\
 &= 396 \times 28 \times 1050^2 \\
 &= 12,224 \text{ Mpa} \\
 &= 1,773 \text{ Ksi}
 \end{aligned}$$

Test Beam 2 similarly to get E_{D2} . If E_{D1} and E_{D2} have more than 5% difference, take a third reading E_{D3} from a third beam and average the values of the two closest readings to get $E_{D12\text{-hour}}$.

$E_{D\ 12\text{-hour}}$ is assumed to be 1,800 Ksi in this example.

Using Equation 8.1, the flexural strength is estimated:

$$f_{r\ 12\text{-hour}} = 49.86 e^{5.29 \cdot 10^{-4} \cdot 1800}$$

$$= 130 \text{ psi}$$

Alternatively, the same value could be estimated using the following plot:

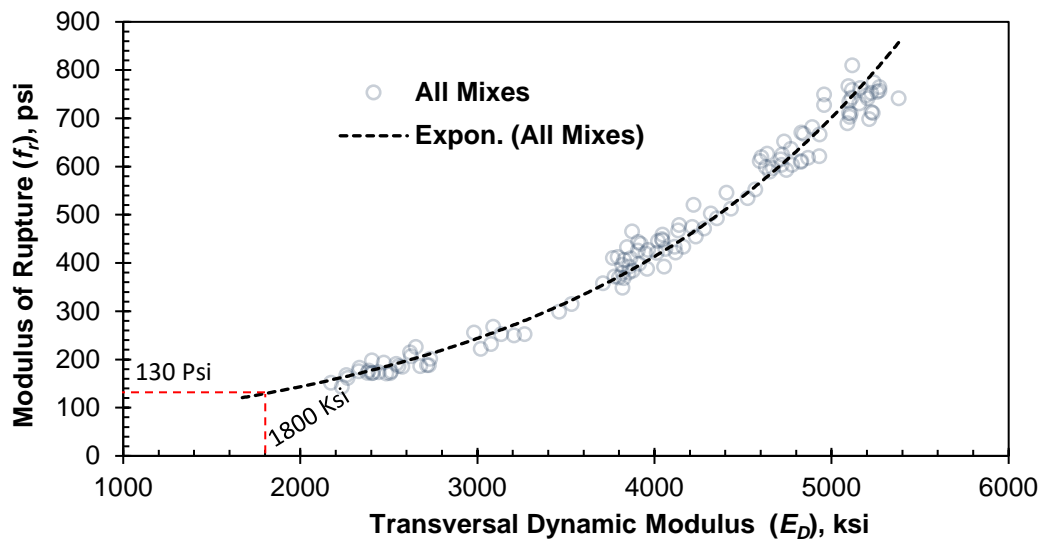


Figure 7-1. Flexural strength estimation using trend line.

2. Estimate flexural stresses in pavement due to ESAL, using charts.

The developed tensile stresses at the bottom of the PCC pavement can be obtained by referring to the graph with the corresponding modulus of subgrade reaction (50 psi/in.). Figure N-2 is used for that, and the stresses are obtained as shown in Figure 7-2. The developed tensile stresses due to ESAL, designated σ_y , equal 270 psi. Alternatively, this value can be obtained through the nomograph corresponding to the 12-hr concrete age, as shown in Figure 7-3.

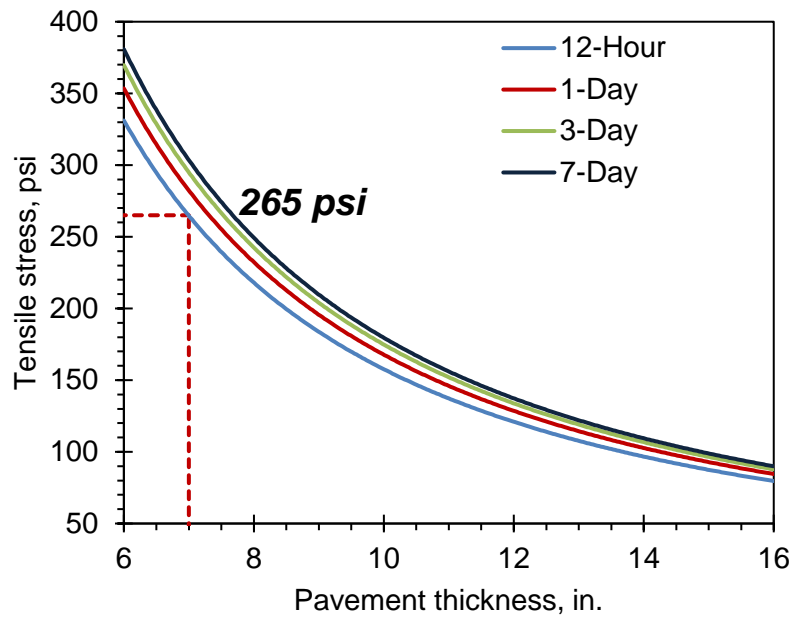


Figure 7-2. Stress estimation at 12-hr with $k = 50 \text{ psi/in.}$

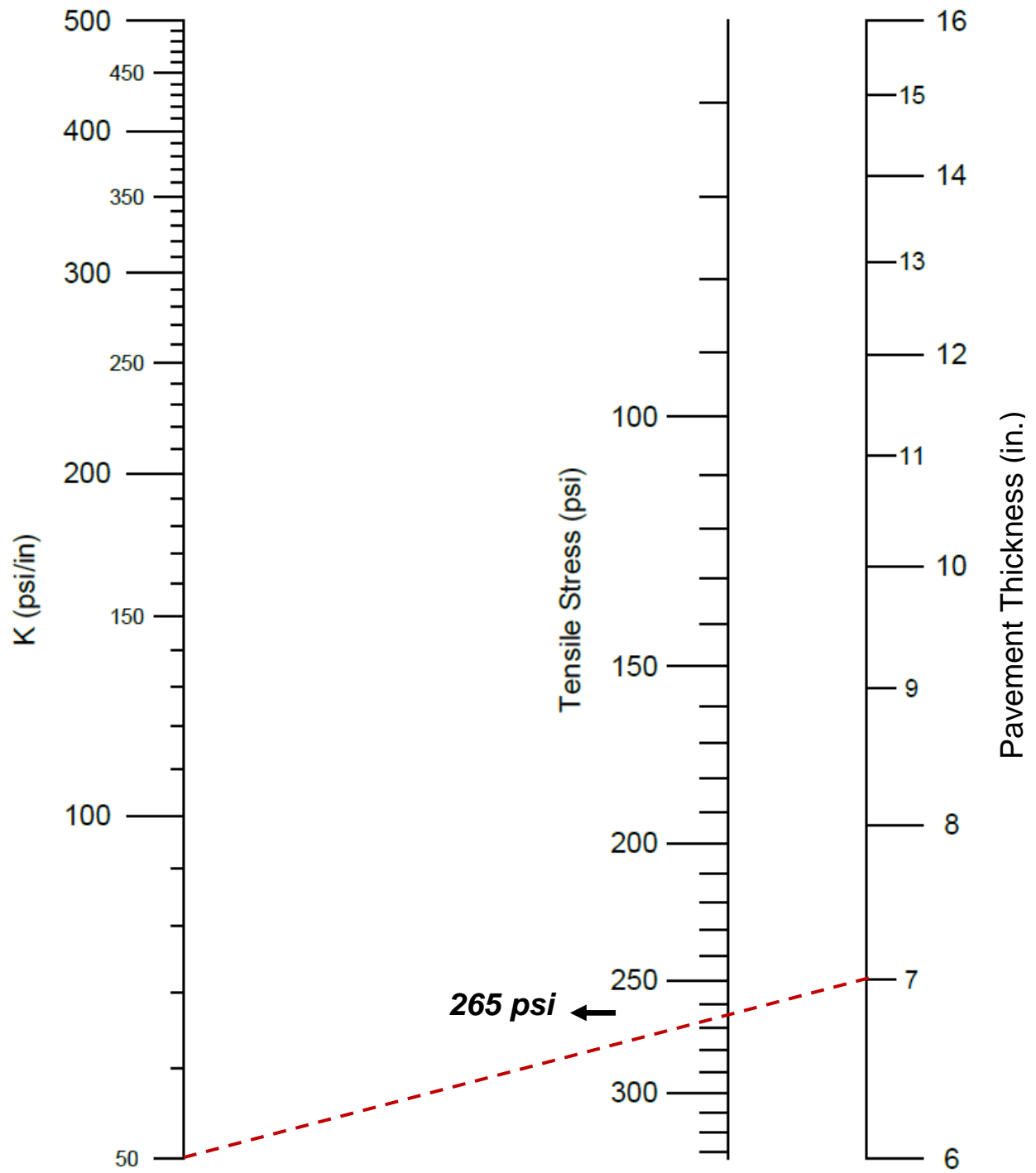


Figure 7-3. Stress-determination nomograph at 12-hr concrete age.

3. Estimate fatigue life for opening to traffic at 12 hr.

The developed stresses in the pavement at this stage are significantly greater than the flexural capacity of the concrete. Therefore, the stress level S will be greater than 1, and opening to traffic at this concrete age could not be achieved.

As per Equation 7-2:

$$\begin{aligned} S &= \sigma_y / f_r \\ &= 270 \text{ psi} / 130 \text{ psi} \\ &= 2.07 \end{aligned}$$

4. Test two 6 x 6 x 21 in. concrete beams at 1-d for E_D .

Similarly to step 1:

Unmold two beams at 1-d.

Test Beam 1:

$$\begin{aligned} \text{mass} &= 28 \text{ kg} \\ \text{resonant transverse frequency} &= 1,250 \text{ Hz} \\ E_{D1} &= C M n^2 \\ &= 396 \times 28 \times 1,250^2 \\ &= 17,325 \text{ Mpa} \\ &= 2,512 \text{ Ksi} \end{aligned}$$

Test Beam 2 similarly to get E_{D2} :

$E_{D1\text{-Day}}$ is assumed to be 2,500 Ksi in this example.

Using Equation 7-1, estimate the flexural strength:

$$\begin{aligned} f_{r\text{ 1-Day}} &= 49.86 e^{5.29 \cdot 10^{-4} \cdot 2500} \\ &= 187 \text{ psi} \end{aligned}$$

5. Estimate flexural stresses in pavement due to ESAL, using charts

The developed stresses due to ESAL are found to be equal to $\sigma_y = 280$ psi, as seen in the plot of Figure 7-4. The same value can be obtained from the 1-d concrete age nomograph, as shown in Figure 7-5.

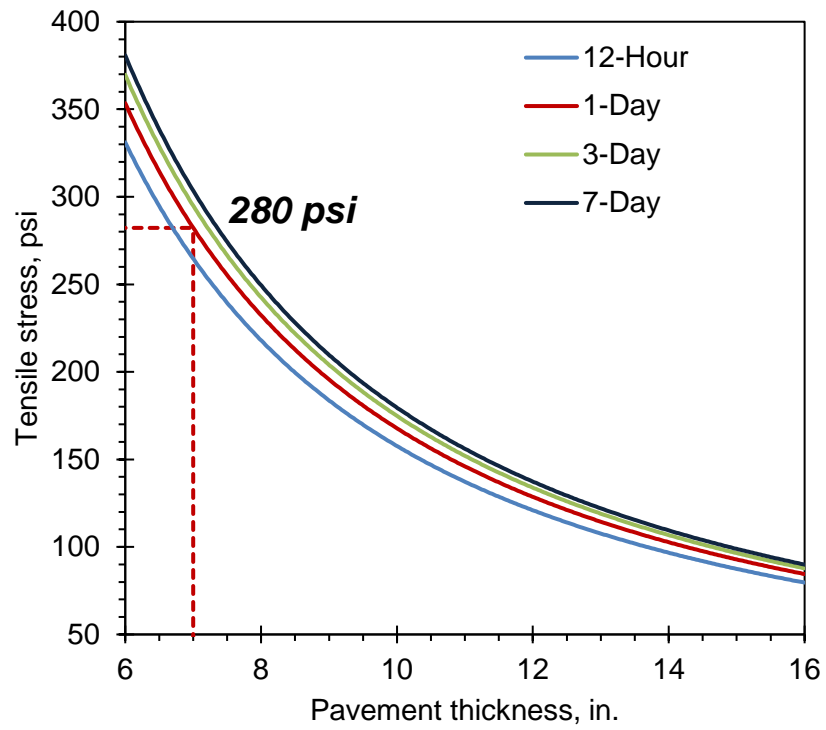


Figure 7-4. Stress estimation at 1-d with $k = 50$ psi/in.

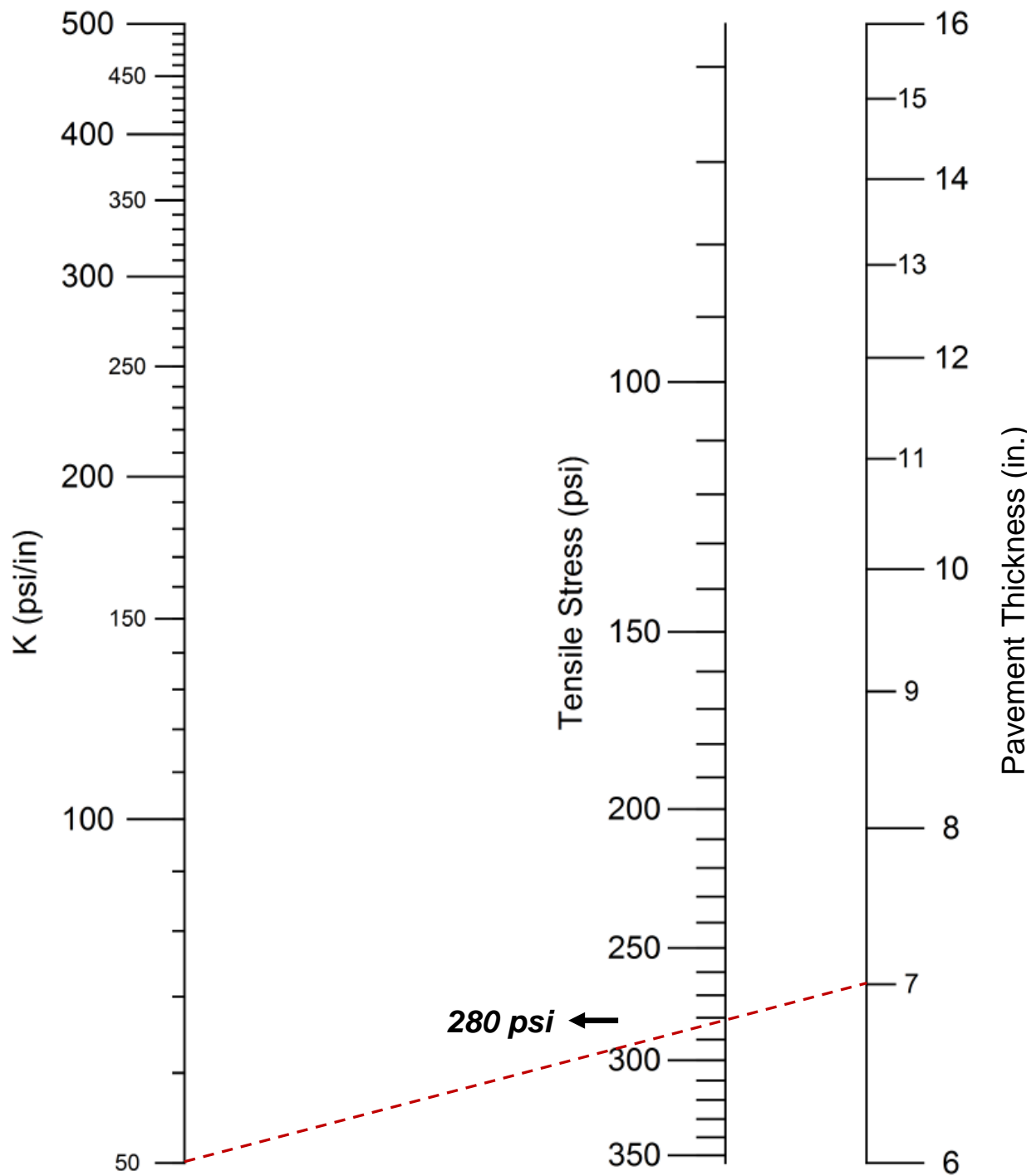


Figure 7-5. Stress-determination nomograph at 1-d concrete age.

6. Estimate fatigue life for opening to traffic at 1-d.

The developed stresses are still greater than the flexural capacity of the concrete. At this stage, opening to traffic should be postponed to the next testing date (3-d testing).

- $S = \sigma_y / f_r$
 $= 285 \text{ p}/187 \text{ Psi}$
 $= 1.49$

7. Test two 6 x 6 x 21 in. concrete beams at 3 d for E_D .

Unmold two beams at 3 d.

Test Beam 1:

mass = 28 Kg

resonant transverse frequency = 1,500 Hz

$$E_{D1} = C M n^2$$

$$= 396 \times 28 \times 1,500^2$$

$$= 24,948 \text{ Mpa}$$

$$= 3,618 \text{ Ksi}$$

Test Beam 2 similarly to get E_{D2} .

$E_{D3\text{-Day}}$ is assumed to be 3,600 Ksi in this example.

Using Equation 7-1, estimate the flexural strength:

$$f_{r3\text{-Day}} = 49.86 e^{5.29 \cdot 10^{-4} \cdot 3600}$$

$$= 335 \text{ psi}$$

8. Estimate flexural stresses in pavement due to ESAL, using charts.

The developed flexural stresses due to ESAL are found to be equal to $\sigma_y = 295 \text{ psi}$, as seen in Figure 7-6. Similarly, this value can be also obtained in the 3-d nomograph shown in Figure 7-7.

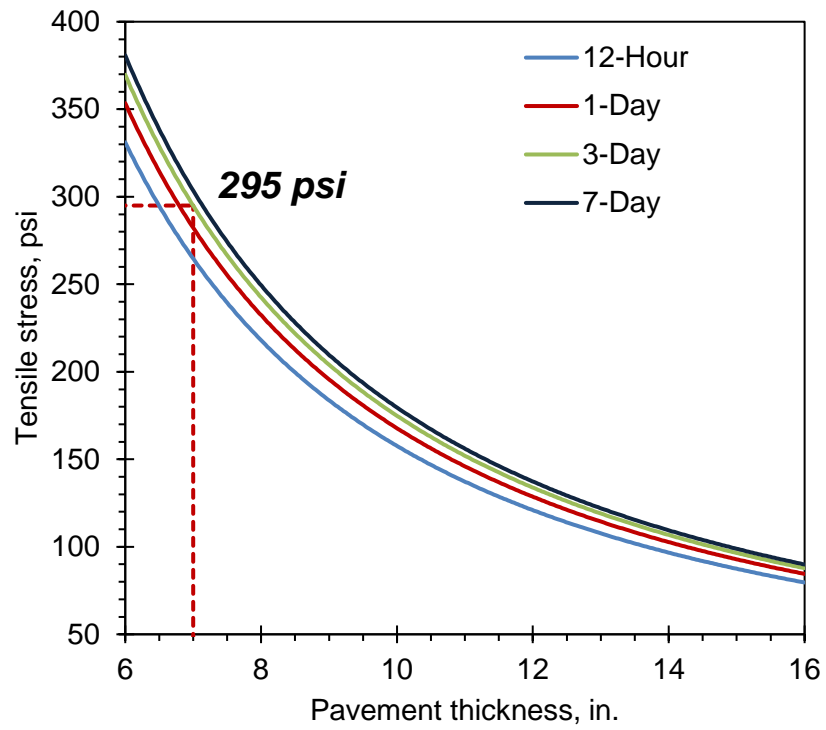


Figure 7-6. Stress estimation at 3-d with $k = 50$ psi/in.

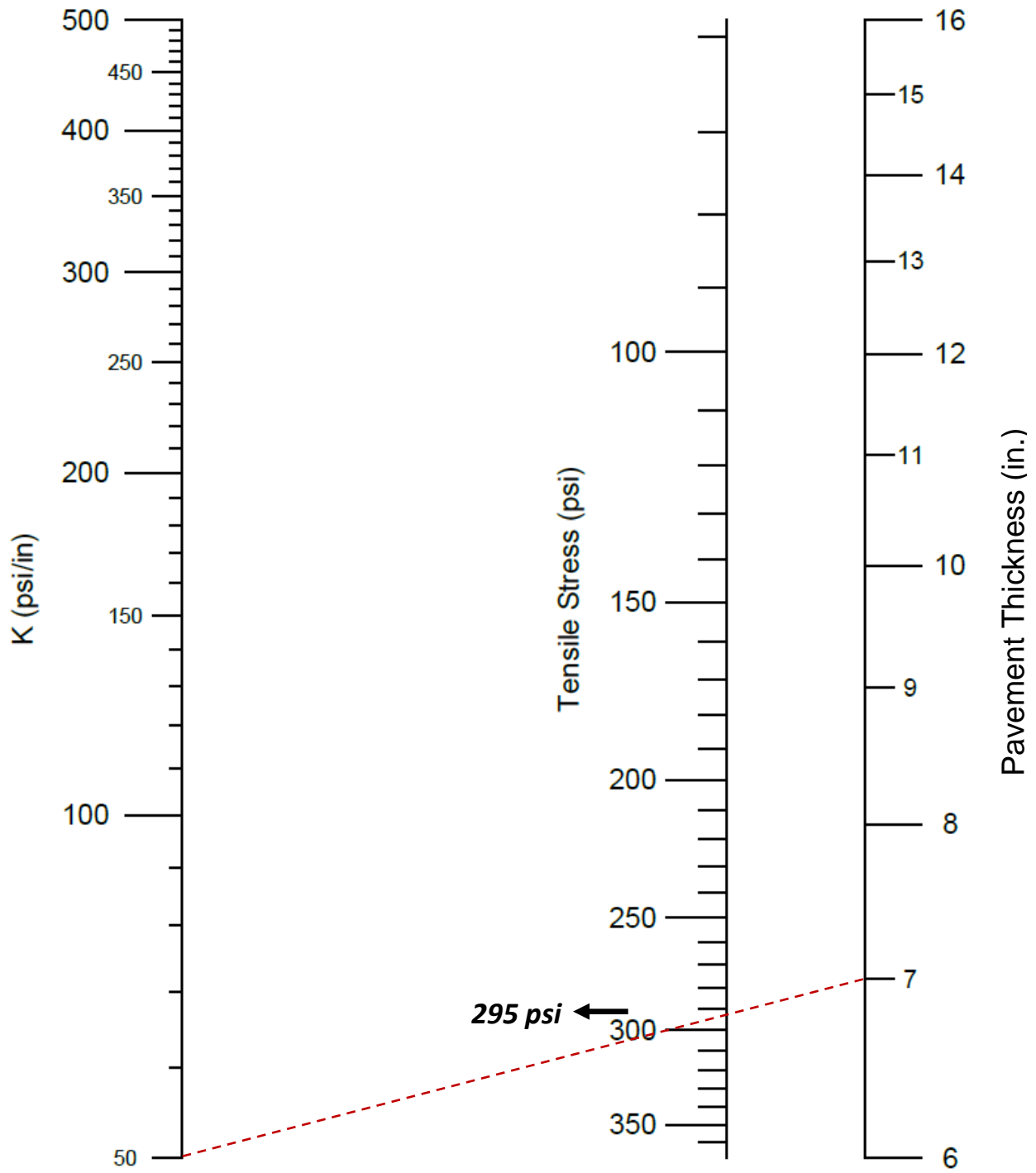


Figure 7-7. Stress-determination nomograph at 3-d concrete age.

9. Estimate fatigue life for opening to traffic at 3-d.

The developed flexural stresses are slightly less than the flexural capacity of the concrete:

$$S = \sigma_y / f_r$$

$$= 295 / 335 = 0.88$$

At this stress level, the PCC pavement can maintain only a few cycles of ESALs before failure. This finding is seen by evaluating N for the 3-d concrete age formulas of Table N-2:

For plain concrete:

$$N = E^{-(S-1.1072)/0.030}, \text{ with } S = 0.88 \rightarrow N = 174 \text{ cycles}$$

$$\text{fatigue life} = N / 4 = 174 / 4 = 43 \text{ sec}$$

For fiber-reinforced concrete:

$$N = E^{-(S-1.0822)/0.036}, \text{ with } S = 0.88 \rightarrow N = 274 \text{ cycles,}$$

$$\text{fatigue life} = N / 4 = 210 / 4 = 68 \text{ sec}$$

Therefore, opening to traffic is not possible at this stage; and the steps are going to be repeated at the 7-d test.

10. Test two 6 x 6 x 21 in. concrete beams at 7-d for E_D .

Unmold two beams at 1-d.

Test Beam 1:

$$\text{mass} = 28 \text{ kg}$$

$$\text{resonant transverse frequency} = 1,660 \text{ Hz}$$

$$E_{D1} = C M n^2$$

$$= 396 \times 28 \times 1,660^2$$

$$= 24,948 \text{ Mpa}$$

$$= 4,431 \text{ Ksi}$$

Test Beam 2 similarly, to get E_{D2} .

$E_{D \text{ 7-Day}}$ is assumed to be 4,450 Ksi in this example.

Using Equation 7-1, estimate the flexural strength:

$$f_{r \text{ 7-Day}} = 49.86 e^{5.29 \cdot 10^{-4} \cdot 4450}$$

$$= 525 \text{ psi}$$

11. Estimate flexural stresses in pavement due to ESAL, using charts.

Flexural stresses developed due to ESAL load are found to be equal to $\sigma_y = 300 \text{ psi}$, as seen in Figure 7-8. Similarly, this value can be also obtained in the 7-d nomograph shown in Figure 7-9.

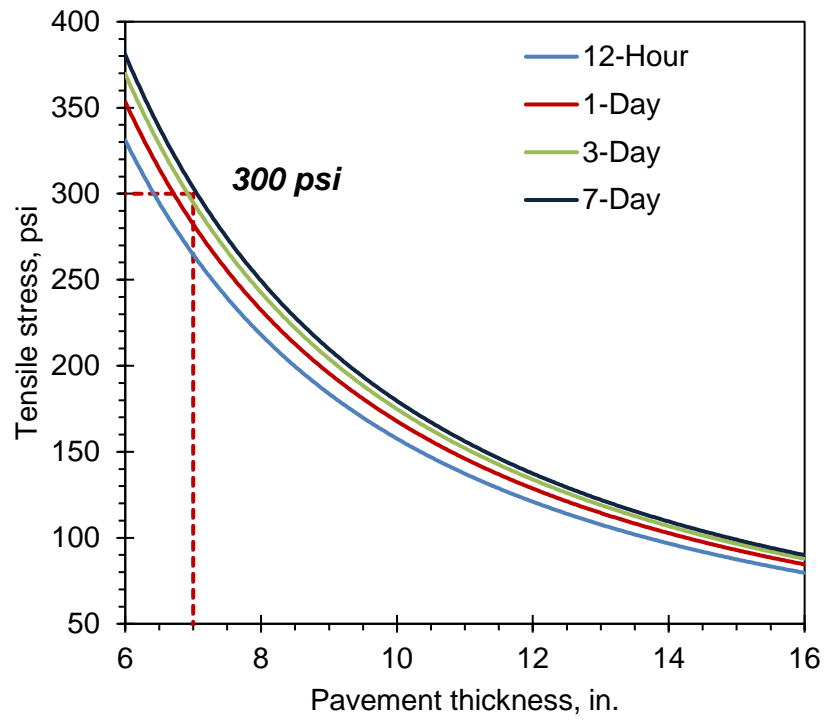


Figure 7-8. Flexural stress estimation at 7-d with $k = 50$ psi/in.

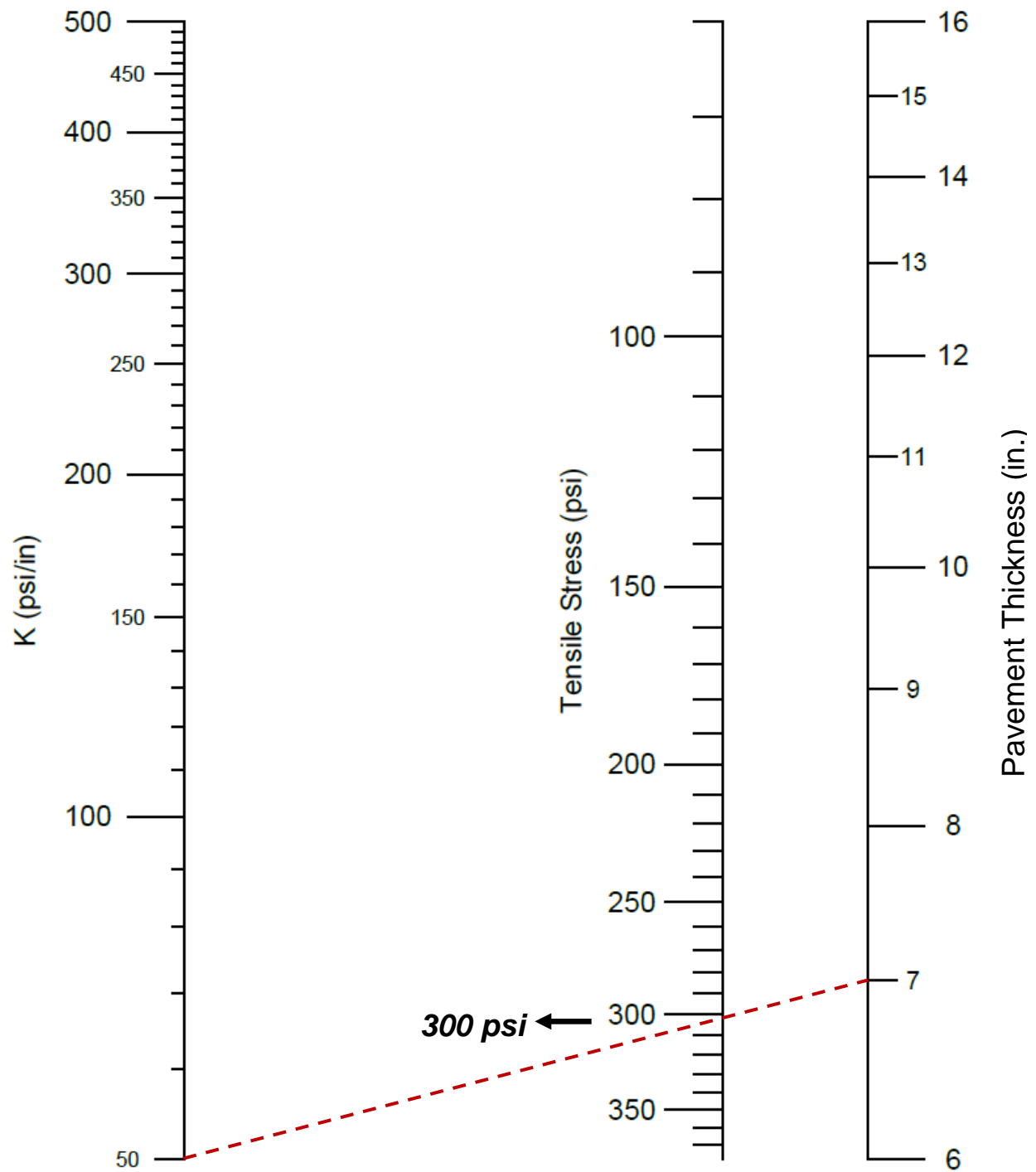


Figure 7-9. Stress-determination nomograph at 7-d concrete age.

12. Estimate fatigue life for opening to traffic at 7-d.

At this stage, the developed stresses are almost half the flexural capacity of the concrete:

$$\begin{aligned}
 S &= \sigma_y / f_r \\
 &= 300 \text{ psi} / 585 \text{ psi} = 0.51
 \end{aligned}$$

By evaluating N for the 7-d concrete age formulas of Table 7-2:

For plain concrete:

$$N = E^{-(S-1.1022)/0.041}, \text{ with } S = 0.51 \rightarrow N = 1.8 \text{ million cycles,}$$

$$\text{fatigue life} = N/4 = 1.8 \text{ Mil. } /4 = 5.4 \text{ d before failure}$$

For fiber-reinforced concrete:

$$N = E^{-(S-1.1616)/0.043}, \text{ with } S = 0.51 \rightarrow N = 3.8 \text{ million cycles,}$$

$$\text{fatigue life} = N/4 = 2.4 \text{ Mil. } /4 = 11 \text{ d before failure}$$

The results show an indication that opening to traffic at this stage is plausible. This example demonstrates that even though the controlling parameters were not ideal, opening to traffic was still achievable after 1 week.

7.3.1 Considerations for the example

Note 1: Flexural strength development at cold temperatures

It should be noted that the transverse resonant frequency values in this example are chosen to demonstrate the effect of cold weather on strength development. The frequency values for the 1-, 3-, and 7-d testing dates correspond to the flexural strength development described in section 6.2.2. The corresponding data is presented in Figure 7-10 for room temperature (RT) and cold temperature (50F) curing. Moreover, Figure 7-11 shows the normalized development of flexural strength versus time. The curves are plotted by dividing flexural strength values by the initial 12-hr value to create a normalized trend. In this example, a more conservative estimation is considered by adopting the trend for the 50F case. Consequently, strength development is governed by Equation 7.4:

$$f_r(t)/f_{r \ 12 \ hour} = 0.560 \ln(t) + 1.39 \quad (7-4)$$

where $f_r(t)$ = concrete flexural strength in psi at a given age t in days, psi
 $f_{r \ 12 \ hour}$ = concrete flexural strength in psi at a 12-hr age

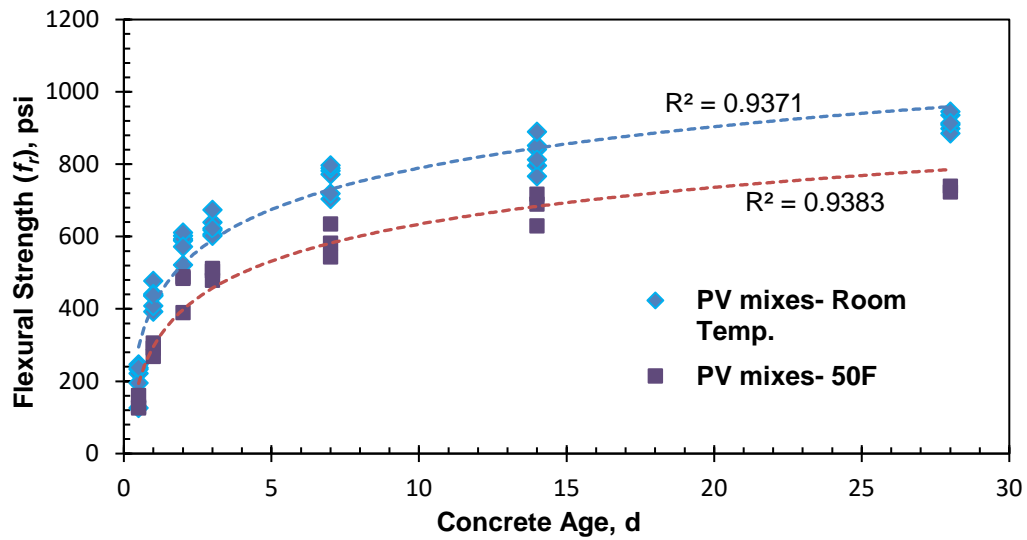


Figure 7-10. Flexural strength development for room and cold temperatures.

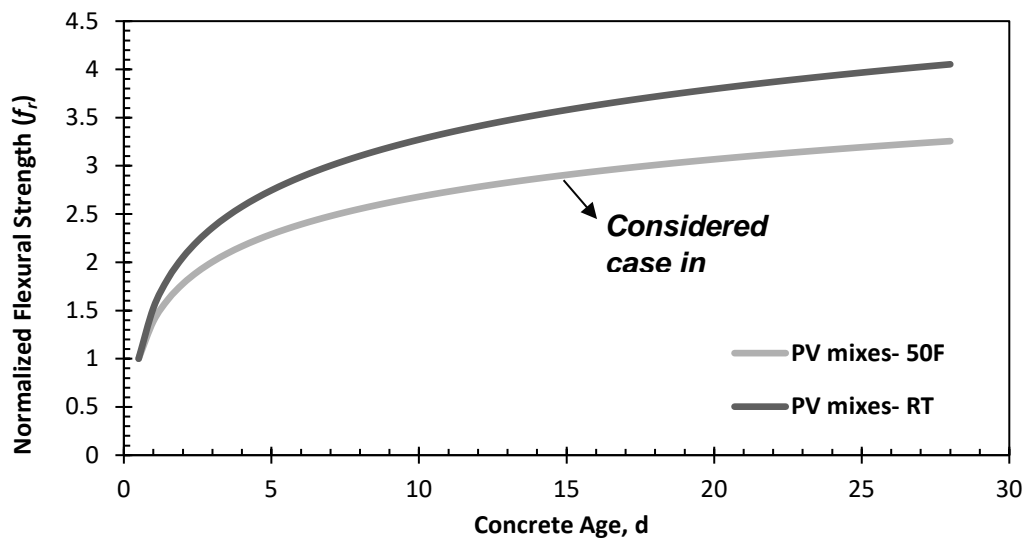


Figure 7-11. Normalized flexural strength development for room and cold temperatures.

Note 2: Validity of E_D readings for different curing regimes

E_D -flexural strength relationships previously established in the fatigue testing program included samples that were cured in a controlled-moisture room at 73°F with no tests for cold-curing cases. However, it should be noted that E_D readings have proved to indicate directly the strength state regardless of the mix design, curing regime, or fiber content. This observation is presented in section 6.2.6.2, where concrete compressive strength showed the same trend

development for all pavement and patch mixes. This outcome is summarized in Figure 7-12 for all mixes.

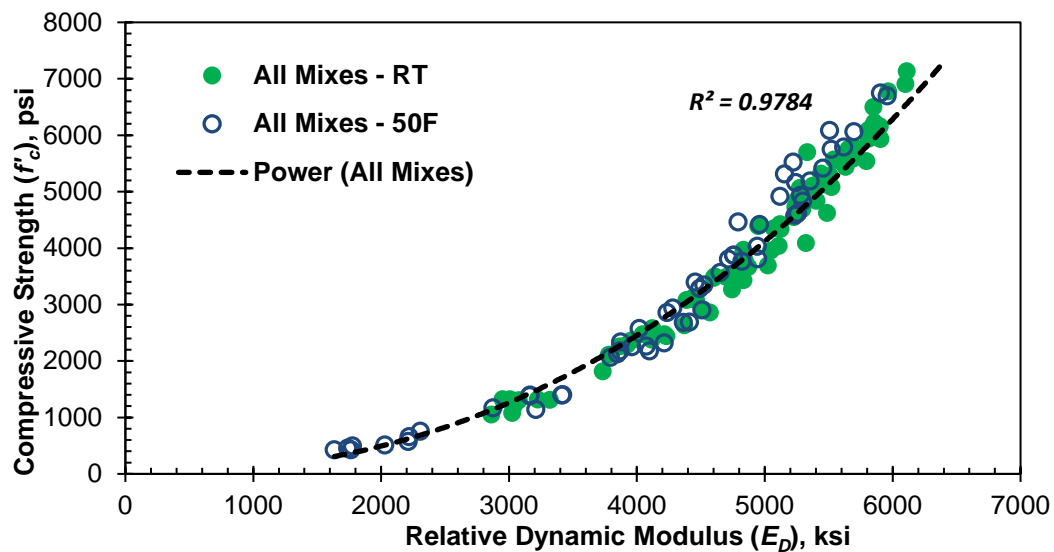


Figure 7-12. Compressive strength vs E_D for all RT and 50F mixes.

Note 3: Estimation of flexural strength using plotted chart

Steps 1, 4, 7, and 10 in the example could use the *Flexural strength– E_D* plot to evaluate flexural strength in a practical manner as an alternative to Equation 7.1:

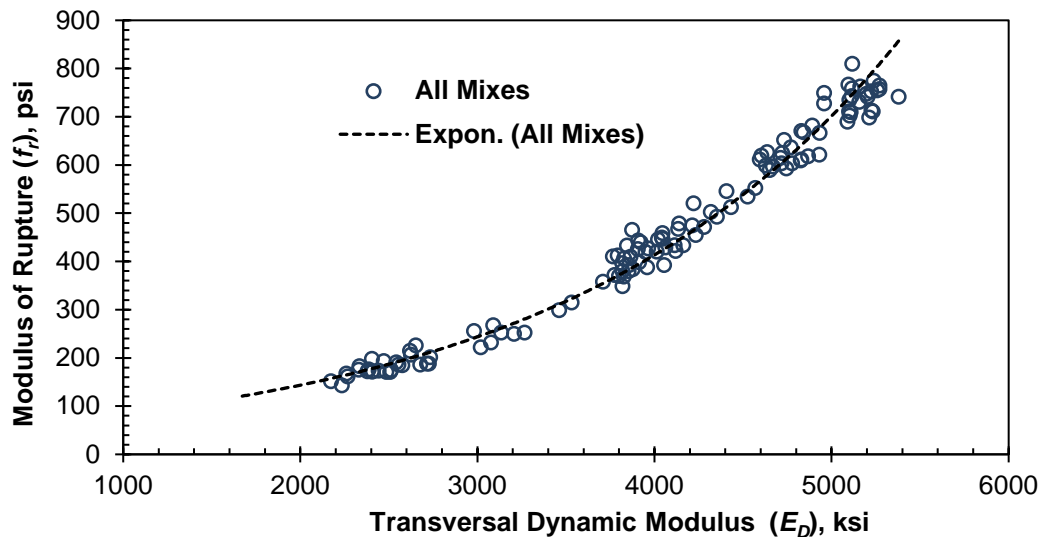


Figure 7-13. Flexural strength estimation, using trend line.

7.4 ANALYTICAL EVALUATION OF JOINTED-PAVEMENT SLAB

A correlation between the experimental results of the cyclic fatigue performance for the jointed-slab specimen (section 6.7.1) and the implementation procedure (section 7.2) was made to validate the proposed analytical method. First, concrete strength at 1-d age was estimated empirically with nondestructive testing (dynamic modulus test). The maximum tensile stresses in the concrete pavement were then evaluated numerically using finite-element analysis software (*ISLAB2000*). With the corresponding stress level, the number of fatigue cycles until pavement failure was calculated from the *S-N* relationships developed from the fatigue testing program. In addition to the implementation procedure, a preliminary finite-element analysis was also conducted for a practical 2D model using *ISLAB2000* software and for a detailed 3D model using ABAQUS/CAE software. The output of the analytical method for every model was compared with the experimental results of the jointed-slab specimen, which showed no failure after application of 2.3 million cyclic loads at 1-d age with a maximum load of ½ ESAL.

7.4.1 Evaluation of Fatigue Life Using Implementation Procedure

Step I: Estimate flexural strength, using nondestructive measures.

The fatigue life of the jointed-slab is first evaluated by estimating concrete flexural strength at 1-d concrete age, as per section 7.2.1. This estimation requires calculating the dynamic modulus of elasticity, as per ASTM C215:

$$E_{D \text{ Trans.}} = CMn^2$$
$$E_{1\text{-Day}} = 29,381\text{MPa} = 4,264.1 \text{ ksi}$$

where $E_{D \text{ Trans.}}$ = dynamic modulus of elasticity based on fundamental transverse frequency, psi
 M = mass of specimen = 28.2 kg
 n = fundamental transverse frequency at 1-d concrete age = 1,621.09 Hz
 L = length of specimen, m = 0.53 m
 t = thickness (depth) of prism, m = 0.15 m
 b = width of prism, m = 0.15 m
 T = correction-factor-based radius of gyration K ($d/4$ for a cylinder and $t/3.464$ for a prism) and Poisson's ratio μ found from Table 1 of ASTM C215 = 1.49
 $C = 0.9464 (L^3T/bt^3)$ for a prism, $m^{-1} = 396 \text{ m}^{-1}$

After obtaining the dynamic modulus of elasticity, the modulus of rupture (f_r) was estimated empirically, as per Equation 7.1. This value can be similarly obtained by using the f_r vs. E_D relationships presented in section 6.2.6.4. The development of f_r with respect to E_D is shown in Figure 7-14, where a dynamic modulus of 4,264.1 ksi corresponds to a flexural strength of 476 psi. Flexural strength testing was carried out at 1-d concrete age, as per ASTM C78, and yielded a value of 465 psi. The outcome of Step I showed great accuracy, as the proposed relation

slightly overestimated the actual strength by a 2.3% margin. Calculation of the estimated flexural strength is presented as follows:

$$f_{r.Estimated} = 49.86 e^{5.29 \cdot 10^{-4} E_D}$$

$$f_{r.Estimated} = 49.86 e^{5.29 \cdot 10^{-4} \cdot 4264.1 \text{ ksi.}} = 476 \text{ psi}$$

$$f_{r.Actual} = 465 \text{ psi}$$

$$f_{r.Actual} = 97.7\% f_{r.Estimated}$$

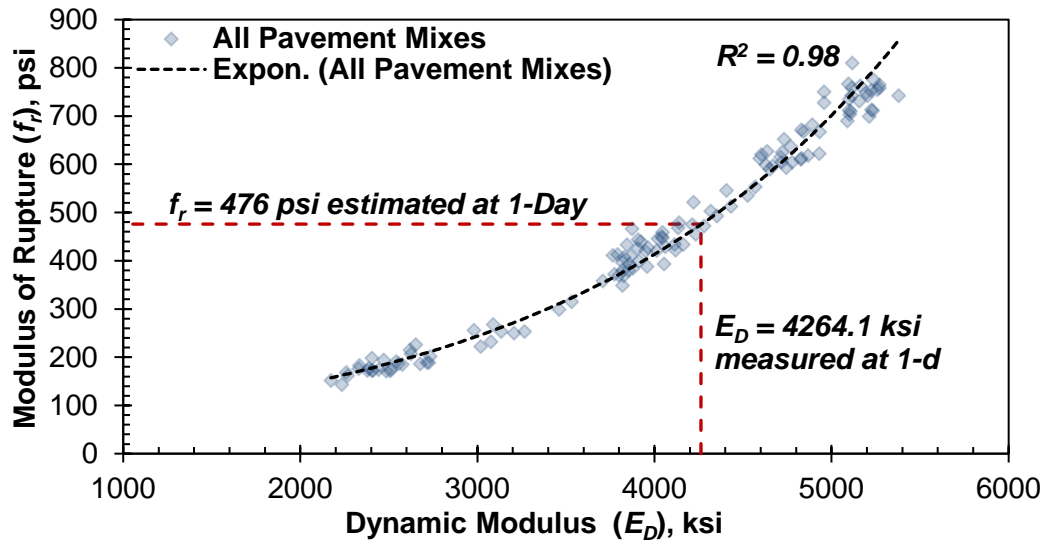


Figure 7-14. Modulus of rupture versus dynamic modulus showing flexural strength estimation at 1-d concrete age.

Step II: Estimate flexural stresses in concrete pavement, using ISLAB2000 analytical model results.

The maximum flexural stresses that developed due to ESAL (18 kip) were evaluated using the numerical modeling results of the implementation procedure of section 7.2.2. The model used for the implementation procedure is presented in Figure 7-15. This model is considered because the applied $\frac{1}{2}$ ESAL at each contact area does not affect flexural stress development at a distance of 6 ft, as shown in Figures 6-50 and 6-51 of section 6.6.1.1. To estimate the maximum developed tensile stresses, the 1-d nomograph is used with the known thickness (6 in.) and subgrade modulus reaction ($k = 324 \text{ psi/in.}$). Figure 7-16 demonstrates that the line connecting the pavement thickness with the subgrade modulus reaction intersects the intermediate axis at 260 psi.

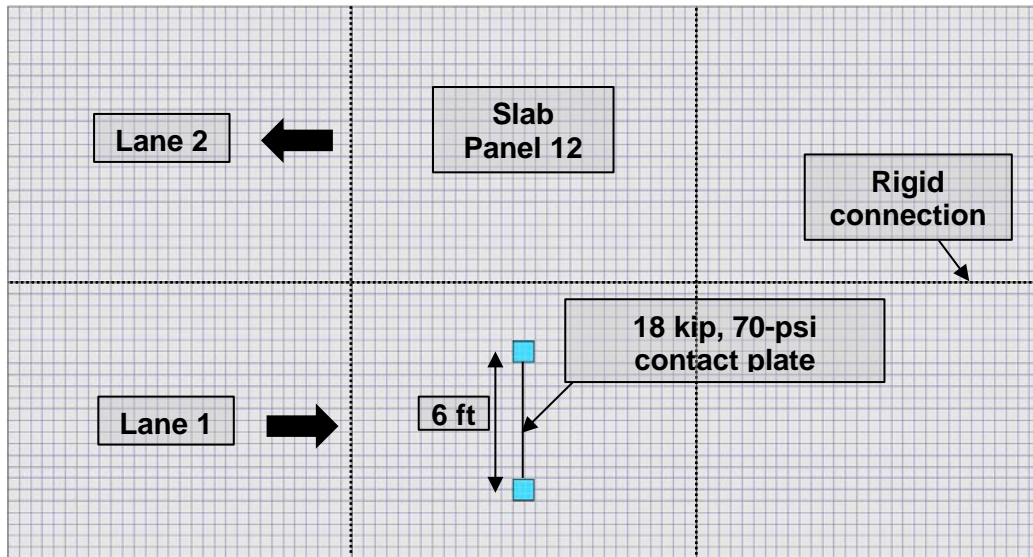


Figure 7-15. Plan view of the implementation pavement model.

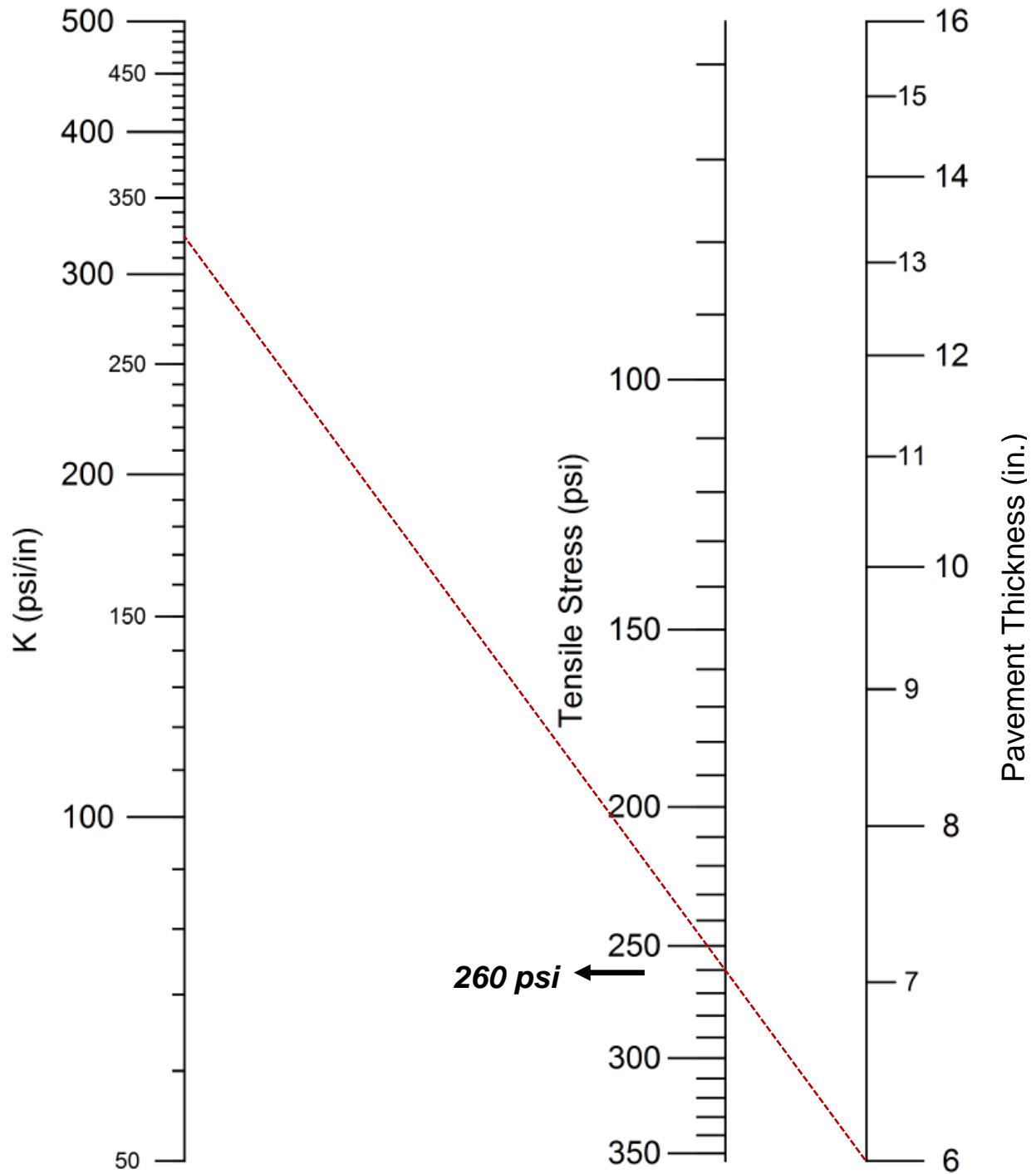


Figure 7-16. Tensile stress evaluation at 1-d concrete age for a 6-in. pavement with $k = 324$ psi/in.

Step III: Estimate flexural fatigue life of jointed-pavement slab.

The flexural fatigue life of the jointed-slab specimen was evaluated in accordance with section 7.2.3 of the implementation procedure. First, the stress level was calculated by dividing the maximum developed flexural stress obtained from Step II by the flexural strength obtained

from Step I. Then, the corresponding fatigue life was calculated using the linear-regression formula corresponding to a fiber-reinforced concrete (FRC) pavement at 1-d concrete age, as listed in Table N-2. Fatigue life calculation is presented as follows:

$$S_{1-Day} = \frac{\sigma_{max}}{f_r} = \frac{260 \text{ psi}}{465 \text{ psi}} = 0.56$$

$$S_{1-Day} = -0.025 \ln(N_{1-Day}) + 1.0066 = 0.56$$

$$N_{1-Day} = e^{-\left(\frac{S_{1-Day}-1.0066}{0.025}\right)} = 57.3 \times 10^6 \text{ cycles}$$

$$\text{Fatigue life} = \frac{N_{1-Day}}{4 \text{ hz}} = 14.32 \times 10^6 \text{ seconds} = 165 \text{ days}$$

where

S_{1-Day} = stress level at 1-d concrete age

N_{1-Day} = number of cycles until failure after 1-d loading

σ_{max} = maximum tensile stress developed at the bottom concrete layer due to ESAL (Step II) = 260 psi.

f_r = modulus of rupture of concrete at 1-d of the jointed-slab specimen (Step I) = 465 psi

The analytical results show that the stress level corresponding to the jointed-slab case is low enough ($S_{1-Day} = 0.56$) that no failure can occur at early opening to traffic (1-d concrete age). Results show that failure is reached after applying 57.3 million ESALs over a span of 165 d. These figures are well beyond the fatigue range of highway pavements (10 million cycles) as specified by Hsu (1981). In addition, experimental results of section 6.7.1.5 confirmed the outcome of the analytical procedure, as the jointed-slab specimen did not show any deterioration within the first 2.3 million cyclic fatigue loads. This loading segment was applied from 1-d concrete age to 7-d, 16-hr concrete age, as presented in Table M-2. Moreover, the fatigue life of the specimen can also be calculated by using the $S-N$ curves developed for the fatigue testing program of section 6.4.1.2. The $S-N$ curves corresponding to 1-d concrete age for pavement mixes are shown in Figure 7-17 for plain- and fiber-reinforced concrete mixes. The fatigue life of the jointed-slab specimen is obtained by intersecting the linear trend line of concrete mixes designated "PVF1-8lbs" with a stress level of 0.56.

Table 7-1. *S-N* Relationships of the Fatigue Testing Program Highlighting the Jointed-Slab Specimen Case (1-d loading, FRC)

Concrete age	Mix type	<i>S-N</i> linear-regression relationships
12-hr	Plain	$N = e^{\frac{S-1.0090}{-0.030}}$
	FRC	$N = e^{\frac{S-1.0257}{-0.028}}$
1-d	Plain	$N = e^{\frac{S-1.0098}{-0.028}}$
	FRC	$N = e^{\frac{S-1.0066}{-0.025}}$
3-d	Plain	$N = e^{\frac{S-1.1072}{-0.044}}$
	FRC	$N = e^{\frac{S-1.0822}{-0.036}}$
7-d	Plain	$N = e^{\frac{S-1.1022}{-0.041}}$
	FRC	$N = e^{\frac{S-1.1616}{-0.043}}$

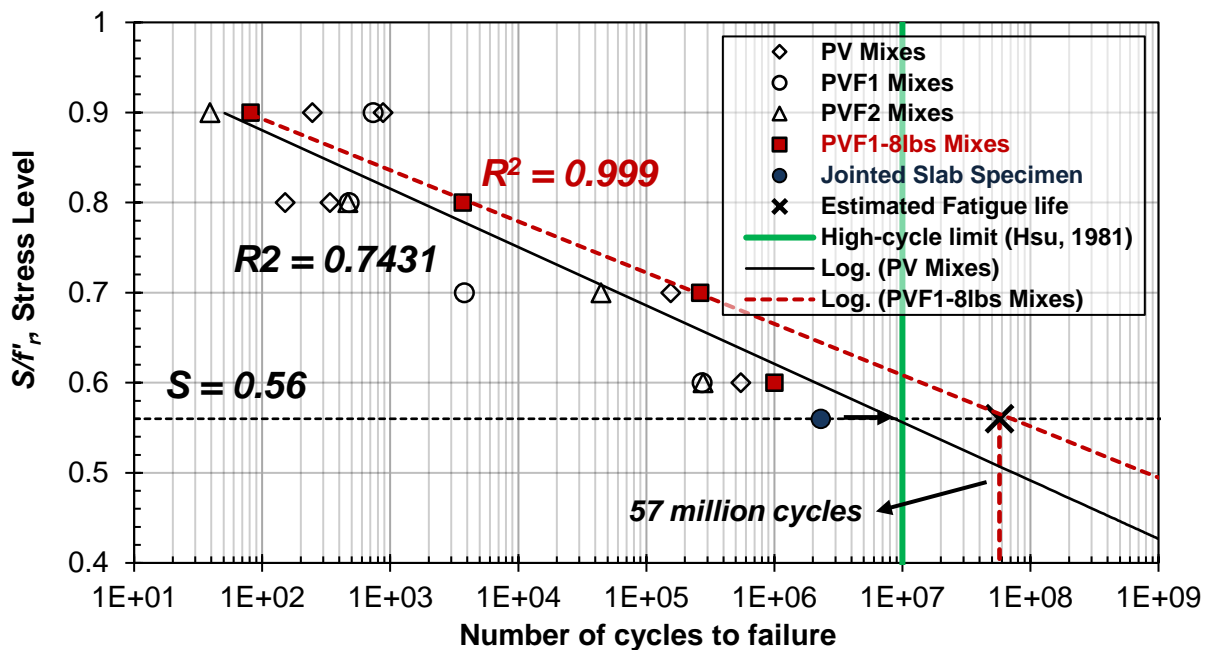


Figure 7-17. *S-N* results for PV, PVF1, PVF2, and PVF1-8lbs mixes at 1-d concrete age, showing estimated fatigue life of jointed-slab specimen.

7.4.2 Evaluation of Fatigue Life, Using *ISLAB2000* Jointed-Pavement Slab Model

Modeling the jointed-slab specimen included experimental properties as input parameters to simulate the loading test with close proximity to actual conditions. The input parameters of the model for dimensions, material properties, loading, and joint characteristics are listed in Table 7-2. The model is composed of a 2 ft x 7 ft x 6 in. jointed-concrete slab. The transfer mechanism was carried out by two dowels spaced at 12 in. and by aggregate interlock. A linear elastic model was considered for the soil, with a subgrade modulus reaction of 324 psi/in., as determined in section 6.7.1.1. In addition, concrete elastic modulus was calculated empirically for 1-d concrete age in accordance with the findings of the mechanical properties testing program of section 6.2. An illustration of the model in the plan view is shown in Figure 7-18. This model was constructed using *ISLAB2000* to account for joint presence and dowel-transfer action.

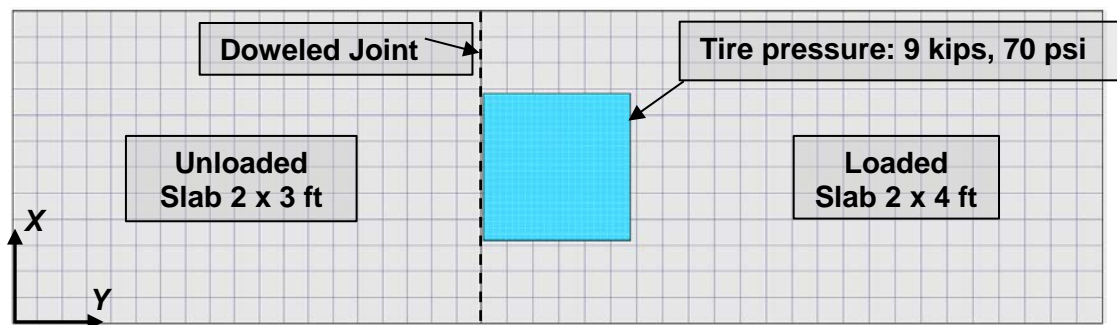


Figure 7-18. Plan view of the jointed-pavement slab model.

Table 7-2. Input Parameters Obtained from the Experimental Setup

Input Category	Input Parameter	
Slab model	Loaded slab dimensions	2 x 4 ft
	Unloaded slab dimensions	2 x 3 ft
	Slab thickness	6 in.
Concrete layer	Static modulus of elasticity	2.56×10^6 psi
	Unit weight	144 lb/ft ³
Soil layer	Subgrade modulus	324 psi/in.
Loading parameters	Aspect ratio of contact area	1
	Axle position (from bottom left)	6.3 in., 36.3 in.
	Axle load	9,000 lb
	Contact area of tires	127.69 in. ²
	Tire pressure	70 psi
Joint parameters	Dowel-bar diameter	1 in.
	Dowel-bar length	18 in.
	Dowel-bar spacing	12 in

The development of flexural stresses at the bottom concrete layer is presented in Figures 7-19 and 7-20 for the transverse and longitudinal directions, respectively. Numerical results revealed that the maximum flexural stress in the transverse direction was 131.3 psi, while the maximum flexural stress in the longitudinal direction was 111.9 psi. In addition, the maximum slab deflection was 0.0789 in., as shown in Figure 7-21. To evaluate the stress level at this stage of loading, Equation 7.2 is considered:

$$S_{1-Day} = \frac{\sigma_y}{f_r} = \frac{Max(140.8 \text{ psi}, 160.1 \text{ psi})}{465 \text{ psi}} = 0.34$$

where

S_{1-Day} = stress level ratio at 1-d concrete age

σ_{max} = maximum tensile stress developed at the bottom of the PCC pavement due to ½ ESAL = 160.1 psi

f_r = modulus of rupture of concrete at 1-d of the jointed-pavement slab = 465 psi

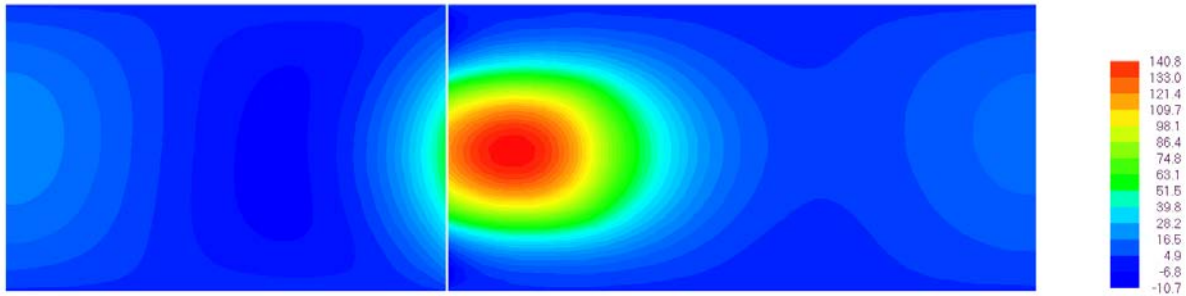


Figure 7-19. Transverse stress distribution in the bottom concrete layer at ½ ESAL.

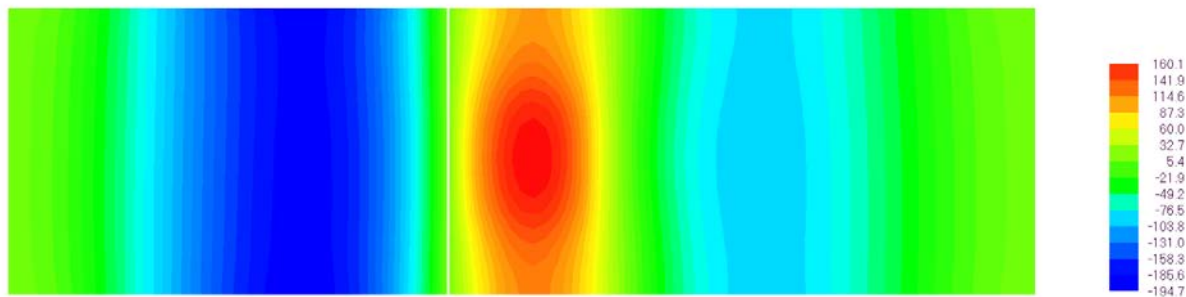


Figure 7-20. Longitudinal stress distribution in the bottom concrete layer at ½ ESAL.

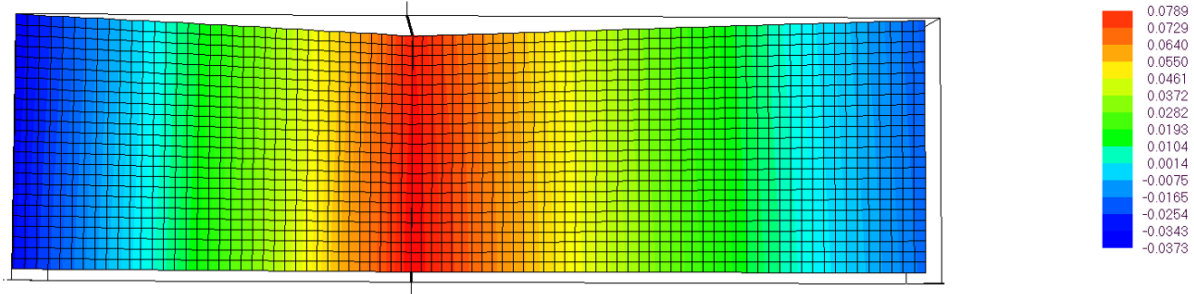


Figure 7-21. Deflection distribution in the bottom concrete layer at ½ ESAL.

The fatigue life of the considered model can now be evaluated after obtaining the stress level corresponding to ½ ESAL at 1-d concrete age. The corresponding number of cycles until failure, designated N is obtained from in the S - N linear-regression relationships of Table 7-1. The specimen was cast with 8 lb/yd³ of synthetic fibers (Strux 90/40) and loaded at 1-d concrete age. Therefore, the fatigue life can be calculated as follows:

$$S_{1-Day} = -0.025 \ln(N_{1-Day}) + 1.0066 = 0.34$$

$$N_{1-Day} = e^{-\left(\frac{S_{1-Day}-1.0066}{0.025}\right)} = 3.8 \times 10^{11} \text{ cycles}$$

$$\text{Fatigue life}_{1-Day} = \frac{N_{1-Day}}{4 \text{ hz}} = 9.5 \times 10^{10} \text{ seconds}$$

where N_{1-Day} = number of cycles until failure after 1-d loading

It can be clearly observed that for a stress level of 0.34, the required number of cycles that can cause failure greatly exceeded the fatigue life spectrum for pavements, which is equal to 10 million cycles (Hsu, 1981). Similar to the findings of section 7.4.1, no considerable fatigue damage was associated with a 0.34 stress level at early opening to traffic. This observation is also demonstrated by the cyclic fatigue performance of the tested specimen, where no deterioration was measured after applying 2.3 million cyclic loads (½ ESAL) at 1-d concrete age. Determining pavement fatigue life can also be achieved by using the S - N curves corresponding to 1-d loading, as presented in Figure 7-22. The obtained stress level for the jointed-slab model ($S = 0.34$) is observed to be less than the stress level of the rigid-slab model in section of 7.4.1 ($S = 0.57$). This difference is due to the presence of the dowel bars, which contribute in the shear and flexural behavior of the joint.

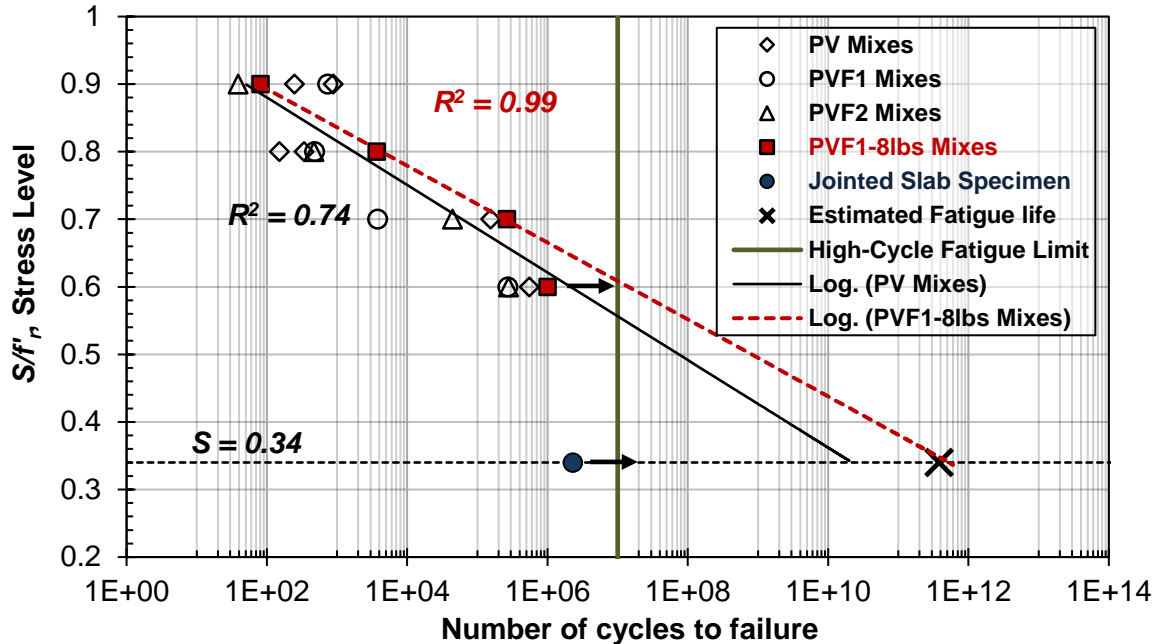


Figure 7-22. *S-N* results for PV, PVF1, PVF2, and PVF1-8lbs mixes at 1-d concrete age, showing estimated fatigue life of jointed-slab specimen (*ISLAB2000* model).

7.4.3 Estimation of Fatigue Life from Finite-Element Analysis Using ABAQUS/CAE Model Description

A 3D finite-element (FE) modeling of a jointed plain-concrete slab was constructed using the ABAQUS/CAE structural-analysis modeling package. The FE model included a concrete pavement cast on granular subgrade, two dowel bars connecting the loaded and unloaded slab, and an 11.3 x 11.3-in. steel loading plate. The slab dimensions were 7 ft x 2 ft x 6 in. The detailed FE modeling of the jointed-pavement slab and the supporting subgrade is shown in Figure 7-23. The model included two dowel bars spaced at 12 in. and placed at mid-height of the concrete pavement slab, as shown in Figure 7-24. A static analysis was performed to obtain the deformation and stress response of the modeled specimen subjected to ½ ESAL (9 kip).

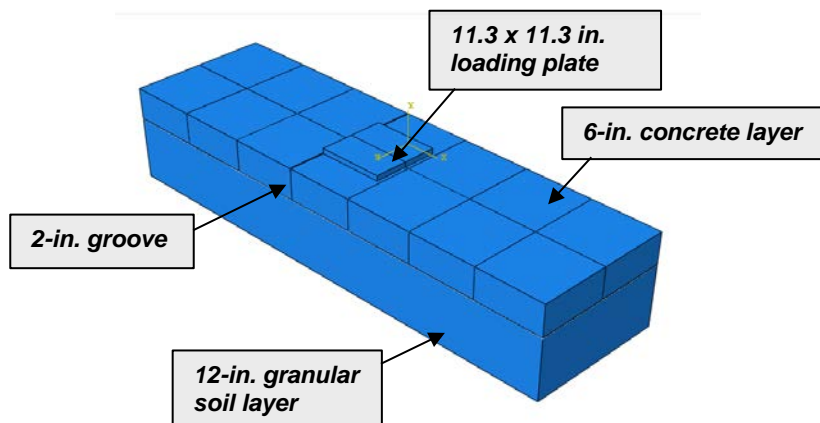


Figure 7-23. Isometric view of the solid modeling, showing supporting soil geometry.

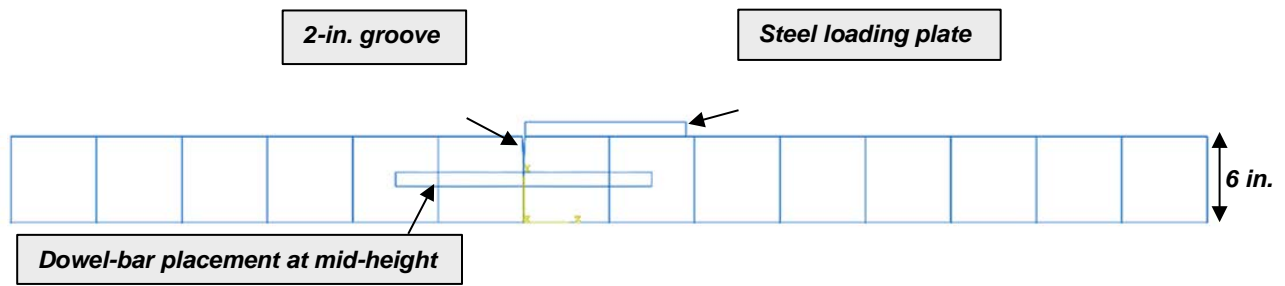


Figure 7-24. Elevation view showing solid modeling of the jointed-pavement.

The plain-concrete slab model was idealized by homogeneous material and modeled with eight-node solid (brick) elements, which are identified as C3D8R elements in ABAQUS. The C3D8R element is a general-purpose linear brick element with reduced integration. The dowels are also modeled using the C3D8R brick element and embedded in the concrete slab. The loading plate was meshed using the C3D8R element. The concrete slab and the loading plate were meshed using the 1-in. square element. A mesh size of 0.5 in. was used for the dowels. The detailed meshed FE model is shown in Figure 7-25.

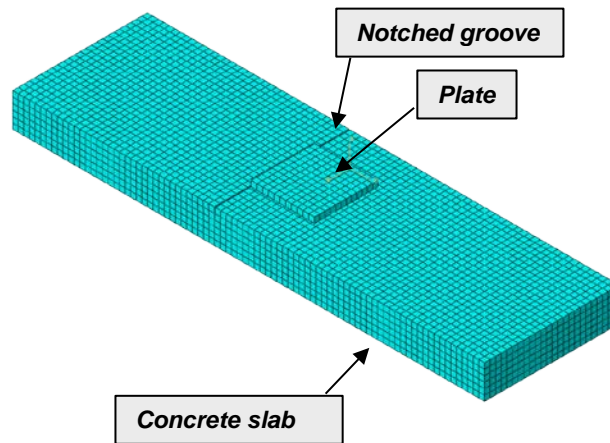
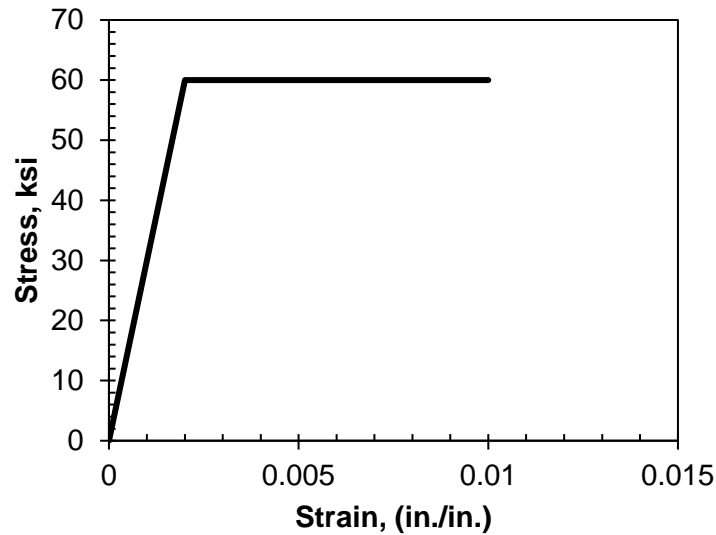


Figure 7-25. Finite-element meshing of concrete slab and loading plate.

The concrete damage plasticity model was used to define the nonlinear properties of concrete. A bilinear elasto-plastic stress–strain curve was used to define the properties of dowel bars as shown in Figure 7-26. The yield strength of dowels was assumed to be 60 ksi. The properties of concrete are shown in Table 7-3.

Table 7-3. Properties of Concrete

Ultimate compressive strength, f'_c	2,510 psi
Modulus of rupture, f_r	465 psi
Modulus of elasticity, E	2,650 ksi
Poisson ratio, μ	0.19

**Figure 7-26. Stress–strain curve for dowels.**

The appropriate boundary conditions that can mimic the experimental setup were assigned to the finite-element model. A frictional contact surface between the loading plate (11.3 x 11.3 in.) and the concrete slab was assigned to simulate the actual load-transfer mechanism from the testing machine actuator to the concrete slab. The load was applied at a low rate for accurate simulation of concrete crack initiation and soil response. For modeling the underlying soil, previous literature noted that the elastic modulus of subgrades can vary greatly, from 3.5 to 14.5 ksi, while subbase layers can vary from 14 to 58 ksi (Alam et al. 2013). Therefore, a value of 22.5 ksi was assigned for modeling the compacted granular layer, as used by Zdiri et al. (2009).

Finite-Element Modeling Results

The FEM results due to applied static load of ½ ESAL (9 kip) are discussed in this section and summarized in Table 7-4. The displacement contour lines at ½ ESAL are shown in Figure 7-27. Inspection of Figure 7-27 reveals a maximum downward displacement of 0.0058 in. underneath the loaded area. The principle stresses in the longitudinal direction for both top and bottom concrete fibers are shown in Figure 7-28. Inspection of Figure 7-28 indicates that the maximum longitudinal tensile stress from the FEM analysis was 175.7 psi at ½ ESAL (9 kip). In addition, the maximum longitudinal compressive stresses in the top concrete fiber were limited to 168.8 psi.

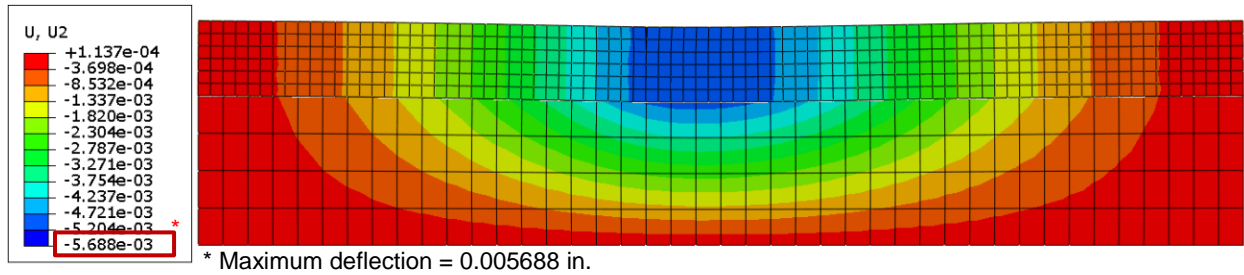


Figure 7-27. Displacement contour in the elevation view for the pavement and the supporting soil at 1/2 ESAL.

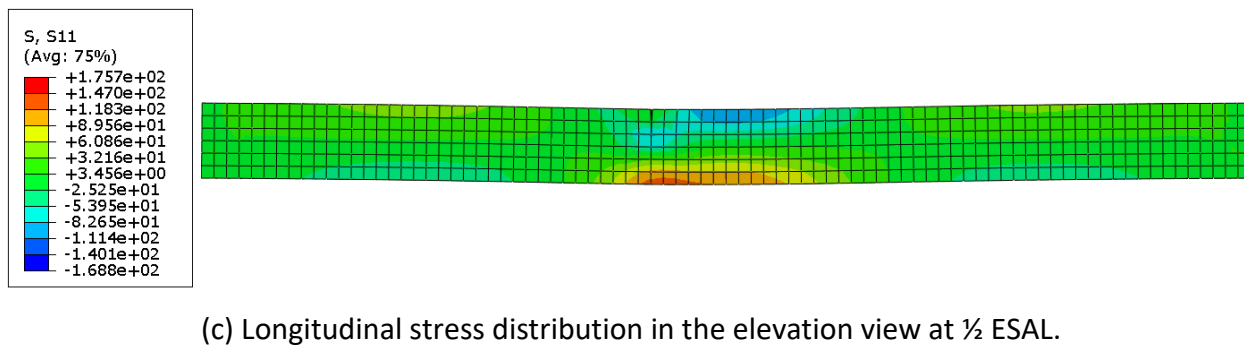
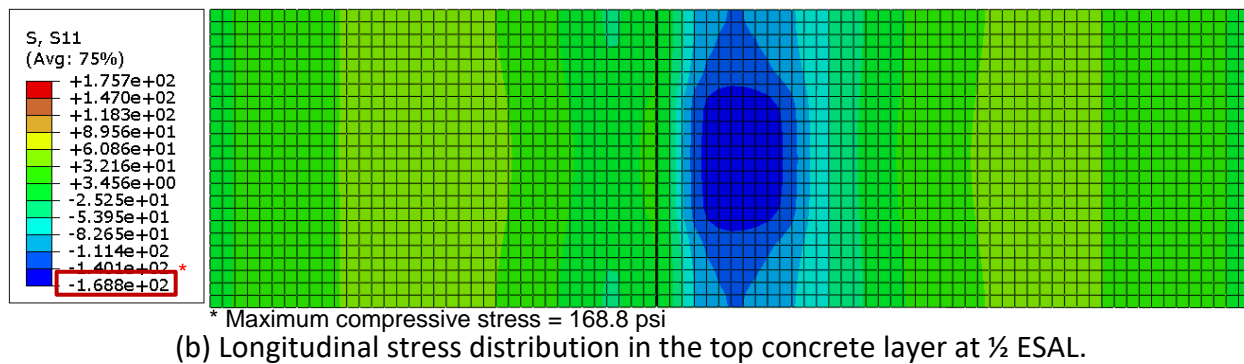
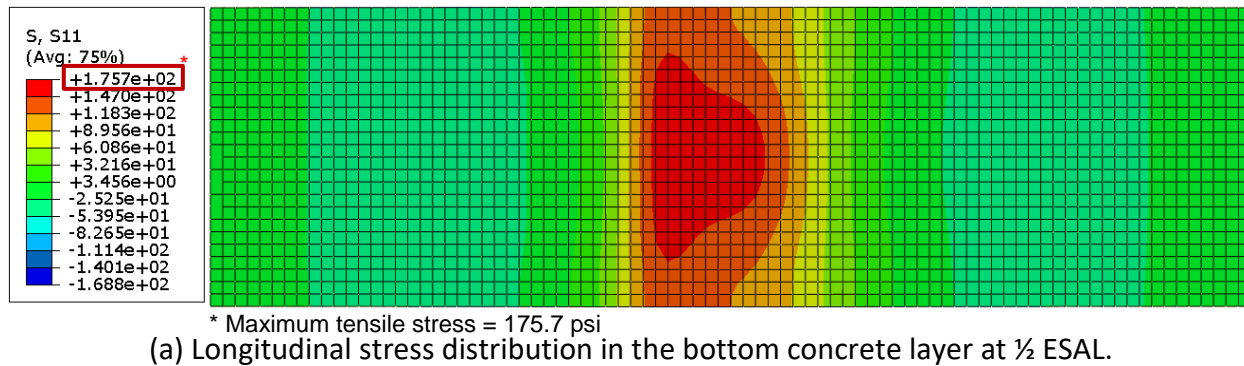
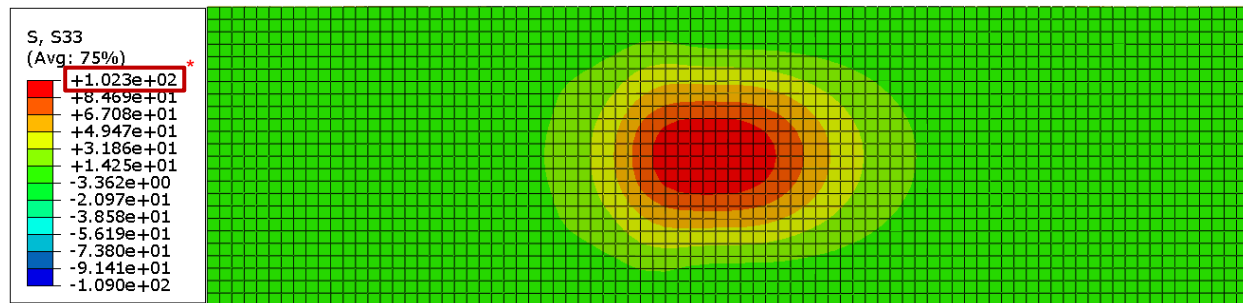


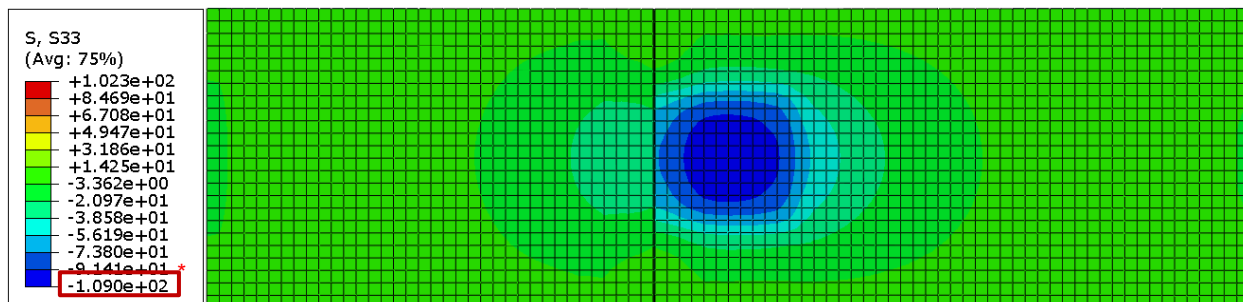
Figure 7-28. Longitudinal stress distribution.

The transverse principle stress distribution for the top and bottom fibers is shown in Figure 7-29. Inspection of Figure 7-29 indicates that the maximum transverse tensile stress obtained from the FEM was 102.3 psi, while the maximum transverse compressive stress was 109 psi. The stress distribution in dowels is shown in Figure 7-30. Inspection of Figure 7-30 reveals that the maximum induced stress in the dowels was 10.96 ksi, which corresponds to 18% of the yield stress (60 ksi). Shear stresses are also presented in Figure 7-31, where the maximum developed shear is limited to 179.3 psi.



* Maximum tensile stress = 102.3 psi

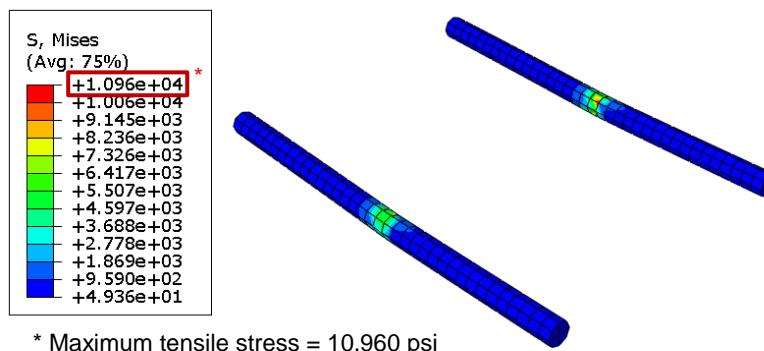
(a) Transverse stress distribution in the bottom concrete layer, due to $\frac{1}{2}$ ESAL.



* Maximum compressive stress = 109 psi

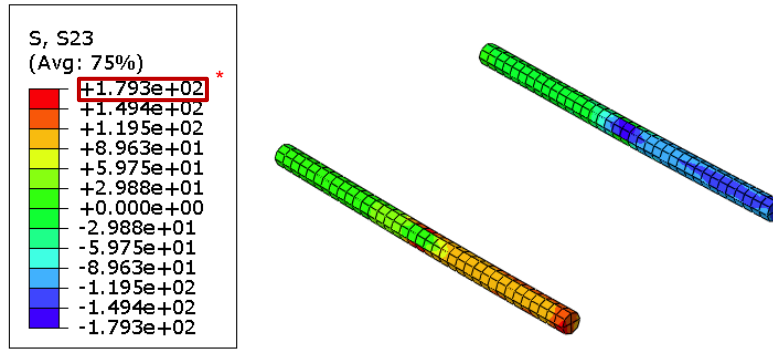
(b) Transverse stress distribution in the top concrete layer, due to $\frac{1}{2}$ ESAL.

Figure 7-29. Transverse stress distribution.



* Maximum tensile stress = 10,960 psi

Figure 7-30. Tensile stress distribution in the dowels bars at $\frac{1}{2}$ ESAL.



* Maximum shear stress = 179.3 psi

Figure 7-31. Shear stress distribution in the dowels bars at ½ ESAL.

Table 7-4. Numerical Results Summary

Element location	Tensile stress, psi	Compressive stress, psi	Shear stress, psi
Concrete slab, longitudinal direction	175.7	168.8	—
Concrete slab, transverse direction	102.3	109	—
Dowel bars	10,960	—	179.3

Estimation of fatigue life

Concrete flexural strength was experimentally measured at 465 psi, as mentioned in section 6.7. In addition, the maximum developed tensile stresses in the concrete pavement were 175.7 and 102.3 psi in the longitudinal and transversal directions, respectively. Accordingly, the stress level is calculated as follows:

$$S_{1-Day} = \frac{\sigma_y}{f_r} = \frac{\text{Max}(175.7 \text{ psi}, 102.3 \text{ psi})}{465 \text{ psi}} = 0.37$$

where S_{1-Day} = stress level ratio at 1-d concrete age

σ_{\max} = maximum tensile stress developed at the bottom of the PCC pavement due to ½ ESAL = 175.7 psi

f_r = modulus of rupture of concrete at 1-d of the jointed-slab specimen = 465 psi

The corresponding fatigue life is obtained by using the linear-regression S-N relationships for PVF1-8lbs mixes at 1-d concrete age (Table 7-1). The calculations shown below indicate that for a stress level of 0.37, no significant fatigue damage is accumulated at early opening to traffic (1-d). The same fatigue life result can be obtained by using the S-N curve plots, as presented in Figure 7-32. The obtained stress level ($S = 0.37$) is close to the calculated stress level in section 7.4.2 ($S = 0.34$). As noted, these results are found to be less critical when compared with the rigid-slab model of section 7.4.1 ($S = 0.57$) due to the embedment of the dowel bars.

$$S_{1-Day} = -0.025 \ln(N_{1-Day}) + 1.0066 = 0.37$$

$$Fatigue\ life_{1-Day} = \frac{N_{1-Day}}{4\text{ hz}} = 2.86 \times 10^{10}\text{ seconds}$$

Figure 10 is a log-log plot showing the relationship between the normalized stress level S/r_n (Y-axis, ranging from 0.2 to 1.0) and the Number of cycles to failure (X-axis, ranging from $1E+00$ to $1E+14$). The plot includes data points for various mixtures and specimens, along with logarithmic regression lines and a high-cycle fatigue limit.

Legend:

- \diamond PV Mixes
- \circ PVF1 Mixes
- \triangle PVF2 Mixes
- \blacksquare PVF1-8lbs Mixes
- \bullet Jointed Slab Specimen
- \times Estimated Fatigue life
- High-Cycle Fatigue Limit
- Log. (PV Mixes)
- - - Log. (PVF1-8lbs Mixes)

Key Features:

- The Y-axis is labeled S/r_n Stress Level.
- The X-axis is labeled Number of cycles to failure.
- A horizontal dashed line indicates $S = 0.37$.
- A vertical green line marks the High-Cycle Fatigue Limit at approximately 3.5×10^7 cycles.
- An arrow points to the 10 million cycles mark on the X-axis.

Figure 7-32. S-N results for PV, PVF1, PVF2, and PVF1-8lbs mixes at 1-d concrete age, showing estimated fatigue life of jointed-slab specimen (ABAQUS/CAE model).

CHAPTER 8: DESIGN AIDS FOR EARLY OPENING TO TRAFFIC

The following steps are presented in a simplified manner to fit the general formatting layout of the Illinois *Bureau Design and Environment Manual (BDE Manual)*. The content of the following can be implemented in future design aids currently under development by IDOT.

(a) Determine dynamic modulus.

$$E_D = C \cdot M \cdot n^2 \quad 8-1$$

where

E_D	=	dynamic modulus in Pascals, <u>converted to ksi for Step 2</u>
M	=	mass of beam specimen, kg
n	=	transverse resonant frequency, Hz
C	=	$0.9464 (L^3 T / b t^3)$
T	=	correction factor ($t / 3.464$)
L	=	length of specimen (0.53 m)
t	=	depth of specimen (0.15 m)
b	=	width of specimen (0.15 m)

(b) Determine modulus of rupture.

$$MOR = 49.86 \cdot EXP^{(5.29 \cdot 10^{-4} \cdot E_D)} \quad 8-2$$

where

MOR	=	modulus of rupture, psi
E_D	=	dynamic modulus of elasticity Step 1, ksi

The modulus of rupture can be alternatively obtained from Figure 8-1:

(c) Determine tensile stress.

The maximum developed tensile stresses due to ESAL (18 kip) are obtained as follows:

- *Option 1:* Use the charts in Figures 8-2 to 8-11 for a specified subgrade modulus reaction value (50–500 psi/in.)
- *Option 2:* Use nomographs in Figures 8-12 to 8-15 or a specified concrete age (12 hr to 7 d).

(d) Determine stress level ratio.

$$S = \sigma / \text{MOR} \quad 8-3$$

where

S = stress level ratio
 σ = maximum developed tensile stress, psi
MOR = modulus of rupture, psi

(e) Determine fatigue life.

The number of cyclic loads until failure (N) is determined using Tables O-1 to O-4 for plain- and fiber-reinforced concrete pavement mixes. Figures O-16 to O-19 can be alternatively used for the same purpose.

(f) Determine fatigue life.

$$\text{FL} = N / 4 \quad 8-4$$

Where

FL = fatigue life of pavement, sec
N = number of cyclic loads until failure

REFERENCES

- AASHTO Guide for Design of Pavement Structures. 1993. American Association of State Highway and Transportation Officials, Washington, DC.
- ACI Committee 215. 1993. "Consideration for design of concrete structures subjected to fatigue loading," pp. 215R-1–215R-24. In ACI Manual of Concrete Practice Part I. ACI 215R-74. American Concrete Institute, Detroit, MI. ACI 215R-74. ACI 215R-74.
- ACI Committee 360. 1992. *Design of Slabs on Grade*. ACI 360R-92. American Concrete Institute, Farmington Hills, MI, 57 pp.
- ACI Committee, American Concrete Institute, and International Organization for Standardization. 2008. *Building code requirements for structural concrete (ACI 318-08) and commentary*.
- Alam, A., Haselbach, L., & Cofer, W. F. 2013. *Three-Dimensional Finite Element Modeling of Pervious Concrete Pavement: Vertical Porosity Distribution Approach*. *International Journal of Research in Engineering and Technology*, 2(12), 767-777.
- Alexander, K. M., and J. H. Taplin. 1962. "Concrete Strength, Paste Strength, Cement Hydration, and the Maturity Rule." *Australian Journal of Applied Science* 13, no. 4:277–284.
- American Concrete Institute. 1956. "Structural Design Considerations for Pavement Joints." Report of ACI Committee 325. *ACI Journal*, 53(7), 1-28. American Concrete Institute. Farmington Hills, MI.
- American Concrete Pavement Association (ACPA). 1991. *Design and Construction of Joints for Concrete Highways*. ACPA, Skokie, IL, 24 pp.
- ARA, Inc., ERES Division. 2003. *Guide for Mechanistic-Empirical Design of new and rehabilitated pavement structures*.
- ASTM C1074-11. 2011. *Standard Practice for Estimating Concrete Strength by the Maturity Method*. ASTM International, West Conshohocken, PA. <https://doi.org/10.1520/C1074-11>
- ASTM C150/C150M-17. 2017. *Standard Specification for Portland Cement*. ASTM International, West Conshohocken, PA. https://doi.org/10.1520/C0150_C0150M-17
- ASTM C157/C157M-08(2014)e1. 2014. *Standard Test Method for Length Change of Hardened Hydraulic-Cement Mortar and Concrete*. ASTM International, West Conshohocken, PA. https://doi.org/10.1520/C0157_C0157M-08R14E01
- ASTM C1609/C1609M-12. 2012. *Standard Test Method for Flexural Performance of Fiber-Reinforced Concrete (Using Beam With Third-Point Loading)*. ASTM International, West Conshohocken, PA. https://doi.org/10.1520/C1609_C1609M-12
- ASTM C192/C192M-16a. 2016. *Standard Practice for Making and Curing Concrete Test Specimens in the Laboratory*. ASTM International, West Conshohocken, PA. https://doi.org/10.1520/C0192_C0192M-16A
- ASTM C215-14. 2014. *Standard Test Method for Fundamental Transverse, Longitudinal,*

- and Torsional Resonant Frequencies of Concrete Specimens*. ASTM International, West Conshohocken, PA. <https://doi.org/10.1520/C0215-14>
- ASTM C231/C231M-17a *Standard Test Method for Air Content of Freshly Mixed Concrete by the Pressure Method*. 2017. ASTM International, West Conshohocken, PA. https://doi.org/10.1520/C0231_C0231M-17A
- ASTM C260/C260M-10a (2016). 2016. *Standard Specification for Air-Entraining Admixtures for Concrete*. ASTM International, West Conshohocken, PA. https://doi.org/10.1520/C0260_C0260M-10AR16
- ASTM C39/C39M-17b. 2017. *Standard Test Method for Compressive Strength of Cylindrical Concrete Specimens*. ASTM International, West Conshohocken, PA. https://doi.org/10.1520/C0039_C0039M-17B
- ASTM C403/C403M-16. 2016. *Standard Test Method for Time of Setting of Concrete Mixtures by Penetration Resistance*. ASTM International, West Conshohocken, PA. https://doi.org/10.1520/C0403_C0403M-16
- ASTM C426-16. 2016. *Standard Test Method for Linear Drying Shrinkage of Concrete Masonry Units*. ASTM International, West Conshohocken, PA. <https://doi.org/10.1520/C0426-16>
- ASTM C457/C457M-16. 2016. *Standard Test Method for Microscopical Determination of Parameters of the Air-Void System in Hardened Concrete*. ASTM International, West Conshohocken, PA. https://doi.org/10.1520/C0457_C0457M-16
- ASTM C469/C469M-14. 2014. *Standard Test Method for Static Modulus of Elasticity and Poisson's Ratio of Concrete in Compression*. ASTM International, West Conshohocken, PA. https://doi.org/10.1520/C0469_C0469M
- ASTM C490/C490M-17. 2017. *Standard Practice for Use of Apparatus for the Determination of Length Change of Hardened Cement Paste, Mortar, and Concrete*. ASTM International, West Conshohocken, PA. https://doi.org/10.1520/C0490_C0490M-17
- ASTM C494/C494M-17. 2017. *Standard Specification for Chemical Admixtures for Concrete*. ASTM International, West Conshohocken, PA. https://doi.org/10.1520/C0494_C0494M-17
- ASTM C666/C666M-15. 2015. *Standard Test Method for Resistance of Concrete to Rapid Freezing and Thawing*. ASTM International, West Conshohocken, PA. https://doi.org/10.1520/C0666_C0666M-15
- ASTM C78/C78M-16. 2016. *Standard Test Method for Flexural Strength of Concrete (Using Simple Beam with Third-Point Loading)*. ASTM International, West Conshohocken, PA. https://doi.org/10.1520/C0078_C0078M-16
- ASTM D1196/D1196M-12. 2016. *Standard Test Method for Nonrepetitive Static Plate Load Tests of Soils and Flexible Pavement Components, for Use in Evaluation and Design of Airport and Highway Pavements*. ASTM International, West Conshohocken, PA. https://doi.org/10.1520/D1196_D1196M-12R16
- ASTM D4694. 2009. *Standard Test Method for Deflections with a Falling-Weight-Type Impulse*

Load Device. ASTM International, West Conshohocken, PA, 3 pp.

- Barker, W. R., and D. R. Alexander. 2012. *Determining the Effective Modulus of Subgrade Reaction for Design of Rigid Airfield Pavements Having Base Layers*. US Army Corps of Engineers, Engineer Research and Development Center, Geotechnical and Structures Laboratory.
- Bazant, Zdenek P., and Jaime Planas. 1998. *Fracture and Size Effect in Concrete and Other Quasibrittle Materials*. CRCP Press: New York, NY.
- Benmokrane, B., E. A. Ahmed, M. Montagu, and D. Thebeau. 2014. "Performance of Glass Fiber-Reinforced Polymer-Doweled Jointed Plain Concrete Pavement under Static and Cyclic Loadings." *ACI Structural Journal* 111(2):331. Université de Sherbrooke, Canada.
- Bricola, J., E. Ahmed, B. Benmokrane, and D. Thebeau. 2014. *Structural Testing of GFRP Dowels in Jointed Plain Concrete Pavement*. Master's thesis, Université de Sherbrooke, Canada.
- Carino, N. J., and V. M. Malhotra. 1991. "The Maturity Method," pp. 101–146. In *Handbook on Nondestructive Testing of Concrete*, 2nd ed. CRC Press: Boca Raton, FL.
- Chavan, H. L. 2012. *Field investigation of subgrade non-uniformity effects on concrete pavement*. Doctoral dissertation, University of Illinois at Urbana–Champaign.
- Clemmer, H. F. 1922. "Fatigue of Concrete," pp. 408–419. In *Proceedings of the American Society for Testing Materials*, vol. 22, II.
- Crovetti, J. A., and L. Khazanovich. 2005. *Early Opening of Portland Cement Concrete (PCC) Pavements to Traffic*. Final report no. WHRP 05-13. Wisconsin Department of Transportation: Division of Transportation Infrastructure Development, Research Coordination Section. Madison. 85 pp.
- Crovetti, J. A. 1994. *Design and evaluation of jointed concrete pavement systems incorporating free-draining base layers*. Doctoral dissertation, University of Illinois at Urbana–Champaign.
- Crepps, R. B. "Fatigue of Mortar," pp. 329–340. In *Proceedings of the American Society for Testing Materials*, vol. 23, II.
- Eddie, D., A. Shalaby, and S. Rizkalla. 2001. "Glass fiber-reinforced polymer dowels for concrete pavements." *ACI Structural Journal* 98(2):201–206.
- Griffith A. A. 1921. "The phenomena of rupture and flow in solids." *Phil. Trans. Roy. Soc.*, series A221:163–168.
- Grzybowski, M., & Meyer, C. 1993. "Damage accumulation in concrete with and without fiber reinforcement". *Materials Journal*, 90(6), 594-604.
- Hatt, W. K. 1924. "Fatigue of Concrete," pp. 47–60. In *Proceedings, 4th Annual Meeting. Highway Research Board*. National Research Council.
- Hilsdorf, H., and C. E. Kesler. 1960. *The Behavior of Concrete in Flexure Under Varying Repeated Loads*. T. & A. M. Report No. 172. University of Illinois.

- Hsu, Thomas T. C. (1981). "Fatigue of Plain Concrete." *ACI Structural Journal* 292–304.
- Illinois Department of Transportation (IDOT). 2016. Bureau of Design and Environment Manual. Springfield, IL
- Illinois Department of Transportation (IDOT). 2016. *Maximum Legal Dimensions & Weights*. <http://www.idot.illinois.gov/Assets/uploads/files/IDOTForms/OPER/OPER%20753.pdf>
- Illinois Department of Transportation (IDOT). 2016. *Standard specifications for road and bridge construction*. Illinois Department of Transportation, Springfield, IL.
- Islam, Md Shahidul. 2000. *Specimen and Aggregate Size Effect on the Fracture Behavior of Concrete*. Ph.D. dissertation, University of Illinois at Chicago. UMI Number; 9978661.
- Issa, M. A. 2014. "Effect of Portland Cement (current ASTM C150/AASHTO M85) with Limestone and Process Addition (ASTM C465/AASHTO M327) on the Performance of Concrete for Pavement and Bridge Decks". Illinois Center for Transportation.
- Jenq, Y. S., and S. P. Shah. 1985a. "A fracture toughness criterion for concrete." *Eng. Fract. Mech.* 21 (5):1055–1069.
- Jenq, Y. S., and S. P. Shah. 1985b. "Two parameter fracture model for concrete." *J. Eng. Mech.* 111(10):1227–1241.
- Johnston, C. D., & Zemp, R. W. 1991. "Flexural Fatigue Performance of Steel Fiber Reinforced Concrete--Influence of Fiber Content, Aspect Ratio, and Type". *Materials Journal*, 88(4), 374-383.
- Kaplan, F. M. 1961. "Crack propagation and fracture of concrete." *Journal of the American of Concrete Institute* 58(5):591–610.
- Karihaloo, B. L., and P. Nallathambi. 1961. "Notched Beam Test: Mode I Fracture Toughness," pp. 1–86. In *RILEM Report 5 Fracture Mechanics Test Methods for Concrete*. S. P. Shah and A. Carpinteri, eds. Chapman and Hall: New York.
- Kazberuk, M. K. 2012. "Effects of Interaction of Static Load and Frost on Damage Mechanism of Concrete Elements." *Journal of Sustainable Architecture and Civil Engineering*. Online ISSN: 2335–2000, DOI: <http://dx.doi.org/10.5755/j01.sace.1.1.2616>.
- Kesler, C. E. 1953. "Effect of Speed of Testing on Flexural Fatigue Strength of Plain Concrete," pp. 251–258. In *Proceedings, Highway Research Board*, vol. 32.
- Klaiber, W., and Dah-Yinn Lee. 1982. "The Effects of Air Content, Water-Cement Ratio, and Aggregate Type on the Flexural Fatigue Strength of Plain Concrete," pp. 111–131. Special Publication SP 75-5. American Concrete Institute.
- Lee, M. K., and B. I. G. Barr. 2004. "An overview of the fatigue behaviour of plain and fibre reinforced concrete." *Cement & Concrete Composites* 26(4):299–305.
- Murdock J. W., and C. E. Kesler. 1958. "Effect of Range of Stress on Fatigue Strength of Plain Concrete Beams." *Journal of the American Concrete Institute* 30(2):221–233.

- Murdock, J. W., and C. E. Kesler. 1960. *The Mechanism of Fatigue Failure in Concrete*. T. & A. M. report no. 587. University of Illinois.
- Nurse, R. W. 1949. "Steam Curing of Concrete." *Magazine of Concrete Research* 1(2):79–88.
- Olek, J., M. D. Cohen, C. F. Scholer, and D. R. Mandrekar. 2002. *Use of Modulus of Rupture, Fatigue Resistance and Maturity in Determining Opening to Traffic Time for Concrete Pavements*. Final contract report no. FHWA/IN/JTRP-2000/25. Indiana Department of Transportation, West Lafayette. 86 pp.
- Paskova, T., & Meyer, C. 1997. "Low-cycle fatigue of plain and fiber-reinforced concrete. *ACI Materials Journal*", 94(4), 273-285.
- Popehn, N. A., M. B. Snyder, and A. E. Schultz. 2003. Performance Testing of Experimental Dowel Bar Retrofit Designs: Part 2—Repeatability and Modified Designs.
- Roesler, J., J. T. Harvey, J. Farver, and F. Long. 2000. *Investigation of Design and Construction Issues for Long Life Concrete Pavement Strategies*. Final report no. FHWA/CA/OR-2000/04. California Department of Transportation. 63 pp.
- Shah, S. P. 1990. "Determination of fracture parameters (K_{Ic} CTOD_c) of plain concrete using three-point bend tests." *Mat. and Struct.* 23:457–460.
- Strange, P. C., and A. H. Bryant. 1979. "Experimental tests on concrete fracture." *Journal of the Engineering Mechanics Division*, AS CE, 105:337–342.
- Suh, P. 2005. *The Effect of Early Opening to Traffic on Fatigue Life of Concrete Pavement*. PhD dissertation, The University of Texas at Austin, Austin, TX. 162 pp.
- Tarr, S. M., and J. A. Farny. 2008. "Concrete floors on ground," pp. 55–76. Skokie: Portland Cement Association.
- Timoshenko, S., & Lessels, J. M. 1925. "Applied Elasticity". Westinghouse Technology. Verbeck, G. J., and R. H. Helmuth. 1968, "Structure and Physical Properties of Cement Paste," pp. 1–32. In *Proceedings, Fifth International Symposium on the Chemistry of Cement*, Part III. Tokyo.
- Vijay, P. V., and H. V. GangaRao, H. Li. 2009. *Design and evaluation of jointed plain concrete pavement with fiber reinforced polymer dowels*. No. FHWA-HRT-06-106.
- Williams, H. A. 1943. "Fatigue Tests of Light-weight Aggregate Concrete Beams," pp. 441–447. In *Proceedings, American Concrete Institute*, vol. 39.
- Wong, W., and R. A. Miller. 1990. "Mixed Mode Fracture at Early Ages," pp. 166–175. In *Micromechanics of Failure of Quasi-Brittle Material*. S. P. Shah, S. E. Swartz, and M. L. Wang, eds. New York: Elsevier.
- Yin, W., and T. C. C. Hsu. 1995. "Fatigue behavior of steel fiber reinforced concrete in uniaxial and biaxial compression." *ACI Mater J* 1995; 92(1):71–81.
- Yoder, E. J., and M. W. Witczak. 1975. *Principles of pavement design*. John Wiley & Sons.

Zdiri, M., Abriak, N., Neji, J., & Ouezdou, M. B. 2009.

“Modelling of the Stresses and Strains Distribution in an RCC Pavement Using the Computer Code "Abaqus"”. *Circulation*, 7, 7m. Zhang, J., and Q. Liu. 2003. “Determination of Concrete Fracture Parameters from a Three-Point Bending Test.” *TSINGHUA SIENCE AND TECHNOLOGY* 8(6):726–733. ISSN 1007-0214 15/21.

APPENDIX A FRESH PROPERTIES OF CONCRETE MIXES

Table A-1. Fresh properties of Pavement (PV) mixes

Mix Type	Fiber s	Mix No.	Batch Type	w/c m ratio	Fiber Content, lb	AEA, fl. Oz/cwt	HRWR, fl. Oz/cwt	Slump, in.	Unit Weight, lb/ft ³	Air Content, %
Pavement (PV)	Plain Concrete	PV-RT	Compression	0.42	0.0	2.69	4.31	4.5	144.08	7.4
			Flexure			2.77	4.27	4.75	144.90	7
			FM			1.73	4.16	4.5	144.4	6.8
			0.9-Fatigue-I			1.96	3.46	4	144.76	6.8
			0.8-Fatigue-I			2.29	4.04	4.75	144.12	7.1
			0.8-Fatigue-II			2.15	4.04	4.75	143.92	7
			0.8-Fatigue-III			2.02	3.91	4.5	144.64	7
			0.7-Fatigue-I			2.02	3.91	5	145.28	6.5
			0.6-Fatigue-I			2.42	4.31	5	143.04	7.5
			0.6-Fatigue-II			2.42	4.47	4	143.6	6.5
			0.6-Fatigue-III			2.42	4.58	5	145.64	6.4
			FT-I			2.42	4.04	4	143.68	7.2
			FT-II			2.42	4.04	5	144.88	6.9
			Slab #2-I			2.77	2.31	5.75	140.8	8
			Slab #2-II			2.77	2.31	5.75	140.8	8
		PV-45F	Compression	0.42	0.0	3.10	4.58	4	144.12	7.2
			Flexure			3.12	4.27	4	144.08	7

FM: Fracture Mechanics; AEA: Air entraining agent; HRWR: high range water reducer

Table A-1. Fresh properties of Pavement (PV) mixes (Continued)

Mix Type	Fibers	Mix No.	Batch Type	w/c m ratio	Fiber Content, lb	AEA, fl. Oz/cwt	HRWR, fl. Oz/cwt	Slump, in.	Unit Weight, lb/ft ³	Air Content, %
Pavement (PV)	Strux 90/40	PVF1-RT	Compression	0.42	4.0	3.37	5.12	3.5	144.76	7
			Flexure			3.58	5.31	3	144.44	7.1
			FM			1.96	4.62	3.5	143.92	7
			0.9-Fatigue-I			1.89	4.58	3.5	145.12	6
			0.8-Fatigue-I			2.02	4.71	3.25	145.28	6.3
			0.7-Fatigue-I			2.02	4.71	3.25	145.08	6.3
			FT-I			3.03	5.05	3.25	142.76	7.6
			FT-II			4.85	8.89	3	144.88	6.6
			FT-III			2.83	5.05	3	144.36	7
			FT-IV			2.83	5.05	2.75	144.56	6.9
		PVF1-45F	Compression	0.42	4.0	3.77	5.25	3.5	144.68	7
			Flexure			3.92	5.31	3.5	144.2	7
		PVF1-6-RT	Compression	0.42	6.0	3.23	5.92	4	143.36	7.3
			Flexure			2.42	5.19	3.25	144.2	7
			FM			1.99	4.62	3	144.84	6
		PVF1-8-RT	Compression	0.42	8.0	2.56	6.33	4	144.76	6.6
			Flexure			2.70	6.58	4	144.36	6.8
			FM			2.14	5.31	3	144.04	6.8
			0.9-Fatigue-I			2.42	6.33	3	144.88	5
			0.8-Fatigue-I			2.42	6.19	3	146.88	5.5
			0.7-Fatigue-I			2.56	6.06	4	143.68	7
			0.6-Fatigue-I			2.53	6.19	3	143.8	5.3
			0.6-Fatigue-II			3.23	5.92	3	143.8	7
			FT-I			3.43	6.87	3	143.2	7
			FT-II			3.43	6.87	3	143.2	7
			Slab #1 -I			2.54	7.04	7	144.88	8
			Slab #1-II			2.65	7.04	7	144.2	7.8
			Slab #3			2.31	4.62	3.5	142.3	8
			Slab #5-I			2.02	4.58	-	143.2	7
			Slab #5-II			2.02	4.58	-	142.5	7.2
			Slab #5-III			2.02	4.58	-	142.5	7.2
	MAC Matrix	PVF2-RT	Compression	0.42	4.0	3.37	5.12	3.5	144.76	7
			Flexure			3.58	5.31	3	144.44	7.1
			FM			1.73	4.39	4	144.44	6.8
			0.9-Fatigue-I			1.89	4.44	4	144.48	6.3
			0.8-Fatigue-I			2.02	4.44	5	144.16	7.1
			0.7-Fatigue-I			1.96	4.66	3	144.88	6.7
		PVF2-45F	Compression	0.42	4.0	3.37	4.71	4	144.44	7
			Flexure			3.58	4.85	3.5	144.36	7.1

FM: Fracture Mechanics; AEA: Air entraining agent; HRWR: high range water reducer

Table A-2. Fresh properties of Pavement Patches (PP1 and PP2) mixes

Mix Type	Fibers	Mix No.	Batch Type	w/cm ratio	Fiber Content, lb	AEA, fl. Oz/cwt	HRWR, fl. Oz/cwt	Slump, in.	Unit Weight, lb/ft ³	Air Content, %
Pavement Patch 1 (PP1)	NA	PP1-RT-0.44	Compression	0.44	0.0	3.51	0.23	4	143.2	6.5
			Flexure			2.61	0.20	4	143.08	6.5
		PP1-RT-0.42	Compression	0.42	0.0	2.46	1.52	5.5	143.12	6.8
			Flexure			2.61	1.50	5.25	143	7
			FM			2.11	1.97	4.8	143.8	6.9
		PP1-45F-0.42	Compression	0.42	0.0	2.34	1.40	5.75	143.28	6.7
			Flexure			2.21	1.50	5.75	143.48	6.7
	Strux 90/40	PP1F1-RT-0.44	Compression	0.44	4.0	3.58	0.94	4	142.28	6.7
			Flexure			3.21	0.80	3.5	143.12	6.4
		PP1F1-45F-0.44	Compression	0.44	4.0	3.82	1.05	4	142.36	6.9
			Flexure			3.41	1.00	4.25	142.08	6.9
		PP1F1-RT-0.42	Compression	0.42	4.0	1.94	2.81	5.5	144.08	6.6
			Flexure			2.21	3.01	5.25	143.76	6
			FM			2.11	1.97	4.8	143.8	6.9
		PP1F1-45F-0.42	Compression	0.42	4.0	1.87	2.58	4	144.08	6.4
			Flexure			1.91	2.61	5	143.76	6.5
Pavement Patch 2 (PP2)	NA	PP2-RT	Compression	0.36	0.0	2.90	4.04	4	145.2	5.85
			Flexure			2.31	3.90	4	145.92	5.6
			FM			1.86	3.55	6	144.64	6
		PP2-45F	Compression	0.36	0.0	2.69	4.14	4.5	146.08	5.6
			Flexure			3.11	4.08	4.25	145.96	5.7
	Strux 90/40	PP2F1-RT	Compression	0.36	4.0	3.73	5.38	3.75	146.28	5.6
			Flexure			3.55	5.06	3.25	146	5.8
			FM			2.04	4.97	3.75	145.76	6
		PP2F1-45F	Compression	0.36	4.0	3.73	5.18	4.75	146.28	5.7
			Flexure			3.90	5.15	3.75	145.48	5.9

FM: Fracture Mechanics; AEA: Air entraining agent; HRWR: high range water reducer

APPENDIX B COMPRESSIVE STRENGTH RESULTS

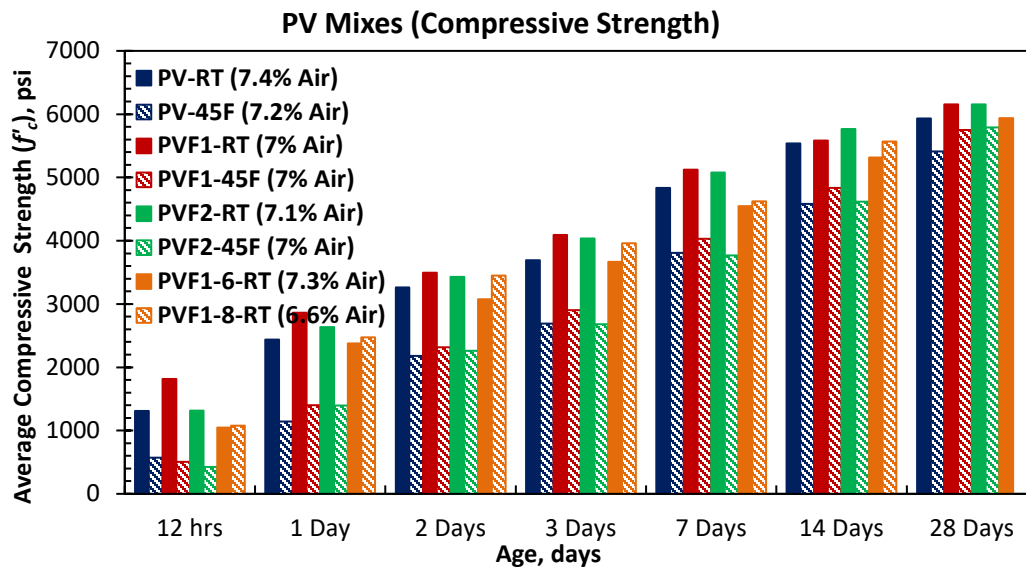


Figure B-1. Compressive strength gain in PV mixes

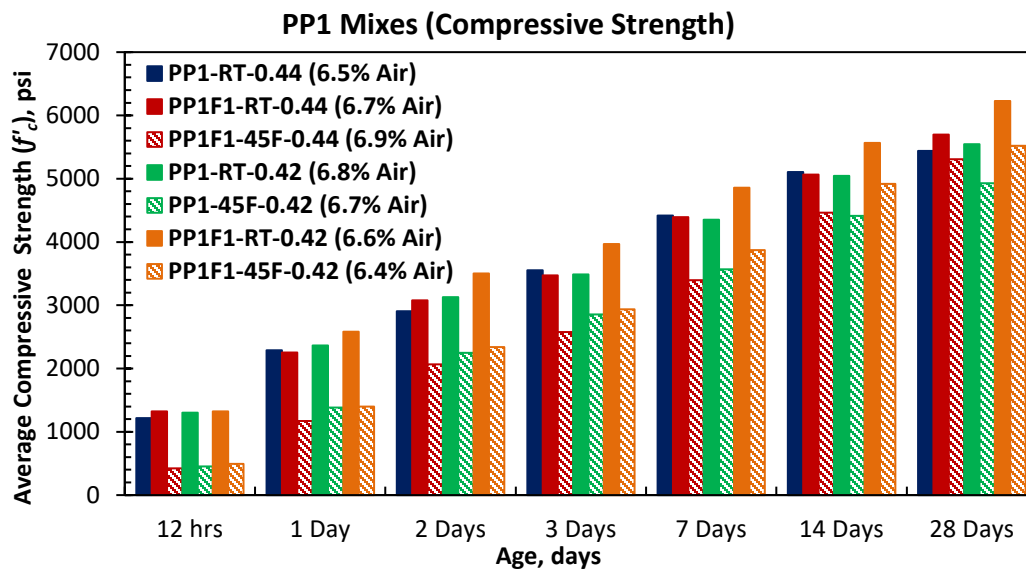


Figure B-2. Compressive strength gain in PP1 mixes

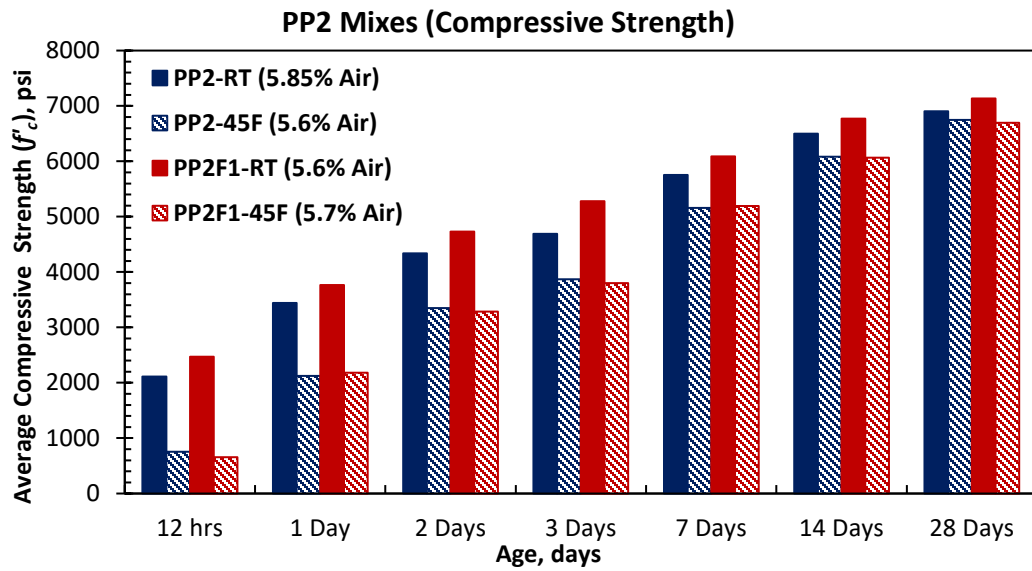


Figure B-3. Compressive strength gain in PP2 mixes

APPENDIX C FLEXURAL STRENGTH RESULTS

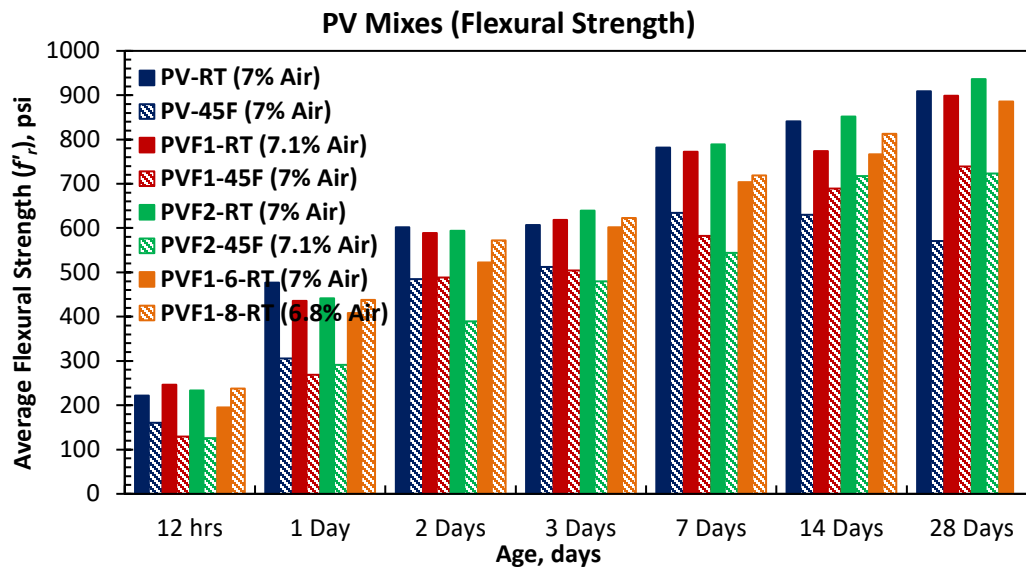


Figure C-1. Flexural strength gain in PV mixes

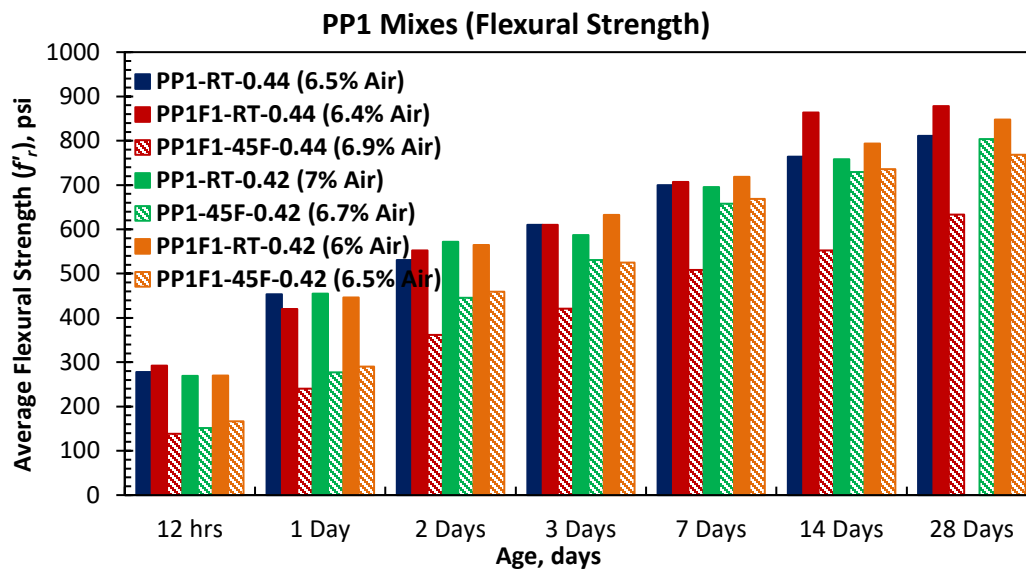


Figure C-2. Flexural strength gain in PP1 mixes

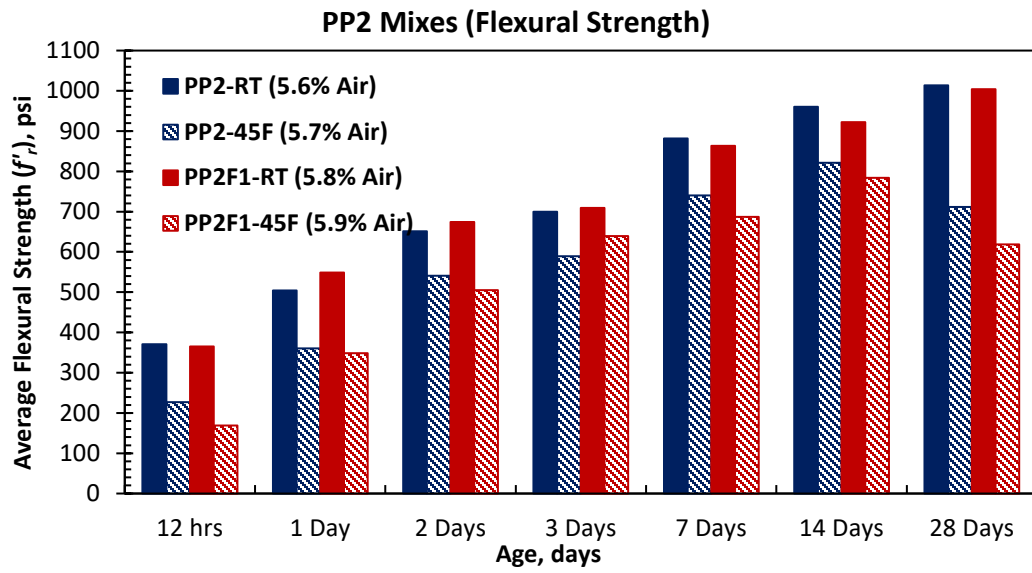


Figure C-3. Flexural strength gain in PP2 mixes

APPENDIX D FLEXURE TOUGHNESS CHARACTERISTICS

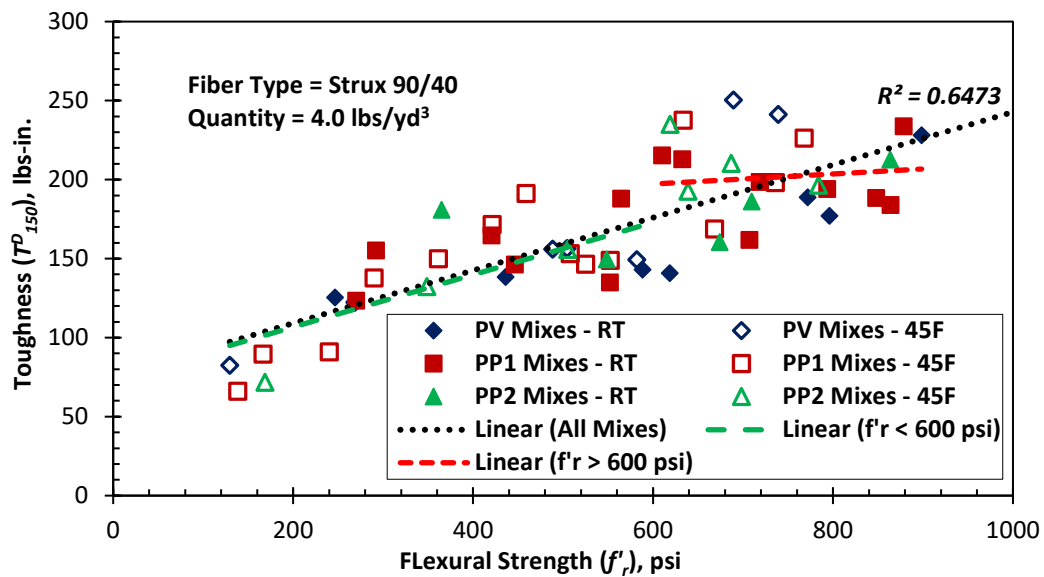


Figure D-1. Flexural toughness vs. flexural strength in PV, PP1, and PP2 mixes (4.0 lb of Strux 90/40)

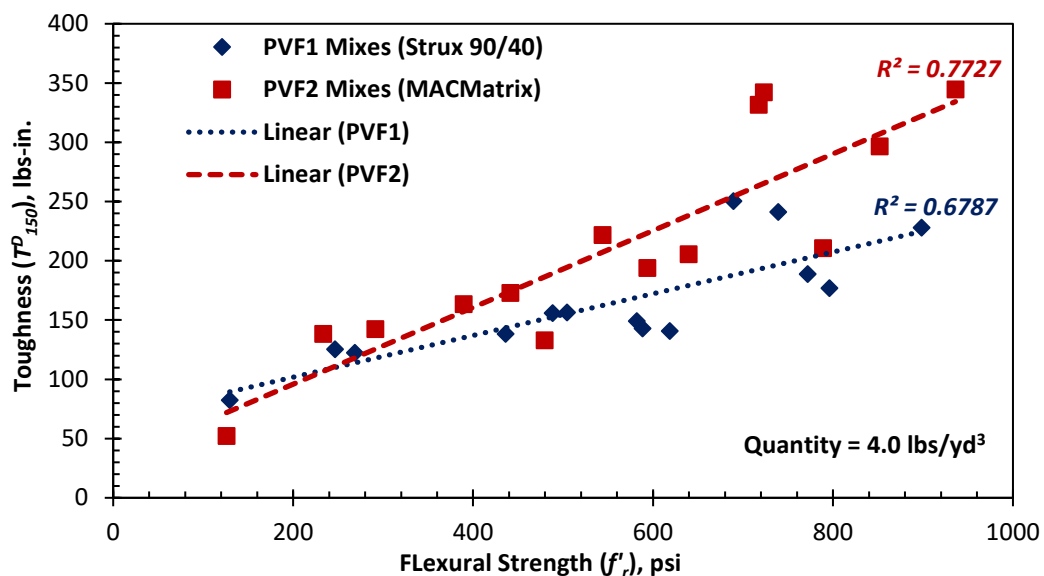


Figure D-2. Flexural toughness vs. flexural strength in PVF1 (Strux 90/40) and PVF2 (MACMatrix)

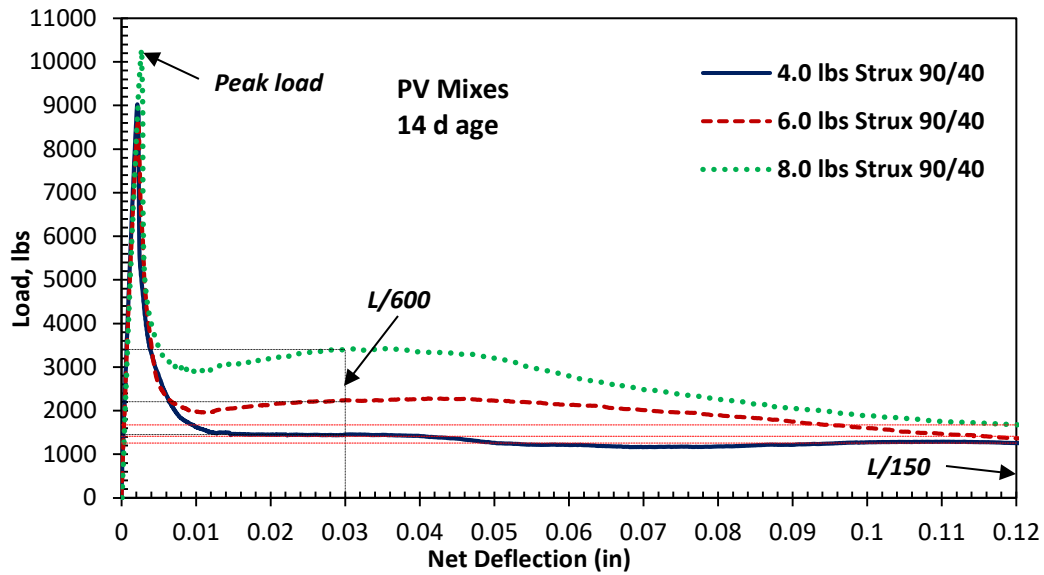


Figure D-3. Flexure Toughness in PVF1 with 4, 6, and 8 lb of Strux 90/40

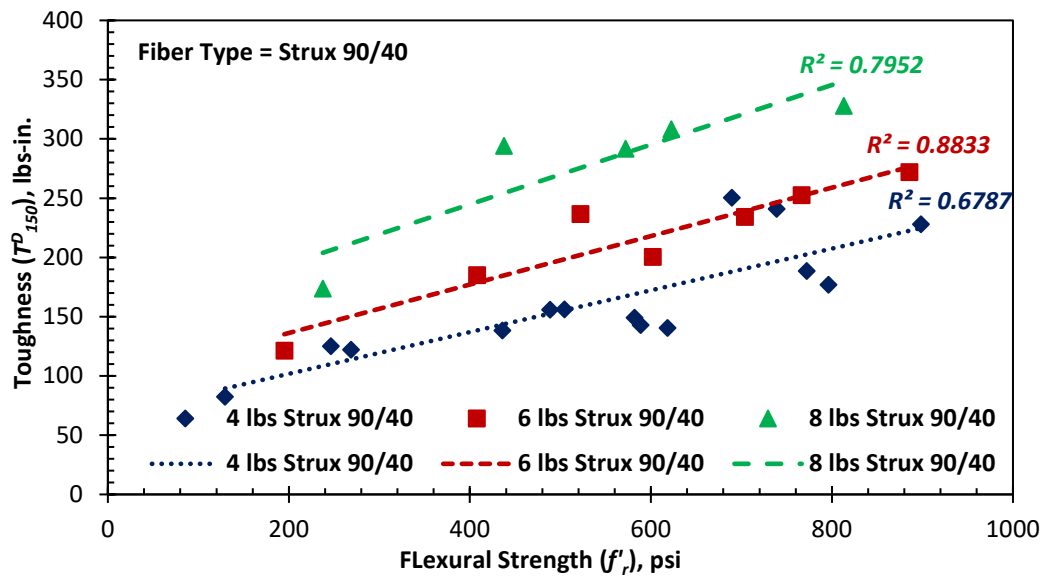


Figure D-4. Flexure toughness vs. flexural strength in PVF1 mixes with different amount of Strux 90/40

APPENDIX E COMPRESSIVE STRENGTH AND STATIC MOE RELATION

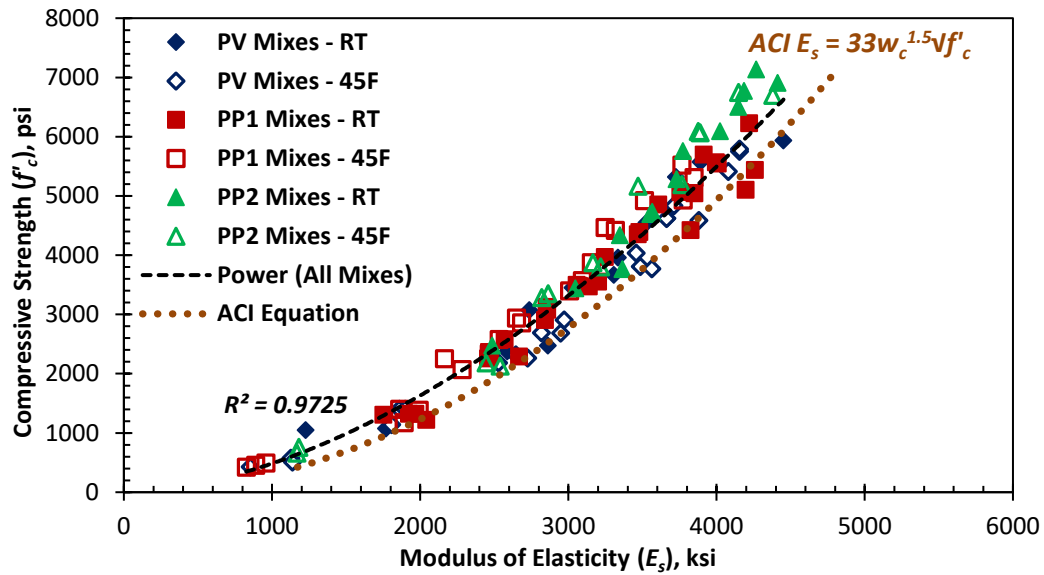


Figure E-1. Compressive strength versus static modulus of elasticity in PV, PP1, and PP2 mixes

APPENDIX F MATURITY IN CONCRETE RESULTS

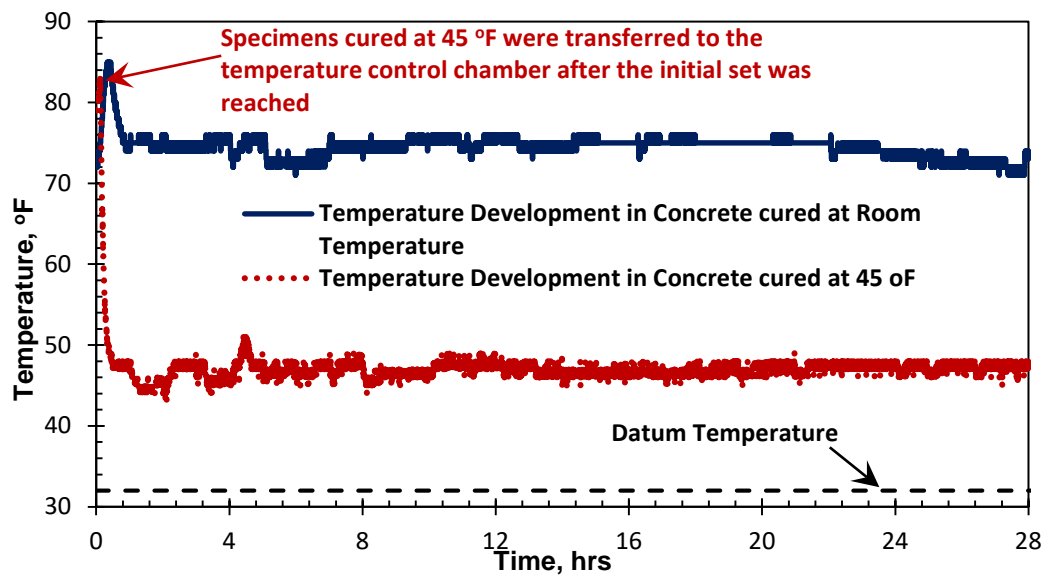


Figure F-1. Temperature development with time for concrete cured at 73 °F and 45 °F

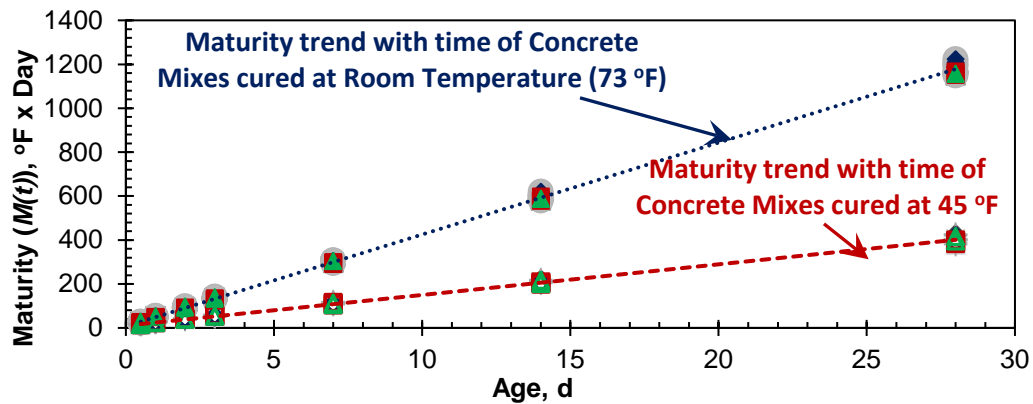


Figure F-2. Maturity development with time in concrete

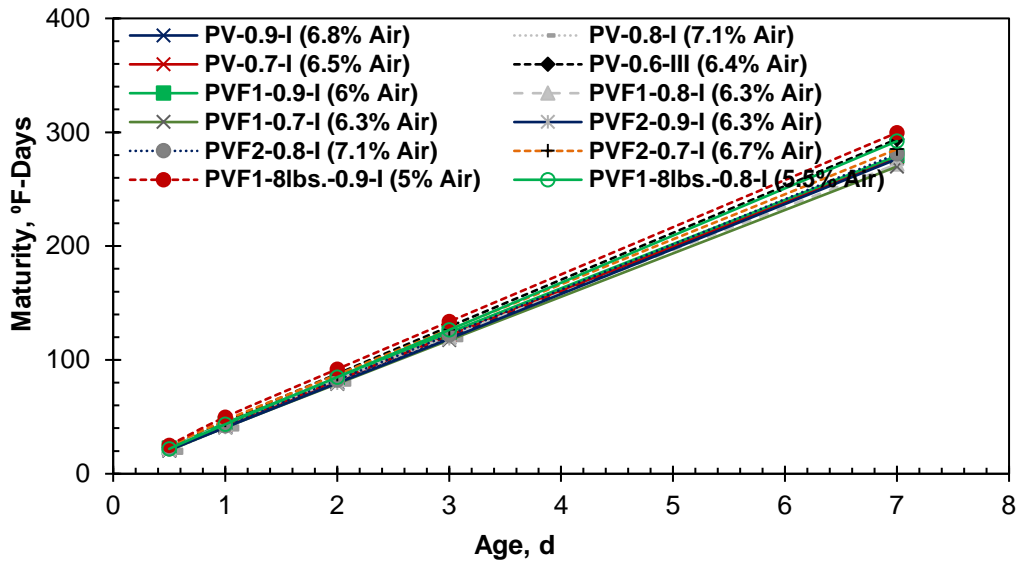


Figure F-3. Maturity development with respect to concrete age for flexural fatigue mixes

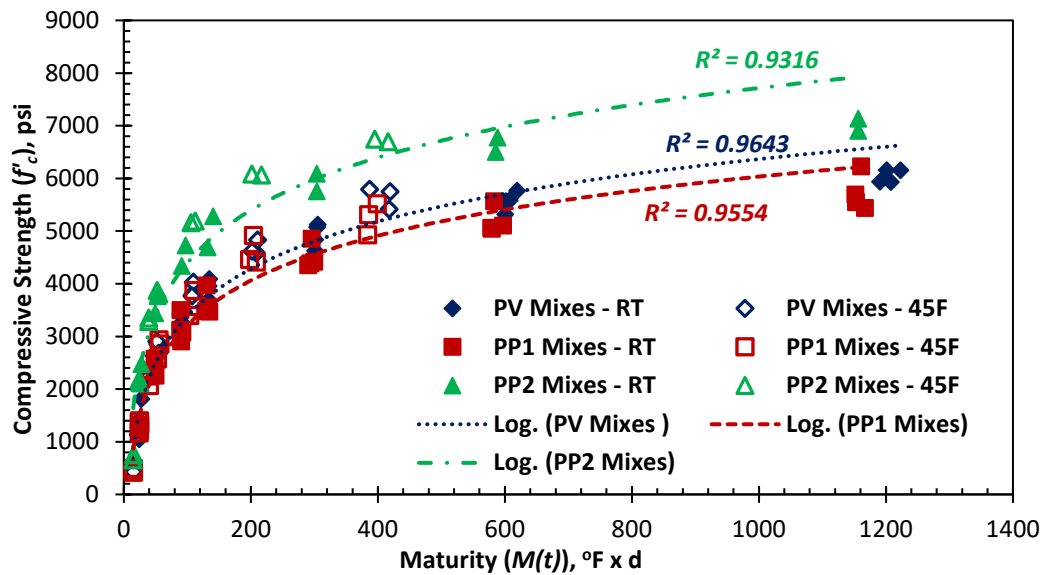


Figure F-4. Compressive strength vs. maturity for PV, PP1, and PP2 mixes

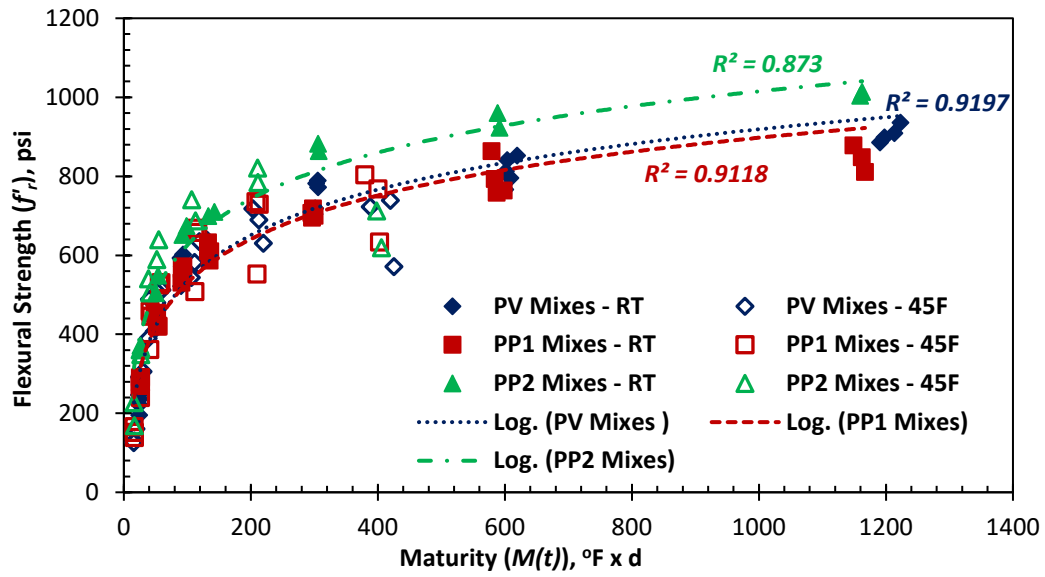


Figure F-5. Flexural strength vs. maturity for PV, PP1, and PP2 mixes

APPENDIX G DYNAMIC MODULUS RESULTS

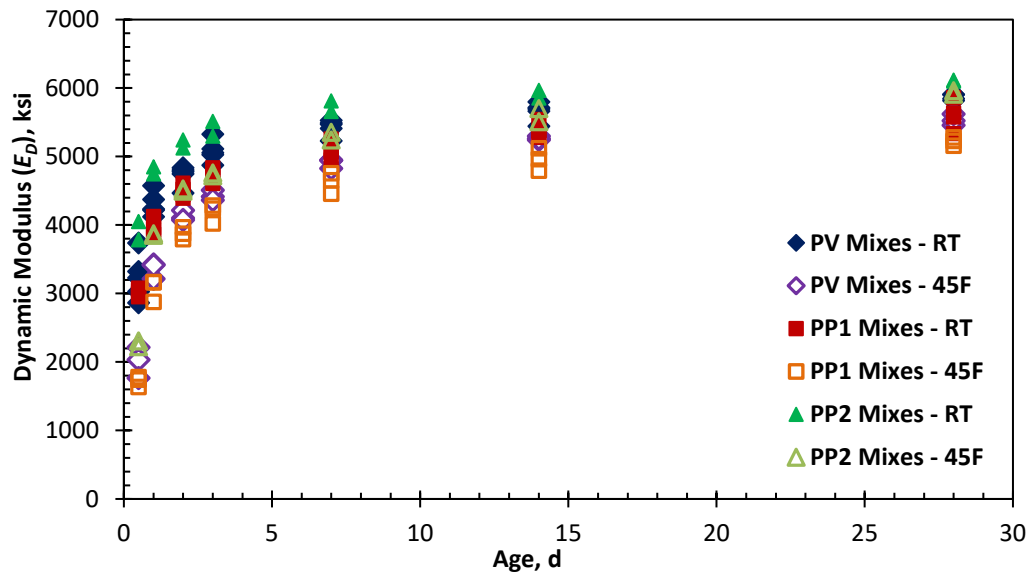


Figure G-1. Development of dynamic modulus with time for PV, PP1, and PP2 mixes

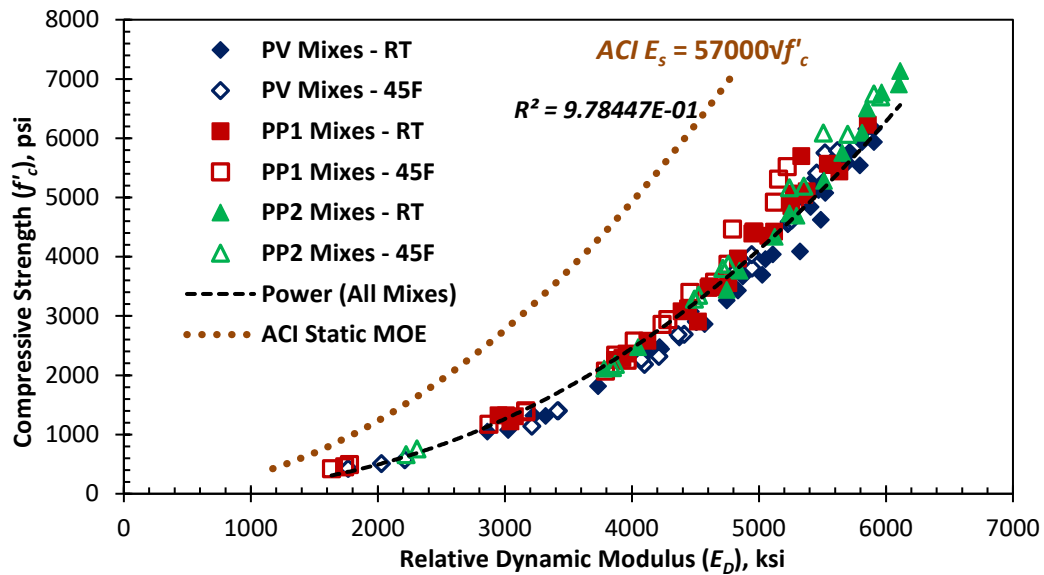


Figure G-2. Compressive strength vs. E_D for PV, PP1, and PP2 mixes

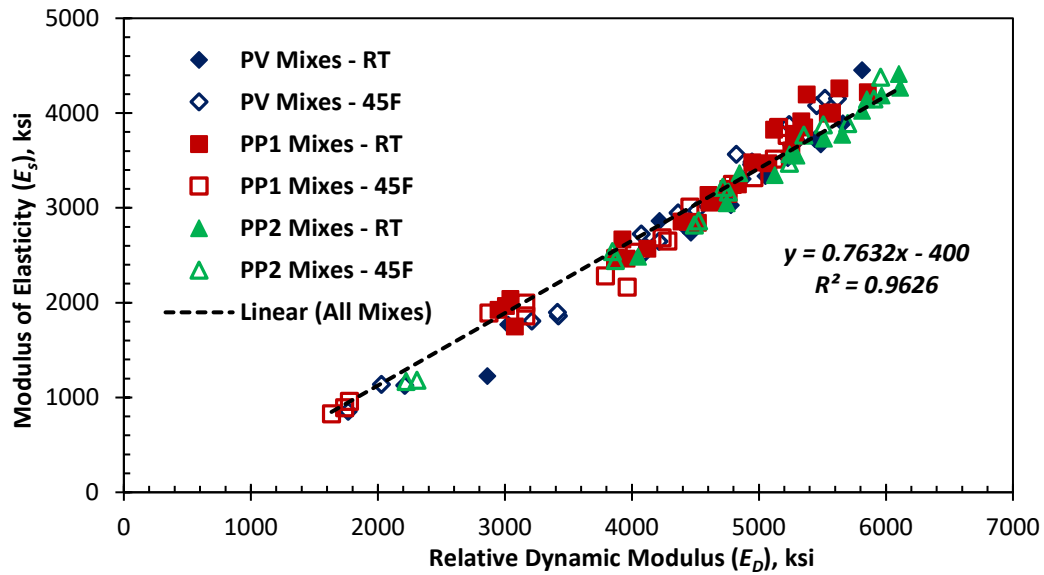


Figure G-3. Static E_s vs. E_D for PV, PP1, and PP2 mixes

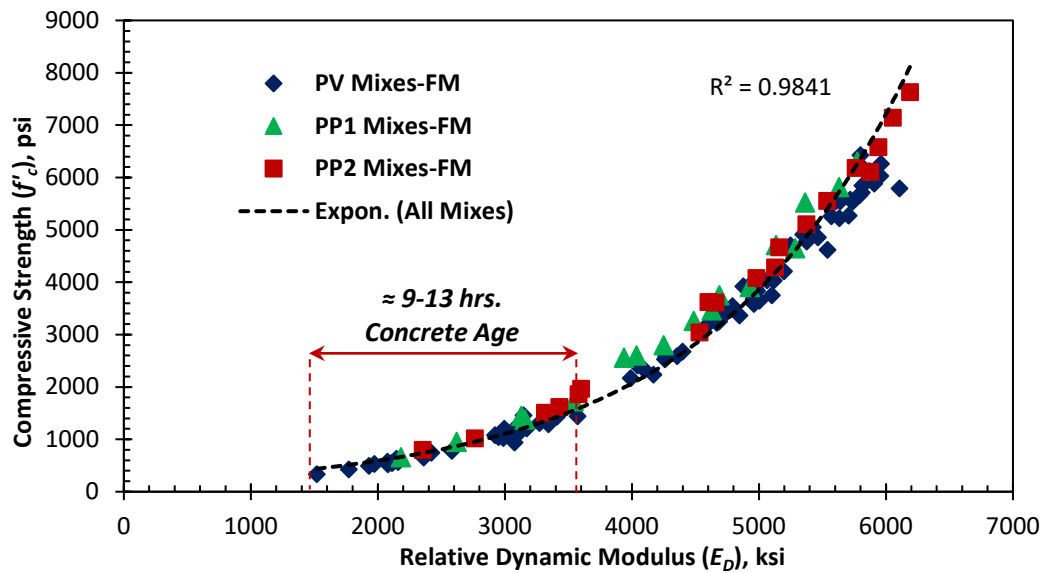


Figure G-4. Compressive strength vs. E_D for PV, PP1, and PP2 fracture mechanics mixes

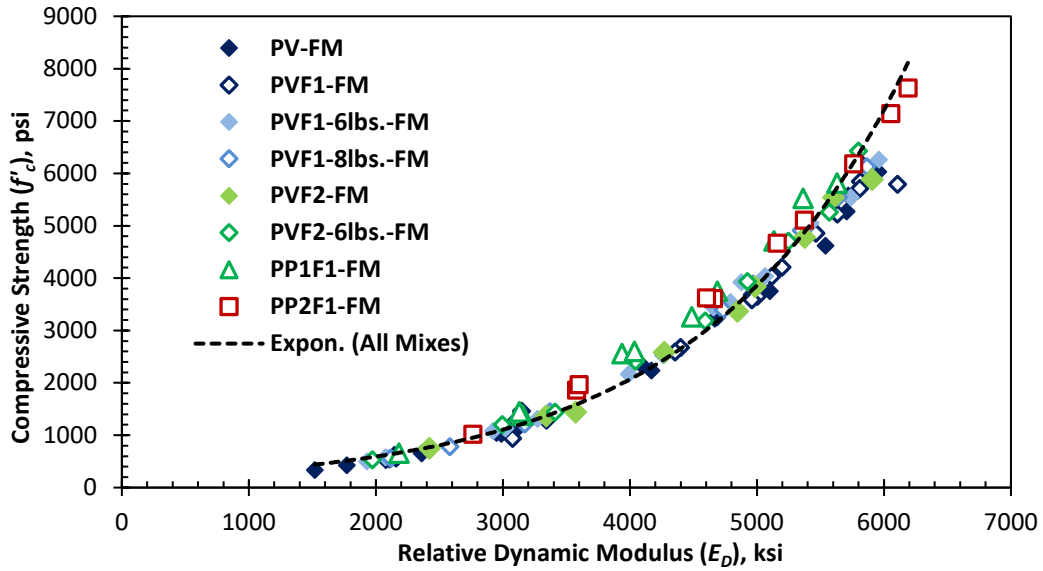


Figure G-5. Compressive strength vs. E_D for PV, PVF1, PVF1-6lbs, PVF1-8lbs, PVF2, PVF2-6lbs, PP1F1, and PP2F1 fracture mechanics mixes

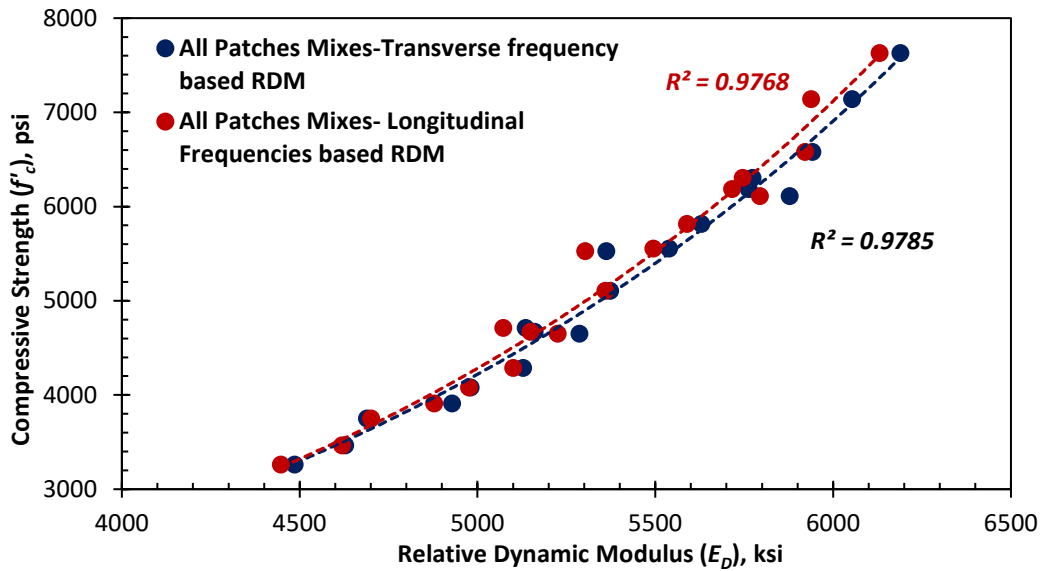


Figure G-6. Compressive strength vs. E_D PP1, and PP2 fracture mechanics mixes for both transverse and longitudinal frequencies.

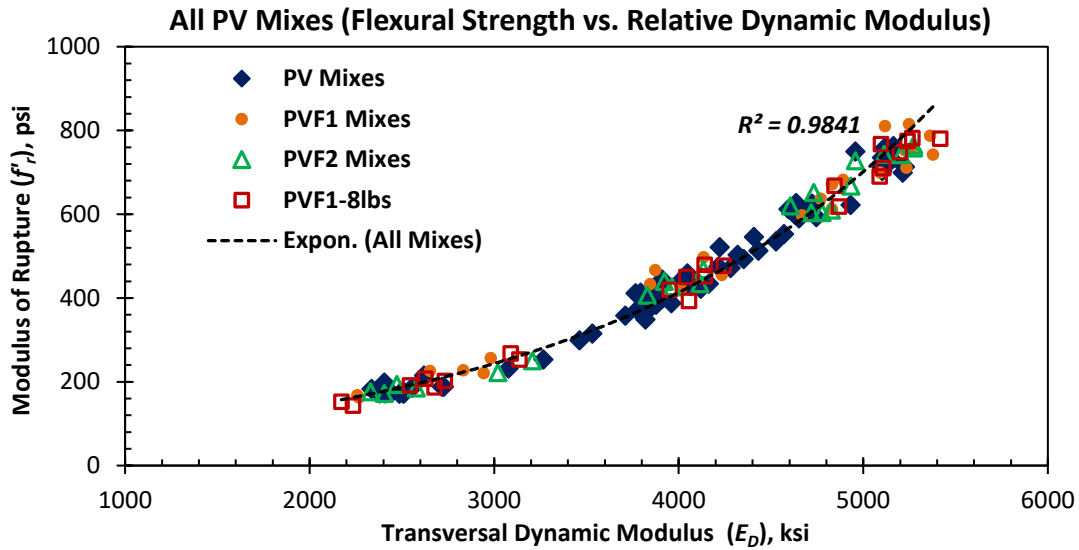


Figure G-7. Flexural strength vs. E_D for PV, PVF1, PVF2, and PVF1-8lbs fatigue mixes

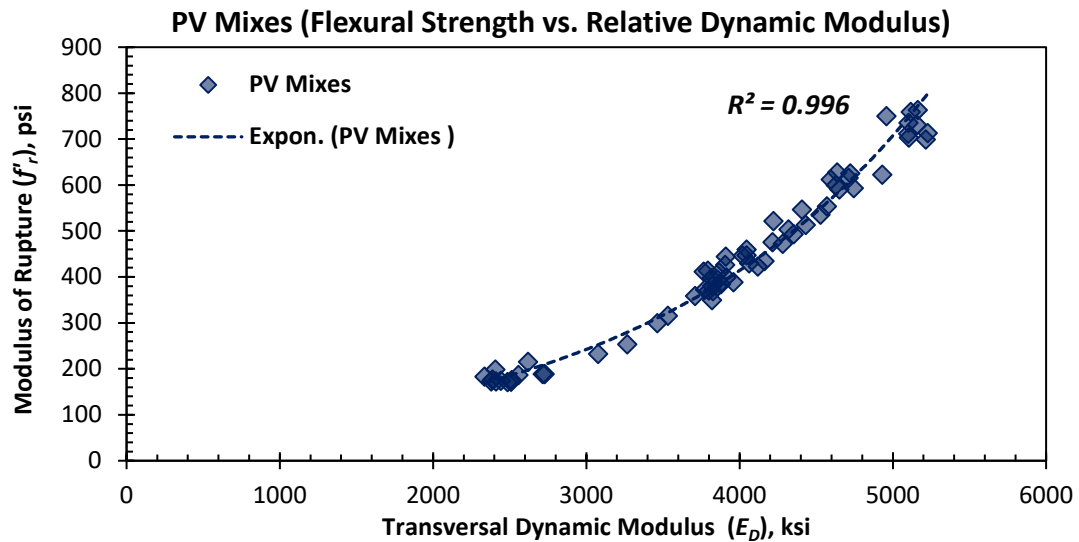


Figure G-8. Flexural strength vs. E_D for PV fatigue mixes

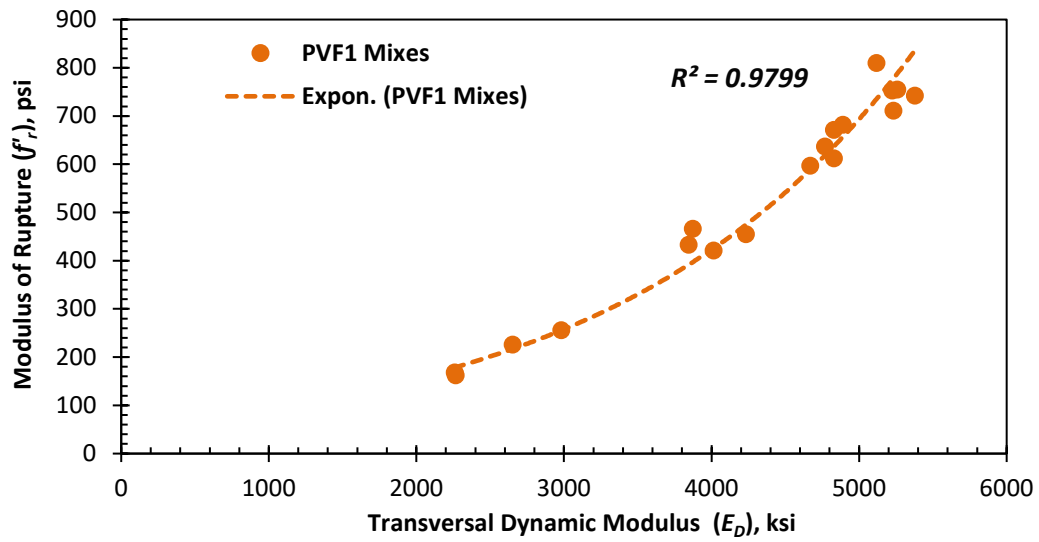


Figure G-9. Flexural strength vs. E_D for PVF1 fatigue mixes

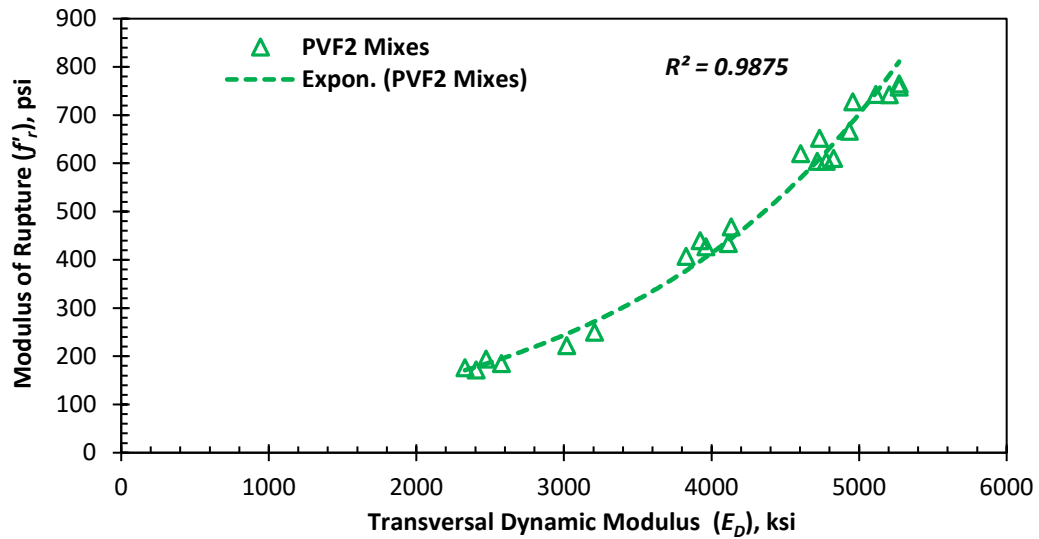


Figure G-10. Flexural strength vs. E_D for PVF2 fatigue mixes

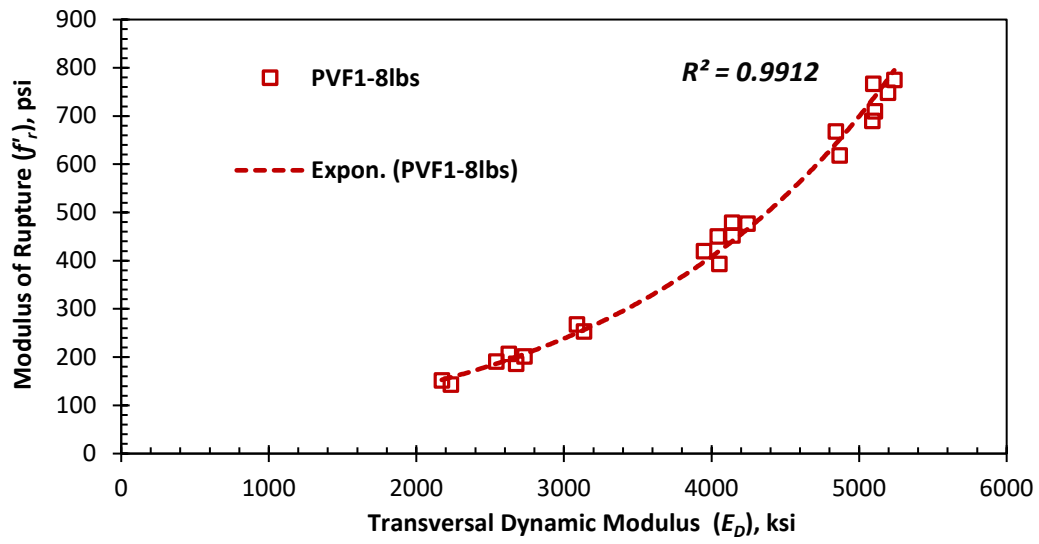


Figure G-11. Flexural strength vs. E_D for PVF1-8lbs. fatigue mixes

APPENDIX H LINEAR DRYING SHRINKAGE RESULTS

Table H-1. Pavement and patch mix properties considered for shrinkage tests

Mix Design	Pavement mix					Patch mix	
	PV	PVF1	PVF1-6lbs.	PVF1-8lbs.	PVF2	PP1	PP2
W/C ratio	0.42					0.42	0.36
Cementitious content (lb/yd ³)	565					650	735
Fiber content (lb/yd ³)	0	4	6	8	4	0	0
Fresh air content (%)	6.8	6.2	6.8	6.8	6.8	6.9	6
Slump (in)	4.5	3.5	3	3	4	4.8	6
Unit weight (lb/ft ³)	144.4	143.9	144.8	144	144.4	143.8	144.6

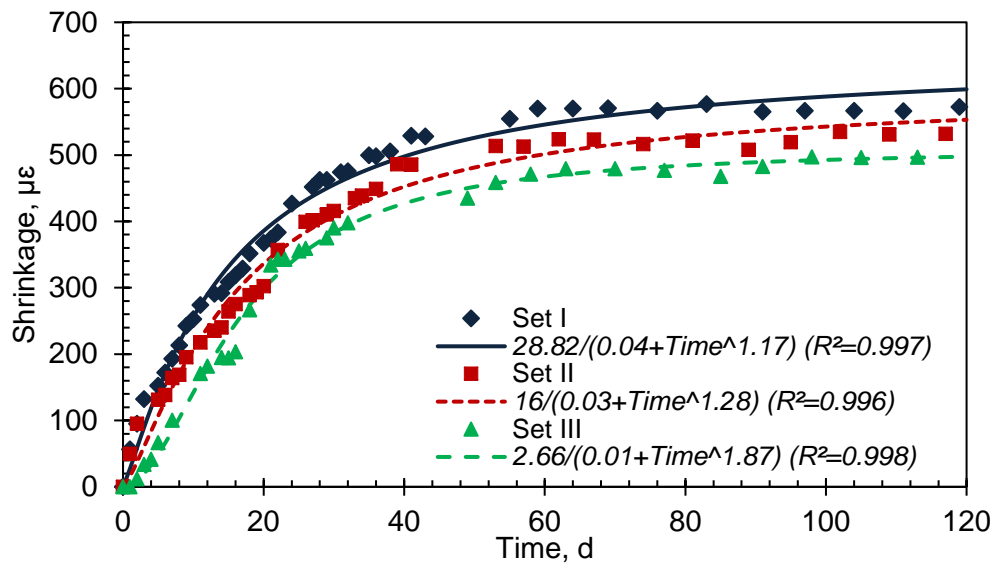


Figure H-1. Linear Drying shrinkage for PV mix

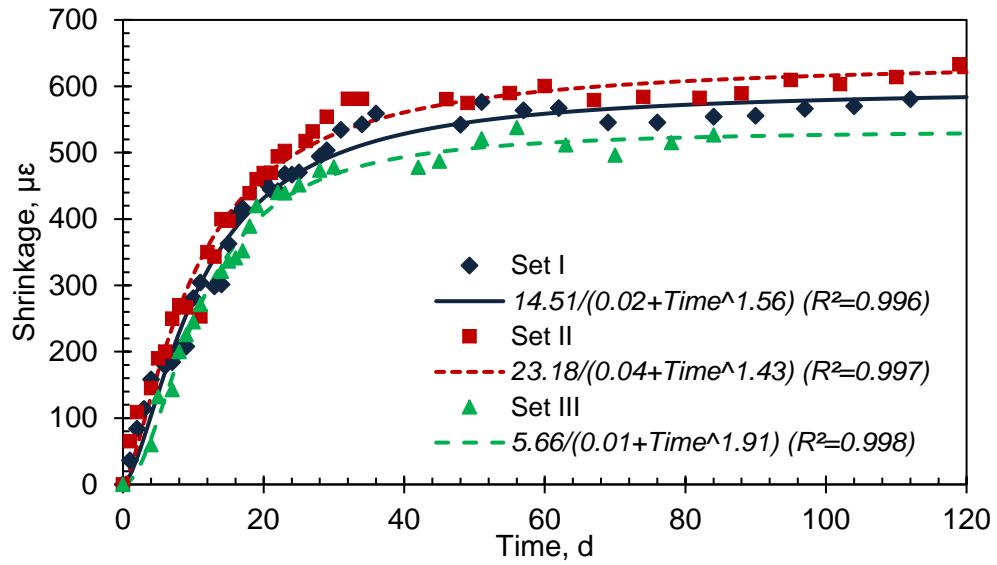


Figure H-2. Linear Drying shrinkage for PVF1 mix

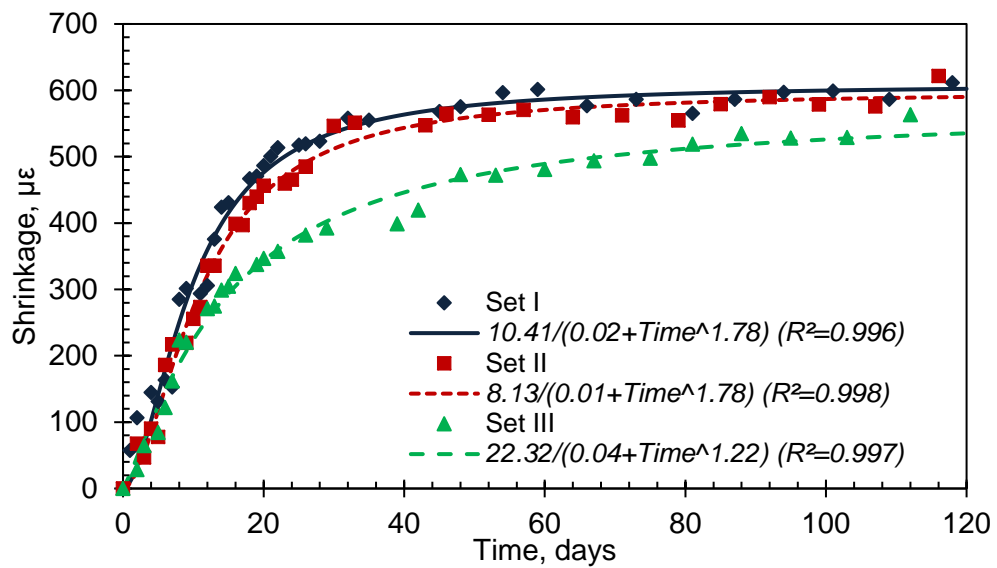


Figure H-3. Linear Drying shrinkage for PVF1-6lbs. mix

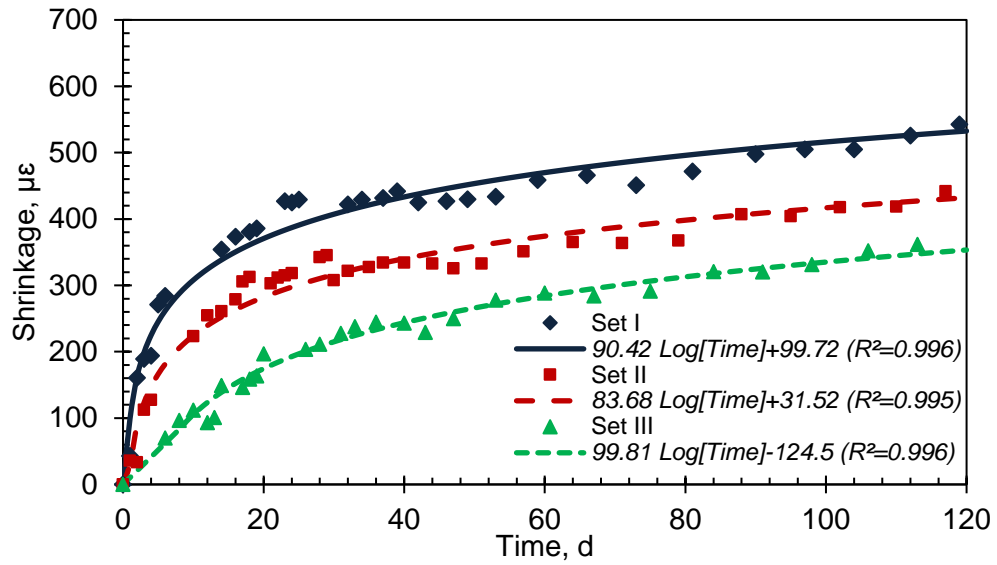


Figure H-4. Linear Drying shrinkage for PVF1-8lbs. mix

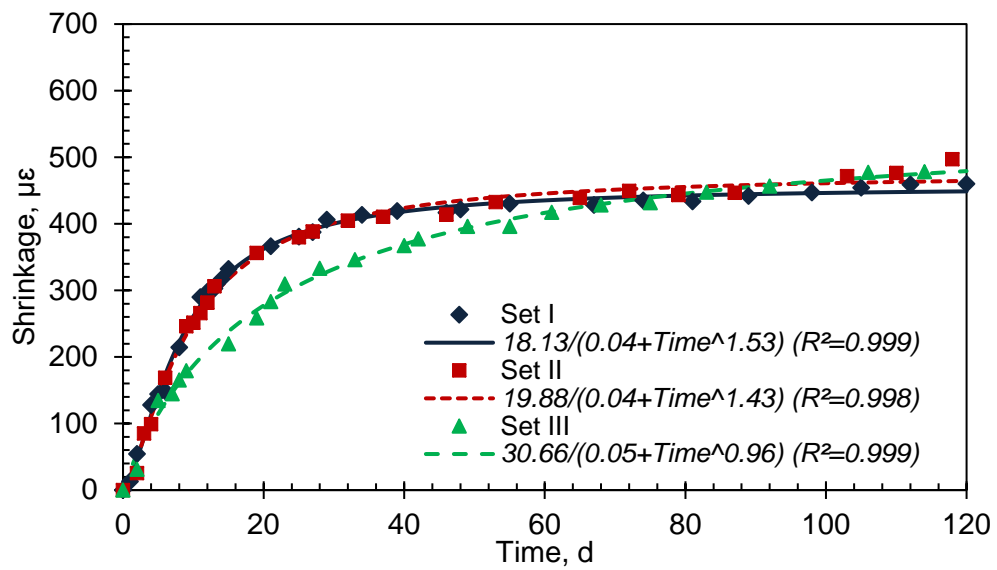


Figure H-5. Linear Drying shrinkage for PVF2 mix

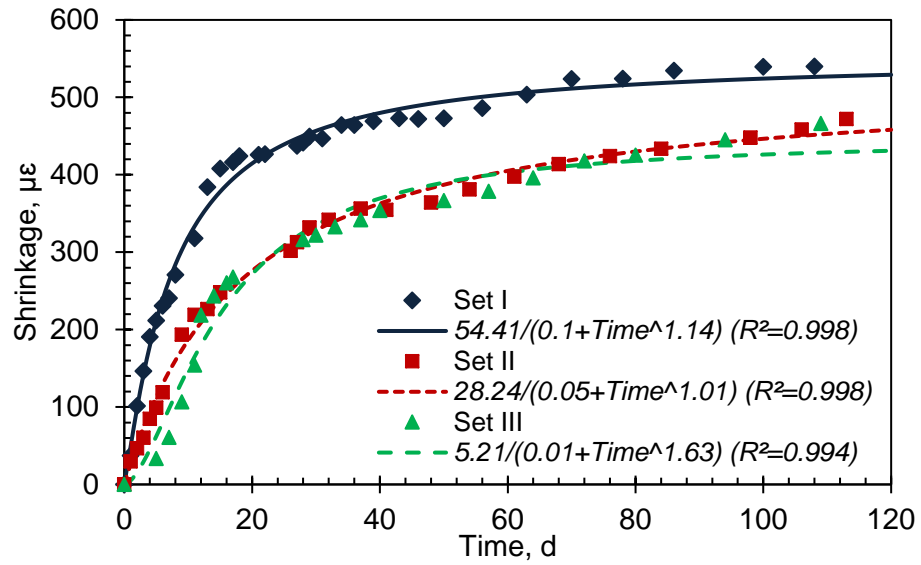


Figure H-6. Linear Drying shrinkage for PP1 mix

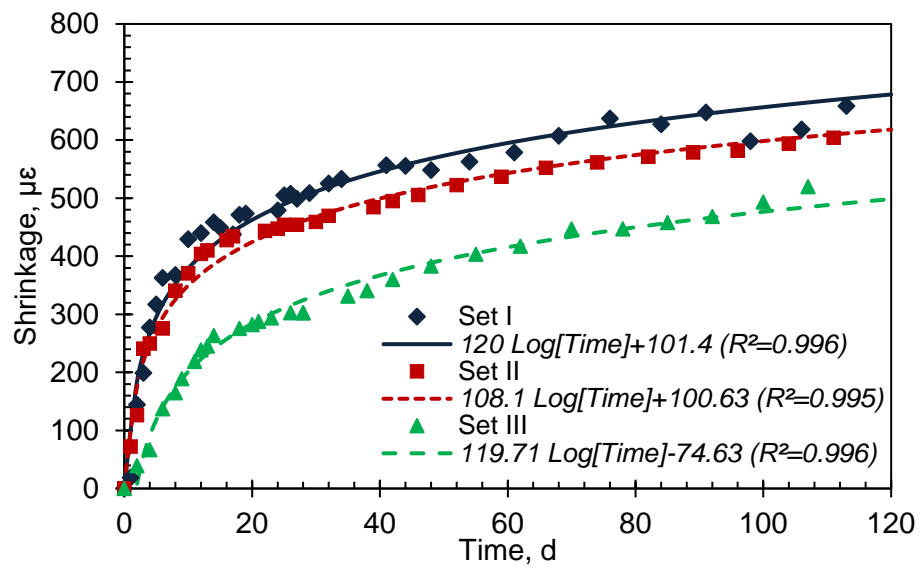
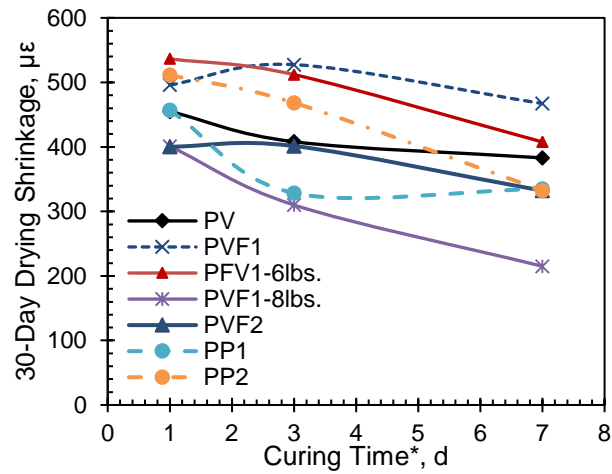
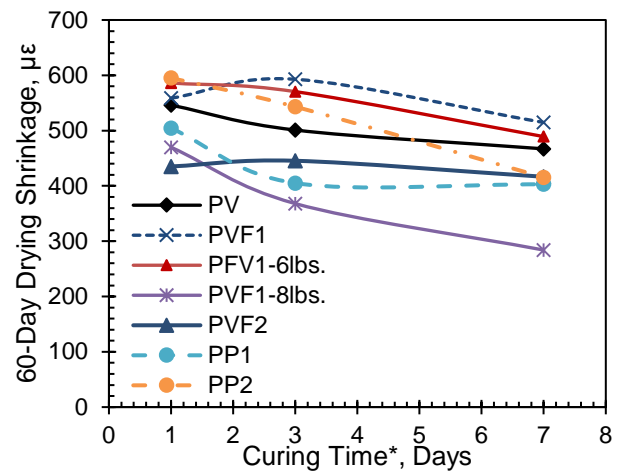


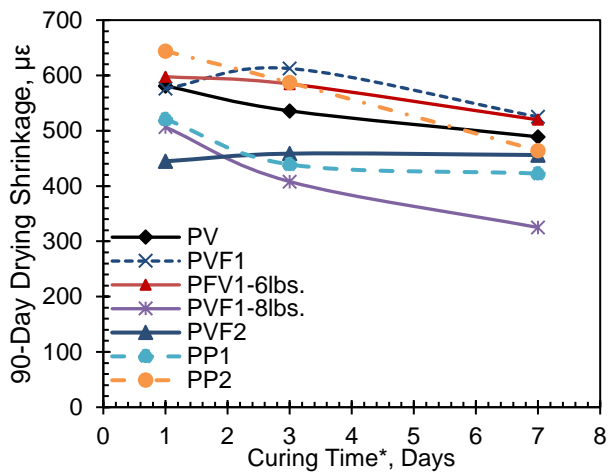
Figure H-7. Linear Drying shrinkage for PP2 mix



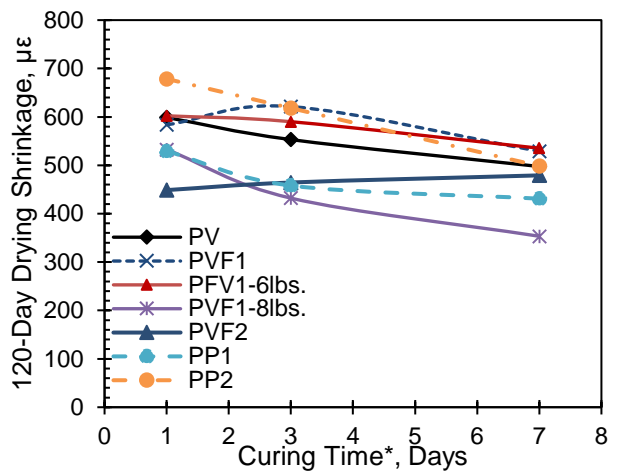
(a) 30 d



(b) 60 Days



(b) 90 Days



(d) 120 Days

*Set I: 1 day curing time, Set II: 3 days curing time, Set III: 7 days curing time

Figure H-8. Drying shrinkage values for pavements and patches mixes at 30 days (a), 60 days (b), 90 days (c), and 120 days (d) with respect to curing time

APPENDIX I FRACTURE MECHANICS RESULTS

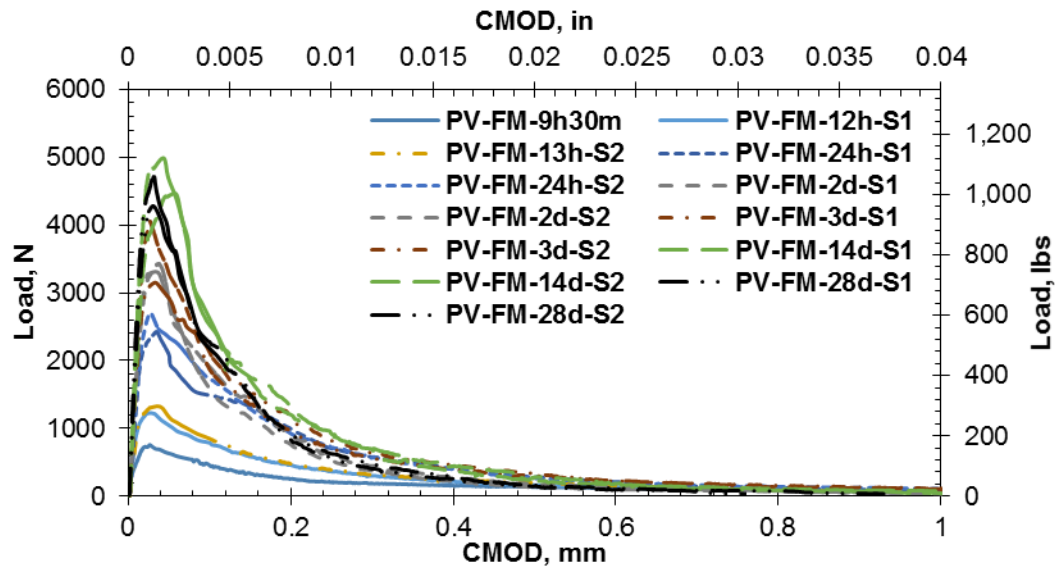


Figure I-1. Load versus CMOD curves at different ages for PV mix without fibers

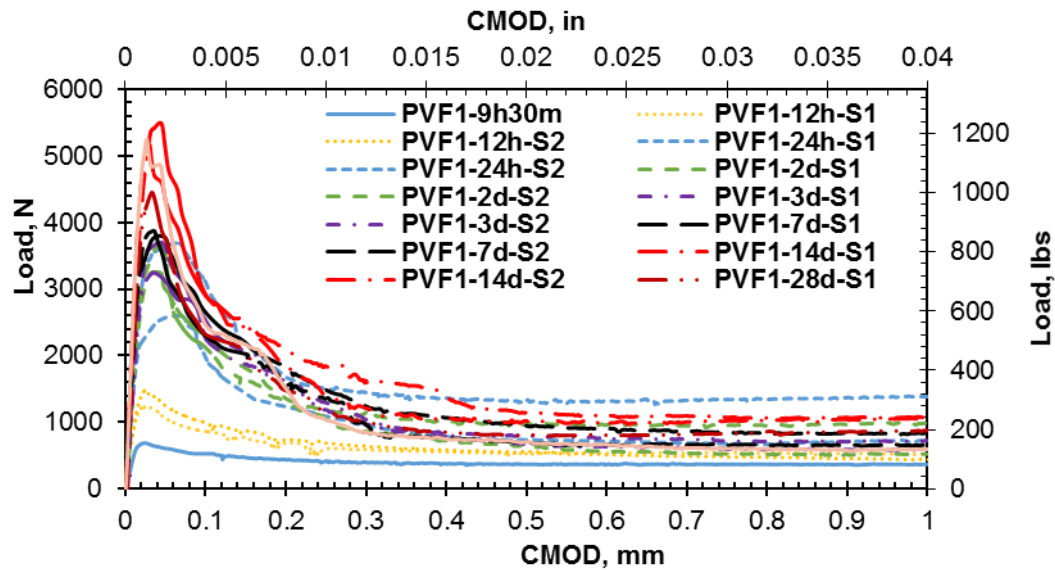


Figure I-2. Load versus CMOD curves at different ages for PVF1- Strux 90-40 mix

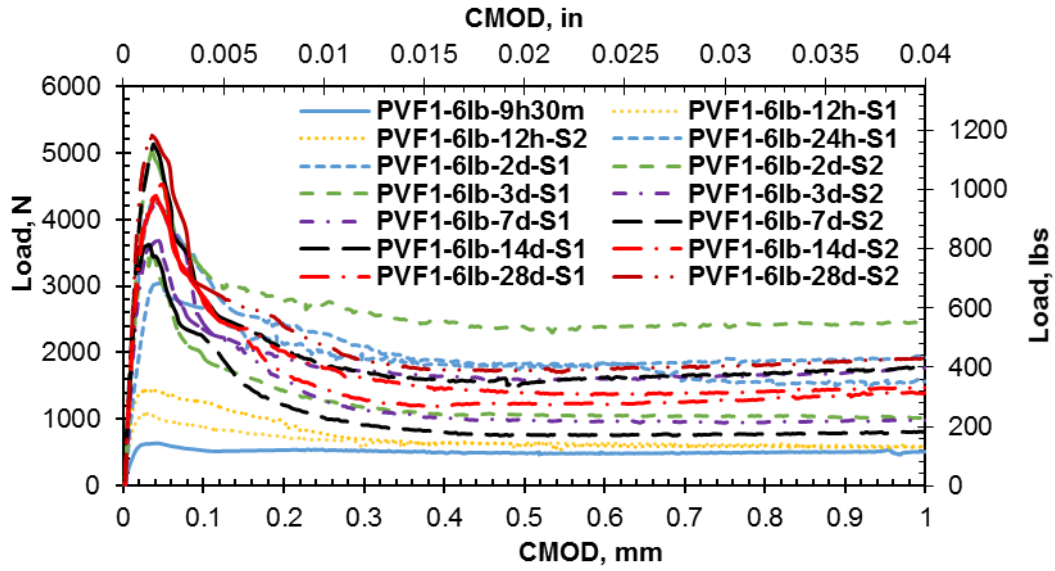


Figure I-3. Load versus CMOD curves at different ages for PVF1- Strux 90-40-6lbs mix

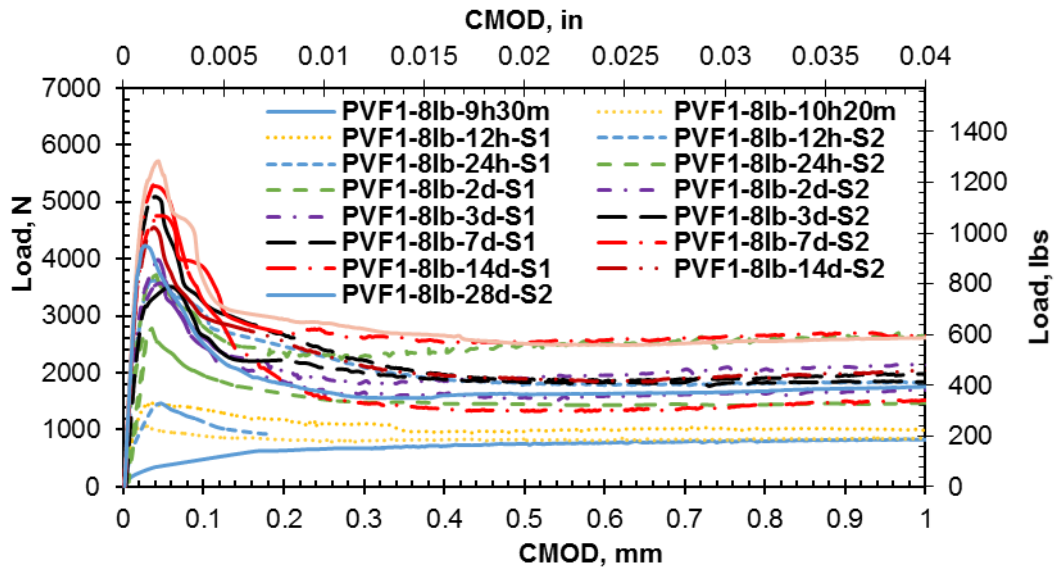


Figure I-4. Load versus CMOD curves at different ages for PVF1- Strux 90-40-8lbs mix

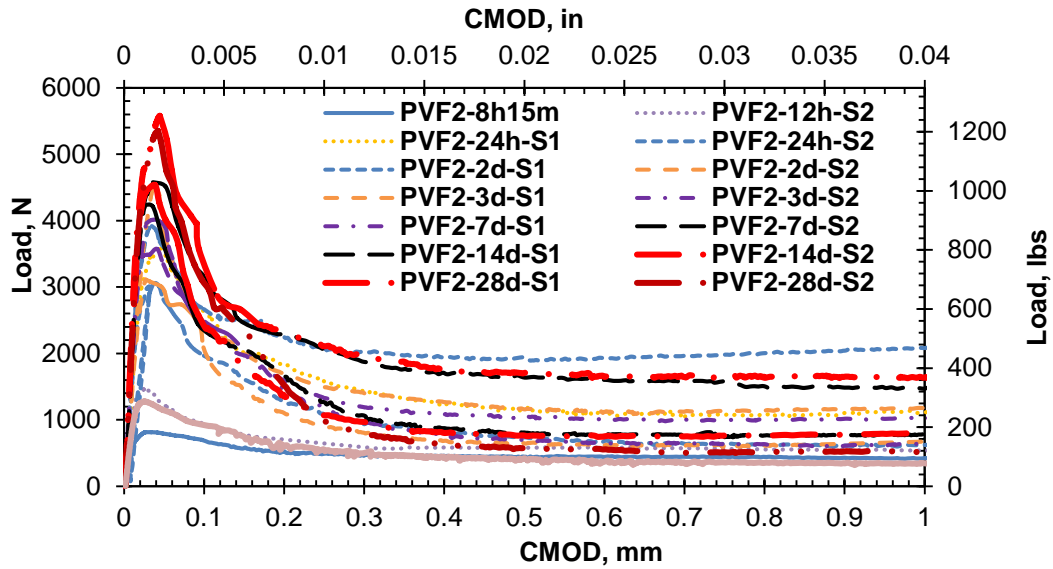


Figure I-5. Load versus CMOD curves at different ages for PVF2- Master Fiber mix

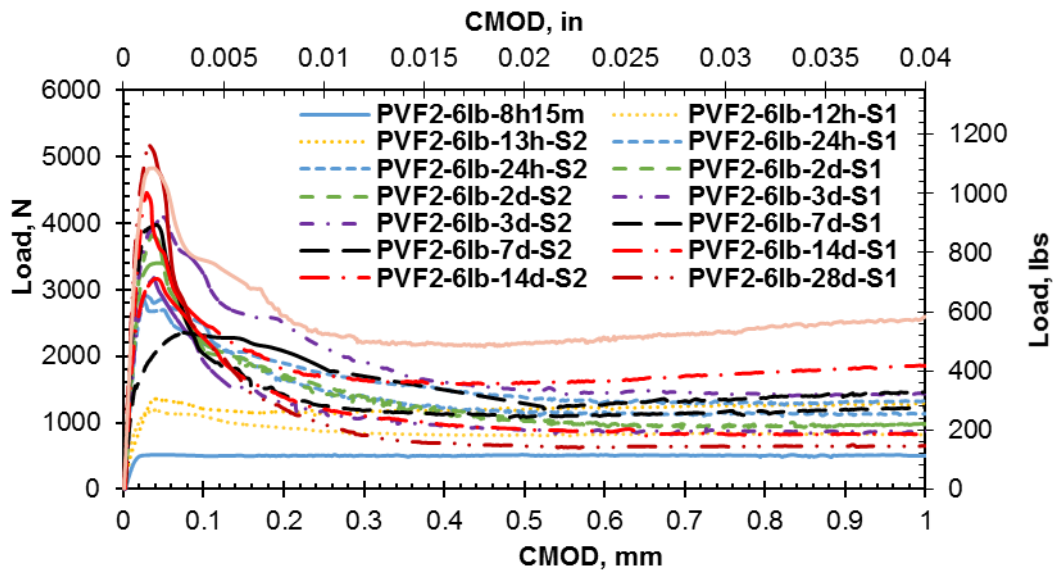


Figure I-6 Load versus CMOD curves at different ages for PVF2-6lbs- Master Fiber mix

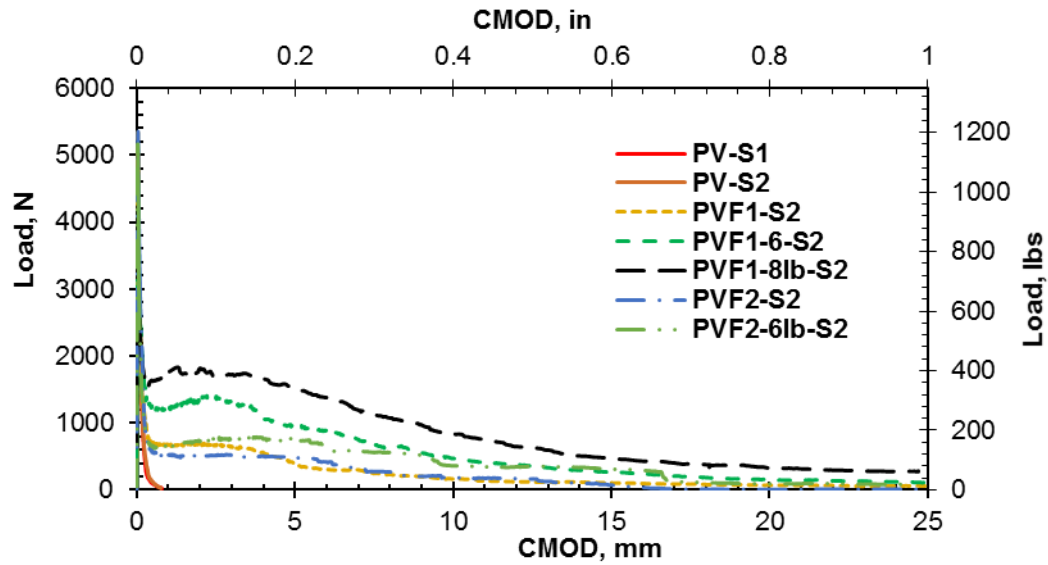


Figure I-7. Load vs. CMOD curves for PV, PVF1, and PVF1-6 lbs mixes at 28 days

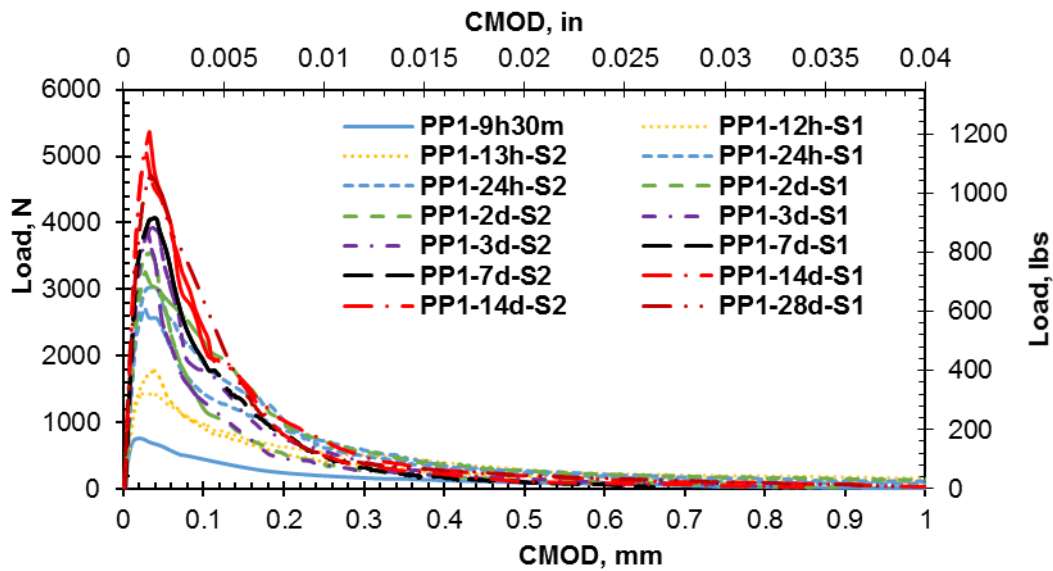


Figure I-8. Load versus CMOD curves at different ages for PP1 mix without fibers

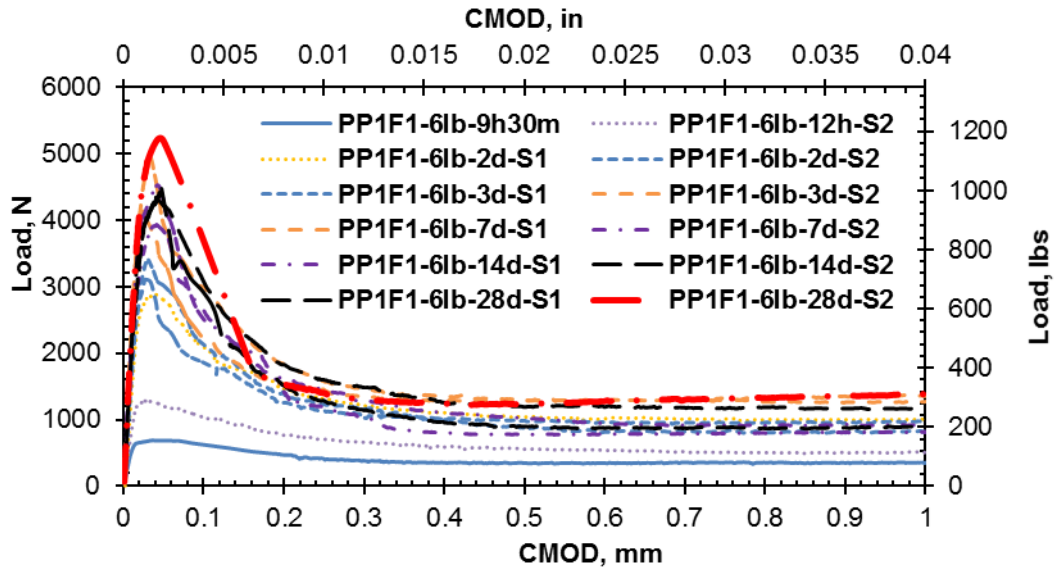


Figure I-9. Load versus CMOD curves at different ages for PP1F1- Strux 90-40-6lbs mix

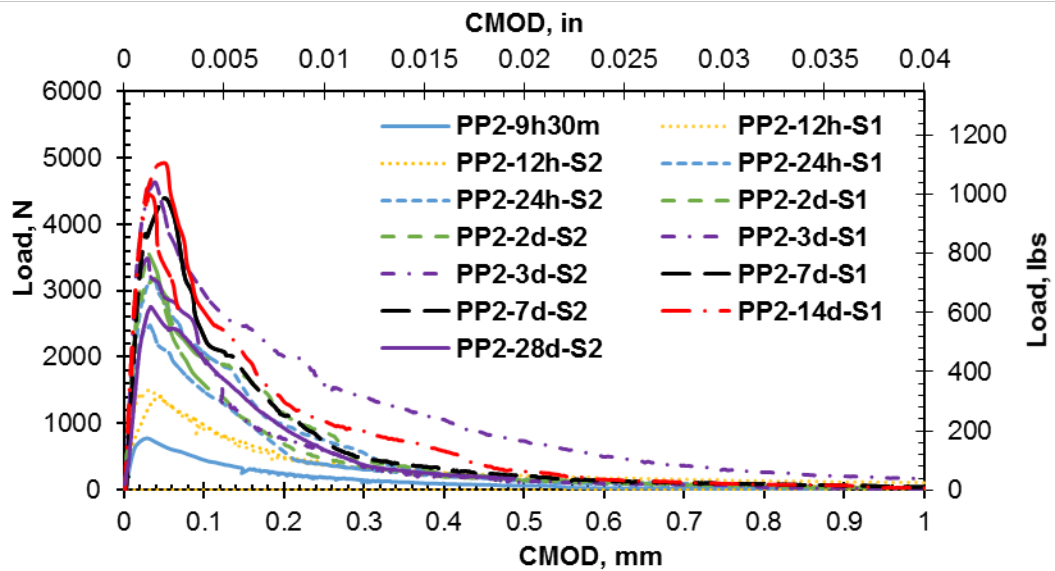


Figure I-10 Load versus CMOD curves at different ages for PP2 mix without fibers

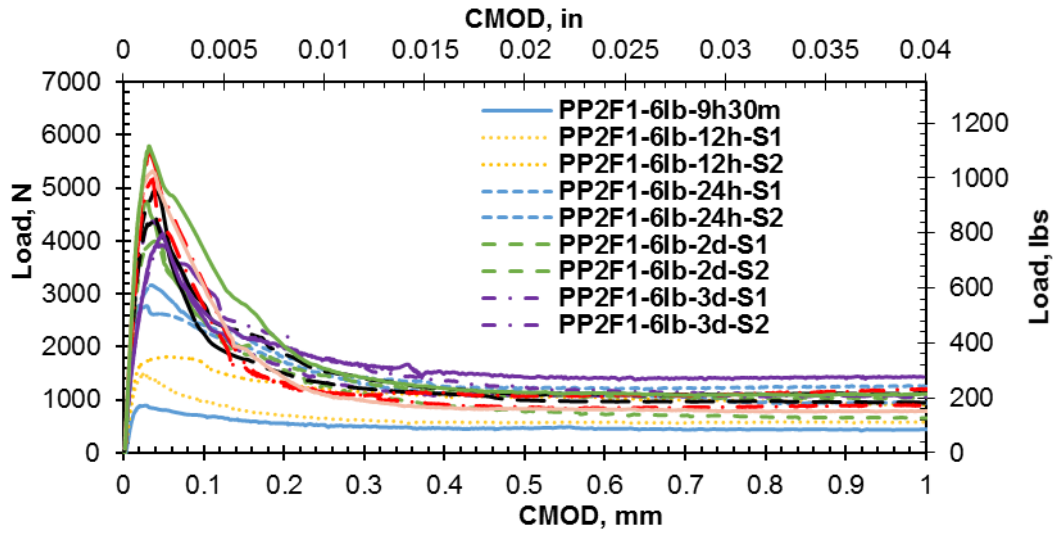


Figure I-11. Load versus CMOD curves at different ages for PP2F1- Strux 90-40-6lbs mix

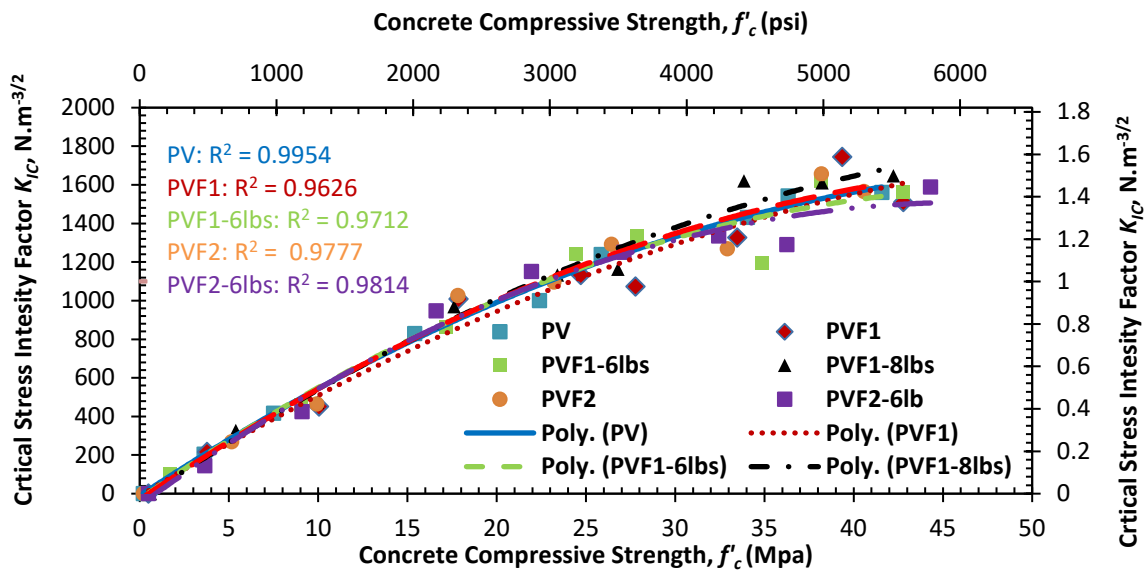


Figure I-12. Critical Stress Intensity Factor vs. concrete compressive strength (f'_c) for PV, PVF1, and PVF1-6 lbs mixes

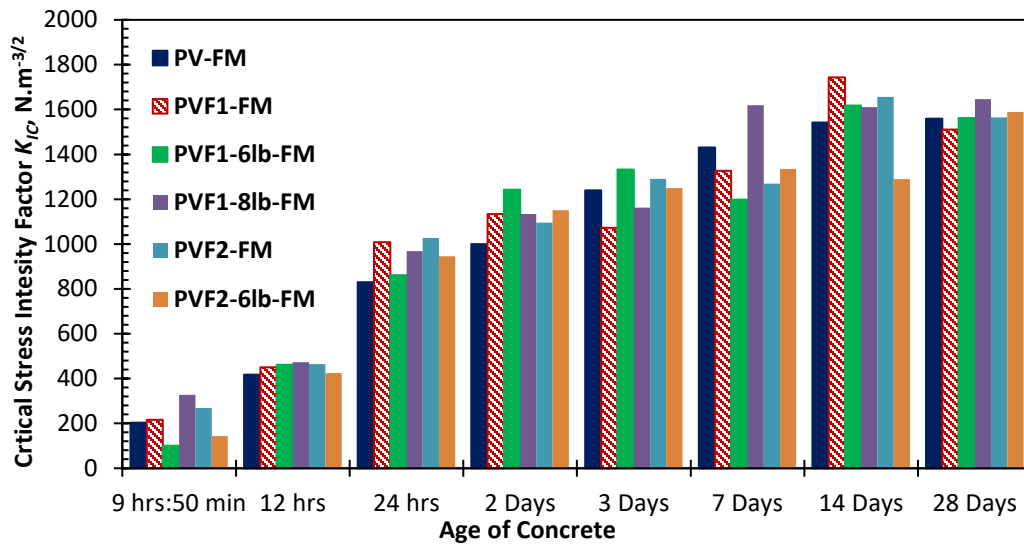


Figure I-13. Critical Stress Intensity Factor vs. age of concrete for PV, PVF1, and PVF1-6 lbs mixes

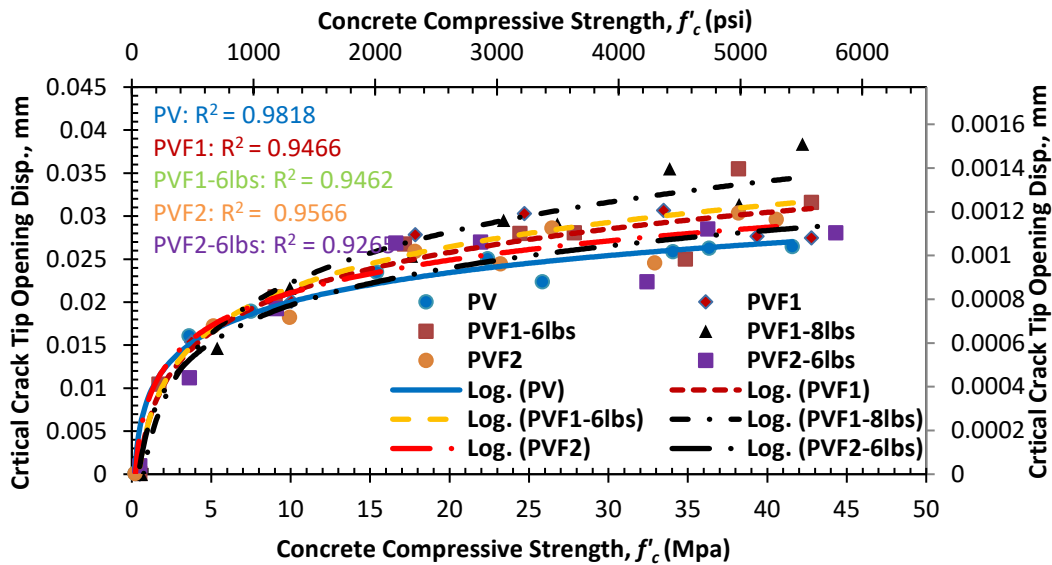


Figure I-14. Critical Crack Tip Opening Displacement vs. concrete compressive strength (f'_c) for PV, PVF1, and PVF1-6 lbs mixes

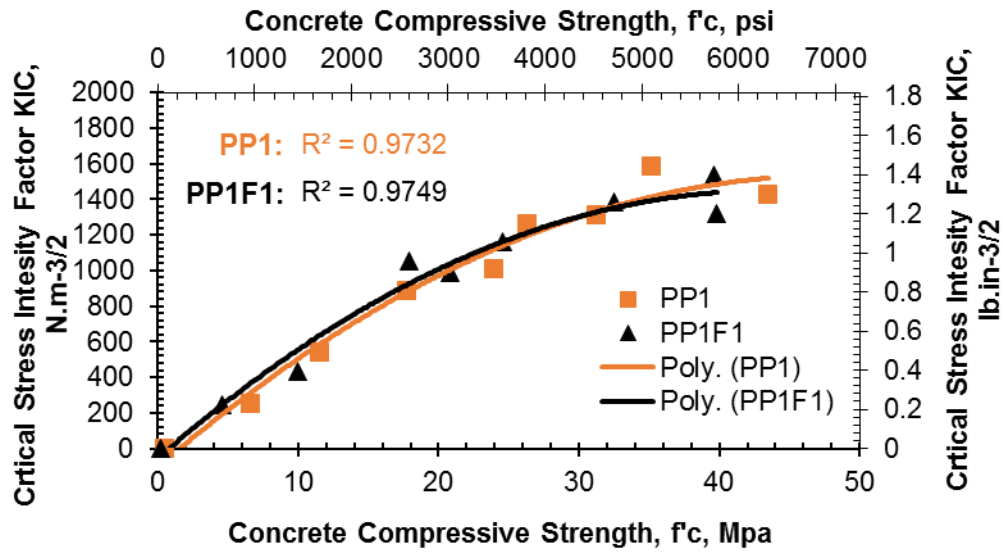


Figure I-15. Critical Stress Intensity Factor vs. concrete compressive strength (f'_c) for PP1, and PP1F1-6lbs mixes

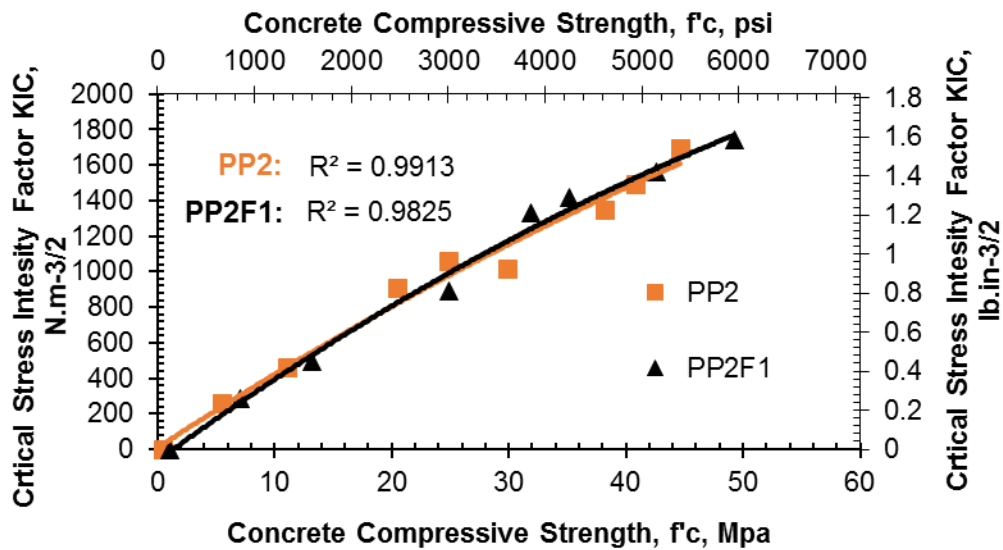


Figure I-16. Critical Stress Intensity Factor vs. concrete compressive strength (f'_c) for PP2, and PP2F1-6lbs mixes

APPENDIX J FATIGUE TEST RESULTS

Table J-1. Twelve-hr test fatigue results

Mix type	Mix name	Concrete Age	Stress Level	Number of cycles until failure*	Testing time
		(hr)			(hr)
PV	PV-0.9-I	12	0.9	189	0.01
	PV-0.8-I	12	0.8	321	0.02
	PV-0.8-II	12	0.8	372	0.03
	PV-0.8-III	12	0.8	1628	0.11
	PV-0.7-I	12	0.7	112914	7.84
	PV-0.6-II	12	0.6	281167	19.53
PVF1	PVF1-0.9-I	12	0.9	45	0
	PVF1-0.8-I	12	0.8	182	0.01
	PVF1-0.7-I	12	0.7	165182	11.47
	PVF1-0.6-II	12	0.6	148975	10.35
PVF2	PVF2-0.9-I	12	0.9	119	0.01
	PVF2-0.8-I	12	0.8	388	0.03
	PVF2-0.7-I	12	0.7	102006	7.08
	PVF2-0.6-II	12	0.6	181376	12.6
PVF1-8lbs	PVF1-8lbs-0.9	12	0.9	66	0
	PVF1-8lbs-0.8	12	0.8	6470	0.45
	PVF1-8lbs-0.7	12	0.7	59255	4.11
	PVF1-8lbs-0.6-I	12	0.6	176730**	12
	PVF1-8lbs-0.6-III	12	0.6	ran out***	69.44
*Number of cycles excluding 120 cycles of ramped loads.				Total testing time (hr)	155.1
**Reading not represented in graphs due to low number of cycles until failure.					
***Test stopped at 1 million cycles.					

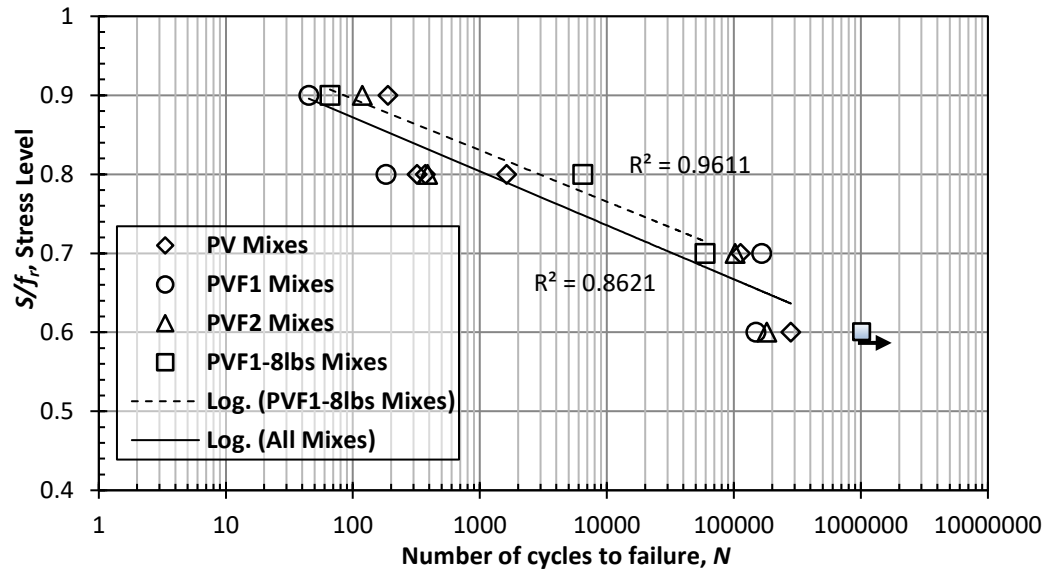


Figure J-1. S-N results for PV, PVF1, PVF2 and PVF1-8lbs at 12-hr testing.

Table J-2. One-day test fatigue results

Mix Type	Mix Name	Concrete Age (hr)	Stress Level	Number of cycles until failure*	Testing Time (hr)
PV	PV-Trial Mix	24	0.9	881	0.06
	PV-0.9-I	24	0.9	246	0.02
	PV-0.8-III	24	0.8	151	0.01
	PV-0.8-III	24	0.8	338	0.02
	PV-0.7-I	24	0.7	154907	10.76
	PV-0.6-I	24	0.6	548721	38.11
PVF1	PVF1-0.9-I	24	0.9	734	0.05
	PVF1-0.8-I	24	0.8	477	0.03
	PVF1-0.7-I	24	0.7	3802	0.26
	PVF1-0.6-I	24	0.6	272623	18.93
PVF2	PVF2-0.9-I	24	0.9	39	0
	PVF2-0.8-I	24	0.8	467	0.03
	PVF2-0.7-I	24	0.7	44328	3.08
	PVF2-0.6-I	24	0.6	278115	19.31
PVF1-8lb	PVF1-8lbs-0.9	24	0.9	81	0.01
	PVF1-8lbs-0.8	24	0.8	3685	0.26
	PVF1-8lbs-0.7	24	0.7	263597	18.31
	PVF1-8lbs-0.6-II	24	0.6	ran out**	69.44
* Number of cycles excluding 120 cycles of ramped loads.				Total Testing Time (hr)	178.7
** Test stopped at 1 million cycles.					

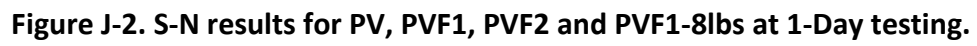


Table J-3. 3-Day test fatigue results

Mix Type	Mix name	Concrete Age (Days)	Stress Level	Number of Cycles Until Failure*	Testing Time (hr)
PV	PV-Trial	3	0.9	5**	0
	PV-0.9-I	3	0.9	105	0.01
	PV-0.8-II	3	0.8	1205	0.08
	PV-0.7-I	3	0.7	8184	0.57
	PV-0.6-III	3	0.6	101685	7.06
PVF1	PVF1-0.9-I	3	0.9	69	0.00
	PVF1-0.8-I	3	0.8	1005	0.07
	PVF1-0.7-I	3	0.7	13064	0.91
	PVF1-0.6-I	3	0.6	183605	12.75
PVF2	PVF2-0.9-I	3	0.9	126	0.01
	PVF2-0.8-I	3	0.8	108	0.01
	PVF2-0.7-I	3	0.7	33062	2.30
	PVF2-0.6-II	3	0.6	91480	6.35
PVF1-8lbs	PVF1-8lbs-0.9	3	0.9	98	0.01
	PVF1-8lbs-0.8	3	0.8	4092	0.28
	PVF1-8lbs-0.7	3	0.7	63972	4.44
	PVF1-8lbs-0.6-I	3	0.6	257393	17.87
* Number of cycles excluding 120 cycles of ramped loads.				Total Testing Time (hr)	52.7
**Data reading excluded due to low number of cycles to failure.					

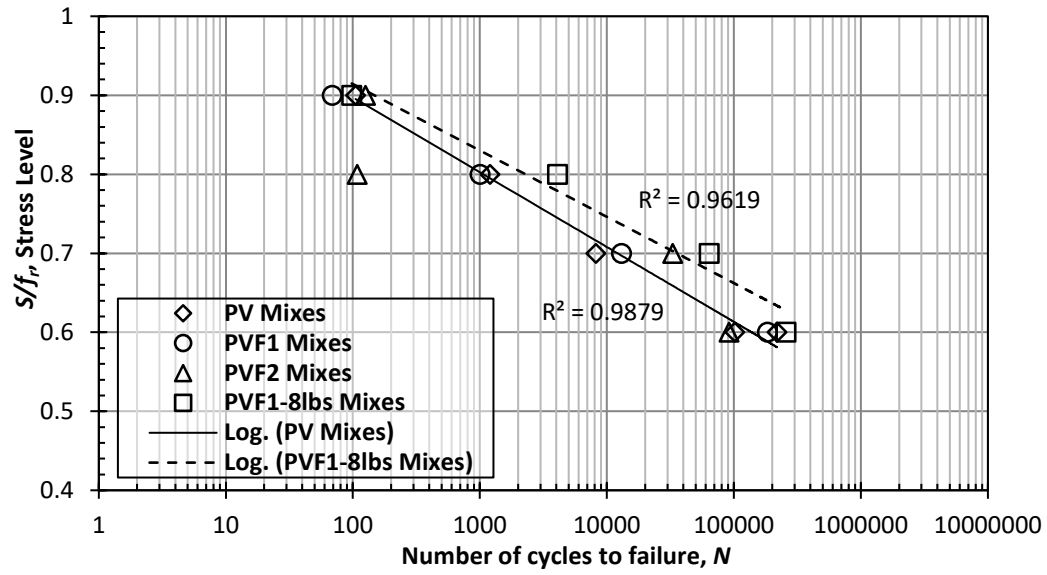
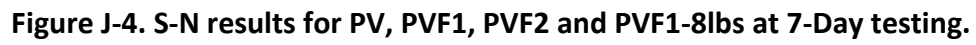


Figure J-3. S-N results for PV, PVF1, PVF2 and PVF1-8lbs at 3-Day testing.

Table J-4. 7-Day test fatigue results

Mix Type	Mix name	Concrete Age (Days)	Stress Level	Number of Cycles Until Failure*	Testing Time (hr)
PV	PV-Trial	7	0.9	110	0.01
	PV-0.9-I	7	0.9	330	0.02
	PV-0.9-I	7	0.9	707	0.05
	PV-0.8-II	7	0.8	837	0.06
	PV-0.8-II	7	0.8	1095	0.08
	PV-0.8-III	7	0.8	338	0.02
	PV-0.7-I	7	0.7	784	0.05
	PV-0.6-I	7	0.6	136821	9.5
	PV-0.6-II	7	0.6	218786	15.19
PVF1	PVF1-0.9-I	7	0.9	156	0.01
	PVF1-0.8-I	7	0.8	4142	0.29
	PVF1-0.7-I	7	0.7	1137	0.08
	PVF1-0.6-II	7	0.6	295672	20.53
PVF2	PVF2-0.9-I	7	0.9	77	0.01
	PVF2-0.8-I	7	0.8	330	0.02
	PVF2-0.7-I	7	0.7	12877	0.89
	PVF2-0.6-I	7	0.6	70773	4.91
PVF1-8lbs	PVF1-8lbs-0.9	7	0.9	290	0.02
	PVF1-8lbs-0.8	7	0.8	10359	0.72
	PVF1-8lbs-0.7	7	0.7	87120	6.05
	PVF1-8lbs-0.6-II	7	0.6	84946**	5.9
	PVF1-8lbs-0.6-III	7	0.6	179453	12.46
* Number of cycles excluding 120 cycles of ramped loads.				Total Testing Time (hr)	76.9
** Reading excluded due to low number of cycles until failure.					



APPENDIX K EFFECT OF FATIGUE ON FREEZE–THAW TEST RESULTS

Table K-1. Mass loss for PV, PVF1, and PVF1-8lbs. at 300 freeze–thaw cycles

Mix No.	Fresh Air Content, %	No. of specimens	Mass Loss, %
PV #1	7.2	6	1.47
PV #2	6.9	5	1.65
<i>Average % loss PV mixes</i>			<i>1.56</i>
PVF1 #3	7	6	0.81
PVF1 #4	6.9	6	1.06
<i>Average % loss PVF1 mixes</i>			<i>0.93</i>
PVF1-8lbs. #1	7	5	0.76
PVF1-8lbs. #2	7	6	0.74
<i>Average % loss PVF1-8lbs. mixes</i>			<i>0.75</i>

Table K-2. Durability factor for PV, PVF1, and PVF1-8lbs. at 300 freeze–thaw cycles

Mix No.	Fresh Air Content, %	Freeze Thaw Performance		
		No. of Specimens		Average <i>DF</i>
		Total	More than 90% <i>DF</i>	
PV #1	7.2	6	5	91.5
PV #2	6.9	5	3	90.6
PVF1 #3	7	6	5	92.6
PVF1 #4	6.9	6	4	89.3
PVF1-8lbs. #1	7	5	4	89.7
PVF1-8lbs. #2	7	6	4	91.9

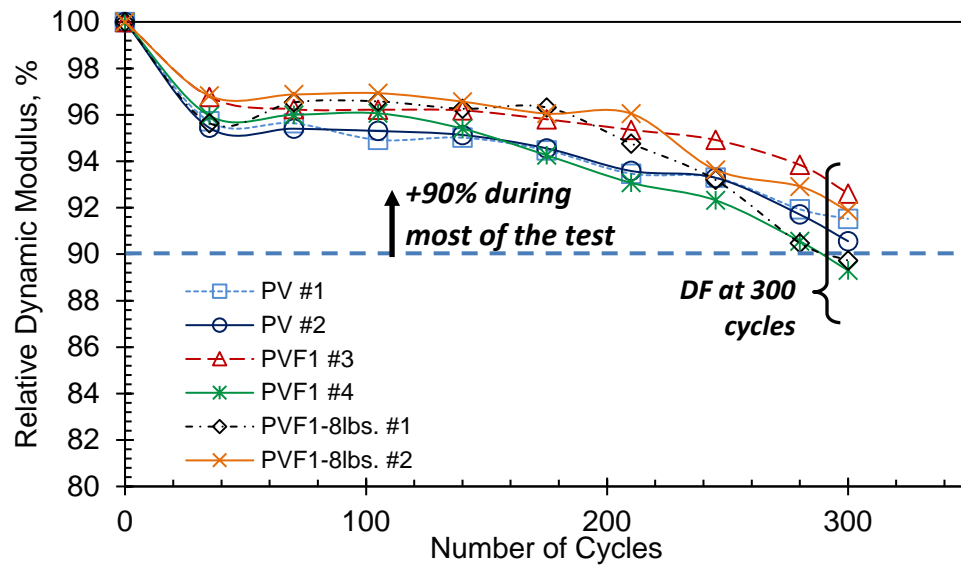


Figure K-1. Relative dynamic modulus versus number of cycles for PV, PVF1, and PVF1-8lbs. mixes

APPENDIX L FINITE-ELEMENT ANALYSIS RESULTS

Table L-1. Maximum flexural stresses in the transverse direction

Concrete Age	Slab Thickness (in.)	Stresses in transverse direction, σ_x (psi)				
		Subgrade Reaction, K (psi/in.)				
		50	100	200	300	500
12-Hrs.	6	278.8	263.4	247.9	238.5	226.3
	8	167.3	158.9	150.3	145.2	138.8
	10	112	106.9	101.5	98.3	94.2
	12	80.3	77.1	73.5	71.3	68.5
	14	64.7	58.2	55.8	54.2	52.2
	16	55.8	45.6	43.8	42.7	41.2
1-Day	6	286.5	271.3	255.9	246.7	234.7
	8	171.5	163.3	154.7	149.6	143.3
	10	114.4	109.6	104.3	101.1	97
	12	84.6	78.8	75.3	73.2	70.4
	14	72	59.4	57.1	55.6	53.6
	16	60.2	50.5	44.8	43.7	42.2
3-Days	6	291.7	276.5	261.1	252.1	240.4
	8	174.1	166.1	157.6	152.6	146.2
	10	115.9	111.3	106.1	103	98.9
	12	91.8	79.9	76.5	74.5	71.7
	14	76.1	62.3	57.9	56.5	54.5
	16	62.6	54.3	45.4	44.3	42.9
7-Days	6	295	279.9	264.6	255.5	244
	8	175.8	168	159.6	154.5	148.1
	10	116.9	112.4	107.3	104.2	100.2
	12	96.1	80.6	77.3	75.3	72.6
	14	78.5	65.8	58.4	57	55.1
	16	64	56.6	45.7	44.7	43.4

Table L-2. Maximum flexural stresses in the longitudinal direction

Concrete Age	Slab Thickness (in.)	Stresses in longitudinal direction, σ_y (psi.)				
		Subgrade Reaction, K (psi/in.)				
		50	100	200	300	500
12-Hrs.	6	331.4	296.7	267.1	251.4	232.6
	8	217.1	191.8	171.3	161	149.1
	10	157.8	138.3	122.3	114.4	105.6
	12	121.5	106.5	93.5	87	79.9
	14	96.9	85.5	74.9	69.4	63.4
	16	79.3	70.5	61.9	57.3	52.1
1-Day	6	352	313.6	281.7	265.1	245.5
	8	232.1	204	181.3	170	157.2
	10	168.8	147.8	130	121.2	111.5
	12	129.4	114	99.9	92.6	84.7
	14	102.8	91.3	80.1	74.1	67.4
	16	83.8	75	66.2	61.3	55.6
3-Days	6	367	325.8	292.1	274.6	254.4
	8	242.8	213	188.5	176.4	162.9
	10	176.3	154.7	135.7	126.2	115.8
	12	134.8	119.2	104.4	96.7	88.2
	14	106.7	95.2	83.8	77.6	70.4
	16	86.9	78	69.2	64.1	58.1
7-Days	6	378	334.3	299.1	281.1	260.3
	8	250.1	219.2	193.5	180.9	166.8
	10	181.3	159.3	139.6	129.7	94.1
	12	138.3	122.6	107.6	99.6	90.6
	14	109.3	97.7	86.3	79.9	72.5
	16	89	79.9	71.1	66	59.9

Table L-3. Maximum slab deflection

Concrete Age	Slab Thickness (in.)	Deflection (in.)				
		Subgrade Reaction, K (psi/in.)				
		50	100	200	300	500
12-Hrs.	6	0.03478	0.02198	0.01428	0.01125	0.00845
	8	0.02633	0.01646	0.01036	0.00798	0.00583
	10	0.02089	0.01327	0.0083	0.00631	0.00452
	12	0.01691	0.011	0.00696	0.00528	0.003742
	14	0.01401	0.00926	0.00597	0.00456	0.003221
	16	0.01191	0.00791	0.00517	0.00398	0.002833
1-Day	6	0.03104	0.01945	0.01244	0.00971	0.00722
	8	0.02335	0.0147	0.00919	0.00703	0.00508
	10	0.01824	0.01177	0.00741	0.00562	0.00399
	12	0.01465	0.00965	0.00619	0.00472	0.003334
	14	0.01213	0.00805	0.00526	0.00405	0.002875
	16	0.01037	0.00684	0.00452	0.00516	0.002522
3-Days	6	0.02877	0.01798	0.0114	0.00885	0.00653
	8	0.02147	0.01362	0.00851	0.00648	0.00465
	10	0.01662	0.01083	0.00686	0.00521	0.003689
	12	0.01329	0.00881	0.00571	0.00437	0.003091
	14	0.01106	0.00732	0.00482	0.00373	0.002663
	16	0.00947	0.00621	0.00412	0.003219	0.002327
7-Days	6	0.02737	0.0171	0.01079	0.00834	0.00612
	8	0.02028	0.01294	0.0081	0.00616	0.0044
	10	0.01562	0.01023	0.00652	0.00496	0.003507
	12	0.01248	0.00829	0.0054	0.00415	0.002942
	14	0.01041	0.00686	0.00454	0.003528	0.00253
	16	0.00893	0.00585	0.00388	0.003036	0.00204

Table L-4. Effect of concrete age (k = 100 psi/in., thickness = 8 in.)

Age	12 Hrs.	Diff %	1 Day	Diff %	3 Days	Diff %	7 Days
Transverse Stresses (psi.)	158.9	2.8	163.3	1.7	166.1	1.1	168
Longitudinal Stresses (psi.)	191.8	6.4	204	4.4	213	2.9	219.2
Deflection (in.)	0.01646	-10.7	0.0147	-7.3	0.01362	-5.0	0.01294

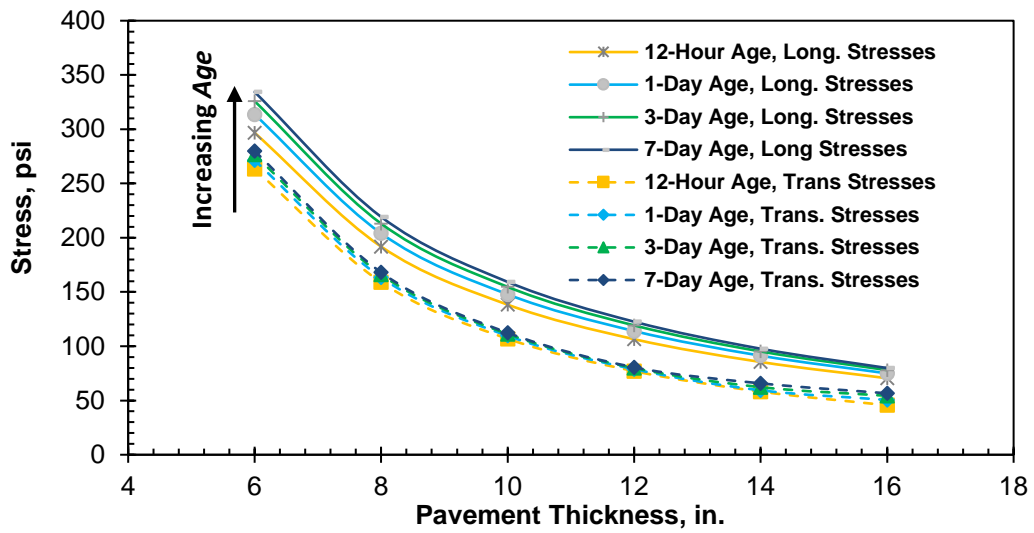


Figure L-1. Variation of transverse and longitudinal stresses versus thickness ($k = 100$ psi/in.)

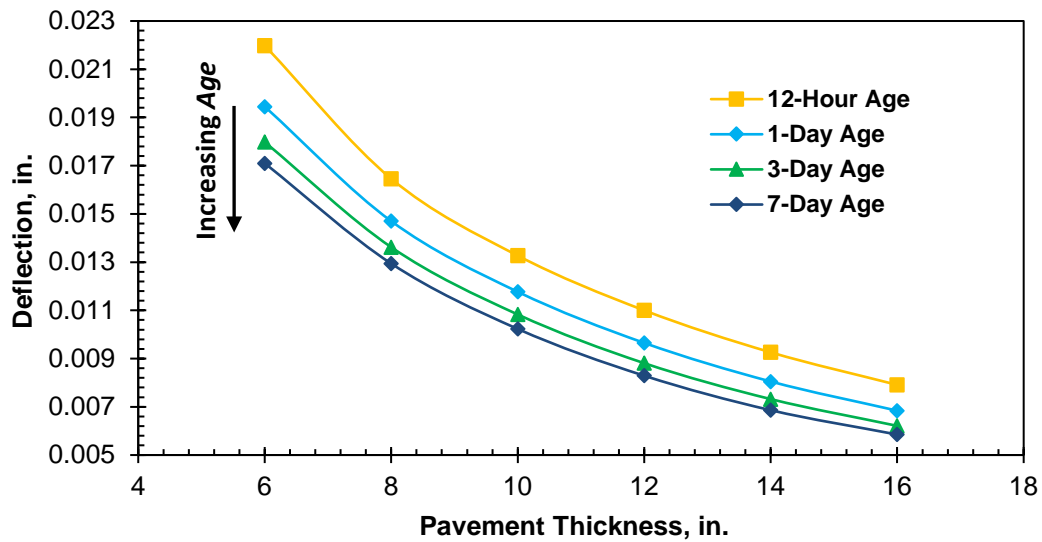


Figure L-2. Variation of deflection versus thickness ($k = 100$ psi/in.)

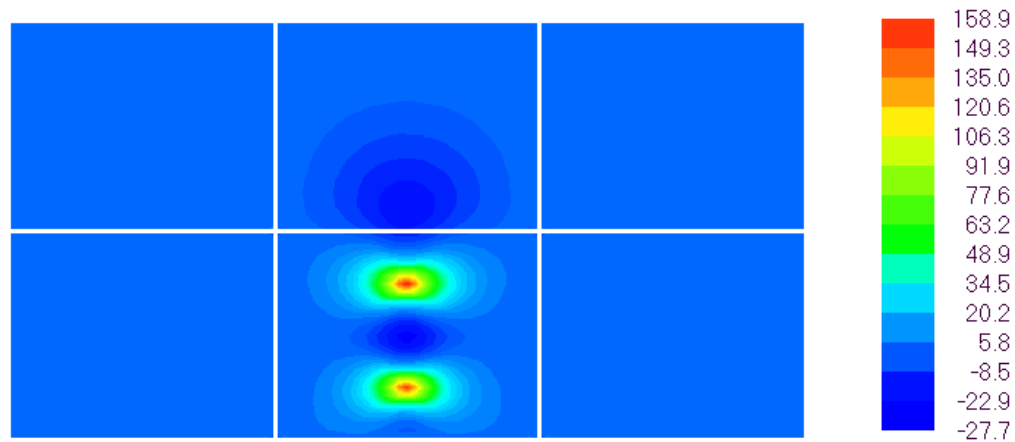


Figure L-3. Typical Transverse stress distribution (Case of: 12-hrs., $k = 100$ psi/in., and 8-in. thickness)

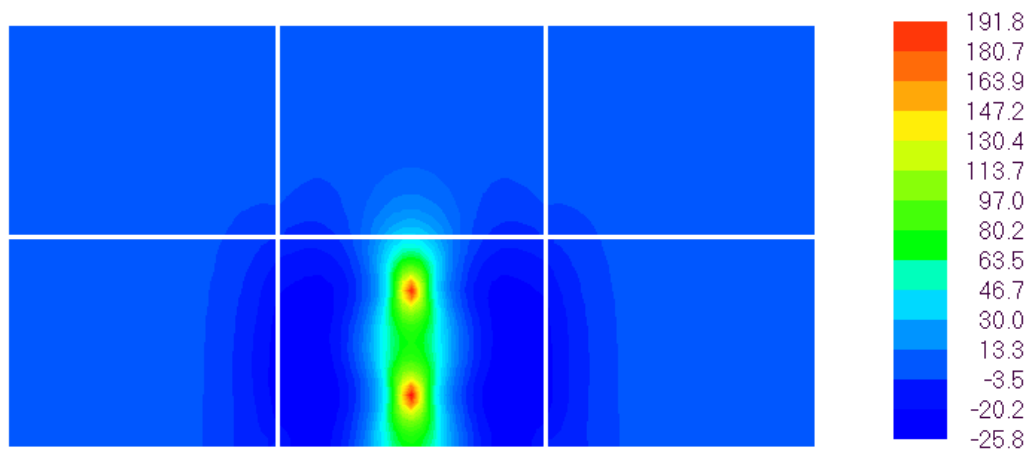


Figure L-4. Typical Longitudinal stress distribution (Case of: 12-hrs., $k = 100$ psi/in., 8-in. depth)

Table L-5. Effect of subgrade modulus (3-day concrete age, thickness = 8 in.)

Subgrade Reaction, K (psi/in.)	50	100	200	300	500	Diff %
Transverse Stresses (psi.)	174.1	166.1	157.6	152.6	146.2	-12.0
Longitudinal Stresses (psi.)	242.8	213	188.5	176.4	162.9	-23.5
Deflection (in.)	0.02147	0.01362	0.00851	0.00648	0.00465	-65.9
Note1: The percentage difference is calculated between the case of $K = 50$ psi/in. and the case of $K = 500$ psi/in.						
Note 2: Negative values mean reduction						

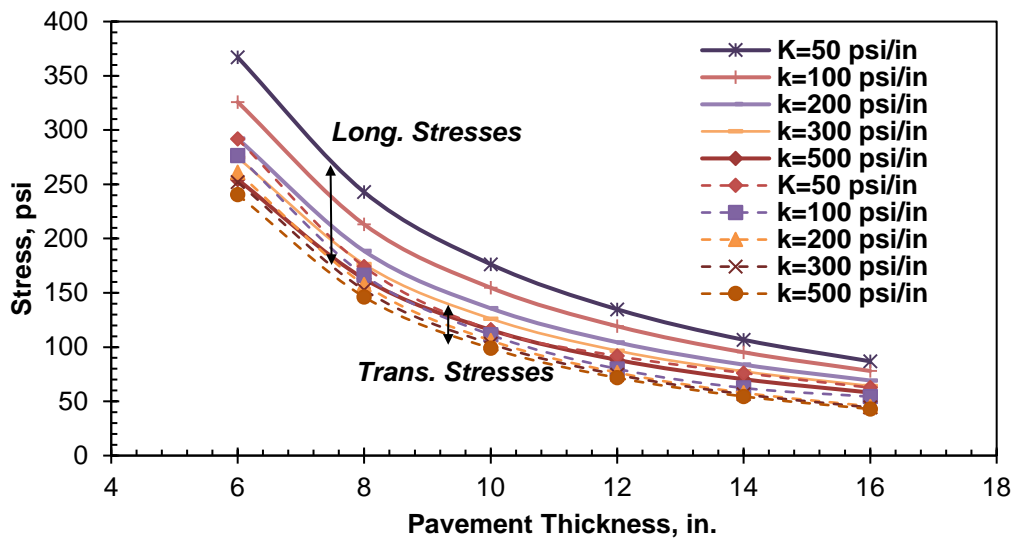


Figure L-5. Variation of stresses versus thickness (Concrete age of 3 days)

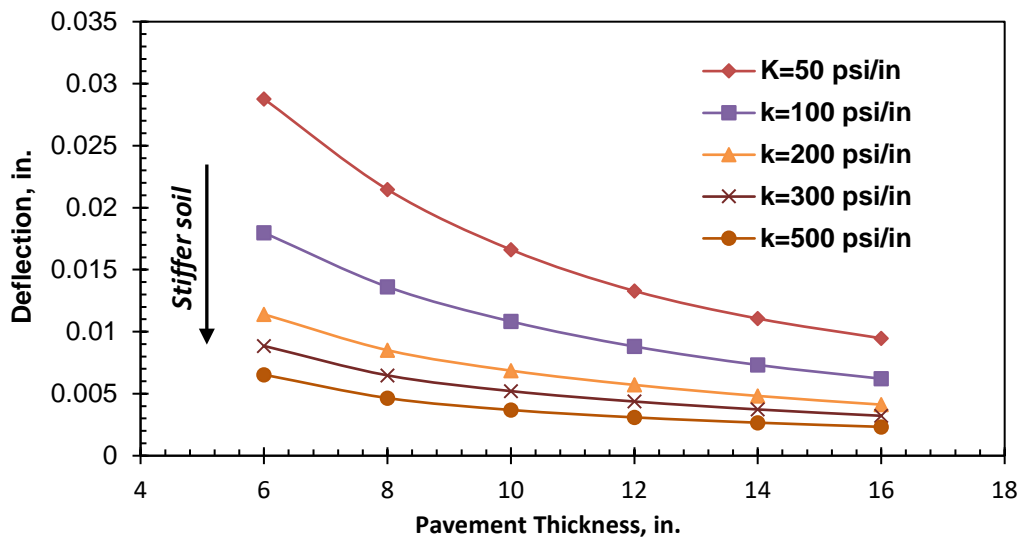


Figure L-6. Variation of deflection versus thickness (Concrete age of 3 days)

Table L-6. Effect of increasing thickness (3-day concrete age, $k = 100$ psi/in.)

Slab Thickness (in.)	6	8	Diff %	10	Diff %	12	Diff %
Transverse Stresses (psi.)	276.5	166.1	-40	111.3	-60	79.9	-71
Longitudinal Stresses (psi.)	325.8	213	-35	154.7	-53	119.2	-63

Deflection (in.)	0.01798	0.01362	-24	0.01083	-40	0.00881	-51
Note1: The percentage difference in each case is taken with respect to the 6 in. thickness.							
Note 2: Negative values mean reduction							

Table L-7. Flexural strength for PV mixes at all ages

Age	12-Hrs	1-Day	3-Day	7-Day
MOR (psi)	161	306	512	782

Table L-8. Stress level calculation results

Age	Mix type	S-N linear regression relationships
12-Hrs.	Plain	$S = -0.030 \ln(M) + 1.0090$
	FRC	$S = -0.028 \ln(M) + 1.0257$
1-Day	Plain	$S = -0.028 \ln(M) + 1.0098$
	FRC	$S = -0.025 \ln(M) + 1.0066$
3-Day	Plain	$S = -0.044 \ln(M) + 1.1072$
	FRC	$S = -0.036 \ln(M) + 1.0822$
7-Day	Plain	$S = -0.041 \ln(M) + 1.1022$
	FRC	$S = -0.043 \ln(M) + 1.1616$

Table L-9. Fatigue life estimation results for 6 in. concrete slabs

Concrete Age	K (psi/in.)	σ_y (psi)	MOR (psi)	$S = \frac{\sigma_y}{MOR}$	N (Plain)	Fatigue Life (Hrs.)	N (FRC)	Fatigue Life (Hrs.)
12 Hrs.	100	296.7	161	1.84	-	-	-	-
	300	251.4	161	1.56	-	-	-	-
1 Day	100	313.6	306	1.02	-	-	-	-
	300	265.1	306	0.87	168	0	273	0
3 Day	100	325.8	512	0.64	44428	1	239266	17
	300	274.6	512	0.54	431214	5	4.0E+06	278

Table L-10. Fatigue life estimation results for 8 in. concrete slabs

Concrete Age	K (psi/in.)	σ_y (psi)	MOR (psi)	$S = \frac{\sigma_y}{MOR}$	N (Plain)	Fatigue Life (Hrs.)	N (FRC)	Fatigue Life (Hrs.)
12 Hrs.	100	191.8	161	1.19	-	-	-	-
	300	161	161	1.00	-	-	-	-
1 Day	100	204	306	0.67	209979	15	803983	56
	300	170	306	0.56	1.E+07	771	6.85E+07	4754

Table L-11. Stresses and deflection results for LTE-based cases

LTE (%)	Trans. Stress (psi)	Long. Stress (psi)	Deflection (in)
50	419	112.6	0.0382
60	408	116.8	0.03603
70	393	120.8	0.03429
80	370	124.9	0.03281
90	333	130.2	0.03146
91	328	130.9	0.03133
92	323	131.6	0.03119
93	317	132.4	0.03106
94	310	133.2	0.03093
95	302	134.2	0.03079

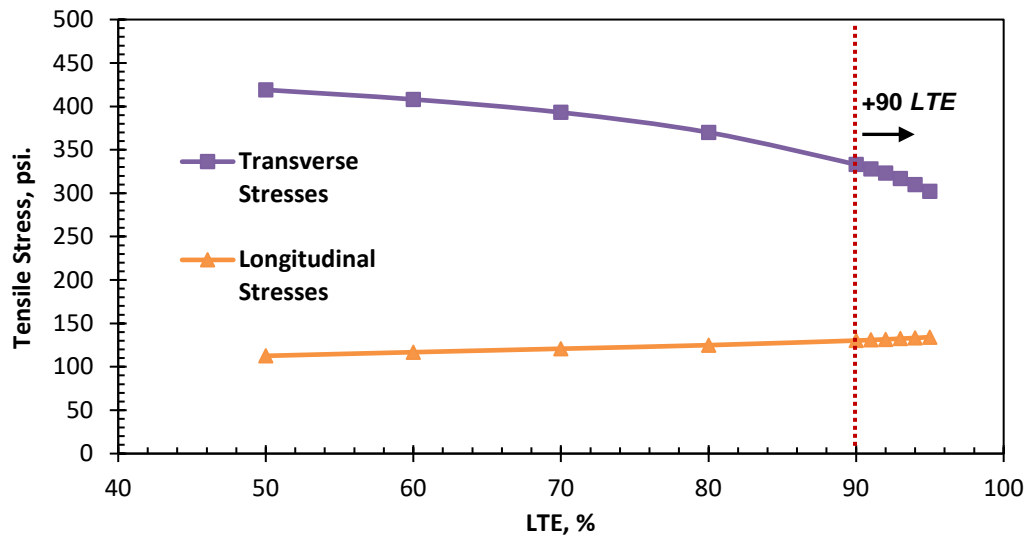


Figure L-7. Variation of transverse and longitudinal stresses vs. LTE (LTE based cases)

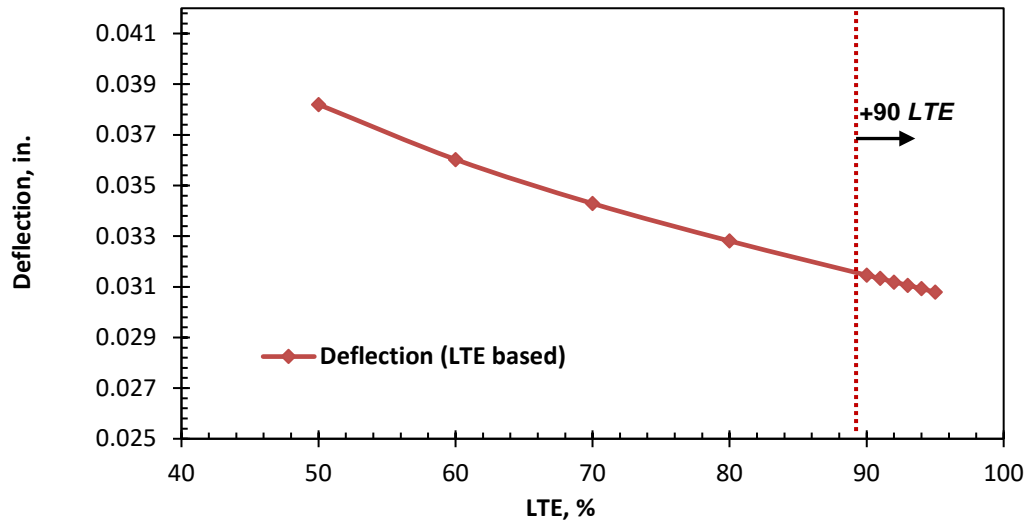


Figure L-8. Variation of deflection versus LTE for LTE based cases

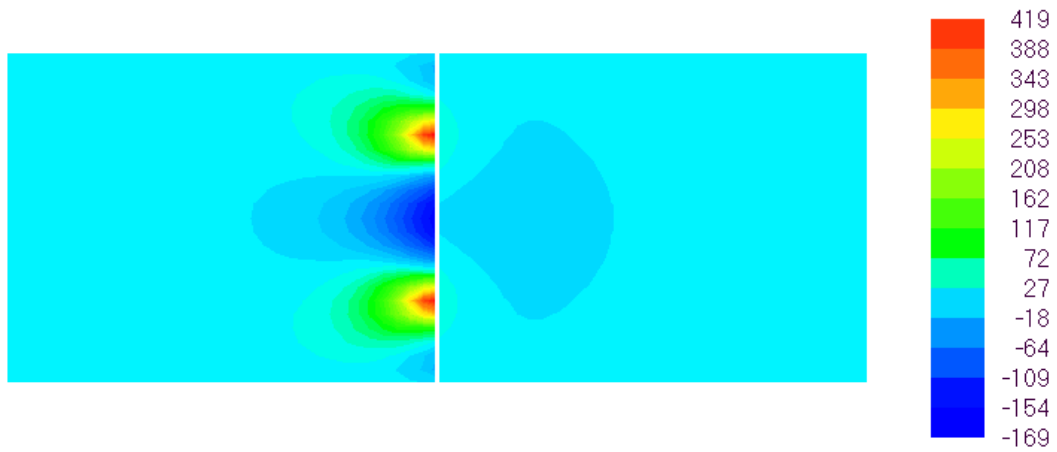


Figure L-9. Transverse stress distribution for 50% LTE

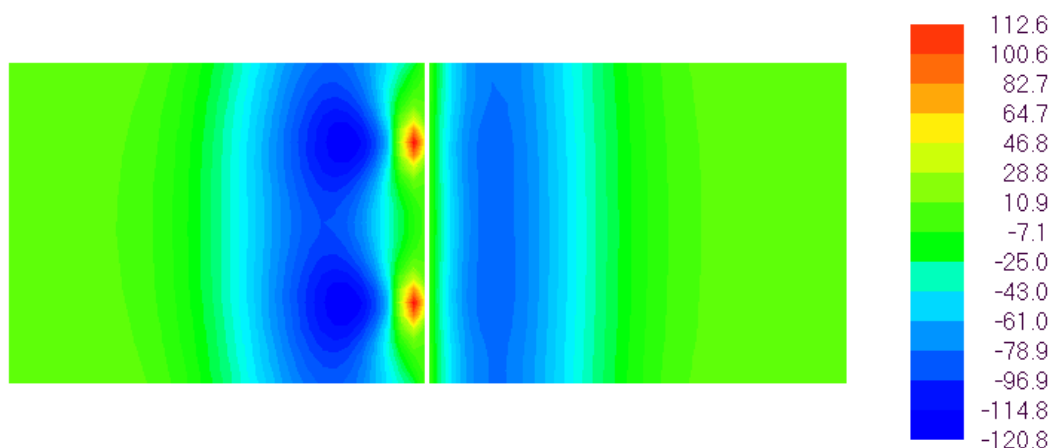


Figure L-10. Longitudinal stress distribution for 50% LTE

Table L-12. Stresses and deflection results for dowel and AGG option

LTE (%)	AGG (psi)	σ_x (psi)	Percentage difference with case of no AGG	σ_y (psi)	Percentage difference with case of no AGG	Deflection (in)	Percentage difference with case of no AGG
50	3432	401	-2.2	130.8	0.8	0.03151	-0.5
60	5533	396	-3.4	131.4	1.2	0.03143	-0.8
70	9310	388	-5.4	132.3	1.9	0.03129	-1.2
80	17565	374	-8.8	133.9	3.2	0.03106	-2.0
90	45654	344	-16.1	137.3	5.8	0.03062	-3.3
91	52363	339	-17.3	137.8	6.2	0.03056	-3.5
92	60935	334	-18.5	138.4	6.6	0.03049	-3.8
93	72228	328	-20.0	139.2	7.2	0.03041	-4.0
94	87706	321	-21.7	140	7.9	0.03033	-4.3
95	110079	313	-23.7	140.9	8.6	0.03024	-4.5
Dowel Transfer with no AGG		410	-	129.8	-	0.03168	-
Note 1: Percentage difference is taken between each stress value and the case of Dowel Transfer with no AGG.							
Note 2: negative values mean reduction							

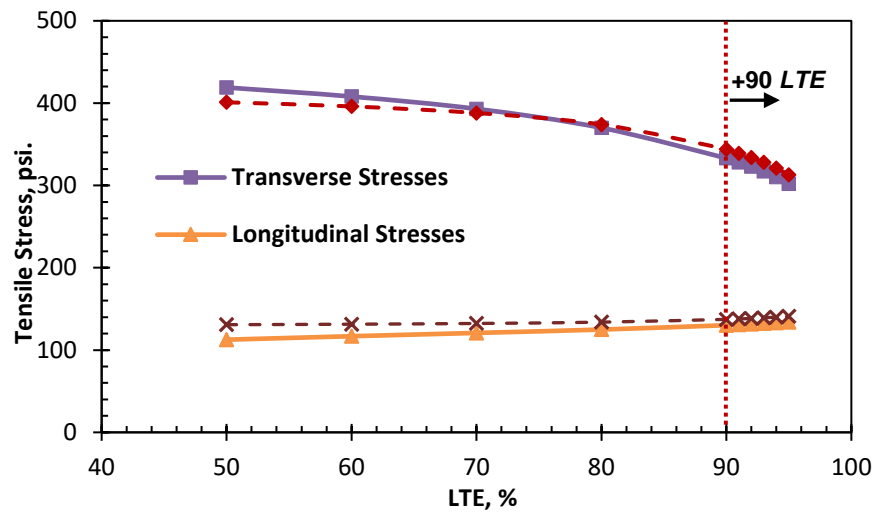


Figure L-11. Variation of transverse and longitudinal stresses versus LTE (LTE-based and dowel transfer based)

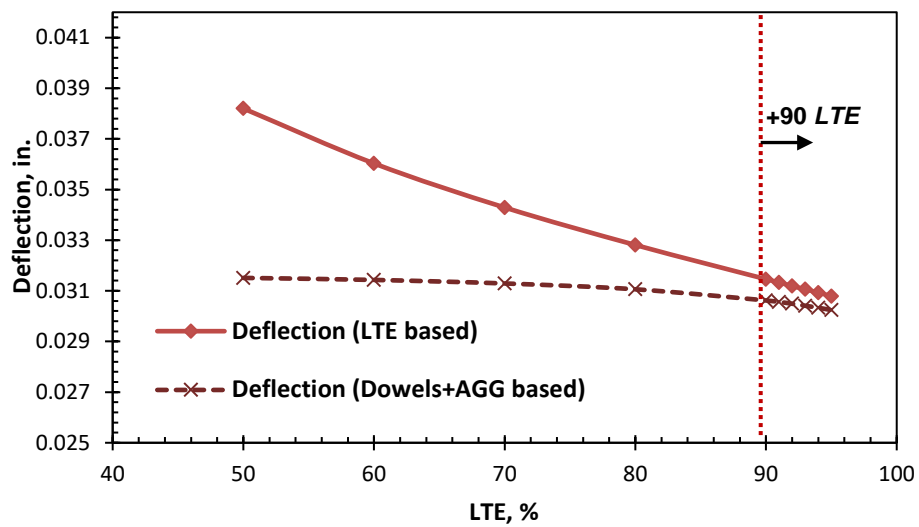
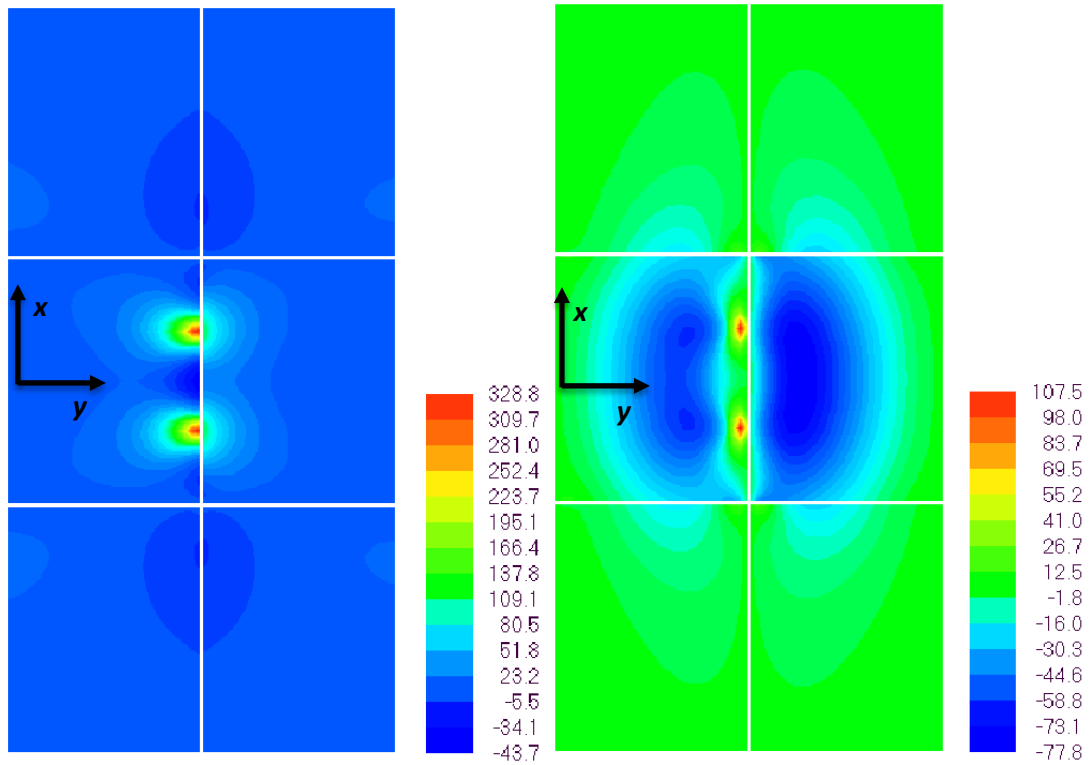


Figure L-12. Variation of deflection versus LTE (LTE-based and dowel transfer based)

Table L-13. Transverse flexural stresses and concrete flexural capacity for PV mixes

Concrete Age	Thickness (in.)	Flexural transverse Stresses* (psi)					Flexural Capacity (psi.)
		K Subgrade Reaction (psi/in.)					
		50	100	200	300	500	
12-hr	6	508	455	407	381	349	161
	8	329	294	263	246	227	
	10	235	210	187	175	162	
	12	177	159	142	133	122	
	14	139	126	113	105	97	
	16	111	102	92	86	79	
1-Day	6	538	481	431	404	371	306
	8	348	311	278	261	240	
	10	248	222	198	186	171	
	12	186	168	151	141	130	
	14	145	132	119	112	103	
	16	116	107	97	91	84	
3-Day	6	559	499	447	419	386	512
	8	362	323	289	271	249	
	10	257	231	206	193	178	
	12	192	174	157	146	135	
	14	149	137	124	116	107	
	16	118	110	101	95	87	
7-Day	6	573	512	458	430	396	782
	8	371	332	296	277	256	
	10	262	236	211	198	182	
	12	196	178	160	150	138	
	14	151	140	127	119	110	
	16	120	112	103	97	89	
* Hatched cells indicates that flexural are exceeding the corresponding flexural capacity.							



(a) Transverse stresses

(b) Longitudinal stresses

Figure L-13. Flexural stress distribution ($t = 8$ in., $k = 50$ psi/in., 12-hr)

Table L-14. Transverse flexural stresses results and estimated shear capacity for PV mixes

Concrete Age	Thickness (in.)	Shear Stresses* (psi)					Shear Capacity (psi.)
		K Subgrade Reaction (psi/in.)					
		50	100	200	300	500	
12-hr	6	106	95	87	82	76	48.3
	8	71	62	54	52	49	
	10	51	45	39	36	34	
	12	38	35	31	28	25	
	14	30	27	24	23	20	
	16	24	22	20	19	17	
1-Day	6	114	99	91	86	80	65.9
	8	76	66	57	54	51	
	10	54	48	42	39	35	
	12	40	37	33	30	27	
	14	31	29	26	24	22	
	16	25	23	21	20	18	
3-Day	6	120	103	94	89	83	81.0
	8	79	70	60	55	52	
	10	56	50	44	41	37	
	12	41	38	34	32	29	
	14	32	30	27	25	23	
	16	26	24	22	21	19	
7-Day	6	123	107	95	91	85	92.7
	8	81	72	62	57	53	
	10	57	51	46	42	38	
	12	42	39	35	33	30	
	14	33	30	28	26	24	
	16	26	24	22	21	19	
*Hatched cells indicate a shear stress larger than the expected shear capacity as per ACI 318-14.							

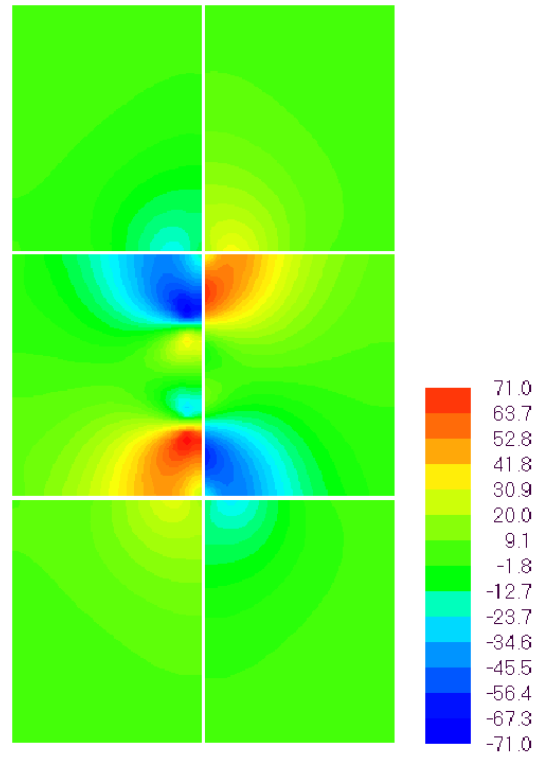


Figure L-14. Shear stress distribution ($t = 8$ in., $k = 50$ psi/in., 12-hr)

APPENDIX M FATIGUE PERFORMANCE OF JOINTED CONCRETE SLABS

Table M-1. Jointed slab specimen characteristics summary

Specimen #	Pavement Thickness	Joint Type	Dowel Dia.	Fiber Content (lb/yd ³)	Testing Time
1	6 in.	Doweled	1 in	8	1-Day
2	6 in.	Doweled	1 in	-	1-Day
3	6 in.	Non-doweled	-	8	1-Day
4	6 in.	Doweled	1	4	1-Day
5	8 in.	Doweled	1.25 in	8	12-hr

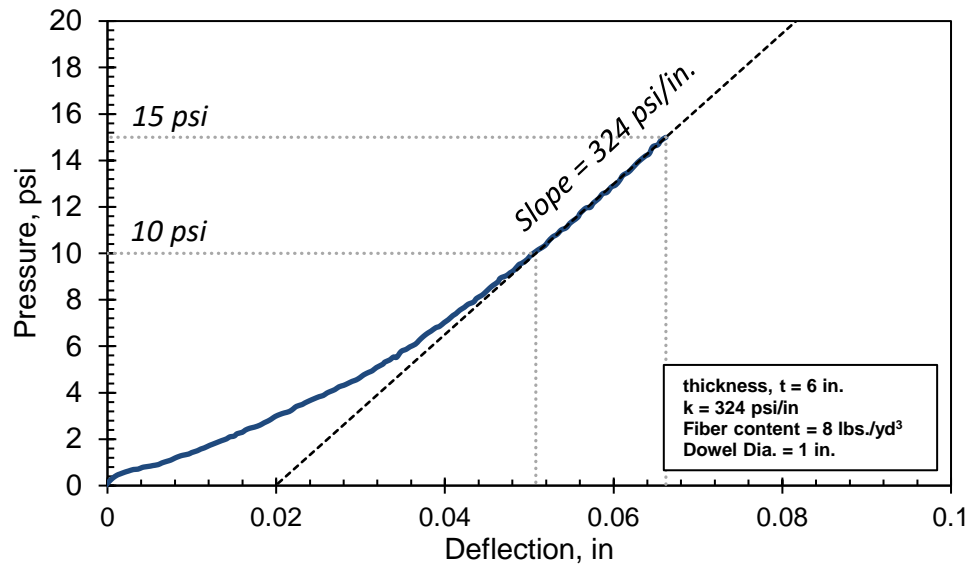


Figure M-1. Plate contact pressure versus deflection (Specimen 1)

Table M-2. Testing segments of the loading schedule (Specimen 1)

Testing Segment	Frequency, Hz.	Maximum Applied Load	Number of Cycles, Millions	Start Date	End Date
1	4	9 kip	2.3	2/11/2017	2/18/2017
2	4	13.5 Kip	1	2/18/2017	2/21/2017
3*	Low cycle*	28 - 40 kip	-	2/21/2017	2/21/2017
4	4	30 kip	1	2/21/2017	2/25/2017
5	4	36 kip	1	2/25/2017	2/28/2017

* Testing segment 3 included six cycles that were applied at a stroke rate of 0.02 in./min. in order to initiate cracking

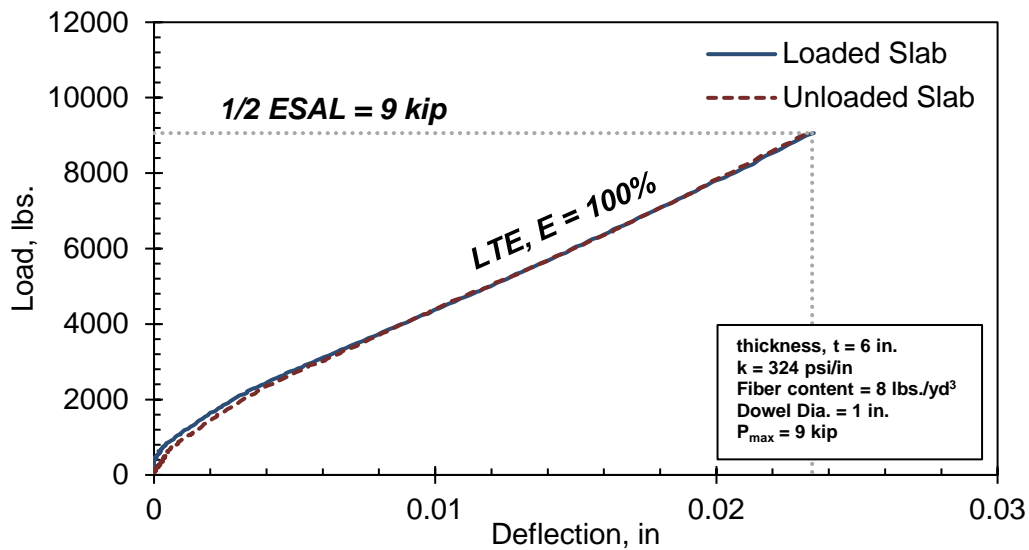


Figure M-2. Load versus deflection for the first static loading (Specimen 1)

Table M-3. Deflection results for static testing (Specimen 1 – Segment 1)

Elapsed Number of Cycles	No. of Static Tests Conducted	Age of Concrete at Time of Testing	Maximum Deflection at 9 kip Loading, in	Residual Deflection after Unloading, in	f'_c , psi	f_r , psi
1	1	1 day	0.024	0.009	2510*	465*
10,000	2	1 day. 1 hr	0.046	0.027	3300	476
100,000	3	1 day - 7 hrs	0.054	0.036	3542	531
300,000	4	1 day- 21 hrs	0.057	0.040	3200*	568*
500,000	5	2 days -11 hrs	0.058	0.043	4155	629
750,000	6	3 days - 4 hrs	0.058	0.043	4249	667
1,000,000	7	3 days - 21 hrs	0.059	0.044	4344	667
1,250,000	8	4 days - 15 hrs	0.059	0.045	4440	706
1,500,000	9	5 days - 8 hrs	0.058	0.046	4489	707
1,750,000	10	6 days - 2 hrs	0.058	0.046	4538	707
2,000,000	11	6 days - 19 hrs	0.057	0.046	4520*	707
2,250,000	12	7 days - 12 hrs	0.057	0.046	4638	707
2,300,000	13	7 days - 16 hrs	0.057	0.046	4638	707

* Strength values determined by testing 6 x 12 in. concrete cylinders for f'_c and 6 x 6 x 21 in. beams for f_r

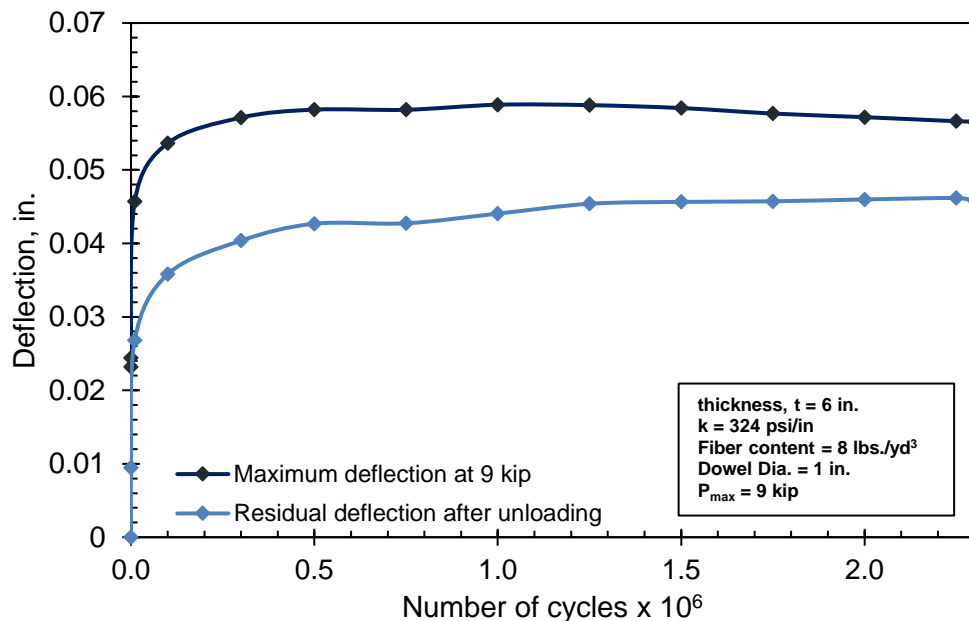


Figure M-3. Deflection versus number of cycles (Specimen 1 – Segment 1)

Table M-4. Deflection results for static testing (Specimen 1 – Segment 2)

Elapsed Number of Cycles	No. of Static Tests Conducted	Age of Concrete at Time of Testing	Maximum Deflection at 13.5 kip, in	Residual Deflection after Unloading, in	f'_c , psi	f_r , psi
1	1	7 days - 16 hrs	0.058	0.046	4638	707
10,000	2	7 days - 16 hrs	0.061	0.046	4638	707
50,000	3	7 days - 19 hrs	0.062	0.047	4638	707
100,000	4	7 days - 23 hrs	0.062	0.047	4638	707
250,000	5	8 days - 9 hrs	0.063	0.048	4638	707
500,000	6	9 days - 2 hrs	0.063	0.049	4638	707
750,000	7	9 days - 20 hrs	0.063	0.050	4739	750
1,000,000	8	10 days - 13 hrs	0.062	0.050	4739	750

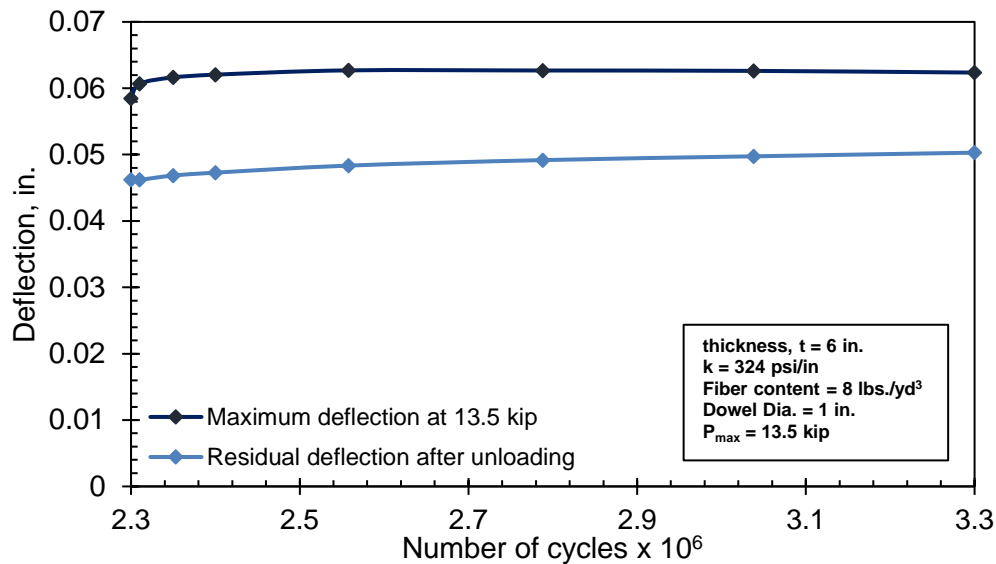


Figure M-4. Deflection versus number of cycles (Specimen 1 – Segment 2)

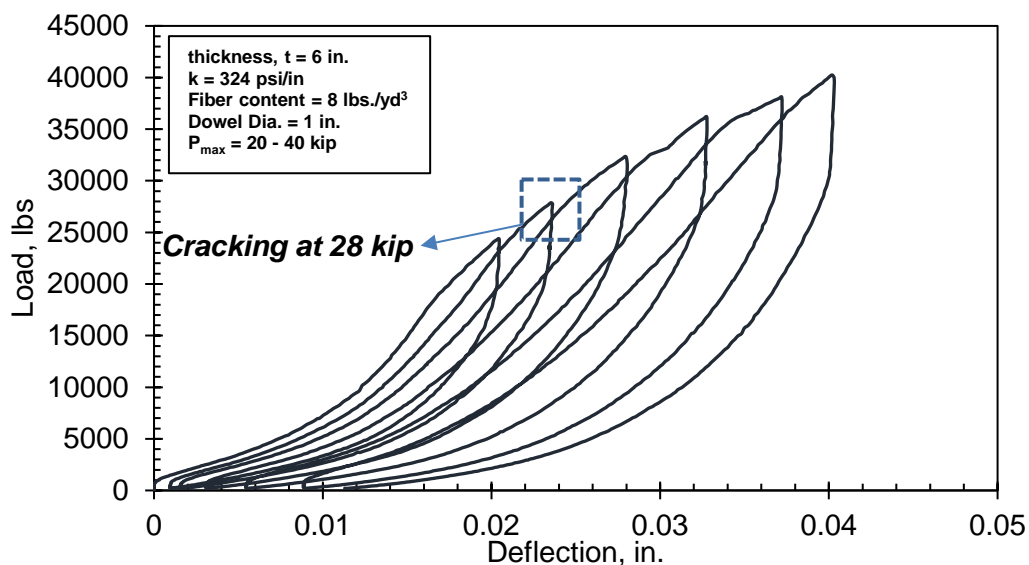


Figure M-5. Load versus overall deflection (Specimen 1 – Segment 3)

Table M-5. Deflection results for static testing (Specimen 1 – Segment 3)

Elapsed Number of Cycles	Peak load, kip	Maximum Deflection at Peak Load, in	Residual Deflection after Unloading, in
1	24	0.071	0.051
2	28	0.074	0.052
3	32	0.078	0.053
4	36	0.080	0.056
5	38	0.088	0.059
6	40	0.091	0.062
Note: Concrete strength was estimated using dynamic modulus testing at an age of 10 days with $f'_c = 4739$ psi and $f_r = 750$ psi.			

Table M-6. Deflection results for static testing (Specimen 1 – Segment 4)

Elapsed Number of Cycles	No. of Static Tests Conducted	Maximum Deflection at 30 kip, in	Residual Deflection after Unloading, in
1,000	1	0.101	0.076
10,000	2	0.104	0.081
100,000	3	0.110	0.088

250,000	4	0.113	0.092
500,000	5	0.114	0.094
750,000	6	0.116	0.097
1,000,000	7	0.116	0.097
Note: Concrete strength was estimated using dynamic modulus testing at an age of 10-13 days with $f'_c = 4739$ psi and $f_r = 750$ psi.			

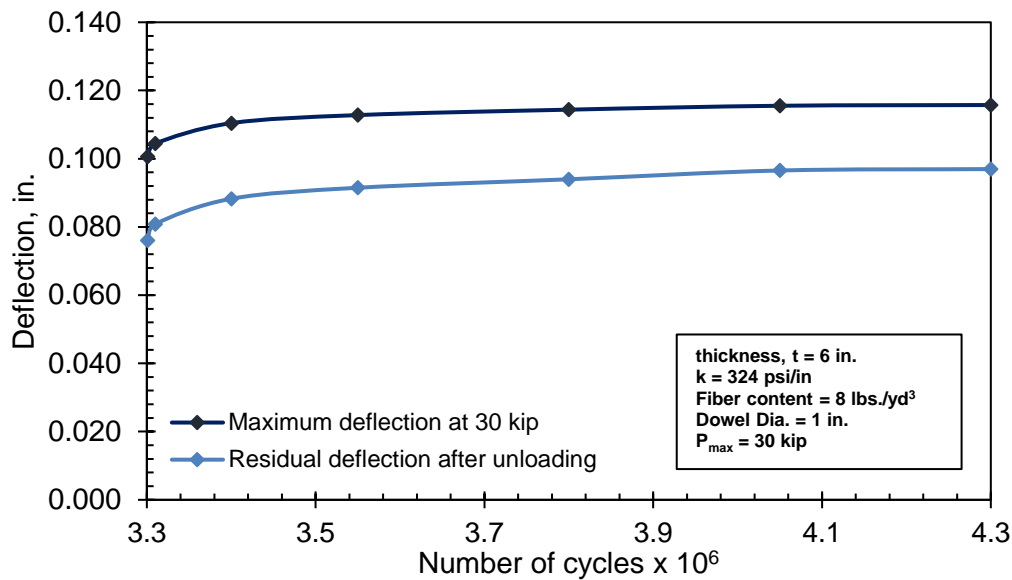


Figure M-6. Deflection versus number of cycles (Specimen 1 – Segment 4)

Table M-7. Deflection results for static testing (Specimen 1 – Segment 5)

Elapsed Number of Cycles	No. of Static Tests Conducted	Maximum Deflection at 36 kip, in	Residual Deflection after Unloading, in
1	1	0.128	0.108
1,000	2	0.129	0.108
10,000	3	0.129	0.108
100,000	4	0.131	0.110
250,000	5	0.133	0.113
500,000	6	0.134	0.114
750,000	7	0.134	0.116
1,000,000	8	0.135	0.117
Note: Concrete strength was estimated using dynamic modulus testing at an age of 13-16 days with $f'_c = 4739$ psi and $f_r = 750$ psi.			

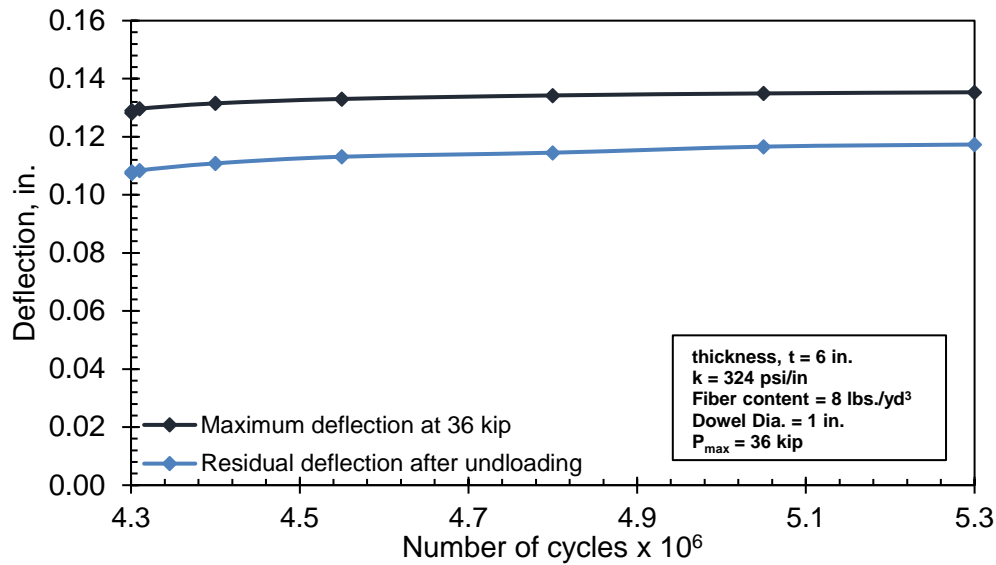


Figure M-7. Deflection versus number of cycles (Specimen 1 – segment 5)

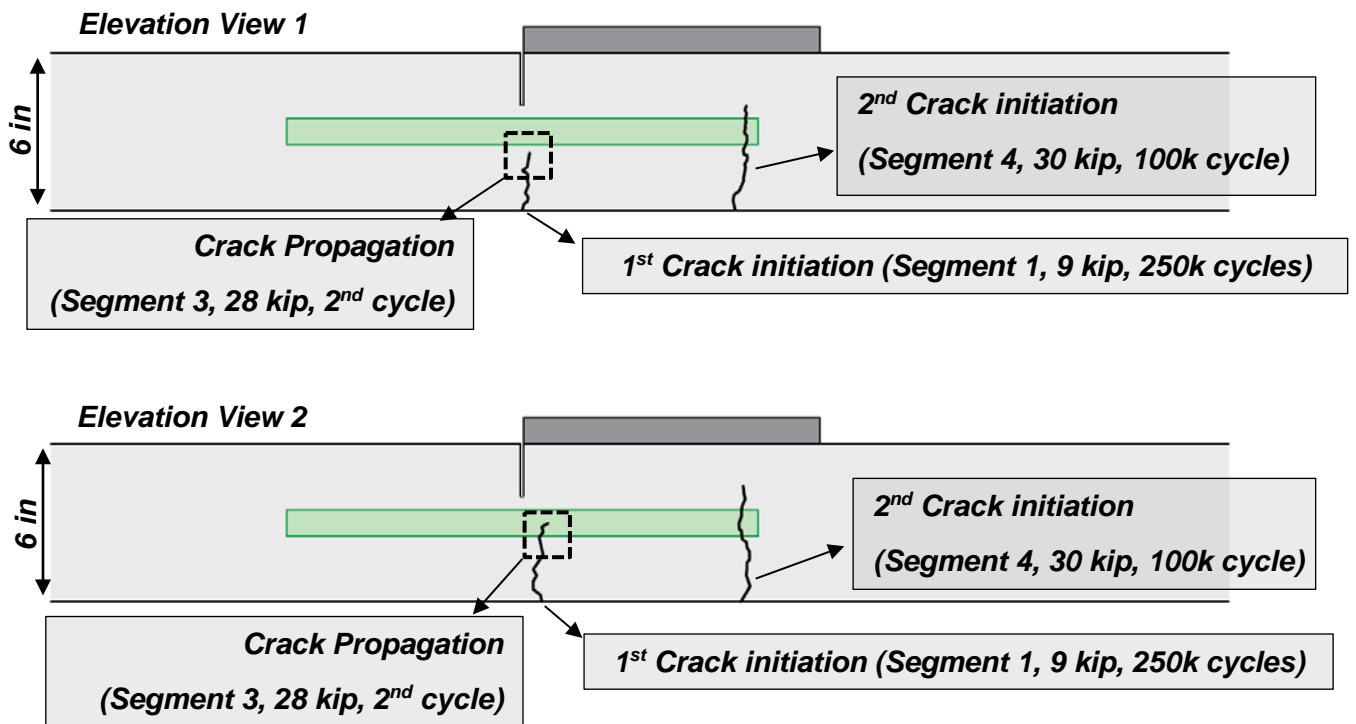


Figure M-8. Crack patterns with respect to dowel bar location (Specimen 1)



Figure M-9. Cracking at the end region of dowel bars (Specimen 1)

Table M-8. Crack initiation and propagation (Specimen 1)

Description	Segment in which cracking happened	Location	Concrete Age
1 st Crack Initiation	Segment 1, 250 k cycles	Groove	1.73 days
Crack propagation	Segment 3, 2nd cycle	Groove	12 days
2 nd Crack Initiation	Segment 4, 100 k cycles	Dowel end	15 days

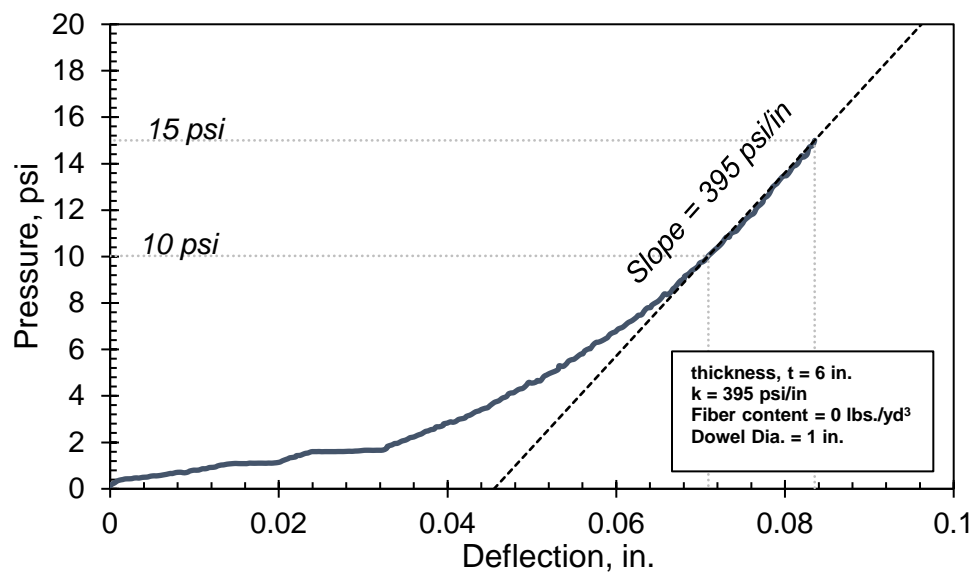


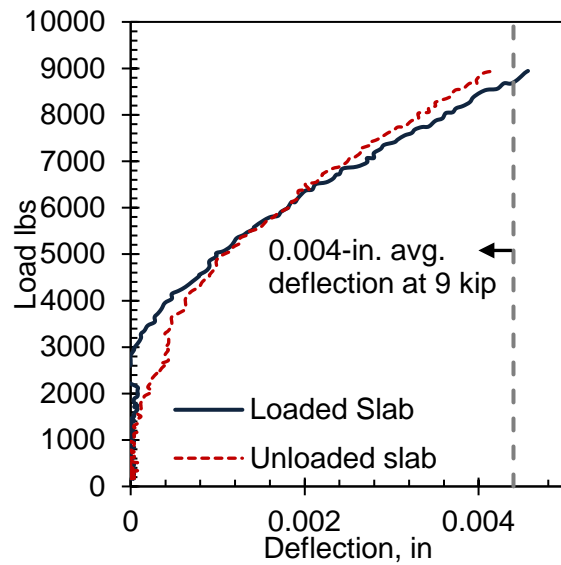
Figure M-10. Plate contact pressure versus deflection (Specimen 2)

Table M-9. Testing segments of the loading schedule (Specimen 2)

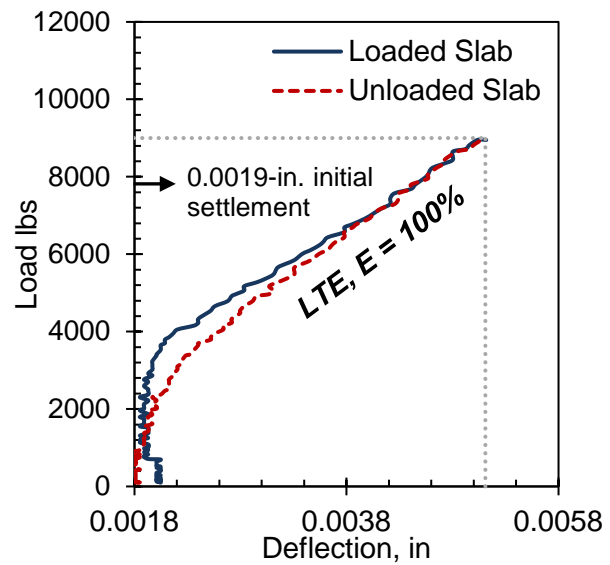
Testing Segment	Frequency, Hz.	Maximum Applied Load	Number of Cycles, Millions	Start Date	End Date
1	4	9 kip	1	6/1/2017	6/4/2017
2	4	13.5 Kip	1	6/4/2017	6/7/2017
3*	Monotonic*	44 kip	-	6/7/2017	
* Testing segment 3 included monotonic loading up to 44 kip at a stroke rate of 0.02 in./min. in order to initiate cracking					

Table M-10. Deflection results for static testing of (Specimen 2 – Segment 1)

Elapsed Number of Cycles	No. of Conducted Static Test	Age of Concrete at Testing Time	Average Deflection at 9 kip Loading, in.	Residual Deflection after Unloading, in.	f_r , psi.
-	-	1 day	-	-	375
-	-	1 day. 6 hrs	-	-	404**
1	1	1 day. 12 hrs	0.004	0.002	427
2*	2	1 day. 12 hrs	0.005	0.002	427
1,000	3	1 day. 12 hrs	0.005	0.002	427
10,000	4	1 day. 13 hrs	0.007	0.002	427
100,000	5	1 day. 18 hrs	0.008	0.002	476
250,000	6	2 days. 5 hrs	0.009	0.003	503
500,000	7	2 days. 23 hrs	0.012	0.005	530**
750,000	8	3 days. 16 hrs	0.012	0.007	562
1,000,000	9	4 days. 10 hrs	0.012	0.007	594
* Second static test was performed to account for large initial settlement					
** Strength values determined by testing 6 x 6 x 21 in. beams for f_r					

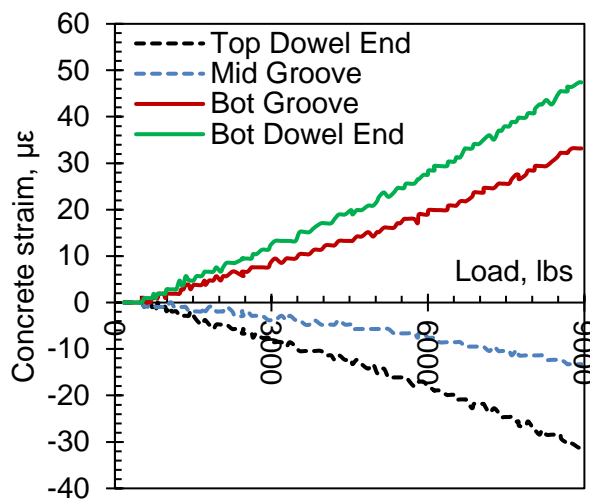


(a) Cycle 1

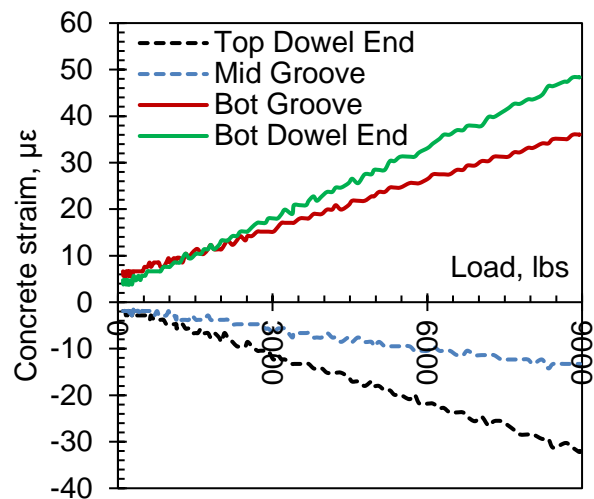


(b) Cycle 2

Figure M-11. Load versus deflection for the first and second static tests (Specimen 1)



(a) Cycle 1



(b) Cycle 2

Figure M-12. Concrete strain versus load for the first and second static tests (Specimen 1)

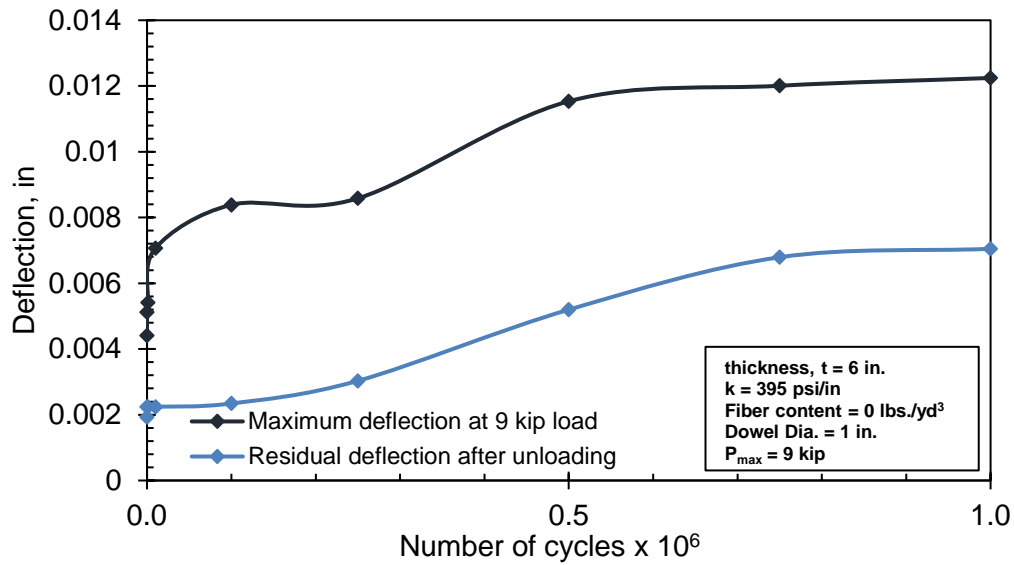


Figure M-13. Deflection versus number of cycles (Specimen 2 – Segment 1)

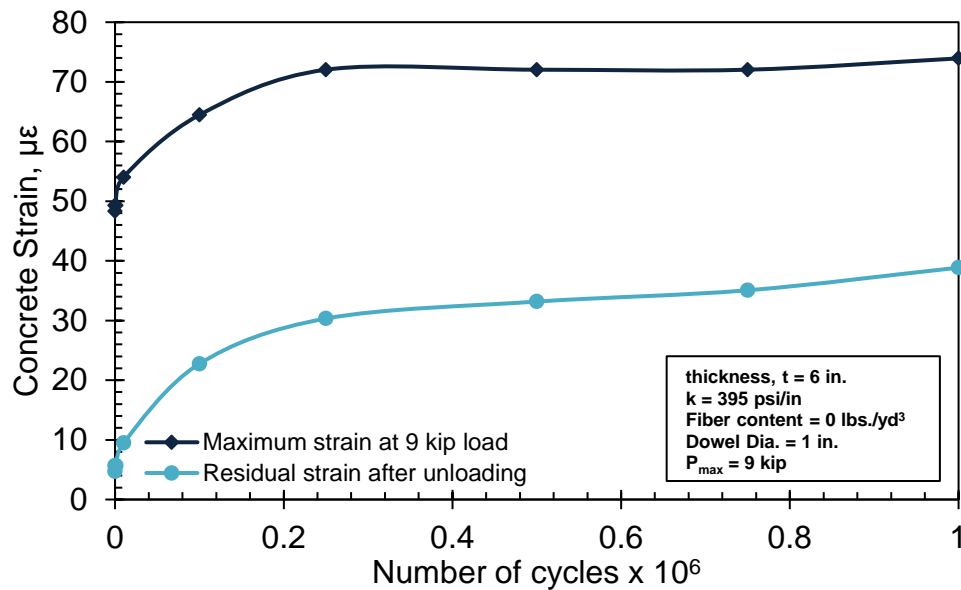


Figure M-14. Concrete tensile strain versus number of cycles at the dowel end region (Specimen 2 – Segment 1)

Table M-11. Deflection results for static testing (Specimen 2 – Segment 2)

Elapsed Number of Cycles	No. of Conducted Static Test	Age of Concrete at Testing Time	Average Deflection at 13.5 kip Loading, in.	Residual Deflection after Unloading, in.	f_r , psi.
1	1	4 days. 10 hrs	0.014	0.007	594
1,000	2	4 days. 10 hrs	0.016	0.009	594
10,000	3	4 days. 11 hrs	0.016	0.009	594
100,000	4	4 days. 17 hrs	0.022	0.014	594
250,000	5	5 days. 3 hrs	0.022	0.014	594
500,000	6	5 days. 21 hrs	0.023	0.015	629
750,000	7	6 days. 14 hrs	0.021	0.016	629
1,000,000	8	7 days. 8 hrs	0.023	0.016	642*

* Strength values determined by testing 6 x 6 x 21 in. beams for f_r

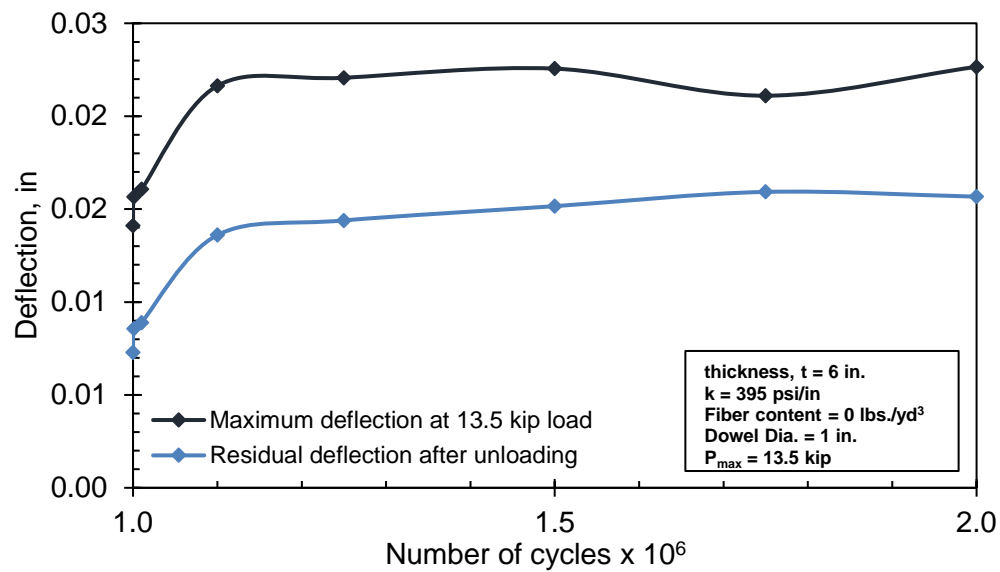


Figure M-15. Deflection versus number of cycles (Specimen 2 – Segment 2)

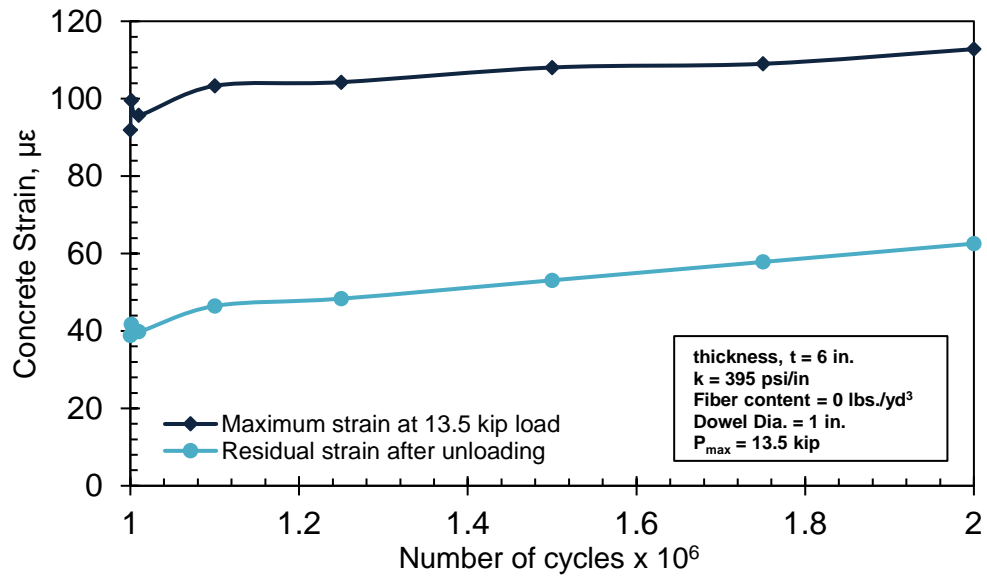


Figure M-16. Concrete tensile strain versus number of cycles at the dowel end region (Specimen 2 – Segment 2)

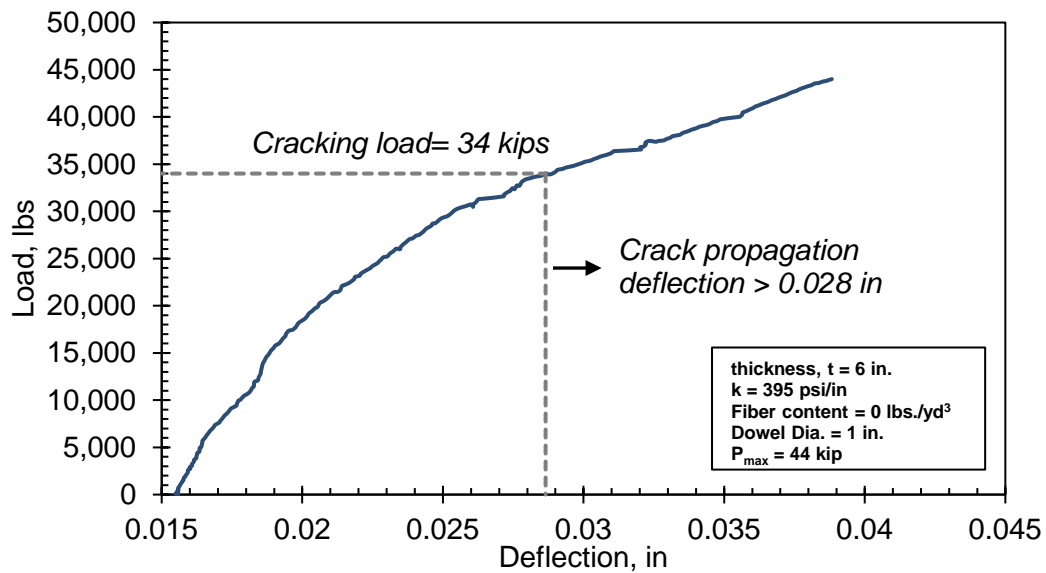


Figure M-17. Load versus slab deflection (Specimen 2 – Segment 3)

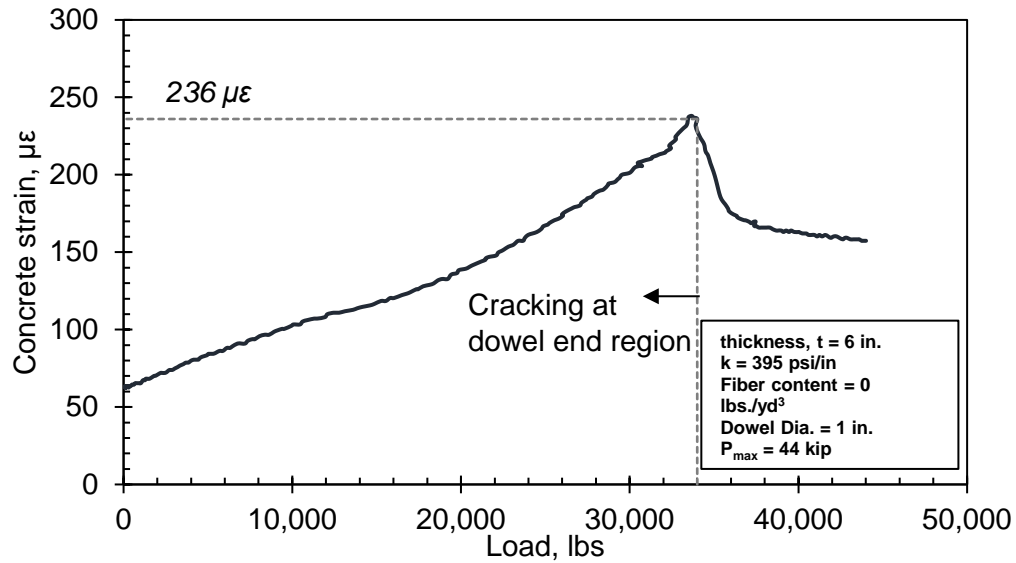


Figure M-18. Concrete tensile strain versus load at the dowel end region (Specimen 2 – Segment 3)

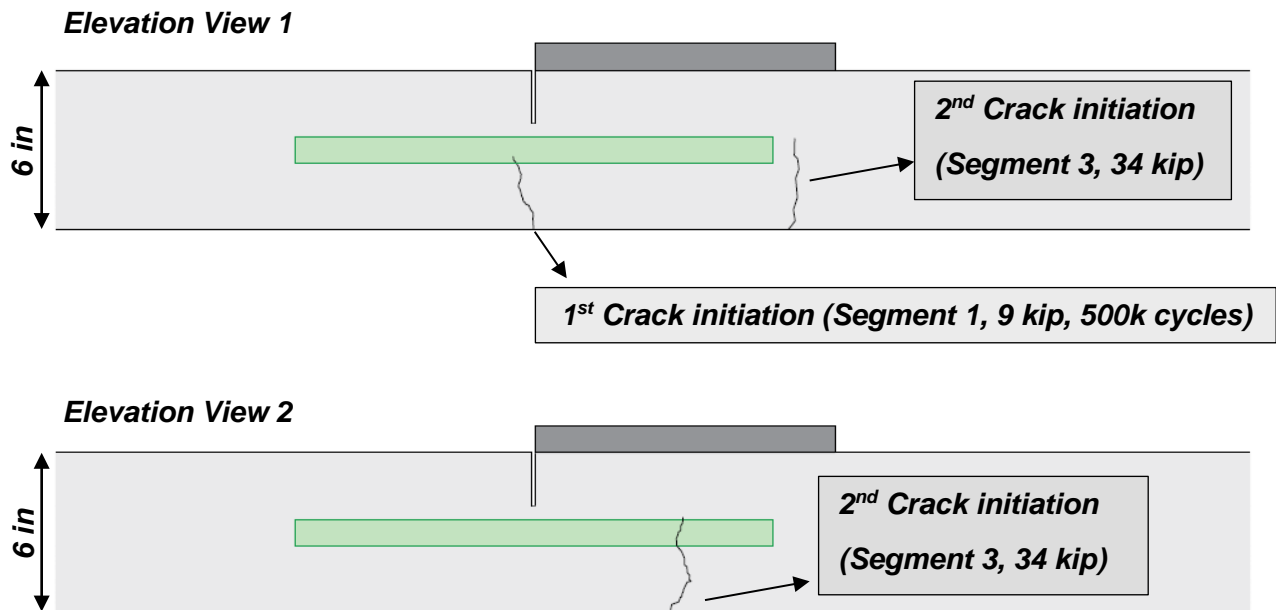


Figure M-19. Crack patterns with respect to dowel location (Specimen 2)



(a)

(b)

Figure M-20. Cracking at the end region of the dowel bars (Specimen 2)

Table M-12. Cracking instances (Specimen 2)

Description	Segment in which cracking happened	Location	Concrete Age
1 st Crack Initiation	Segment 1, 500 k cycles	Groove	2 days, 23 hrs
2 nd Crack Initiation	Segment 3	Dowel end	7 days, 8 hrs

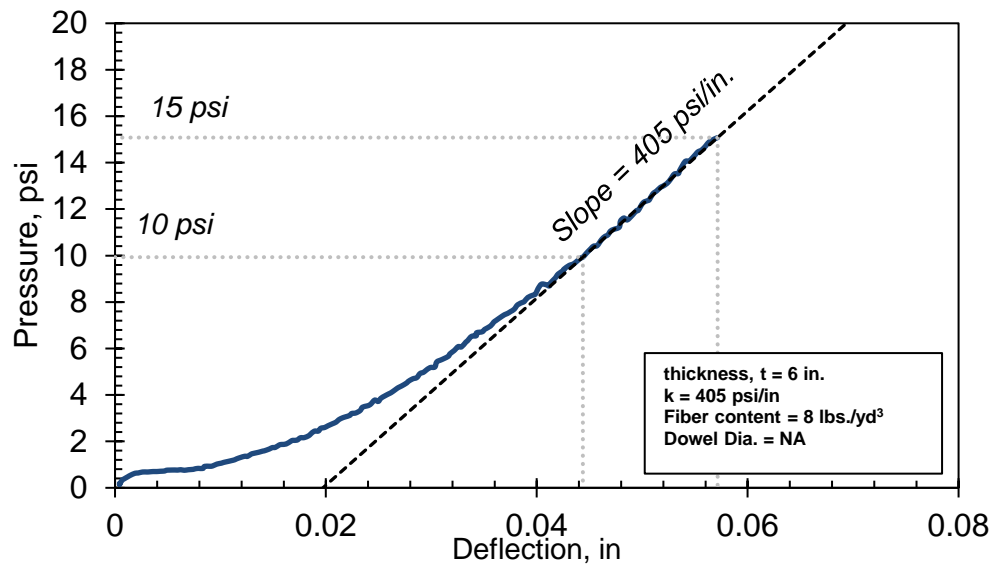


Figure M-21. Plate contact pressure versus deflection (Specimen 3)

Table M-13. Testing segments of the loading schedule (Specimen 3)

Testing Segment	Frequency, Hz.	Maximum Applied Load	Number of Cycles, Millions	Start Date	End Date
1	4	9 kip	1	6/29/2017	7/2/2017
2	4	13.5 Kip	1	7/2/2017	7/5/2017
3*	Monotonic*	44 kip	-	7/5/2017	
* Testing segment 3 included monotonic loading up to 44 kip at a stroke rate of 0.02 in./min. in order to initiate cracking					

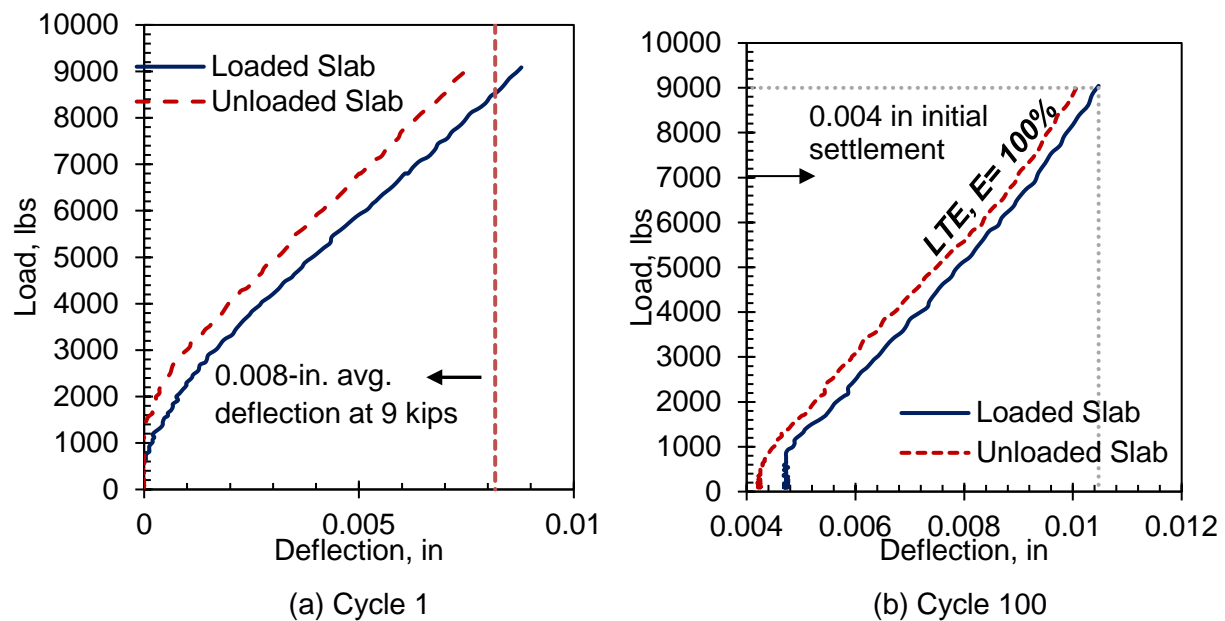
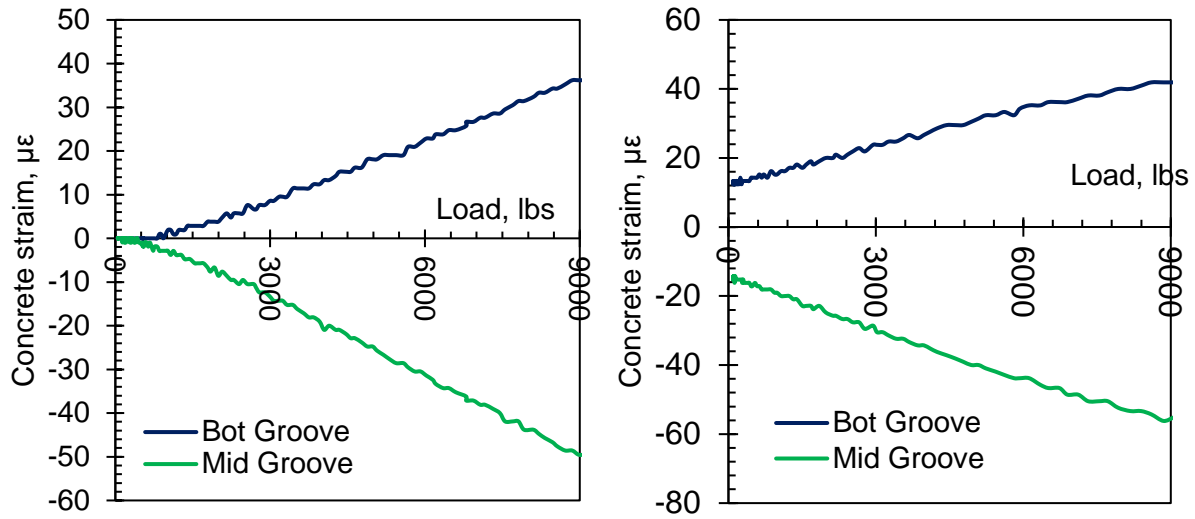


Figure M-22. Load versus deflection for: (a) cycle 1 and (b) cycle 100 (Specimen 3)



(a) Cycle 1

(b) Cycle 100

Figure M-23. Concrete strain versus load for: (a) cycle 1 and (b) cycle 100 (Specimen 3)

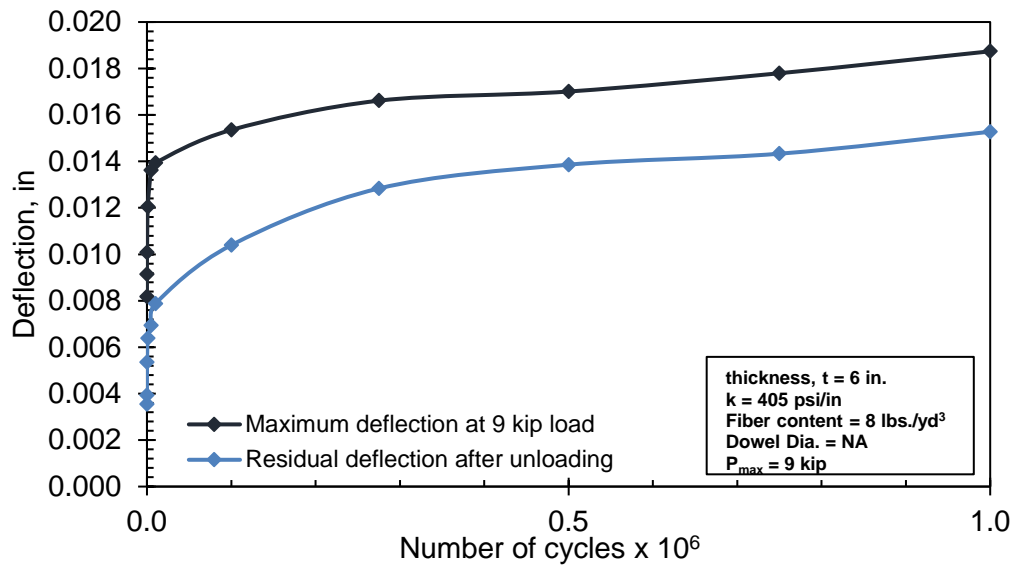


Figure M-24. Deflection versus number of cycles (Specimen 3 - Segment 1)

Table M-14. Deflection results for static testing (Specimen 3 – Segment 1)

Elapsed Number of Cycles	No. of Conducted Static Test	Age of Concrete at Testing Time	Average Deflection at 9 kip Loading, in.	Residual Deflection after Unloading, in.	f_r , psi.
-	-	1 day	-	-	331
1	1	1 day - 18 hrs	0.008	0.004	493*
2	2	1 day - 18 hrs	0.009	0.004	493*
100	3	1 day - 18 hrs	0.010	0.005	493*
1,000	4	1 day - 18 hrs	0.012	0.006	493*
5,000	5	1 day - 18 hrs	0.014	0.007	493*
10,000	6	1 day - 19 hrs	0.014	0.008	493*
100,000	7	2 days - 1 hr	0.015	0.010	501*
275,000	8	2 days - 14 hrs	0.017	0.013	553
500,000	9	3 days - 5 hrs	0.017	0.014	555*
750,000	10	3 days - 22 hrs	0.018	0.014	647
1,000,000	11	4 days - 5 hrs	0.019	0.015	647
* Strength values determined by testing 6 x 6 x 21 in. beams for f_r					

Table M-15. Deflection results for static testing (Specimen 3 – Segment 2)

Elapsed Number of Cycles	No. of Conducted Static Test	Age of Concrete at Testing Time	Average Deflection at 13.5 kip Loading, in.	Residual Deflection after Unloading, in.	f_r , psi.
1	-	4 days - 5 hrs	0.020	0.015	647
1,000	1	4 days - 5 hrs	0.021	0.016	647
10,000	2	4 days - 6 hrs	0.022	0.016	647
100,000	3	4 days - 13 hrs	0.023	0.017	647
310,000	4	5 days - 11 hrs	0.024	0.020	647
500,000	5	6 days - 5 hrs	0.026	0.021	647
750,000	6	6 days - 23 hrs	0.027	0.022	667*
1,000,000	7	7 days - 17 hrs	0.027	0.021	667*
* Strength values determined by testing 6 x 6 x 21 in. beams for f_r					

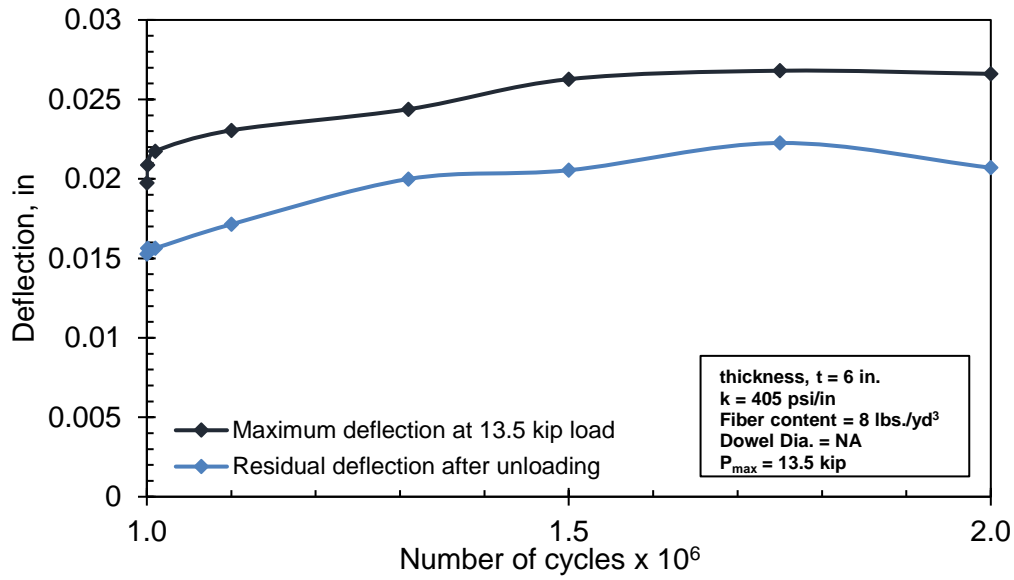


Figure M-25. Deflection versus number of cycles (Specimen 3 – Segment 2)

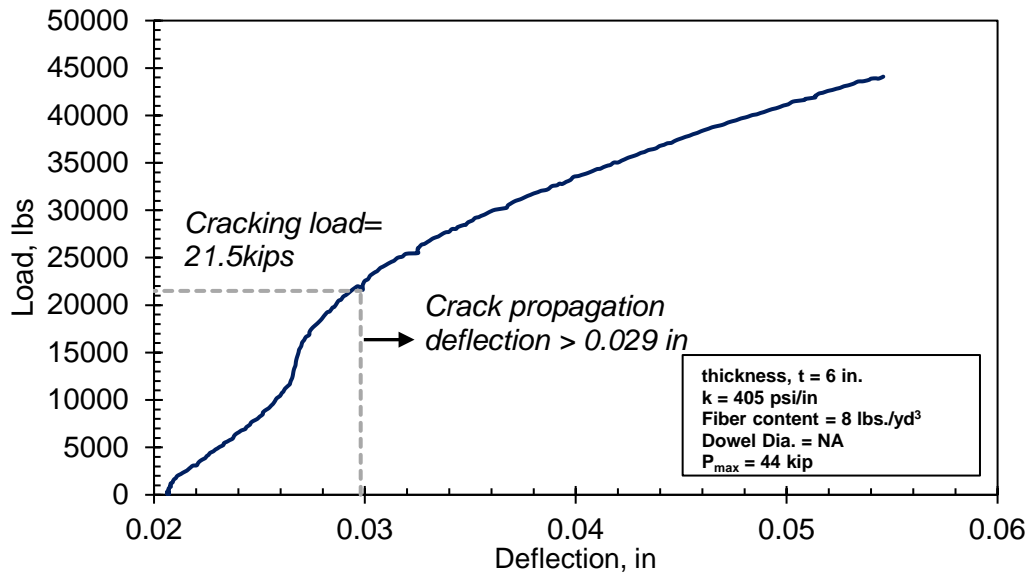


Figure M-26. Load versus slab deflection (Specimen 3 – Segment 3)

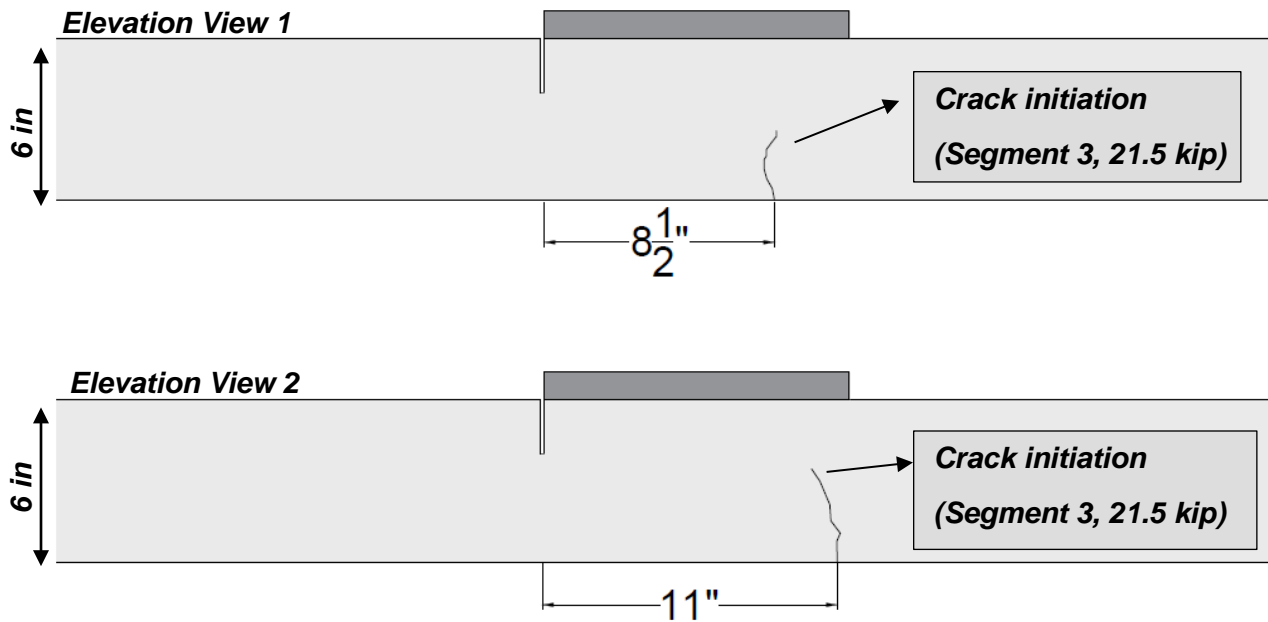


Figure M-27. Crack patterns with respect to dowel location (Specimen 3)

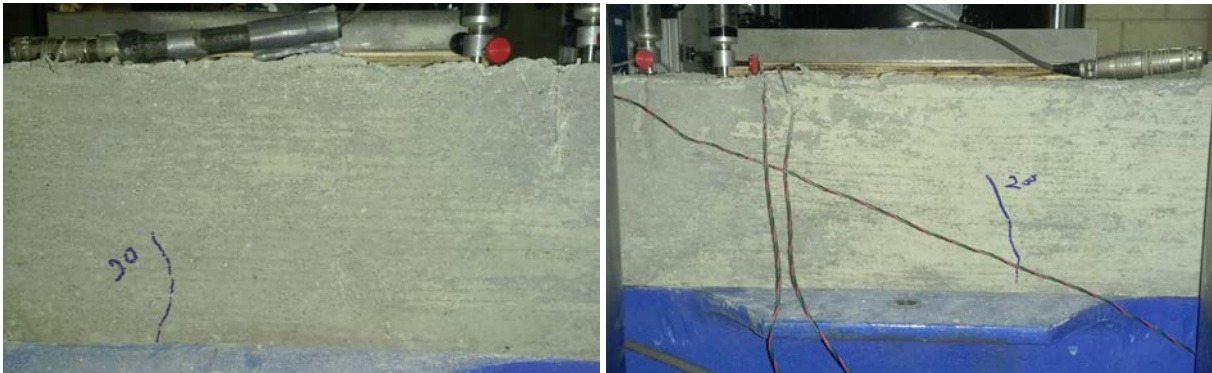


Figure M-28. Cracking at the end region of the dowel bars (Specimen 3)

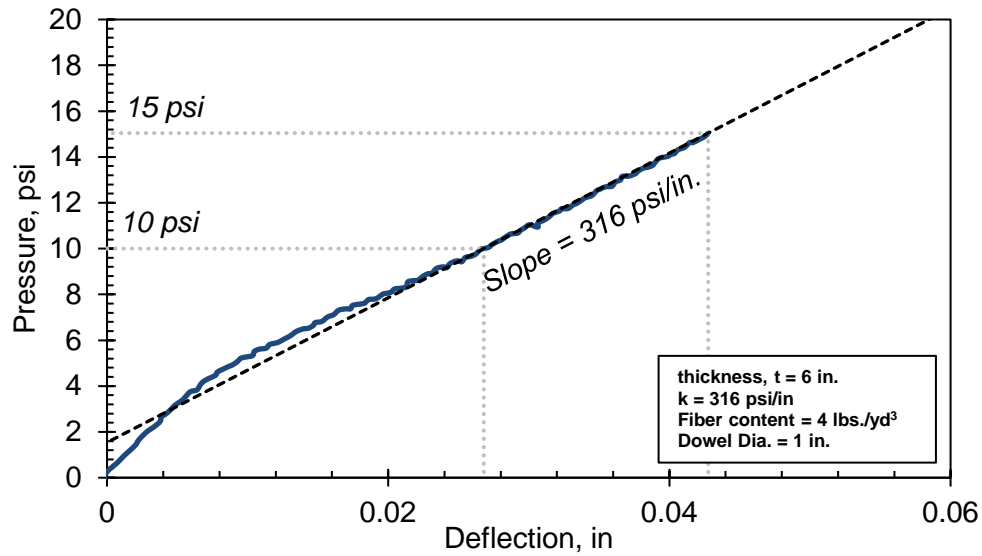


Figure M-29. Plate contact pressure versus deflection (Specimen 4)

Table M-16. Testing segments of the loading schedule (Specimen 4)

Testing Segment	Frequency, Hz.	Maximum Applied Load	Number of Cycles, Millions	Start Date	End Date
1	4	9 kip	1	7/18/2017	7/21/2017
2	4	13.5 Kip	2	7/21/2017	7/27/2017

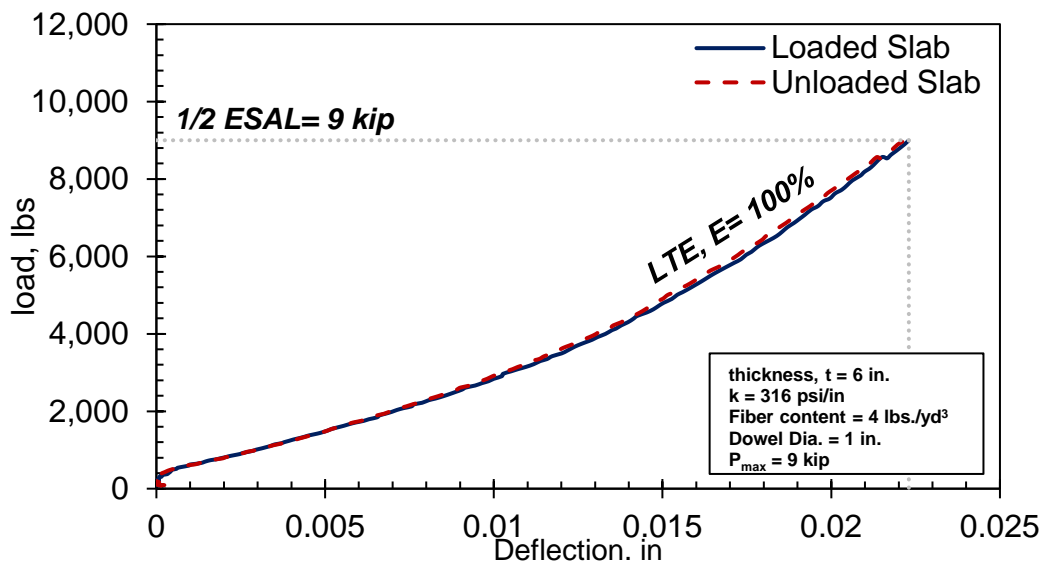


Figure M-30. Load versus deflection for the first static loading (Specimen 4)

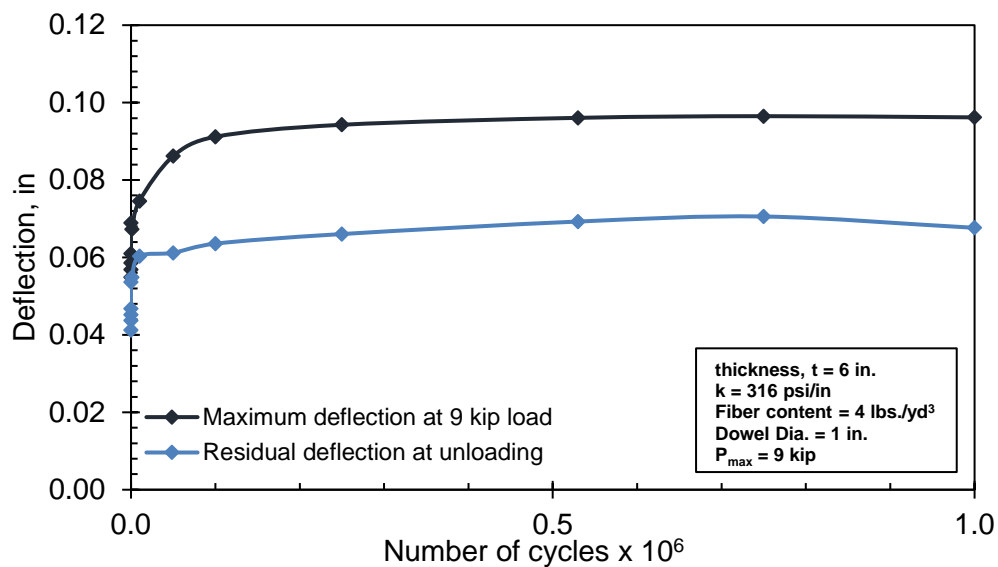


Figure M-31. Load versus deflection (Specimen 4 - Segment 1)

Table M-17. Deflection results for static testing (Specimen 4 - Segment 1)

Elapsed Number of Cycles	No. of Conducted Static Test	Age of Concrete at Testing Time	Average Deflection at 9 kip Loading, in.	Residual Deflection after Unloading, in.	f_r , Psi.
1	1	1 day	0.022	0.007	457*
1,000	2	1 day	0.020	0.008	457*
10,000	3	1 day - 1hr	0.028	0.014	457*
50,000	4	1 day - 4 hrs	0.039	0.014	545
100,000	5	1 day - 7 hrs	0.044	0.017	545
250,000	6	1 day - 18 hrs	0.048	0.019	573*
530,000	7	2 day - 13 hrs	0.049	0.023	573*
750,000	8	3 days - 4 hrs	0.050	0.024	594*
1,000,000	9	3 days - 22 hrs	0.049	0.021	689

* Strength values determined by testing 6 x 6 x 21 in beams for f_r

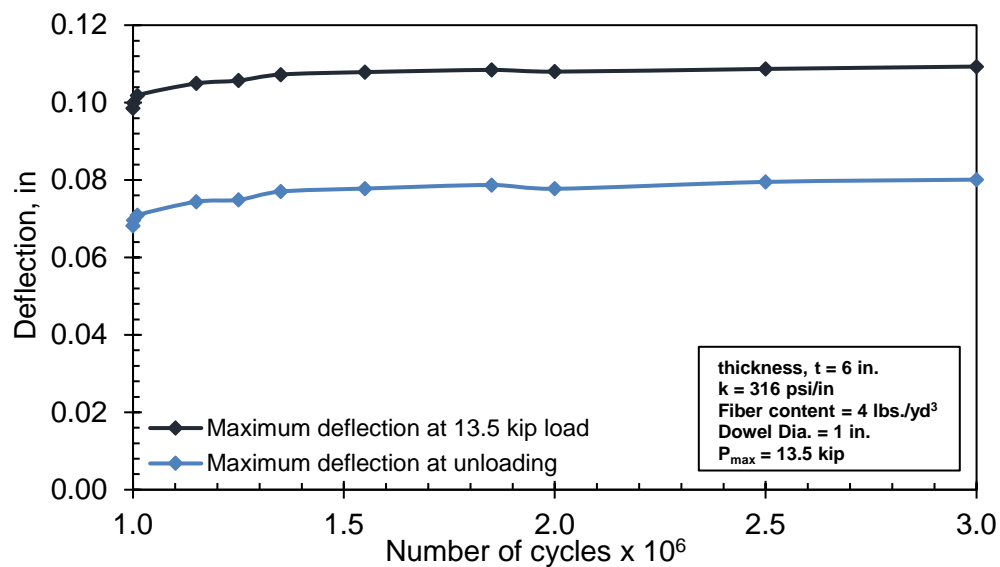


Figure M-32. Load versus deflection (Specimen 4 – Segment 2)

Table M-18. Deflection results for static testing (Specimen 4 – Segment 2)

Elapsed Number of Cycles	No. of Conducted Static Test	Age of Concrete at Testing Time	Average Deflection at 13.5 kip Loading, in.	Residual Deflection after Unloading, in.	f_r , Psi.
1	1	3 days - 22 hrs	0.052	0.021	689
1,000	2	3 days - 22 hrs	0.053	0.023	689
10,000	3	3 days - 23 hrs	0.055	0.024	689
150,000	4	4 days - 9 hrs	0.058	0.028	689
250,000	5	4 days - 16 hrs	0.059	0.028	689
350,000	6	4 days - 22 hrs	0.060	0.030	689
550,000	7	5 days - 13 hrs	0.061	0.031	763
850,000	8	6 days - 9 hrs	0.062	0.032	763
1,000,000	9	6 days - 19 hrs	0.061	0.031	763
1,500,000	10	8 days - 7 hrs	0.062	0.033	826
2,000,000	11	9 days - 17 hrs	0.063	0.033	826
* Strength values determined by testing 6 x 6 x 21 in beams for f_r					

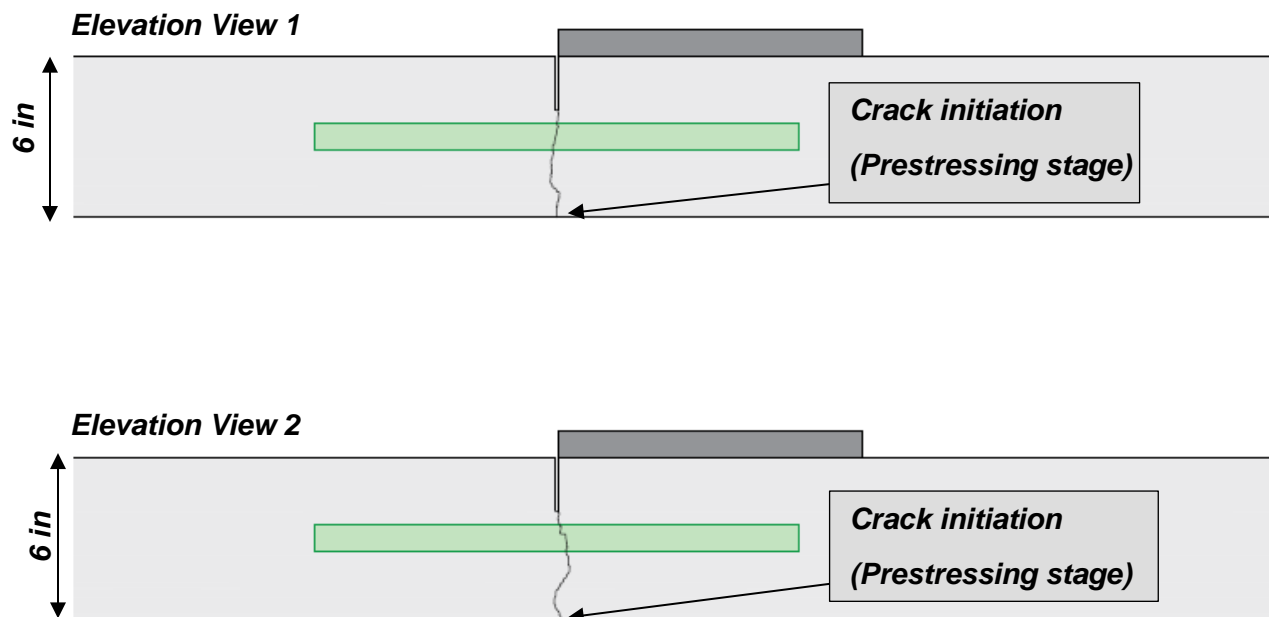


Figure M-33. Crack patterns with respect to dowel location (Specimen 4)

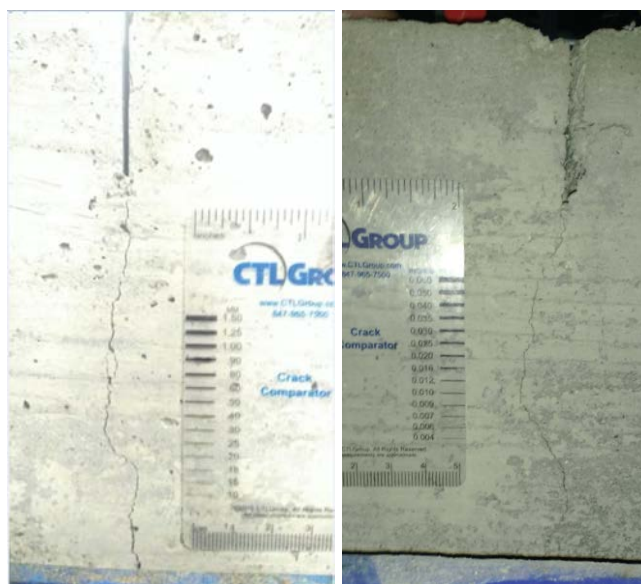


Figure M-34. Cracking at the joint region (Specimen 4)

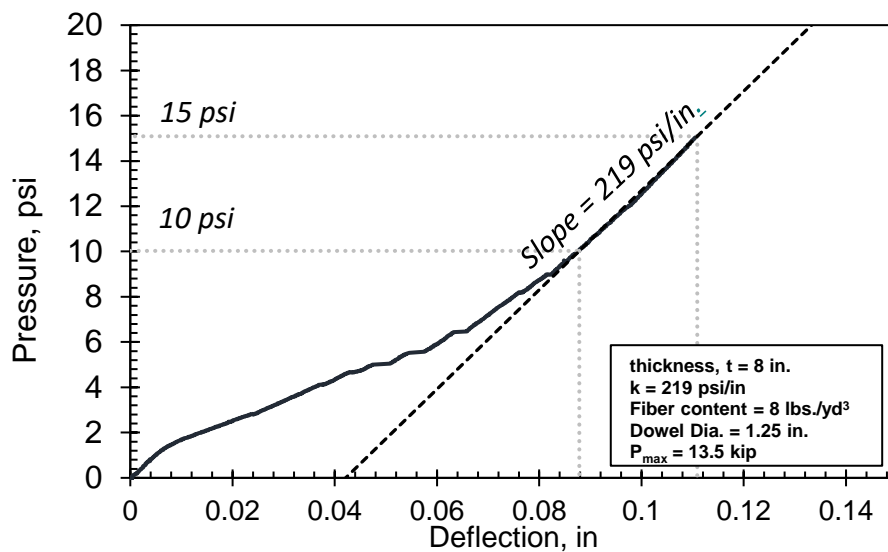
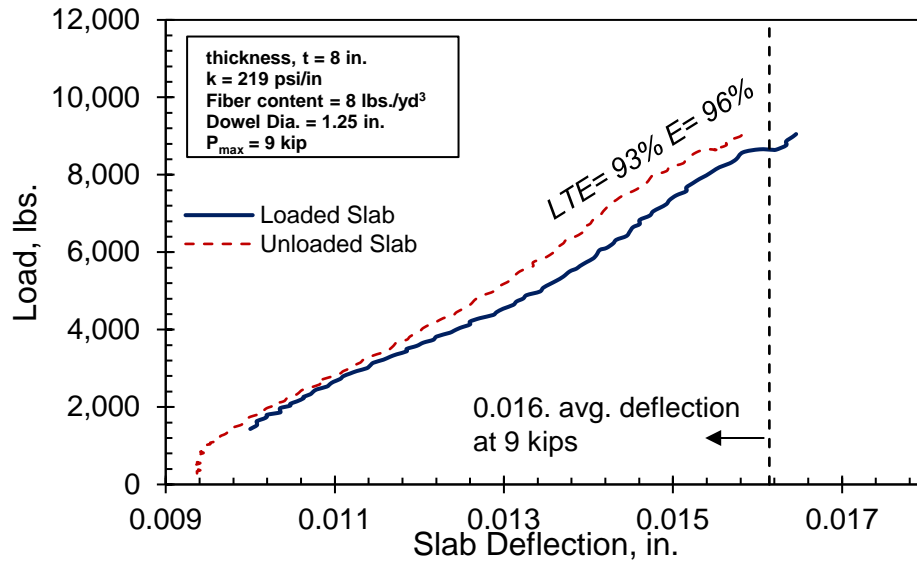


Figure M-35. Plate contact pressure versus deflection (Specimen 5)

Table M-19. Testing segments of the loading schedule (Specimen 5)

Testing Segment	Frequency, Hz.	Maximum Applied Load	Number of Cycles, Millions	Start Date	End Date
1	4	9 kip	1.2	9/24/2017	9/27/2017
2	4	13.5 Kip	1	9/27/2017	10/1/2017
3	4	18 kip	1	10/1/2017	10/4/2017
4	4	27 kip	1	10/4/2017	10/7/2017
5	4	36 kip	1	10/7/2017	10/10/2017



(a)

(b)

Figure M-36. Load versus deflection for the first static loading (Specimen 5)

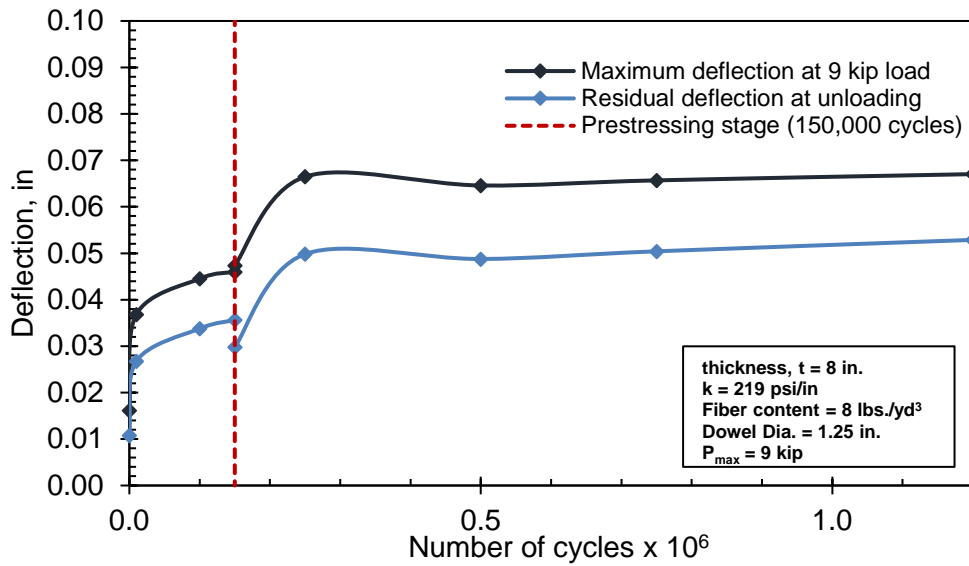


Figure M-37. Load versus deflection (Specimen 5 – Segment 1)

Table M-20. Deflection results for static testing of Segment 1 (Specimen 5 - Segment 1)

Elapsed Number of Cycles	No. of Conducted Static Test	Age of Concrete at Testing Time	Average Deflection at 9 kip Loading, in.	Residual Deflection after Unloading, in.	f_r , Psi.
1	1	12 hrs	0.016	0.011	261*
10,000	2	13 hrs	0.037	0.027	266
100,000	3	20 hrs	0.045	0.034	349
150,000	4	23 hrs	0.046	0.036	449*
<i>Prestressing operations (Crack initiation at the joint)</i>					
150,000	5	1 day - 1 hrs	0.047	0.030	449*
250,000	6	1 day - 8 hrs	0.067	0.050	447
500,000	7	2 days - 2 hrs	0.065	0.049	528
750,000	8	2 days - 20 hrs	0.066	0.050	591
1,200,000	9	4 days - 2 hrs	0.067	0.053	627
* Strength values determined by testing 6 x 6 x 21 in beams for f_r					

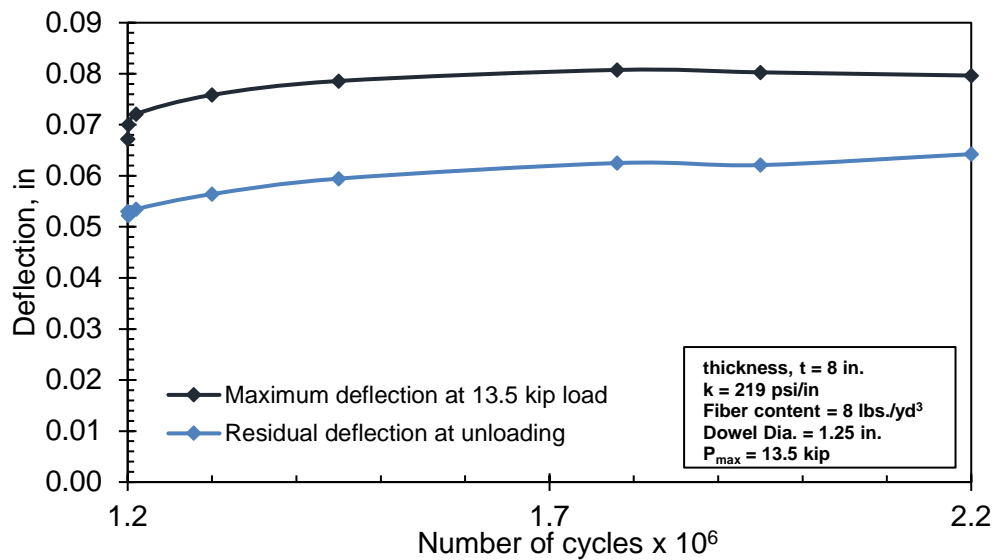
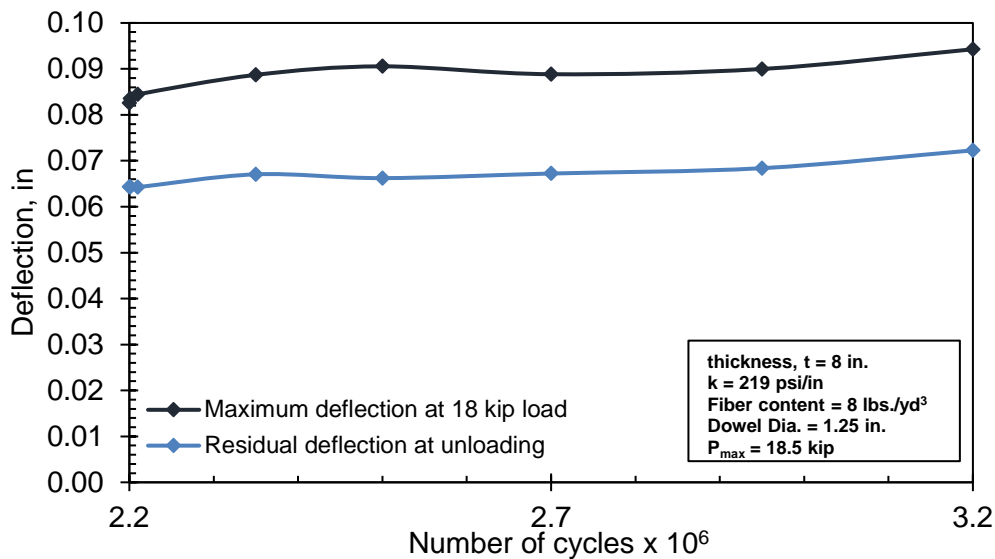


Figure M-38. Load versus deflection (Specimen 5 – Segment 2)

Table M-21. Deflection results for static testing (Specimen 5 – Segment 2)

Elapsed Number of Cycles	No. of Conducted Static Test	Age of Concrete at Testing Time	Average Deflection at 13.5 kip Loading, in.	Residual Deflection after Unloading, in.	f_r , Psi.
1	1	4 days - 3 hrs	0.067	0.053	627
1,000	2	4 days - 3 hrs	0.070	0.052	627
10,000	3	4 days - 4 hrs	0.072	0.054	627
100,000	4	4 days - 10 hrs	0.076	0.056	627
250,000	5	4 days - 21 hrs	0.079	0.059	627
580,000	6	5 days - 20 hrs	0.081	0.063	664
750,000	7	6 days - 8 hrs	0.080	0.062	664
1,000,000	8	7 days - 22 hrs	0.080	0.064	664

**Figure M-39. Load versus deflection (Specimen 5 – Segment 3)****Table M-22. Deflection results for static testing (Specimen 5 – Segment 3)**

Elapsed Number of Cycles	No. of Conducted Static Test	Age of Concrete at Testing Time	Average Deflection at 18 kip Loading, in.	Residual Deflection after Unloading, in.	f_r , Psi.
1	1	7 days - 22 hrs	0.083	0.064	664
1,000	2	7 days - 23 hrs	0.084	0.064	664
10,000	3	8 days - 0 hrs	0.084	0.064	664
150,000	4	8 days - 10 hrs	0.089	0.067	664
300,000	5	8 days - 22 hrs	0.091	0.066	664
500,000	6	9 days - 12 hrs	0.089	0.067	664

750,000	7	10 days - 7 hrs	0.090	0.068	664
1,000,000	8	11 days - 2 hrs	0.094	0.072	705

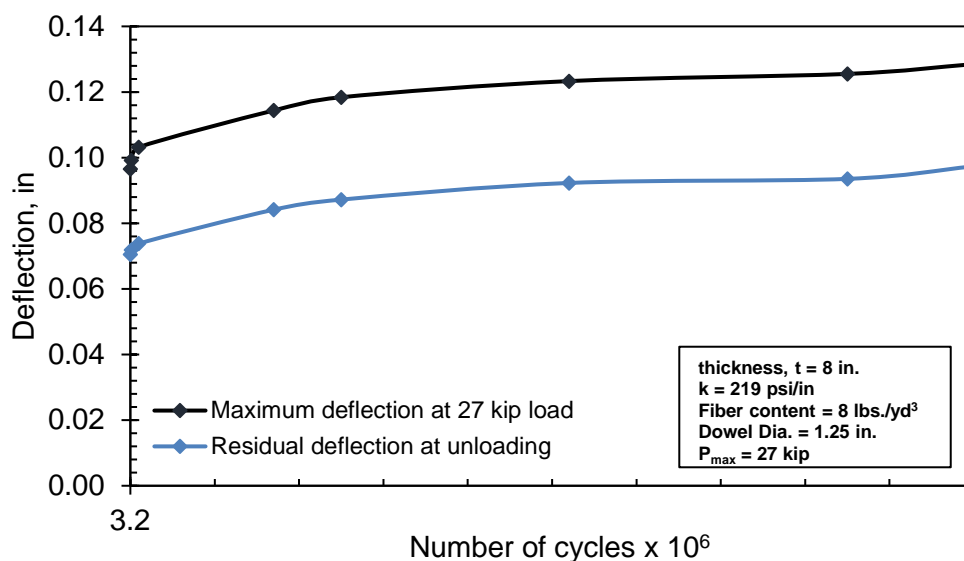


Figure M-40. Load versus deflection (Specimen 5 – Segment 4)

Table M-23. Deflection results for static testing (Specimen 5 – Segment 4)

Elapsed Number of Cycles	No. of Conducted Static Test	Age of Concrete at Testing Time	Average Deflection at 27 kip Loading, in.	Residual Deflection after Unloading, in.	f_r , Psi.
1	1	11 days - 7 hrs	0.097	0.071	705
1,000	2	11 days - 8 hrs	0.099	0.072	705
10,000	3	11 days - 9 hrs	0.103	0.074	705
170,000	4	11 days - 20 hrs	0.114	0.084	705
250,000	5	12 days - 3 hrs	0.118	0.087	705
520,000	6	12 days - 22 hrs	0.123	0.092	705
850,000	7	13 days - 23 hrs	0.126	0.094	705
1,000,000	8	14 days - 9 hrs	0.129	0.097	705

* Strength values determined by testing 6 x 6 x 21 in beams for f_r

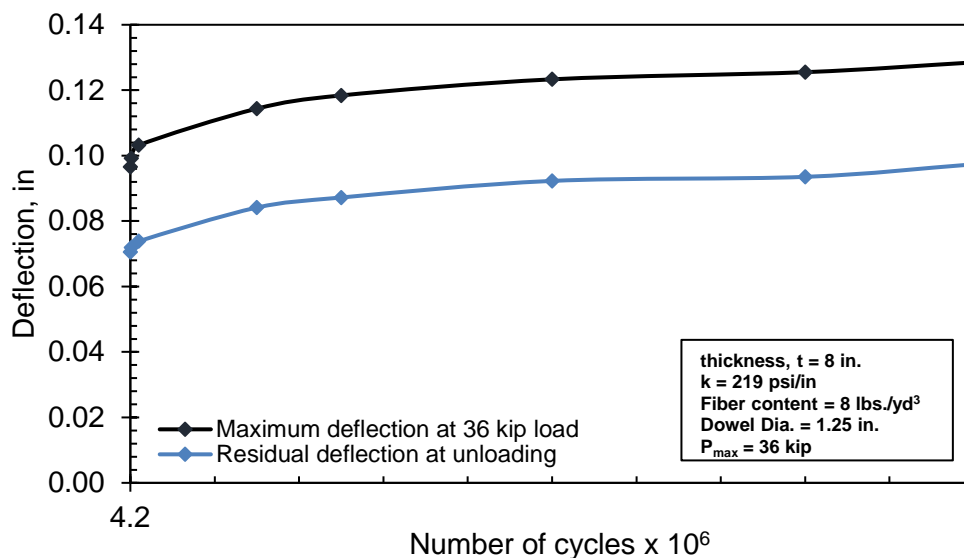


Figure M-41. Load versus deflection (Specimen 5 – Segment 5)

Table M-24. Deflection results for static testing (Specimen 5 – Segment 5)

Elapsed Number of Cycles	No. of Conducted Static Test	Age of Concrete at Testing Time	Average Deflection at 36kip Loading, in.	Residual Deflection after Unloading, in.	f_r , Psi.
1	1	14 days - 9 hrs	0.131	0.097	705
1,000	2	14 days - 10 hrs	0.136	0.101	705
10,000	3	14 days - 11 hrs	0.141	0.104	705
150,000	4	14 days - 21 hrs	0.159	0.117	705
250,000	5	15 days - 5 hrs	0.166	0.121	705
500,000	6	15 days - 22 hrs	0.176	0.128	705
800,000	7	16 days - 20 hrs	0.186	0.135	705
1,000,000	8	17 days - 10 hrs	0.194	0.139	705

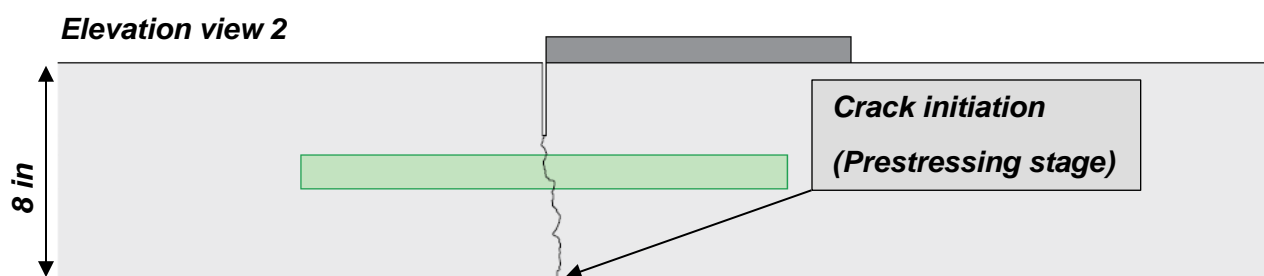
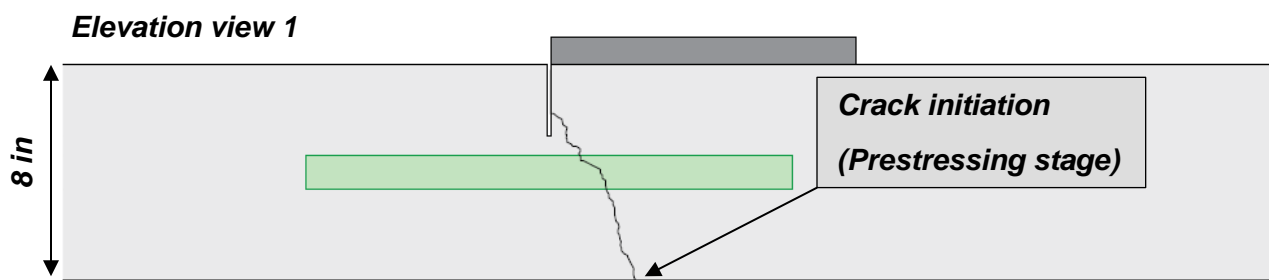


Figure M-42. Crack patterns with respect to dowel location (Specimen 5)



(elevation 1)



(elevation 2)

Figure M-43. Cracking at the joint location (Specimen 5)

Table M-25. Experimental considerations prior to fatigue loading (All specimens)

Specimen #	t (in.)	Fiber Content (lbs./cu-yd)	Joint Type	K (psi/in.)
1	6	8	Doweled	324
2	6	-	Doweled	395
3	6	8	Non-doweled	405
4	6	4	Doweled	316
5	8	8	Doweled	219

Where,

t= Concrete layer thickness, in

k = Subgrade modulus reaction, psi/in.

Table M-26. Cracking instances at groove location and boundary conditions (All specimens)

Specimen #	Cracking at Groove	Cracking Age (Days)	Crack Type	Vertical Edge condition	Lateral Edge Condition	Joint Construction Condition
1	✓	1.73	Hairline	Non-restrained	Non-restrained	Non-cracked
2	✓	2.95	Hairline	Restrained	Non-restrained	Non-cracked
3	x	-	-	Restrained	Restrained	Non-cracked
4	✓	0.83	Hairline	Restrained	Non-restrained	Pre-cracked
5	✓	1.00	Hairline	Restrained	Non-restrained	Pre-cracked

Table M-27. Jointed slab performance summary at 1 million cycles (1/2 ESAL)

Specimen #	LTE (%)	E (%)	Joint Faulting (in.)	Joint Opening (in.)
	≥ 60 (ACPA)	≥ 75 (ACPA)	≤ 0.2 (IDOT)	Low/Mid/High (IDOT)
1	96	98	5.90E-04	Low
2	91	95	3.15E-04	Low
3	94	97	NA	NA
4	98	99	1.97E-04	Low
5	88	94	1.61E-03	Low

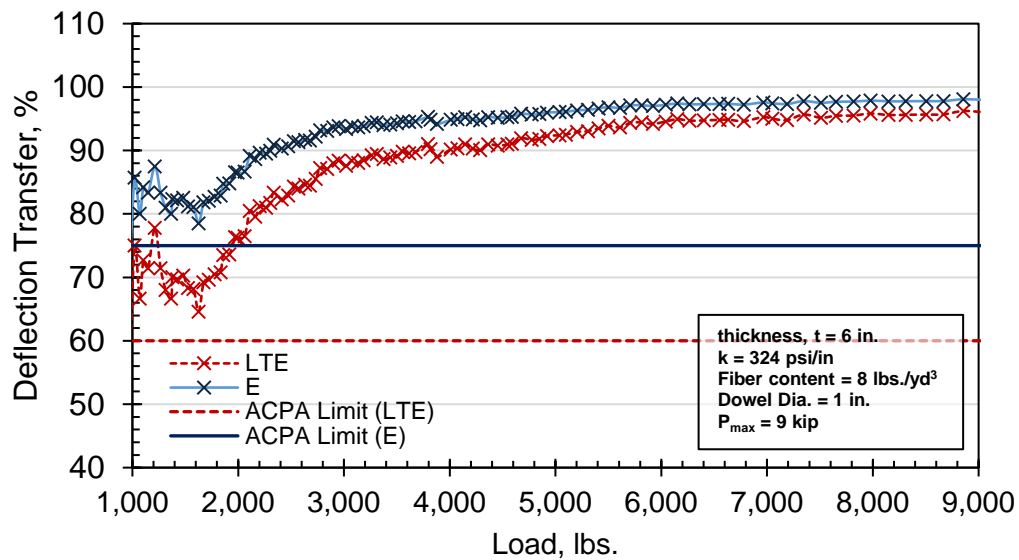


Figure M-44. LTE and E development after 1 million cyclic loads (Specimen 1)

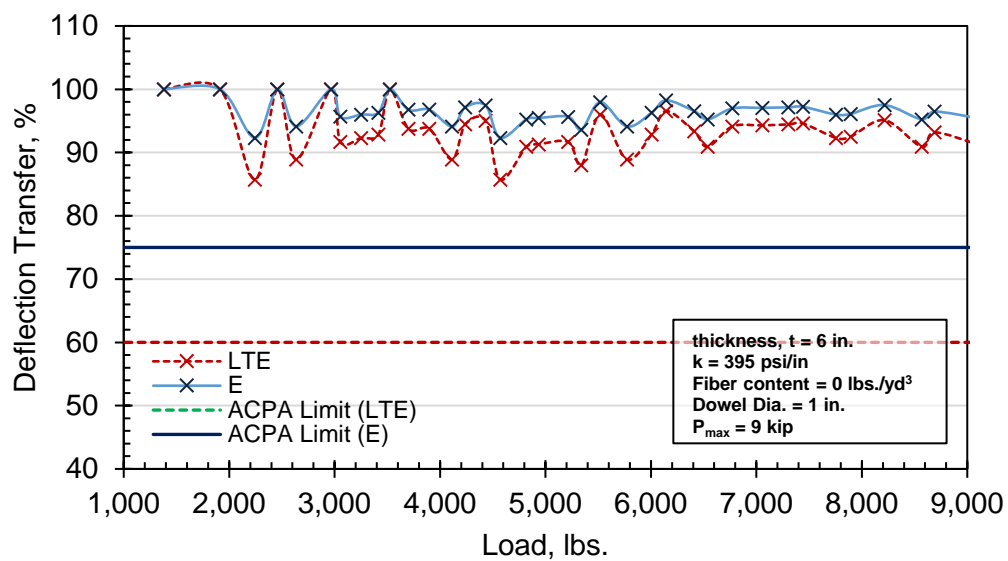


Figure M-45. LTE and E development after 1 million cyclic loads (Specimen 2)

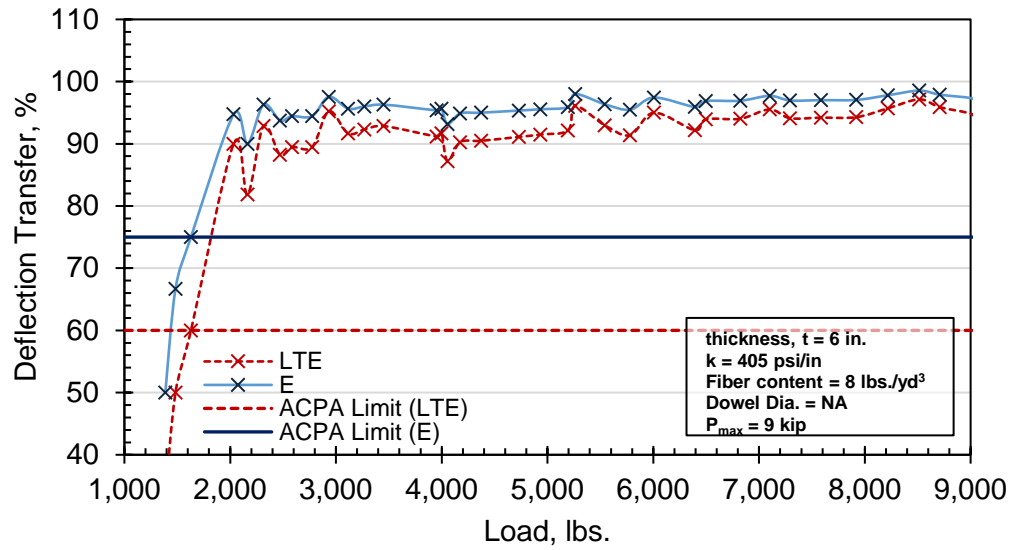


Figure M-46. LTE and E development after 1 million cyclic loads (Specimen 3)

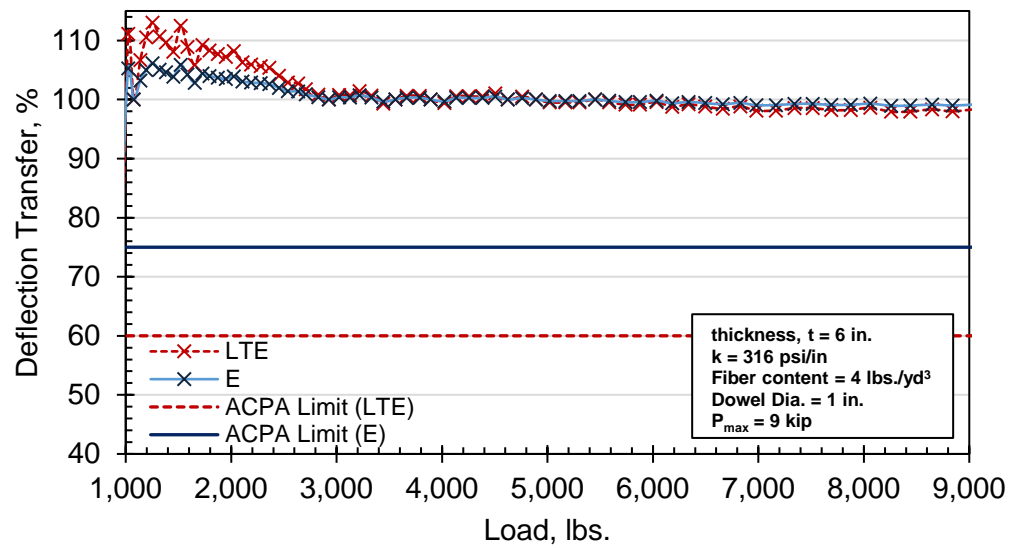


Figure M-47. LTE and E development after 1 million cyclic loads (Specimen 4)

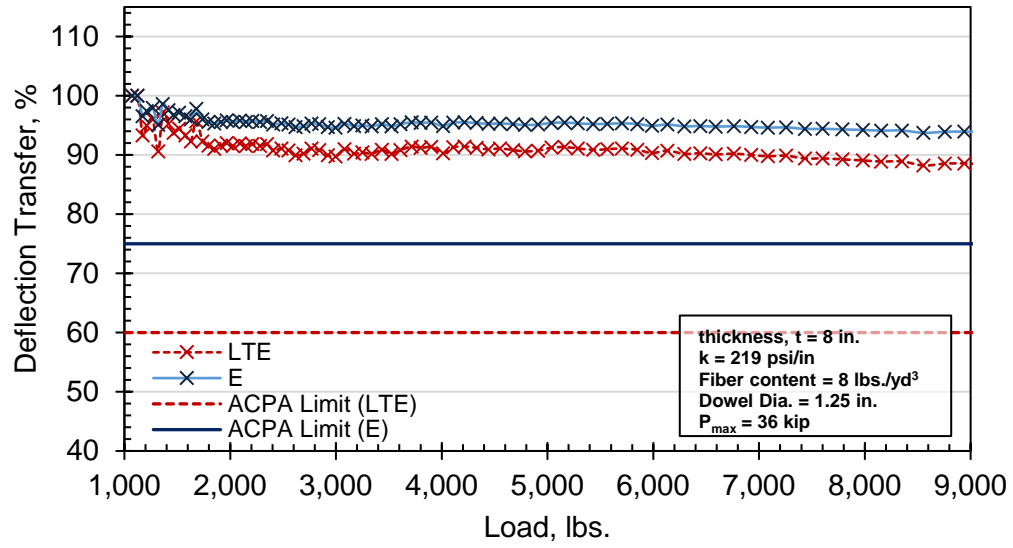


Figure M-48. LTE and E development after 1 million cyclic loads (Specimen 5)

APPENDIX N PROCEDURE CHARTS AND NOMOGRAPHS

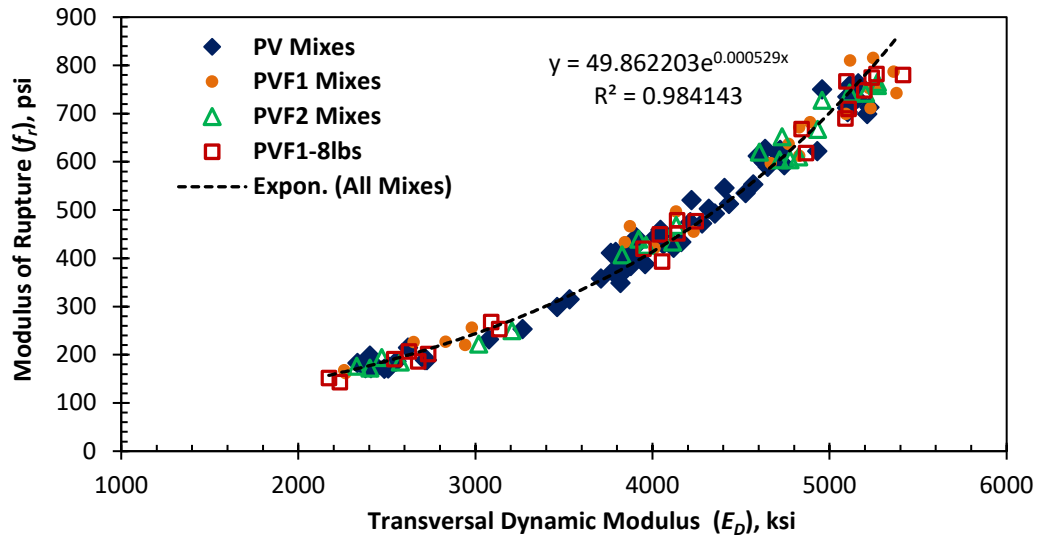


Figure N-1. Flexural strength vs. E_D for PV, PVF1, PVF2, and PVF1-8lbs fatigue mixes

Table N-1. Static MOE values for 12-hr, 1-Day, 2-Day, and 7-Day concrete age

Concrete age	12-hr	1-Day	3-Day	7-Day
f'_c (psi)	1312	2440	3692.5	4836
MOE (ksi)	1767	2518	3190	3722

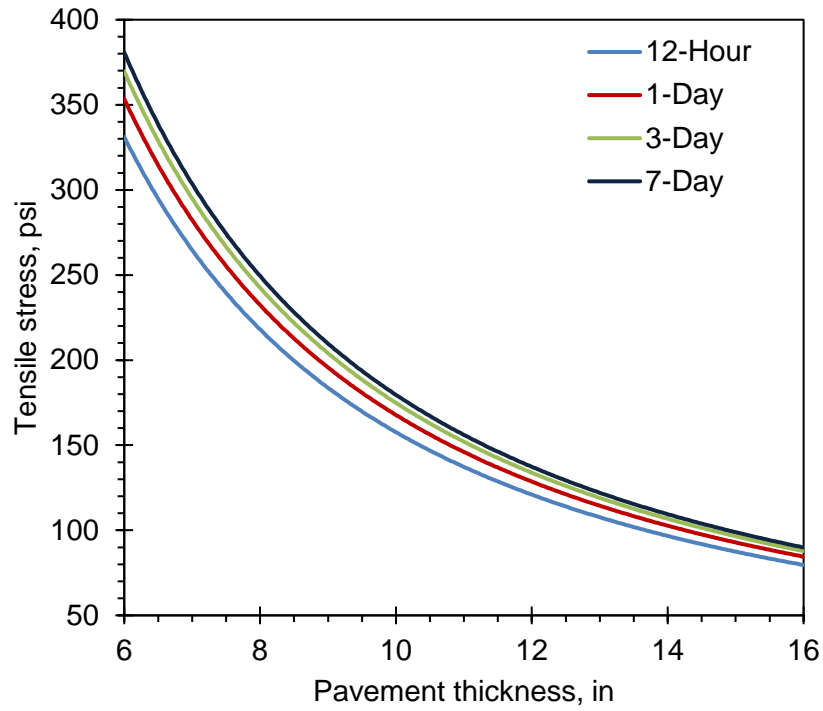


Figure N-2. Variation of tensile stress versus PCC thickness ($k = 50$ psi/in.)

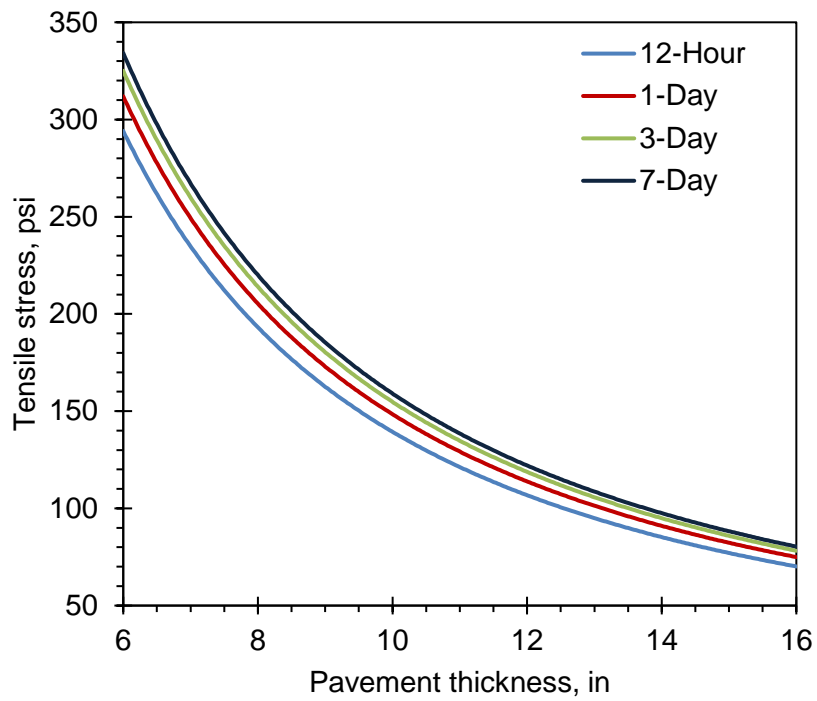


Figure N-3. Variation of tensile stress versus PCC thickness ($k = 100$ psi/in.)

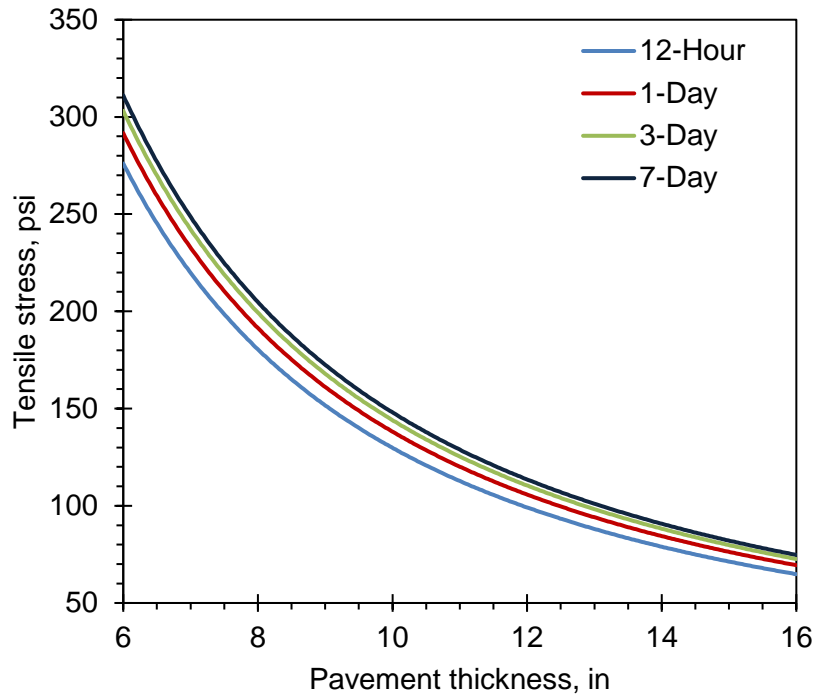


Figure N-4. Variation of tensile stress versus PCC thickness ($k = 150$ psi/in.)

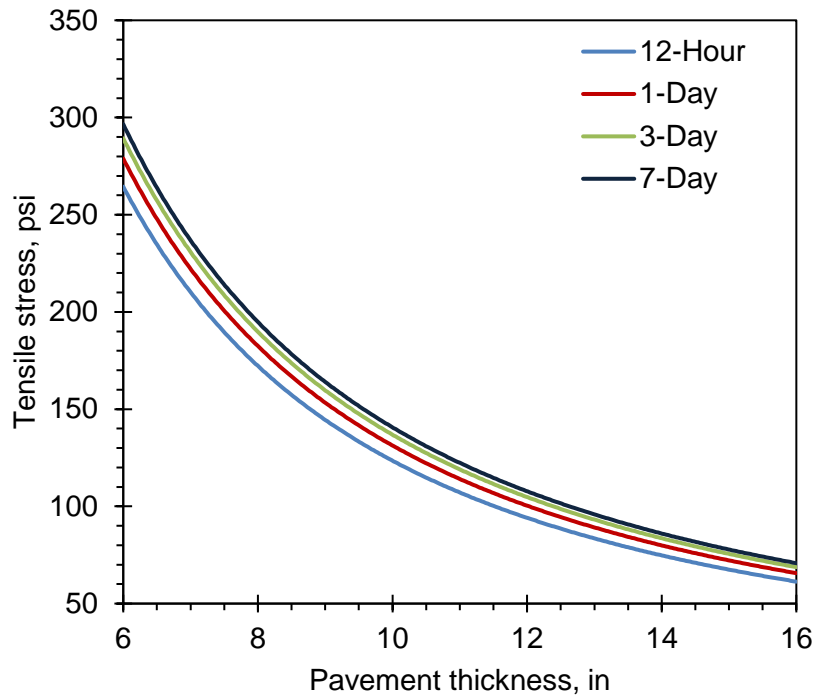


Figure N-5. Variation of tensile stress versus PCC thickness ($k = 200$ psi/in.)

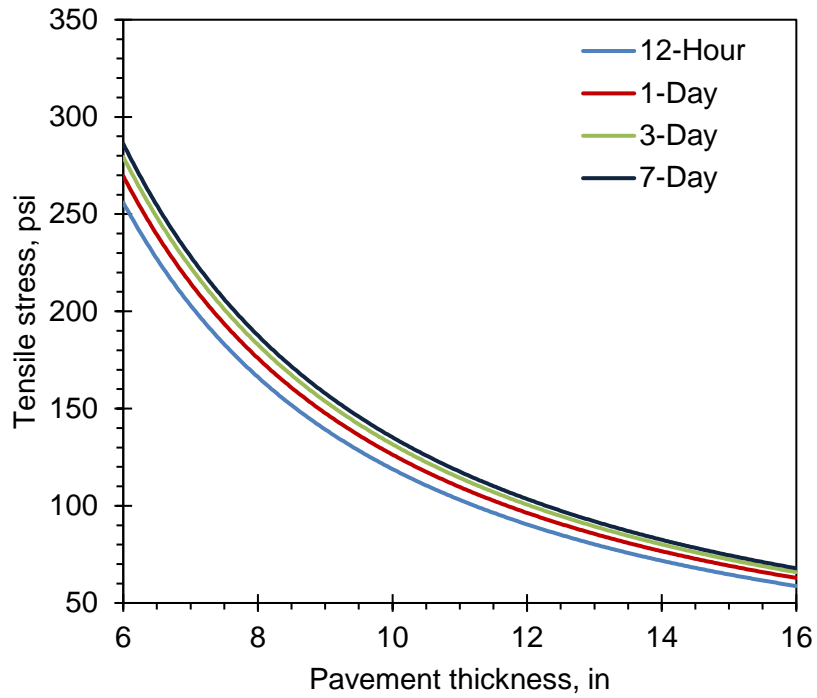


Figure N-6. Variation of tensile stress versus PCC thickness ($k = 250$ psi/in.)

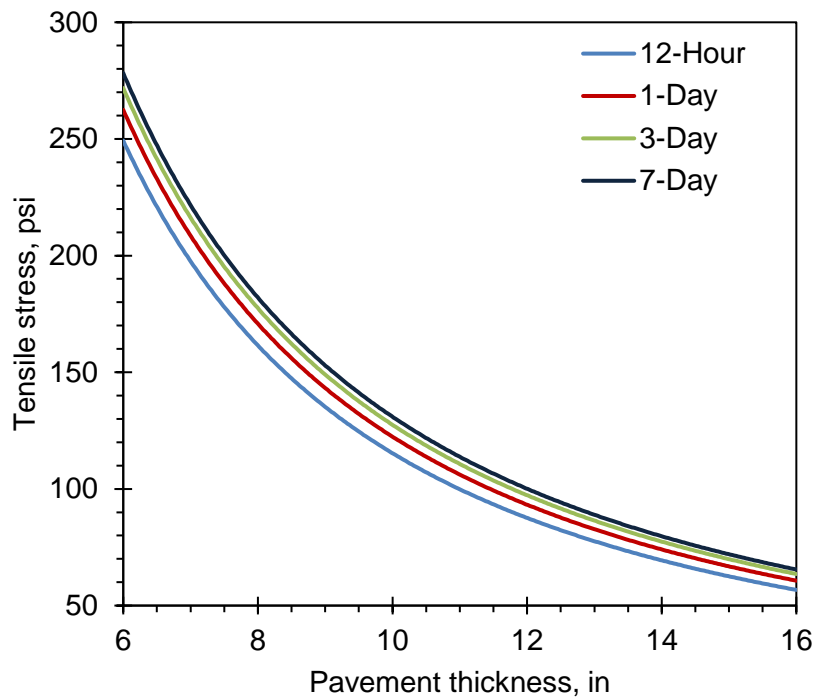


Figure N-7. Variation of tensile stress versus PCC thickness ($k = 300$ psi/in.)

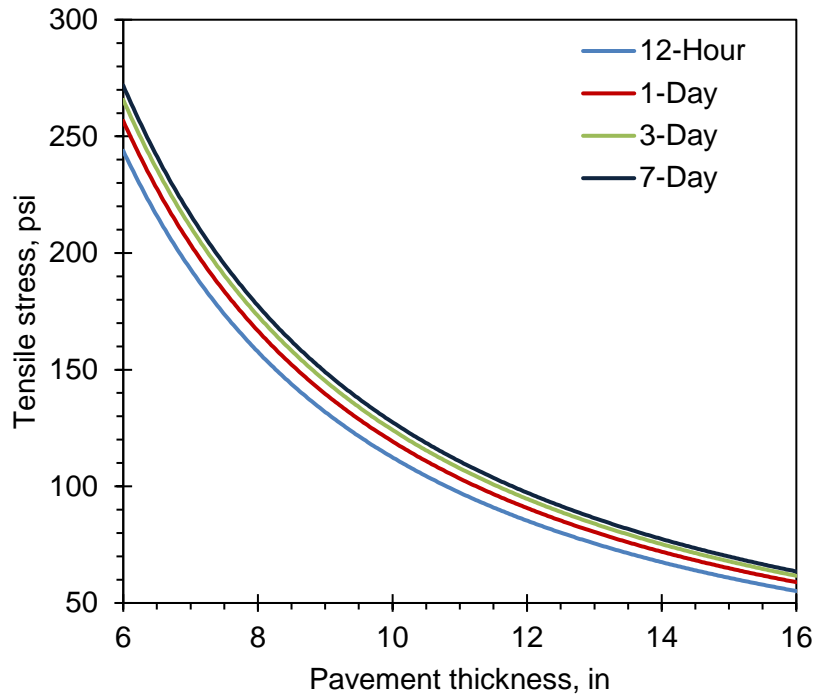


Figure N-8. Variation of tensile stress versus PCC thickness ($k = 350$ psi/in.)

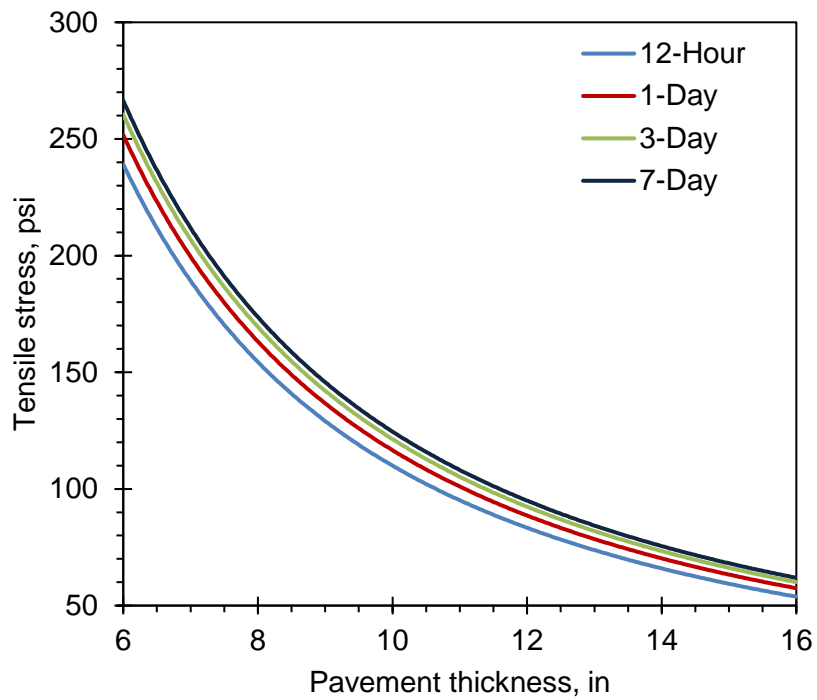


Figure N-9. Variation of tensile stress versus PCC thickness ($k = 400$ psi/in.)

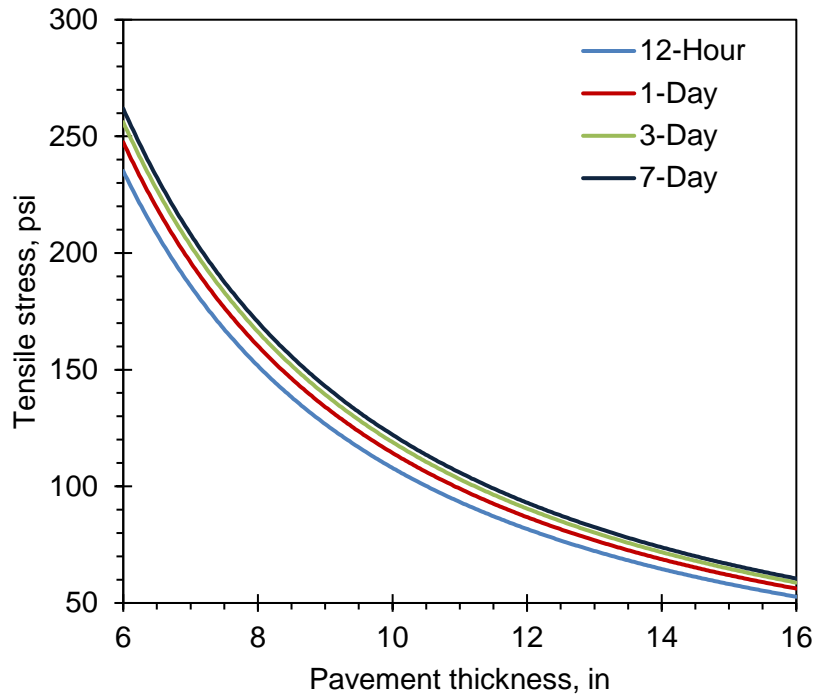


Figure N-10. Variation of tensile stress versus PCC thickness ($k = 450$ psi/in.)

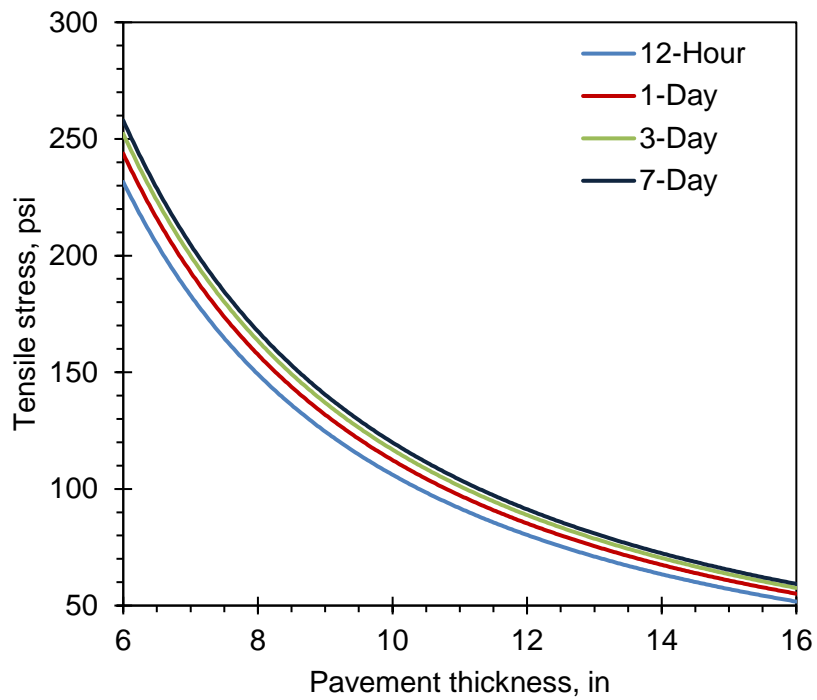


Figure N-11. Variation of tensile stress versus PCC thickness ($k = 500$ psi/in.)

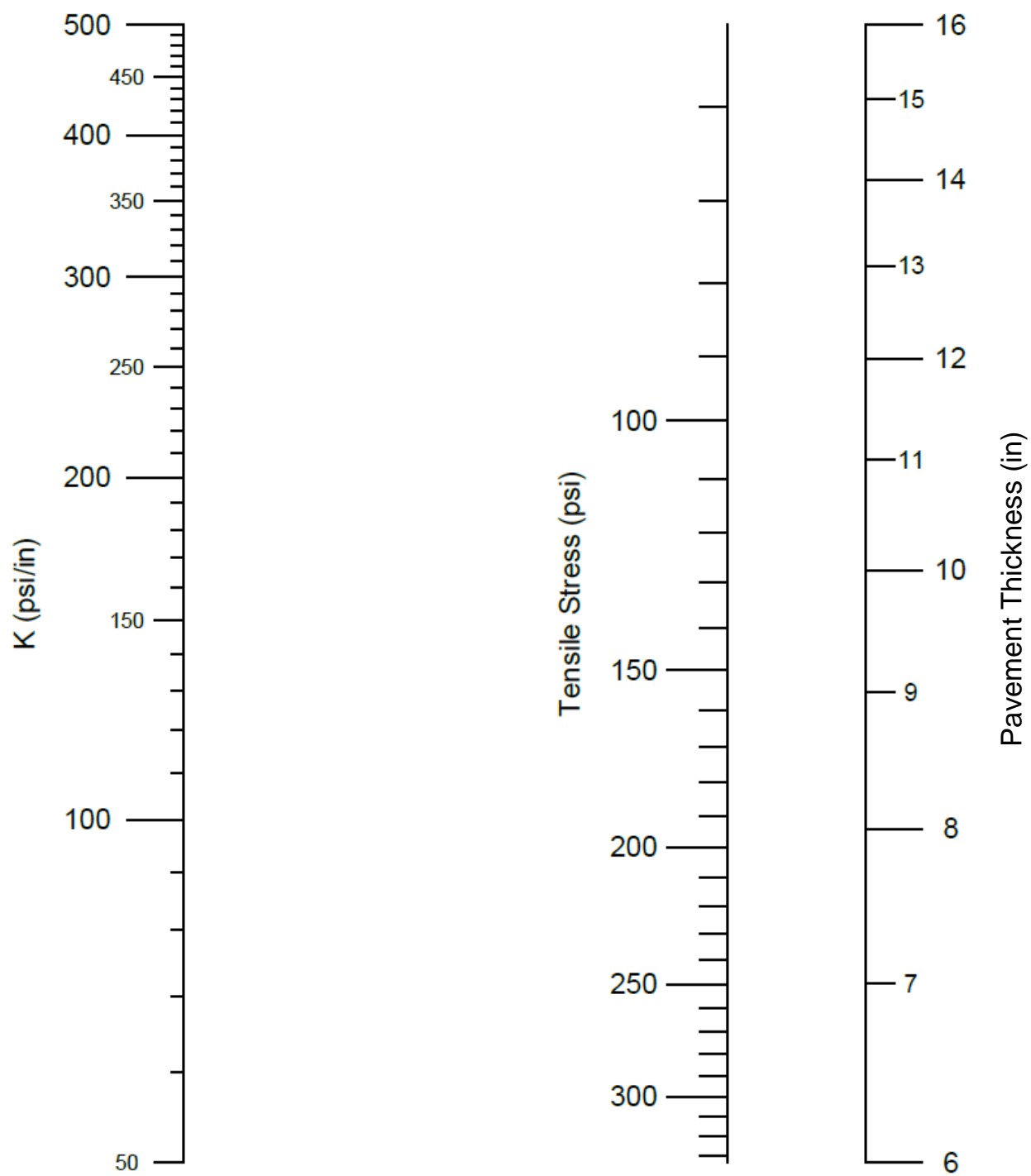


Figure N-12. Stress determination nomograph at 12-hr concrete age

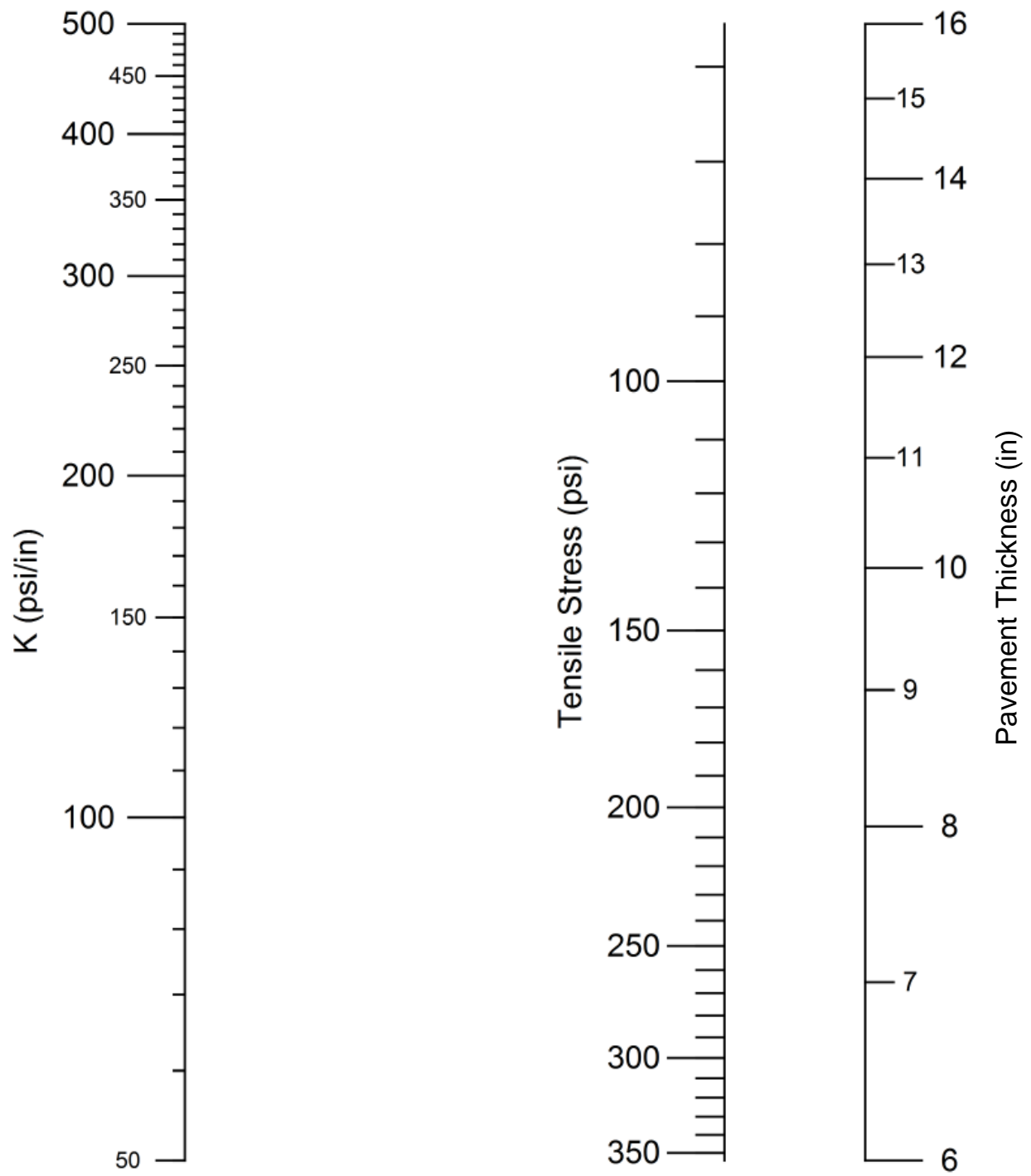


Figure N-13. Stress determination nomograph at 1-Day concrete age

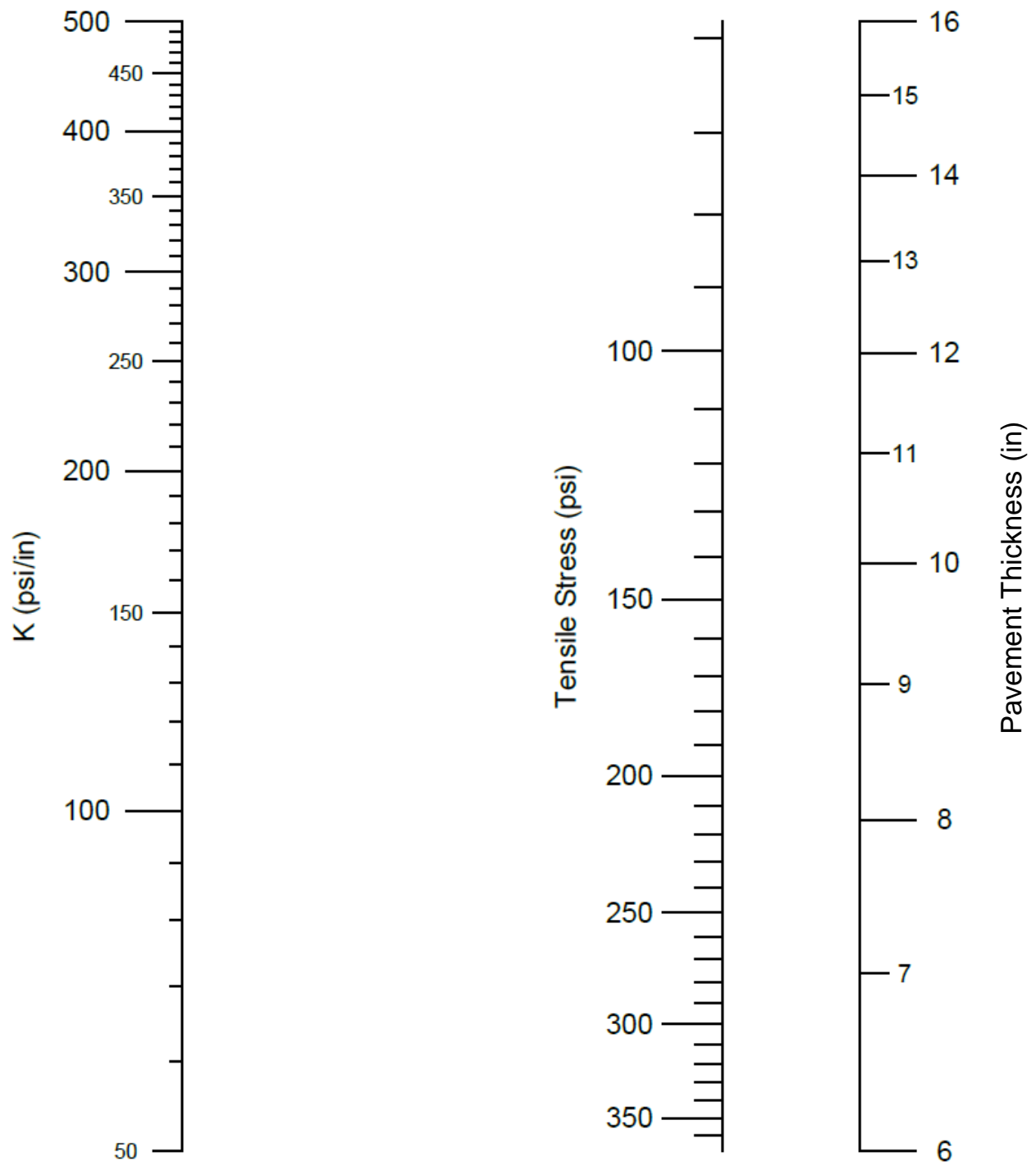


Figure N-14. Stress determination nomograph at 3-Day concrete age

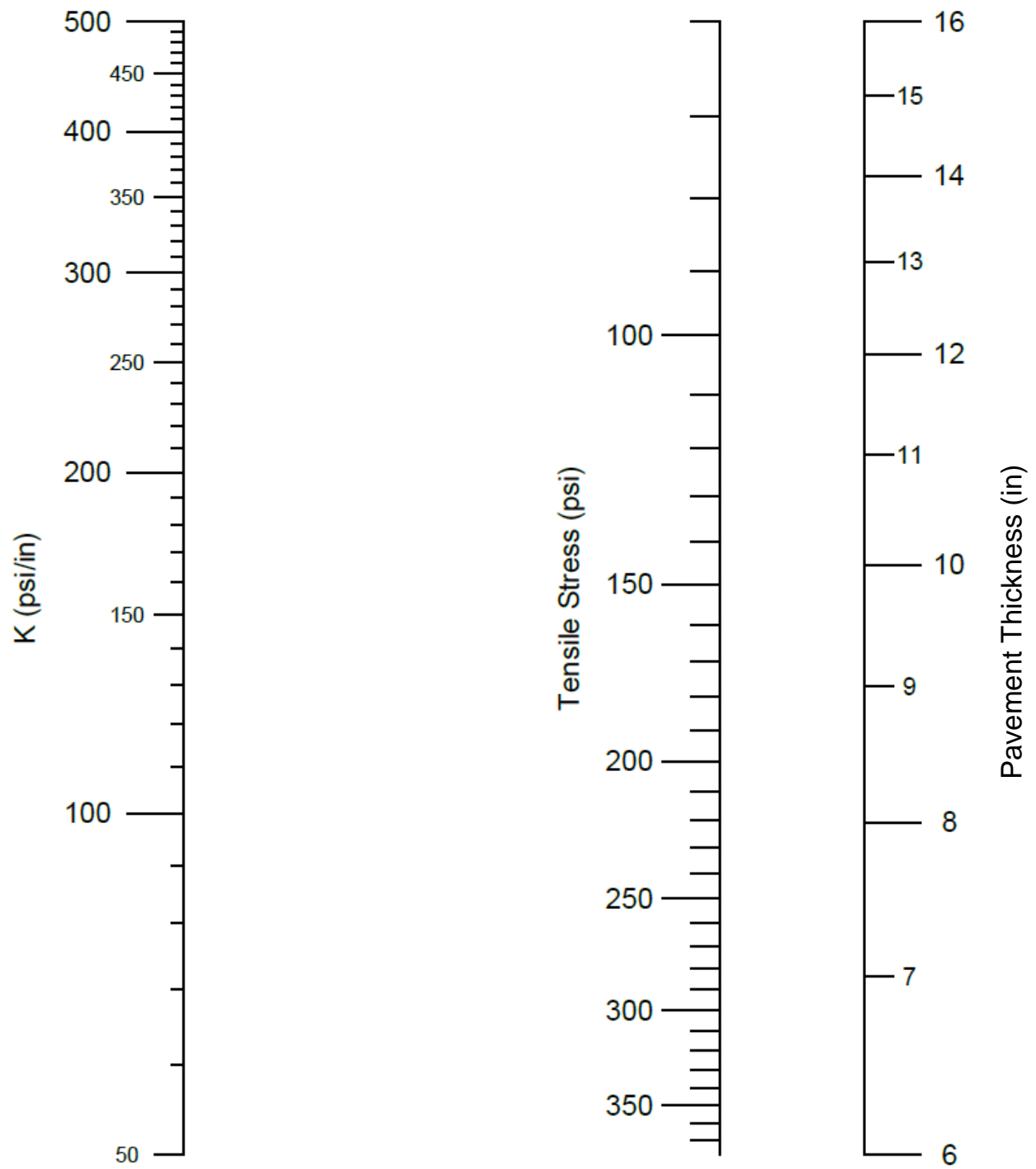
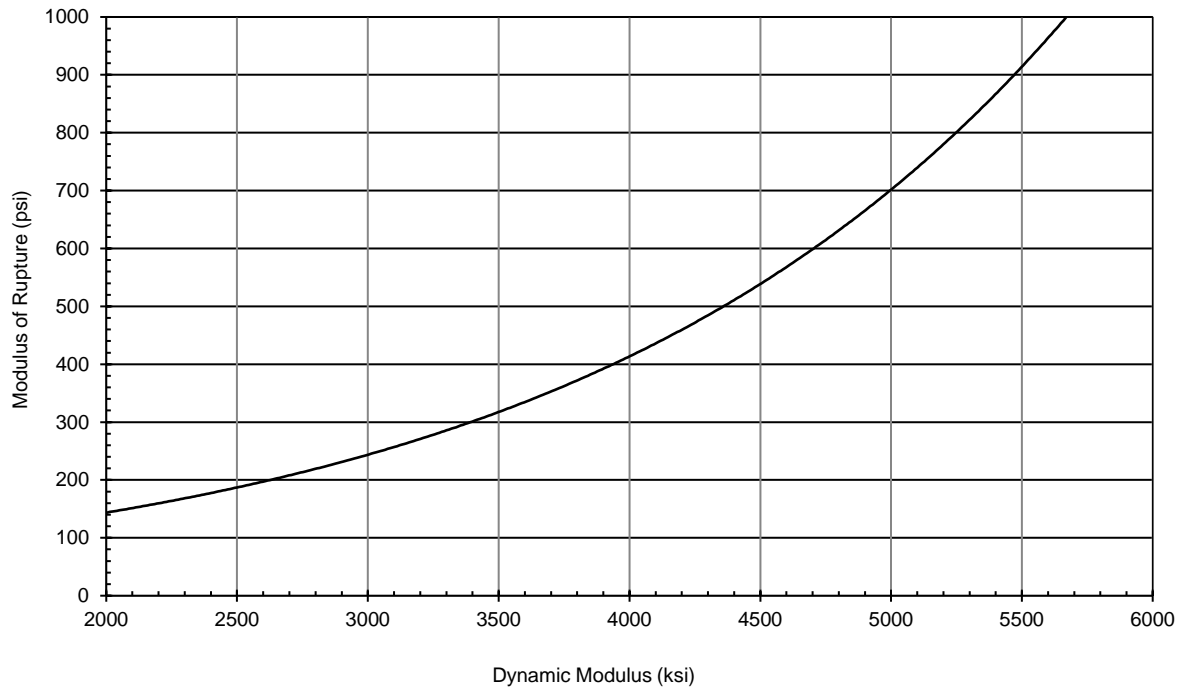


Figure N-15. Stress determination nomograph at 7-Day concrete age

Table N-2. *S-N* relationships of the fatigue testing program

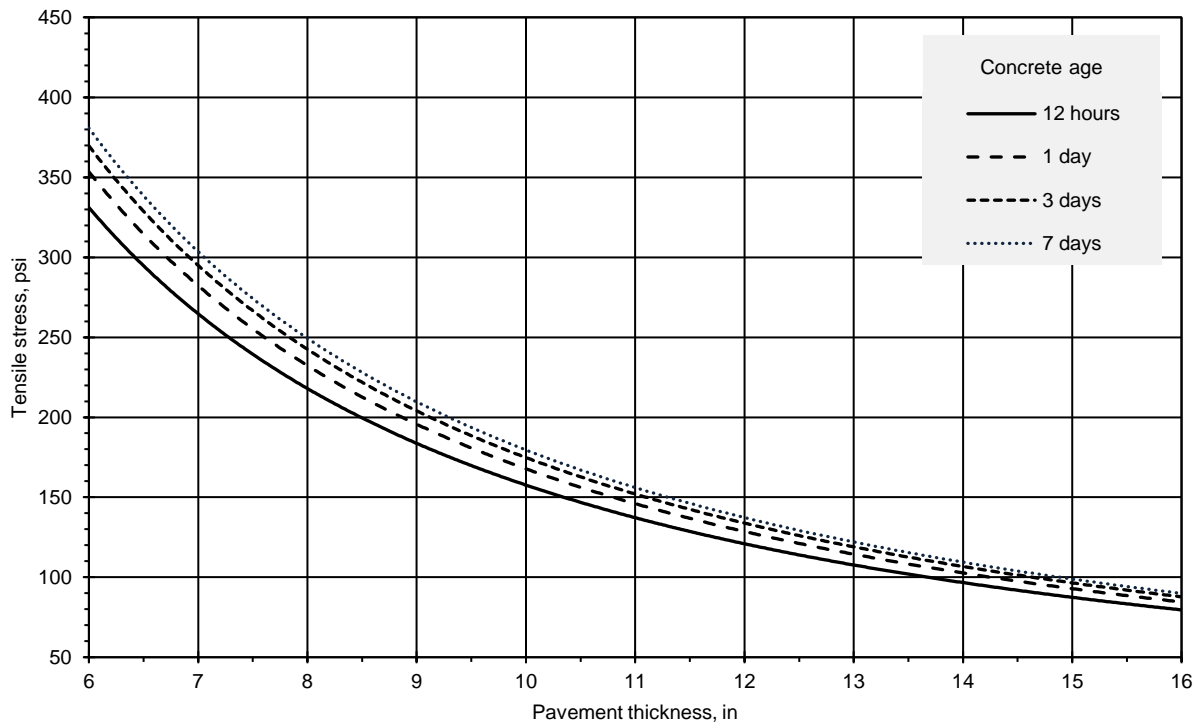
Concrete Age	Mix type	<i>S-N</i> linear regression relationships
12-hr	Plain	$N = e^{\frac{1.0090-S}{0.030}}$
	FRC	$N = e^{\frac{1.0257-S}{0.028}}$
1-Day	Plain	$N = e^{\frac{1.0098-S}{0.028}}$
	FRC	$N = e^{\frac{1.0066-S}{0.025}}$
3-Day	Plain	$N = e^{\frac{1.1072-S}{0.044}}$
	FRC	$N = e^{\frac{1.0822-S}{0.036}}$
7-Day	Plain	$N = e^{\frac{1.1022-S}{0.041}}$
	FRC	$N = e^{\frac{1.1616-S}{0.043}}$

APPENDIX O DESIGN AIDS FOR EARLY OPENING TO TRAFFIC



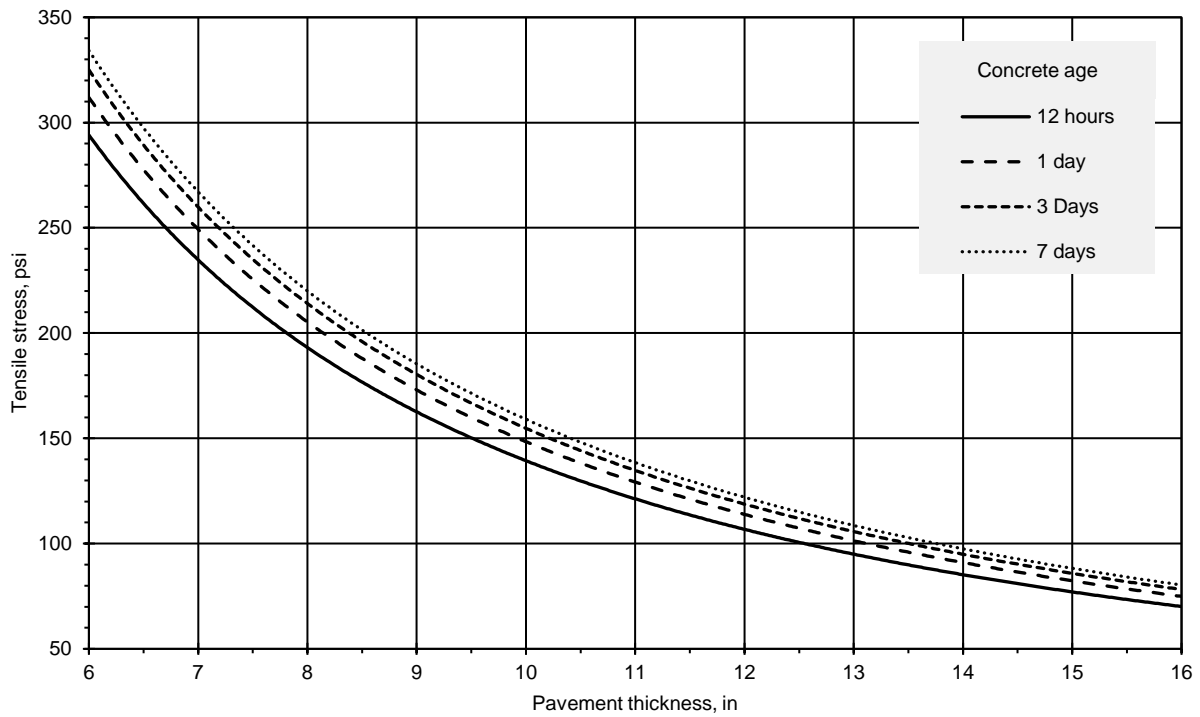
MODULUS OF RUPTURE VERSUS DYNAMIC MODULUS CHART

Figure O-1



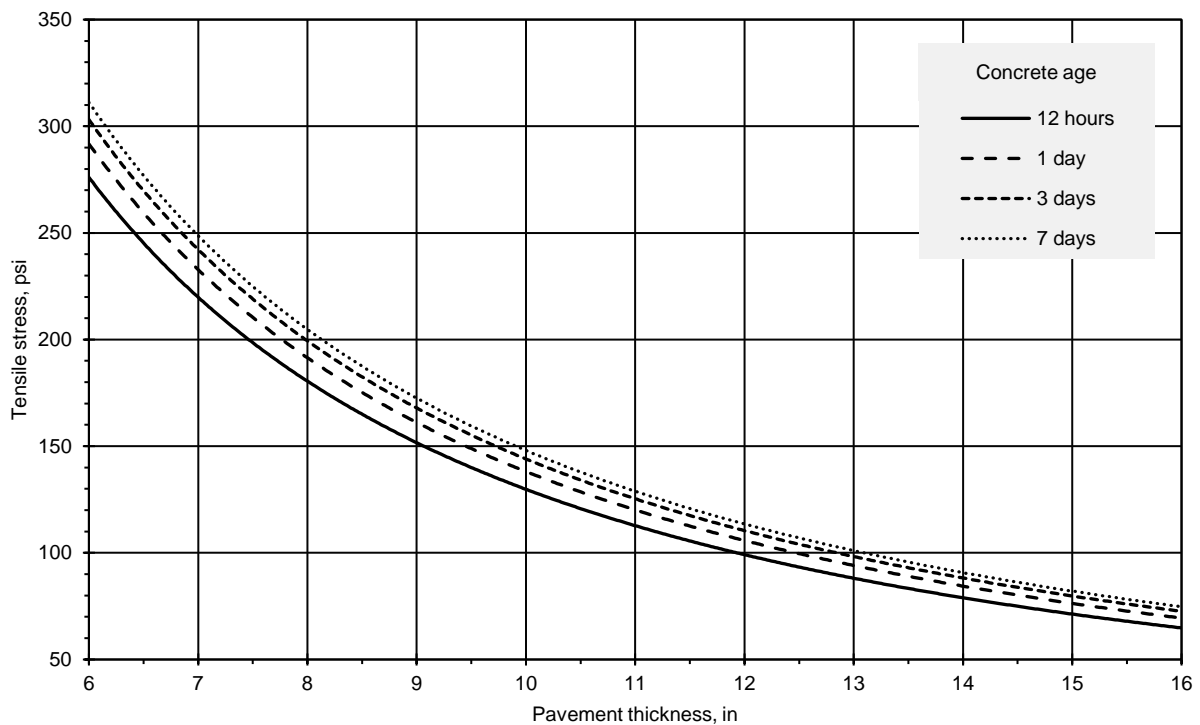
TENSILE STRESSES IN RIGID PAVEMENT CHART
(k = 50 psi/in.)

Figure O-2



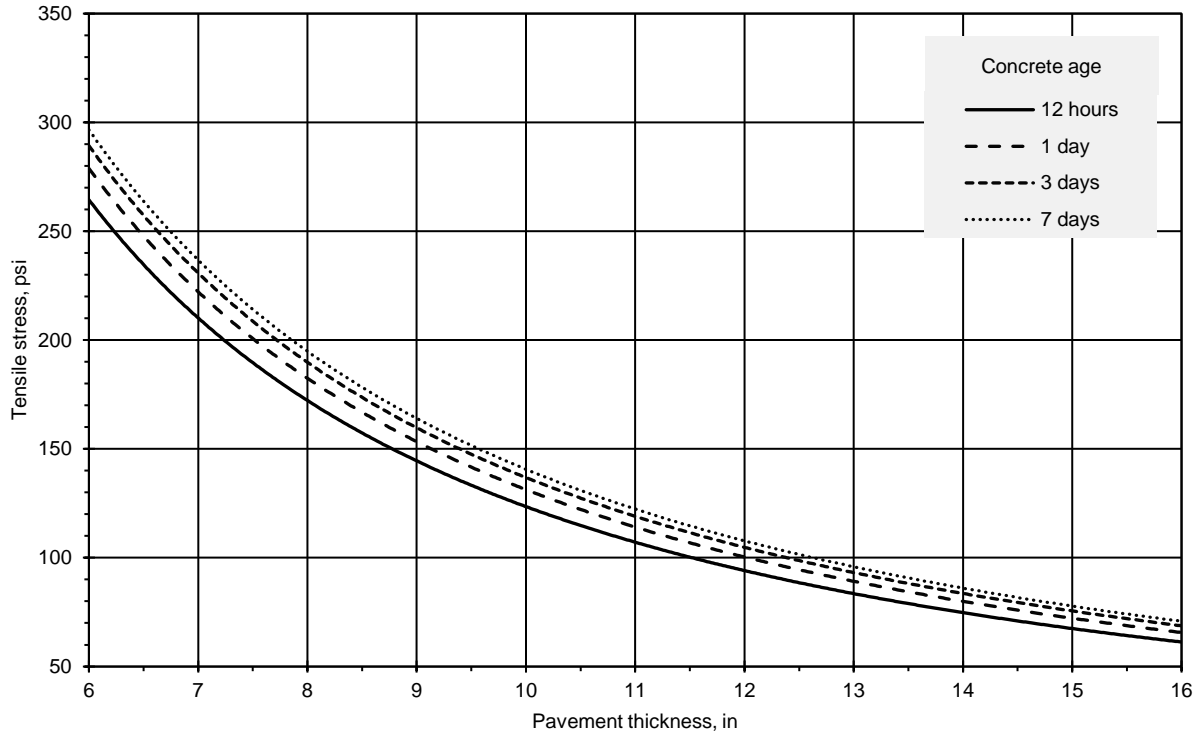
TENSILE STRESSES IN RIGID PAVEMENT CHART
(k = 100 psi/in.)

Figure O-3



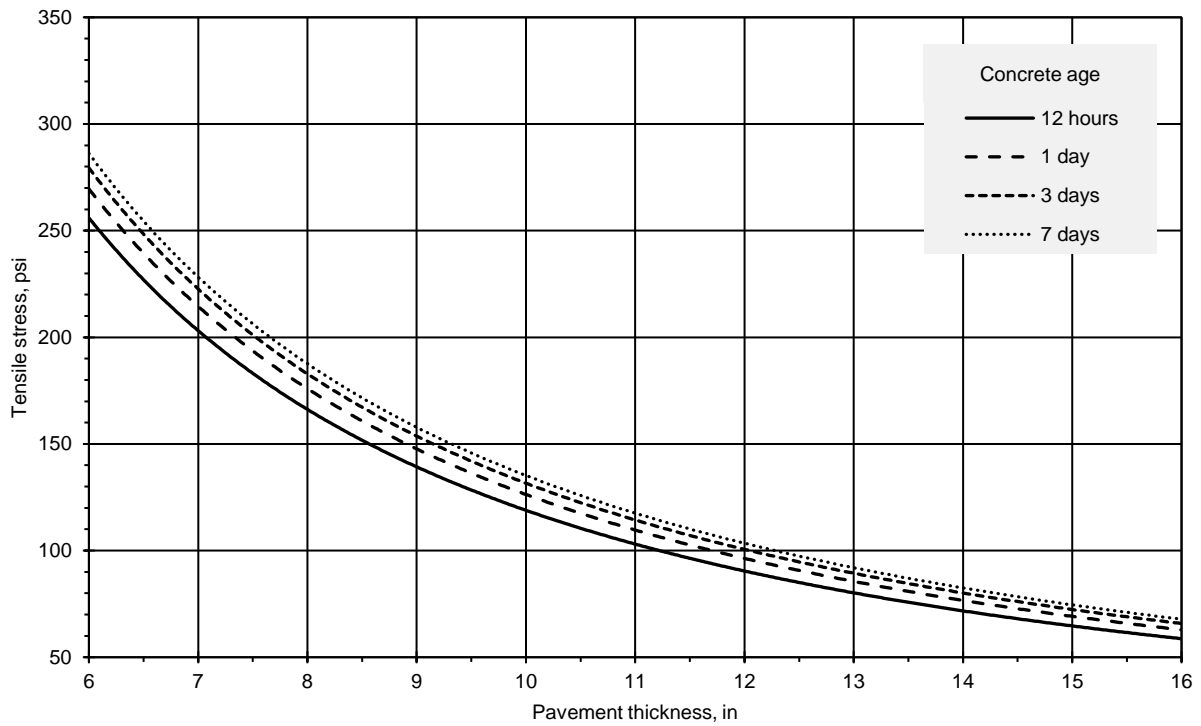
TENSILE STRESSES IN RIGID PAVEMENT CHART
(k = 150 psi/in.)

Figure 8-4



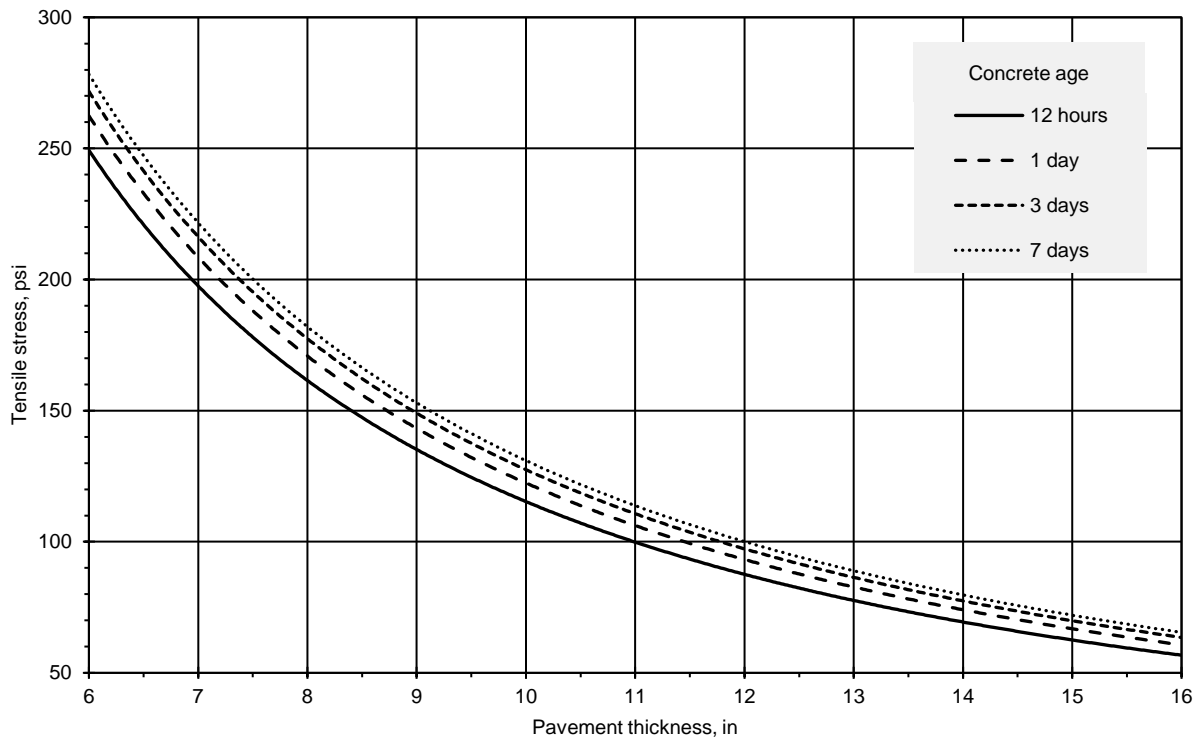
TENSILE STRESSES IN RIGID PAVEMENT CHART
(k = 200 psi/in.)

Figure O-5



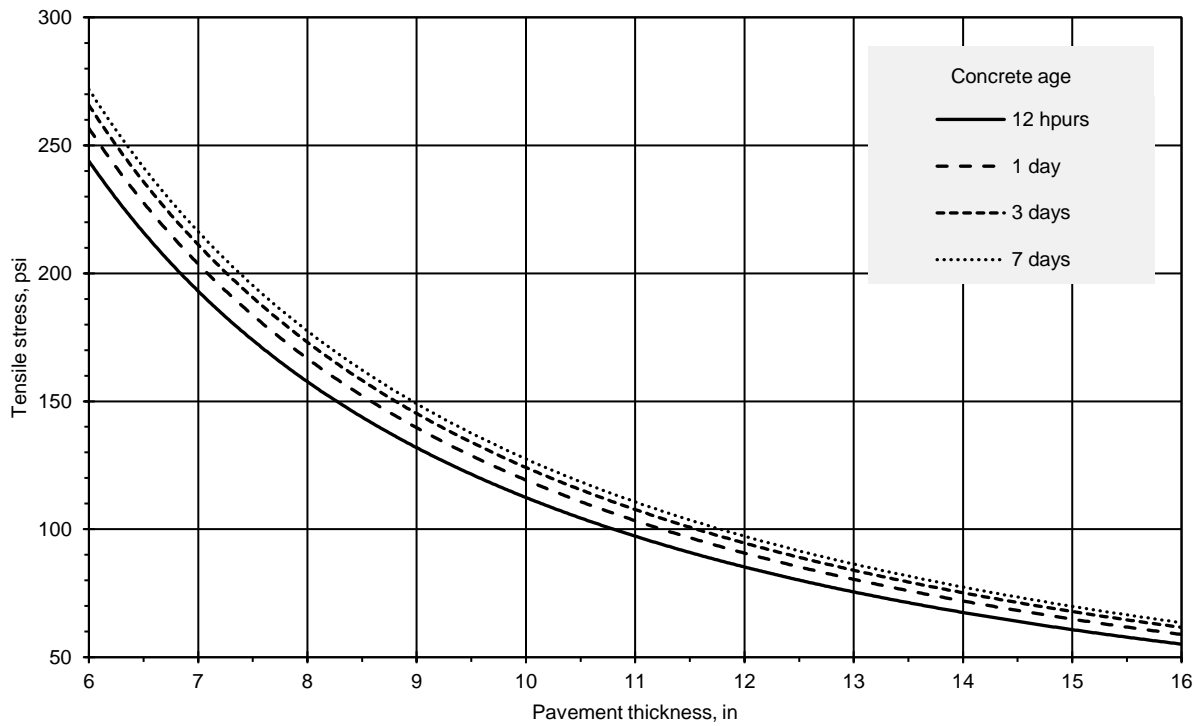
TENSILE STRESSES IN RIGID PAVEMENT CHART
(k = 250 psi/in.)

Figure O-6



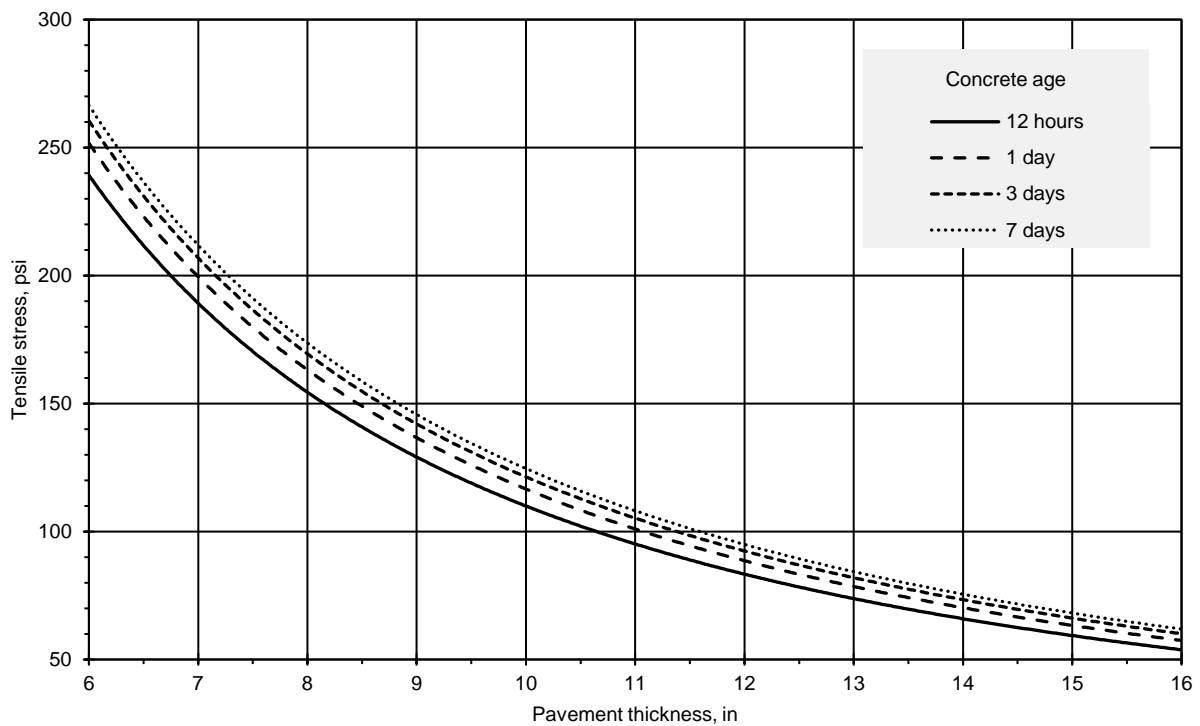
TENSILE STRESSES IN RIGID PAVEMENT CHART
(k = 300 psi/in.)

Figure O-7



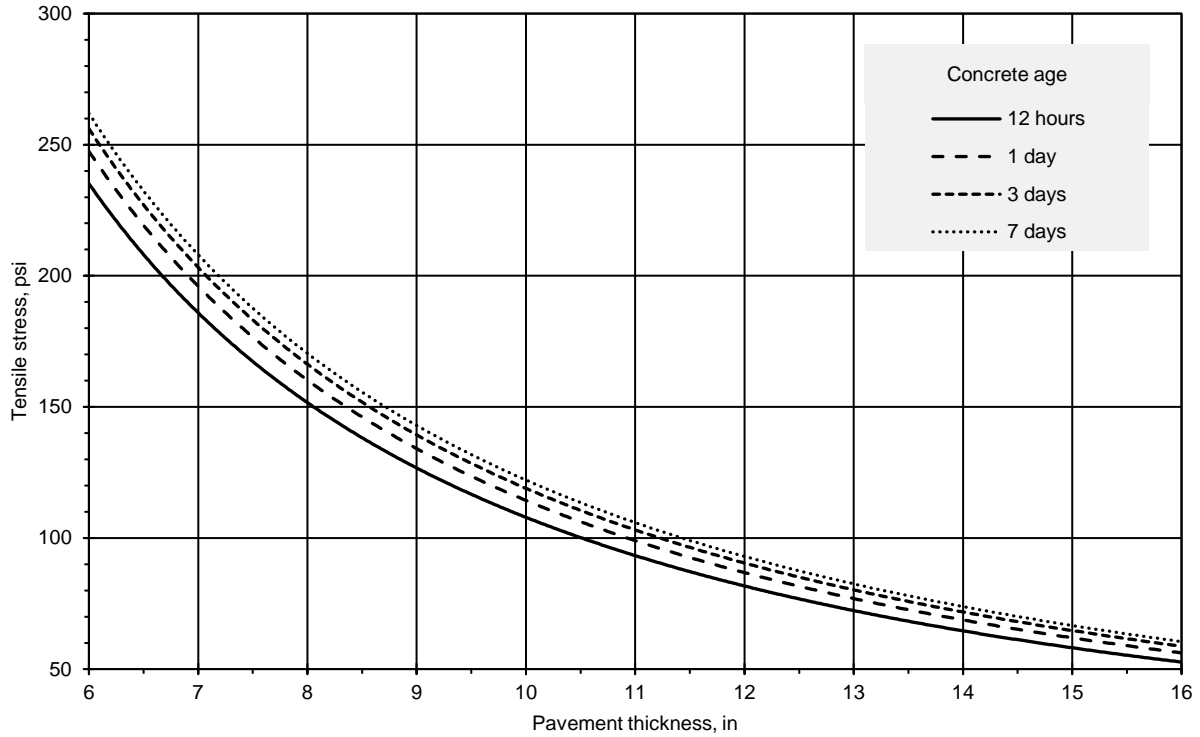
TENSILE STRESSES IN RIGID PAVEMENT CHART
(k = 350 psi/in.)

Figure O-8



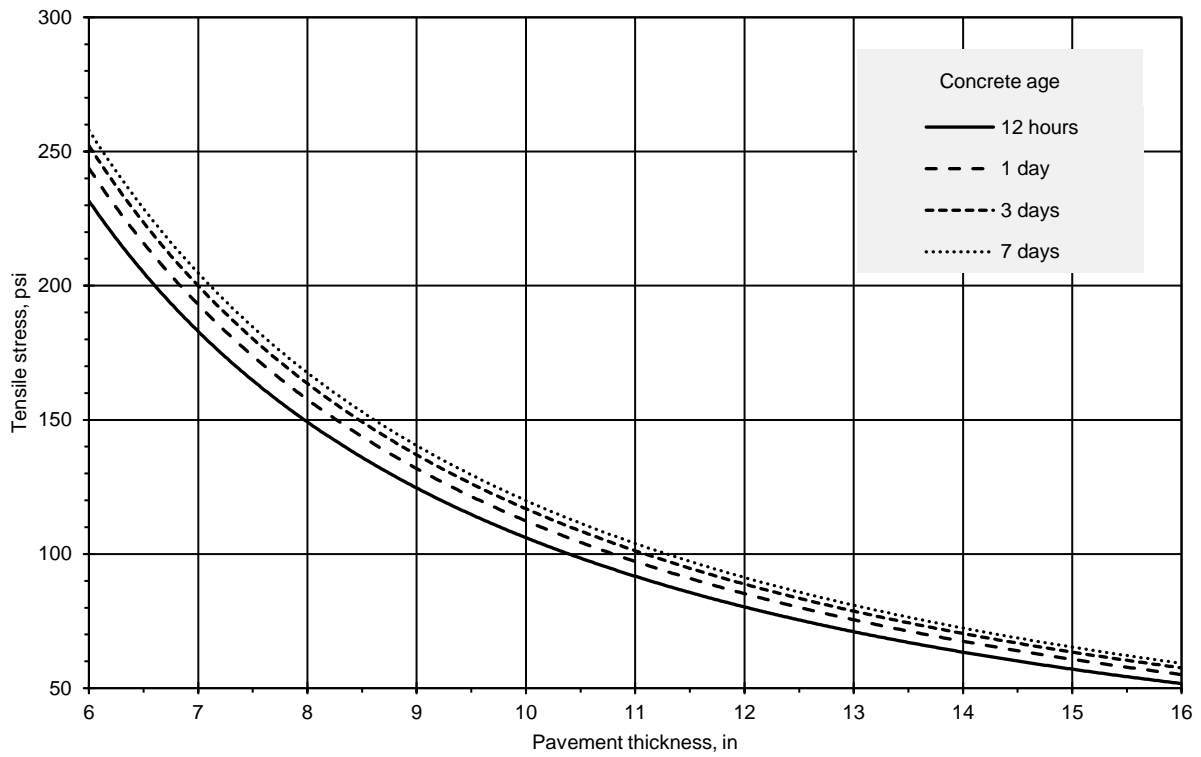
TENSILE STRESSES IN RIGID PAVEMENT CHART
(k = 400 psi/in.)

Figure O-9



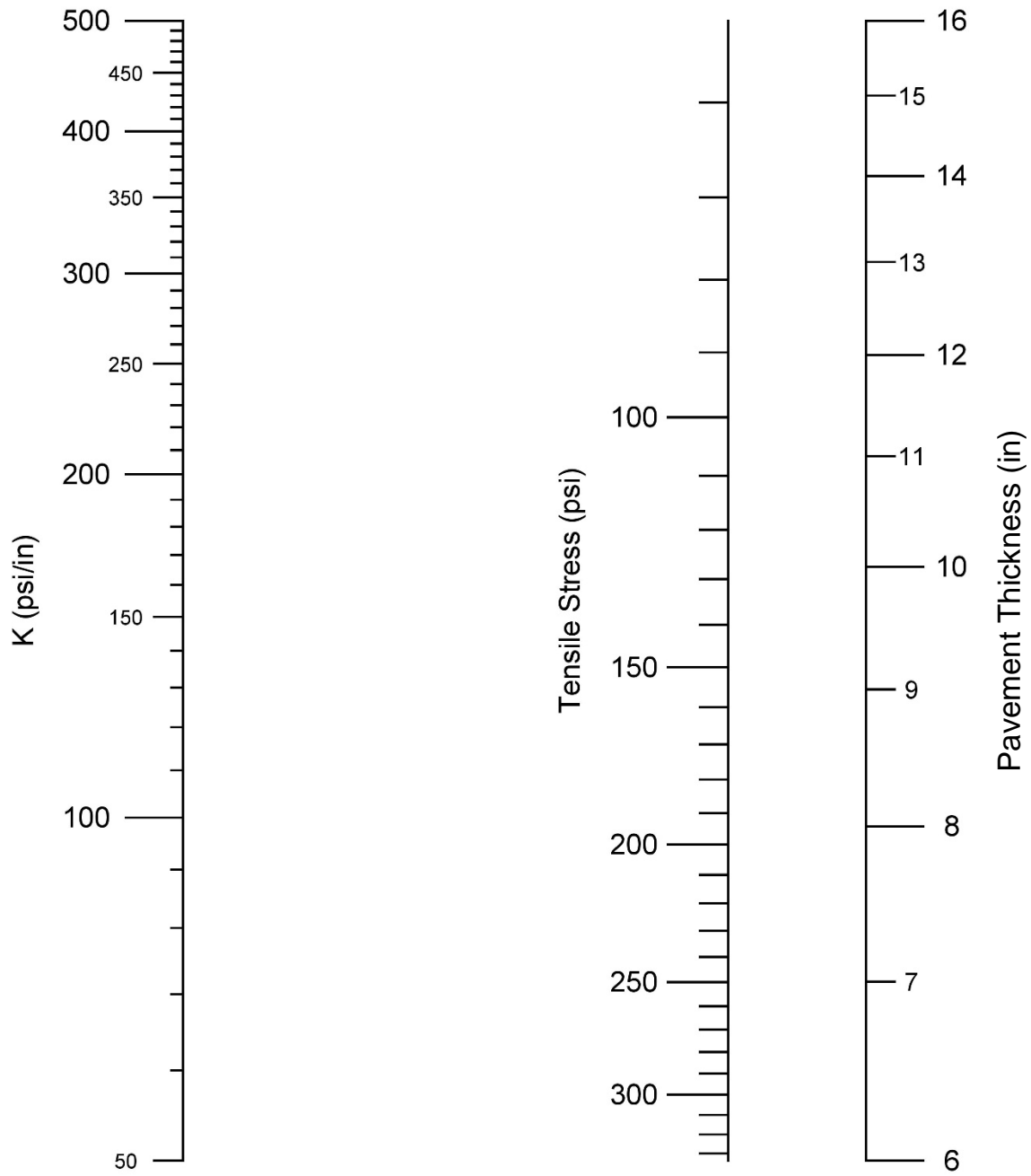
TENSILE STRESSES IN RIGID PAVEMENT CHART
(k = 450 psi/in.)

Figure O-10



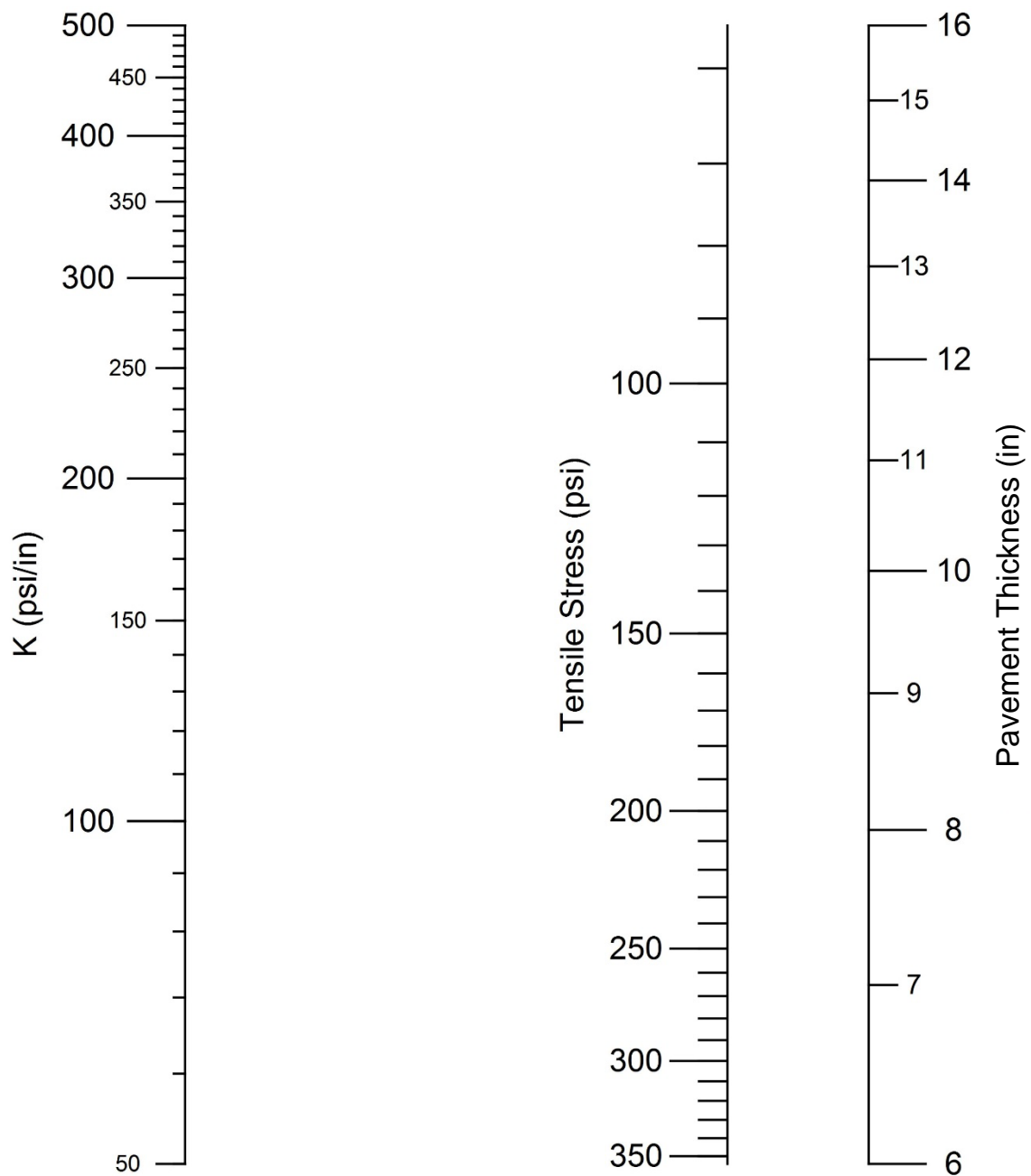
TENSILE STRESSES IN RIGID PAVEMENT CHART
(k = 500 psi/in.)

Figure O-11



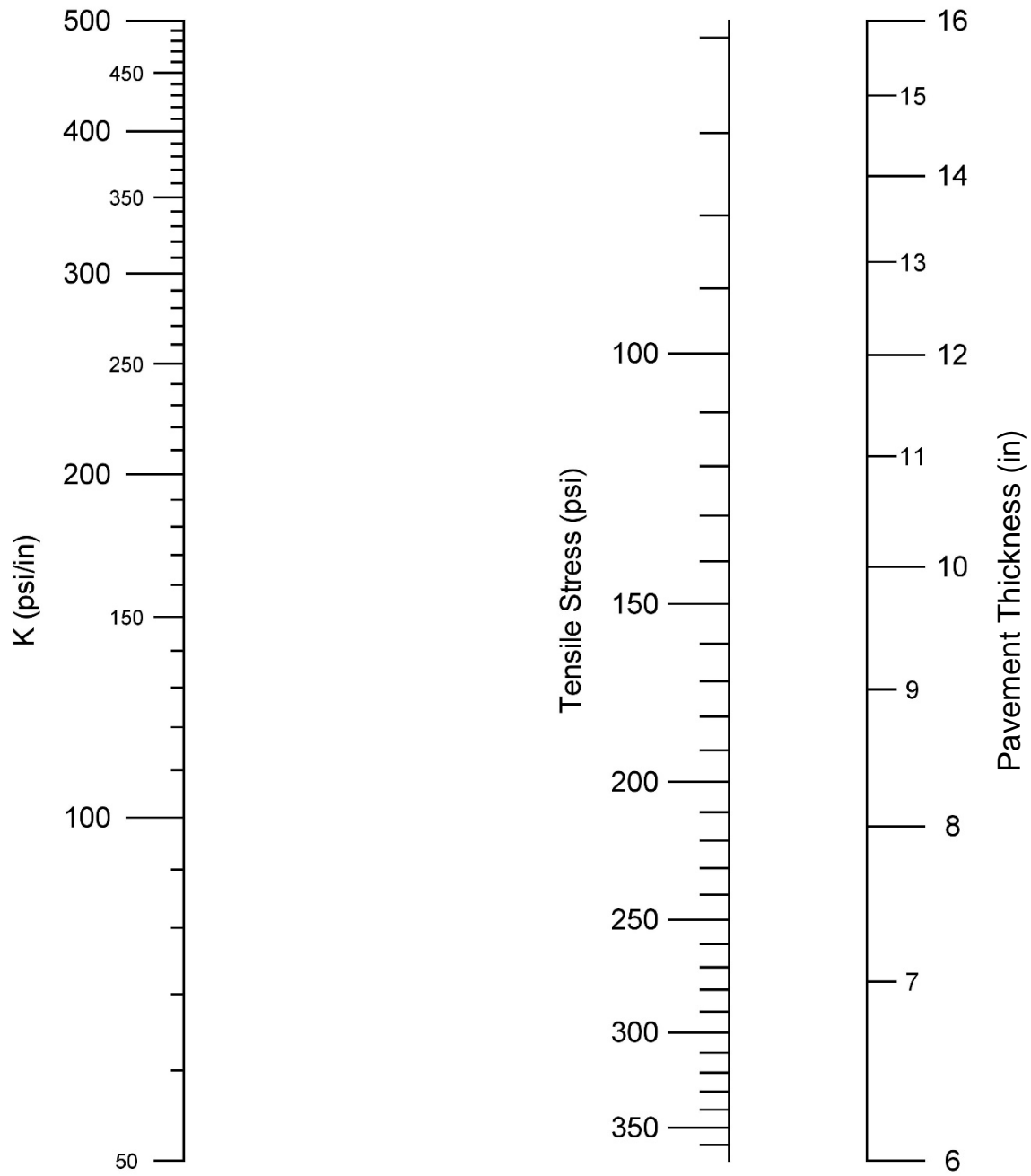
TENSILE STRESSES IN RIGID PAVEMENT NOMOGRAPH
(12 hr concrete age)

Figure O-12



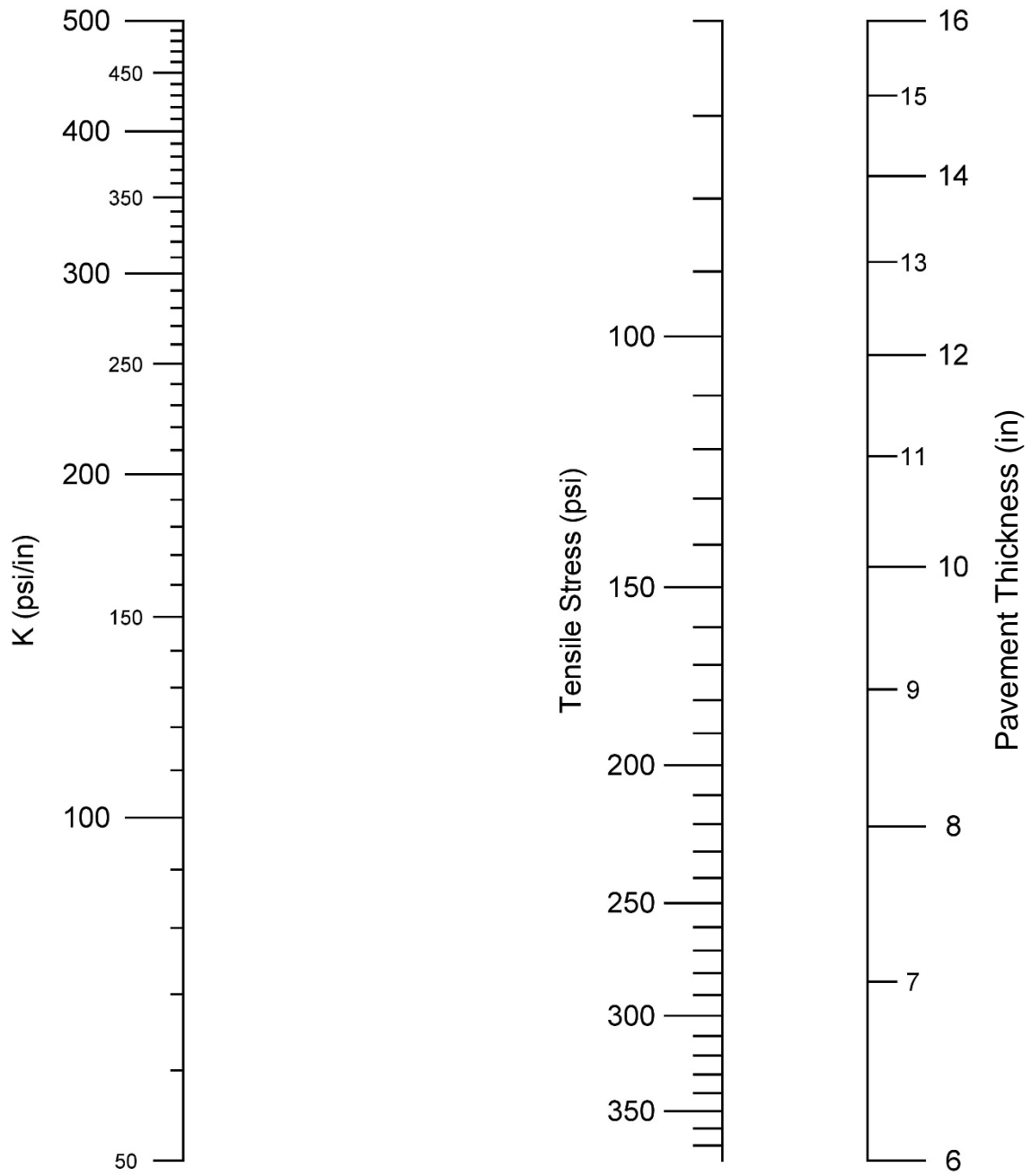
TENSILE STRESSES IN RIGID PAVEMENT NOMOGRAPH
(1 day concrete age)

Figure O-13



TENSILE STRESSES IN RIGID PAVEMENT NOMOGRAPH
(3 days concrete age)

Figure O-14



**TENSILE STRESSES IN RIGID PAVEMENT NOMOGRAPH
(7 days concrete age)**

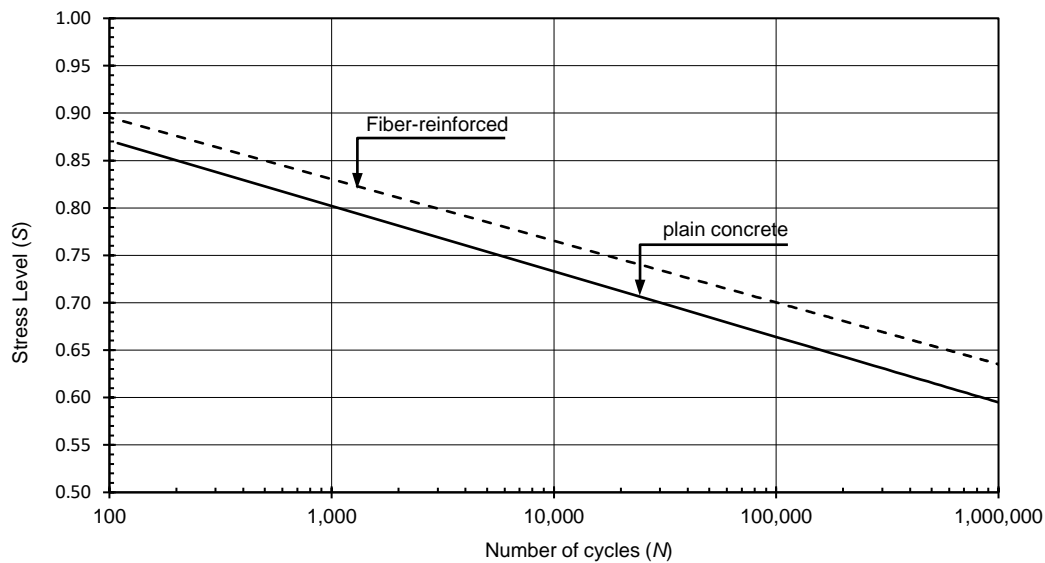
Figure O-15

- Opening to traffic at 12 hr concrete age

Age	Mix type	S-N linear regression relationships	Equation Number
12 hr	Plain	$N = E^{(1.0090-S)/0.030}$	Equation 8-5
	FRC	$N = E^{(1.0257-S)/0.028}$	Equation 8-6

S-N RELATIONSHIPS (12 hr concrete age)

Table O-1



S-N CHARTS (12 hr concrete age)

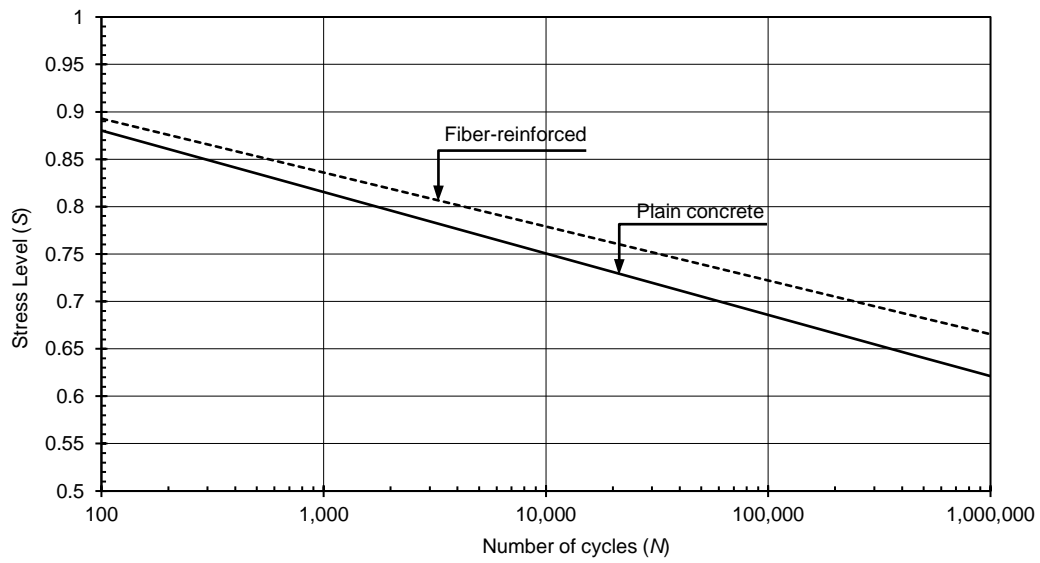
Figure O-16

- Opening to traffic at 24 hr concrete age

Age	Mix type	S-N linear regression relationships	Equation Number
24 hr	Plain	$N = E^{(1.0098-S)/0.028}$	Equation 8-7
	FRC	$N = E^{(1.0066-S)/0.025}$	Equation 8-8

S-N RELATIONSHIPS (24 hr concrete age)

Table O-2



S-N CHARTS
(24 hr concrete age)

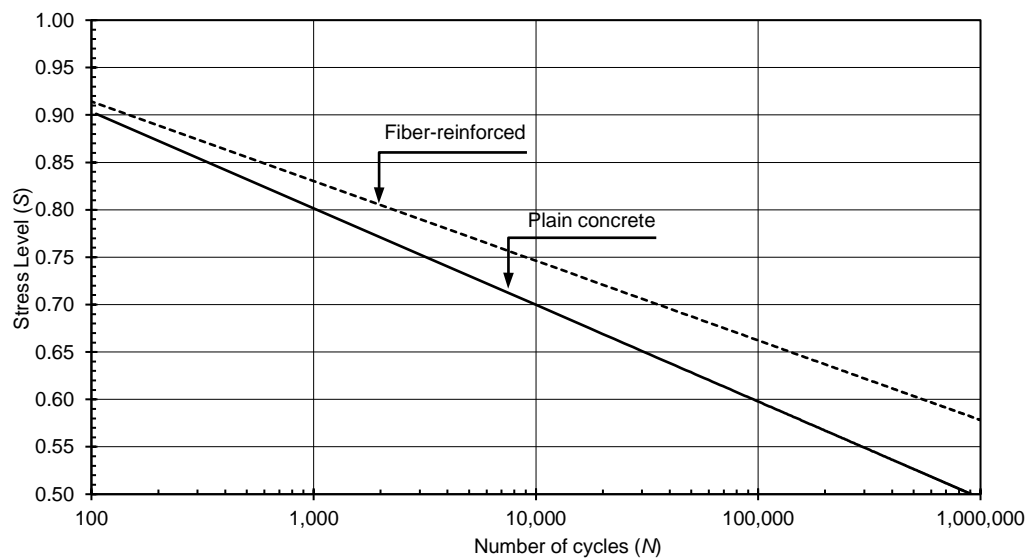
Figure 17

3. Opening to traffic at 3 days concrete age

Age	Mix type	S-N linear regression relationships	Equation Number
3 days	Plain	$N = E^{(1.1072-S)/0.044}$	Equation 8-9
	FRC	$N = E^{(1.0822-S)/0.036}$	Equation 8-10

**S-N RELATIONSHIPS
(3 days concrete age)**

Table O-3



**S-N CHARTS
(3 days concrete age)**

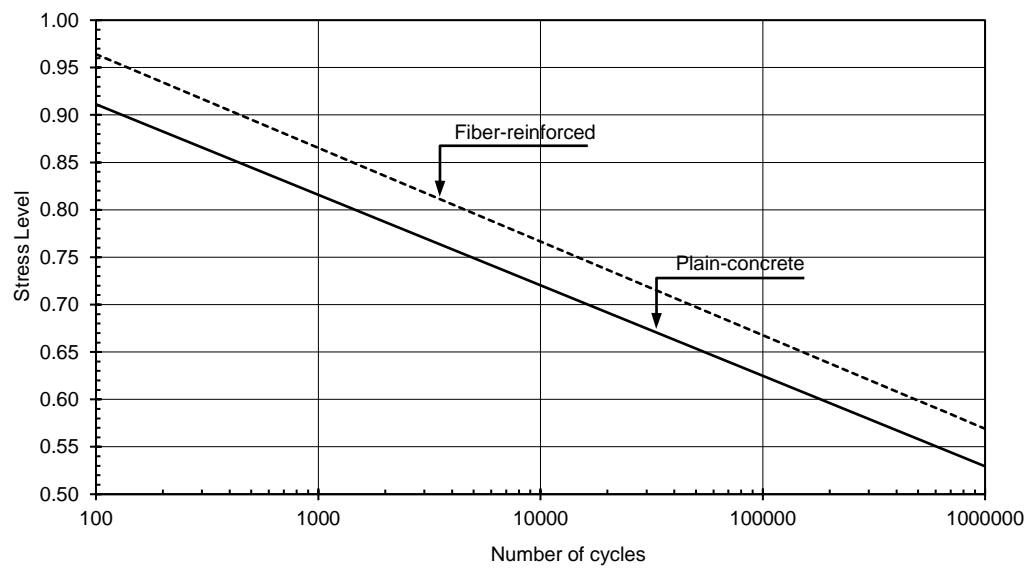
Figure 8-18

4. Opening to traffic at 7 days concrete age

Age	Mix type	S-N linear regression relationships	Equation Number
7 days	Plain	$N = E^{(1.1022-S)/0.041}$	Equation 8-11
	FRC	$N = E^{(1.1616-S)/0.043}$	Equation 8-12

**S-N RELATIONSHIPS EQUATIONS
(7 days concrete age)**

Table O-4




**S-N CHARTS
(7 days concrete age)**


Figure 8-19

APPENDIX P CHEMICAL AND PHYSICAL PORPERTIES OF CEMENTIOUS MATERIALS

Version 6.42



Holcim



Material Certification Report

Material: Portland Cement
Type: I-II

Test Period: 01-Jul-2015
To: 31-Jul-2015

Certification

This Holcim cement meets the specifications of ASTM C150 for Type I-II cement, and complies with AASHTO M85 specifications for Type I-II cement.

General Information

Supplier: Holcim (US) Inc.	Source Location: Ste. Genevieve Plant
Address: 2942 US Highway 61 Bloomsdale, MO 63627	2942 US Highway 61 Bloomsdale, MO 63627
Telephone: 636-524-8155	Contact: Erin Watson
Date Issued: 17-Aug-2015	

The following information is based on average test data during the test period.
The data is typical of cement shipped by Holcim; individual shipments may vary.

Tests Data on ASTM Standard Requirements

Chemical	Physical
Item	Item
SiO ₂ (%)	Air Content (%)
Al ₂ O ₃ (%)	Blaine Fineness (m ² /kg)
Fe ₂ O ₃ (%)	Autoclave Expansion (%) (C151)
CaO (%)	Compressive Strength MPa (psi):
MgO (%)	3 days
SO ₃ (%)	7 days
Loss on Ignition (%)	Initial Vicat (minutes)
Insoluble Residue (%)	Mortar Bar Expansion (%) (C1038)
CO ₂ (%)	
Limestone (%)	
CaCO ₃ in Limestone (%)	
Inorganic Processing Addition (%)	
Potential Phase Compositions ^c :	
C ₂ S (%)	
C ₃ S (%)	
C ₄ A (%)	
C ₄ AF (%)	
C ₂ S + 4.75C ₃ A (%)	

Tests Data on ASTM Optional Requirements

Chemical	Physical
Item	Item
Equivalent Alkalies (%)	False Set (%)

Notes

^a Dashes in the limit / result columns mean Not Applicable.

^b It is permissible to exceed the specification limit provided that ASTM C1038 Mortar Bar Expansion does not exceed 0.020 % at 14 days.

^c Adjusted per Annex A1.6 of ASTM C150 and AASHTO M85.

^d Test result represents most recent value and is provided for information only. Analysis of Heat of Hydration has been carried out by CTLGroup, Skokie, IL.

Equivalent Alkalies (%) Minimum = 0.53, Maximum = 0.57


This data may have been reported on previous mill certificates.

Additional Data


Inorganic Processing Addition Data	Base Cement Phase Composition
Item	Item
Type	C ₂ S (%)
Amount (%)	C ₃ S (%)
SiO ₂ (%)	C ₄ A (%)
Al ₂ O ₃ (%)	C ₄ AF (%)
Fe ₂ O ₃ (%)	
CaO (%)	
SO ₃ (%)	

By _____, Quality Manager

Figure P-1. Physical and chemical properties of type 1 Portland cement



**SKYWAY CEMENT
COMPANY**



Material Certification Report

Brand: GranCem®
Material: Slag Cement
Grade: 100
Date Range: July 1-31, 2015
Lot Number: Multiple Lots

Certification					
This cement meets the requirements of ASTM specification C989 for Grade 100 Slag Cement.					
General Information					
Supplier:	Skyway Cement Company LLC.	Source Location: Skyway Cement Company LLC.			
Address:	3020 East 103rd Street Chicago, IL 60617	3020 East 103rd Street Chicago, IL 60617			
Telephone:	(800)643-1808 x 5910	Contact: Roberto Carrillo			
Date Issued:	25-Aug-2015				
<p>The following information is based on average test data during the test period. The data is typical of slag cement shipped by Skyway Cement Company LLC.; individual shipments may vary.</p>					
Test Data on ASTM Standard Requirements					
Chemical			Physical		
Item	Limit ^A	Result	Item	Limit ^A	Result
Sulfide S (%)	2.5 max	1.02	+45 µm (No. 325) Sieve (%)	20 max	0.65
			Blaine Fineness (m ² /kg)	-	558
Sulfate Ion - SO ₃ (%)	-	0.04	Air Content (%)	12 max	4.17
			Slag Activity Index (%)		
			Avg 7 Day Index	75 min	88
			Avg 28 Day Index	95 min	115
			Compressive Strength - MPa (psi):		
			Slag + Reference Cement		
			7 Day	-	26 (3770)
			28 Day	-	42 (6140)
			Reference Cement ^B		
			7 Day	-	30 (4290)
			28 Day	-	37 (5390)
Reference Cement Qualification Data					
Chemical			Physical		
Item	Limit ^A	Result	Item	Limit ^A	Result
Total Alkalies as Na ₂ O (%)	0.60 - 0.90	0.84	Blaine Fineness (m ² /kg)	-	368
C ₂ S	-	55.3	Compressive Strength - MPa (psi):		
C ₂ S	-	16.6	7 Day	-	30.3 (4390)
C ₃ A	-	7.9	28 Day	34.5 (5000) min	38.9 (5640)
C ₄ AF	-	8.8			
Notes					
^A Dashes in the limits columns means Not Applicable ^B Reference cement results from procedure "Preparation of Specimens". Information on Reference Cement qualification available upon request. Specific Gravity: 2.89 This data may have been reported on previous mill certificates. It is typical of the cement being currently shipped which was produced in July of 2015					

Figure P-2. Physical and chemical properties of slag cement.



I ILLINOIS